LEVEL III

(12) 22

AD A100345

CORRECTION OF PHASE DISTORTION
BY NONLINEAR OPTICAL TECHNIQUES

Hughes Research Laboratories
3011 Malibu Canyon Road
Malibu, CA   90265

DTIC
ELECTED
JUN 17 1981
E

May 1981
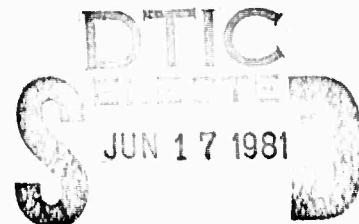
Contract No. N00014–77–C–0593
Final Technical Report
For period 15 July 1977 through 31 December 1980
DARPA Order No. 3427, Amendment No. 5

Approved for public release; distribution unlimited.

Sponsored By

DEFENSE ADVANCED RESEARCH PROJECTS AGENCY
1400 Wilson Boulevard
Arlington, VA   22209

Monitored By

OFFICE OF NAVAL RESEARCH
Boston, MA   02210

DTIC FILE COPY

81 6 16 106

REPORT DOCUMENTATION PAGE	READ INSTRUCTIONS BEFORE COMPLETING FORM

1. REPORT NUMBER	2. GOVT ACCESSION NO. AD-A100 345	3. RECIPIENT'S CATALOG NUMBER

4. TITLE (and Subtitle)	5. TYPE OF REPORT & PERIOD COVERED
CORRECTION OF PHASE DISTORTION BY NONLINEAR OPTICAL TECHNIQUES	Final Technical Report 15 Jul 1977 — 31 Dec 1980
	6. PERFORMING ORG. REPORT NUMBER

7. AUTHOR(s)	8. CONTRACT OR GRANT NUMBER(s)
R.C. Lind, W.B. Brown, C.R. Giuliano, R.K. Jain, J.F. Lam, B.M. Merchant, R.A. McFarlane, T.R. O'Meara, and G.C. Valley	N00014-77-C-0593

9. PERFORMING ORGANIZATION NAME AND ADDRESS	10. PROGRAM ELEMENT, PROJECT, TASK AREA & WORK UNIT NUMBERS
Hughes Research Laboratories 3011 Malibu Canyon Road Malibu, CA 90265	DARPA Order No. 3427 Amendment No. 5 Program Code No. NR 395-578

11. CONTROLLING OFFICE NAME AND ADDRESS	12. REPORT DATE
Defense Advanced Research Projects Agency 1400 Wilson Blvd. Arlington, VA 22209	May 1981
	13. NUMBER OF PAGES 286

14. MONITORING AGENCY NAME & ADDRESS(if different from Controlling Office)	15. SECURITY CLASS. (of this report)
Office of Naval Research Boston, MA 02210	UNCLASSIFIED
	15a. DECLASSIFICATION DOWNGRADING SCHEDULE

16. DISTRIBUTION STATEMENT (of this Report)

Approved for public release; distribution unlimited

17. DISTRIBUTION STATEMENT (of the abstract entered in Block 20, if different from Report)

18. SUPPLEMENTARY NOTES

19. KEY WORDS (Continue on reverse side if necessary and identify by block number)

Nonlinear phase conjugation, Adaptive optics, Laser compensation, SBS, Four-wave mixing.

20. ABSTRACT (Continue on reverse side if necessary and identify by block number)

This is the final report on a program designed to explore a recently recognized property of certain nonlinear optical interactions of generating conjugate wavefronts that can be used to correct optical distortions in laser systems. These distortions include optical train aberrations, laser medium distortions, and atmospheric propagation aberrations. The program was divided into three basic areas that bridge

DD FORM 1473 EDITION OF 1 NOV 65 IS OBSOLETE
1 JAN 73

the gap between a preliminary exploration of the applicable nonlinear processes and realization of their potential usefulness to laser systems. The areas were (1) to measure quantitatively the properties of phase conjugation by four-wave mixing and SBS (2) to develop a theoretical understanding of nonlinear phase conjugation, and (3) to determine the applicability of nonlinear phase conjugation to various systems of interest to DARPA. We made significant advances in each of these areas during this program; these accomplishments are described in this report.

The main accomplishments of this program are listed below·

Experimentally Demonstrated:

Four-wave reflectivity exceeding unity in the green,

Complete aberration correction by four-wave mixing and SBS for severely aberrated beams (∿35X diffraction limit),

Viable approaches to angle offset using four-wave mixing, and

Input/output separation using polarization properties of four-wave mixing.

Theory and Analysis:

Developed fundamental theories of four-wave mixing and SBS

Developed viable approach to doppler compensation using DFWM

Established criteria for probe/pump alignment and coherence requirements in DFWM

Showed feasibility of candidate uplink system concepts

Developed model for phase conjugate resonator showing ability to compensate for intracavity aberration.

FOREWORD

This report was prepared by Hughes Research Laboratories under
Contract No. N00014-77-C-0593. It describes work performed from 1 October 1978
to 31 December 1980. The work performed from 15 July 1977 to 30 September 1978
is covered in the Interim Technical Report dated March 1979. The principal
investigator is R. C. Lind, and the program manager is C. R. Giuliano. The
experimental effort during this reporting period has principally been the work
of R. C. Lind and B. M. Merchant. J. F. Lam, T. R. O'Meara, and W. P. Brown
contributed to further development of the theory of optical phase conjugation.
T. R. O'Meara and G. C. Valley developed and analyzed concepts for laser sys-
tems employing nonlinear phase conjugation. Additional efforts were provided
by R. A. McFarlane and R. K. Jain, who assisted in the analysis and selection
of new conjugator materials.

The authors wish to acknowledge the technical criticism and advisory
support by R. L. Abrams, manager of the Optical Physics Department. We also
wish to thank M. B. White of ONR, the technical monitor, and Col. R. F. Prater
of DARPA for their interest and support in this work.

TABLE OF CONTENTS

LIST OF ILLUSTRATIONS

CHAPTER 1

INTRODUCTION AND SUMMARY

1.1 BACKGROUND

This final report describes work carried out in a new and rapidly growing area of research - wavefront conjugation, or nonlinear phase conjugation (NPC), using nonlinear optical phenomena. Shortly after the first Soviet results were published showing wavefront reversal via stimulated Brillouin scattering (SBS), workers at Hughes Research Laboratories recognized the potential applicability of these phenomena to the fields of lasers and adaptive optics.

The principal attraction for applying nonlinear phase conjugation to adaptive optics is in its potential simplicity. The promise is in replacing the combined functions of wavefront sensors, electronic servos, and deformable mirrors with one element, the nonlinear conjugator. The payoff is especially attractive when one considers applications involving large apertures at visible wavelengths for which thousands of mirror actuators and sensor channels may be required to compensate atmospheric turbulence.

When this program began in 1977 there existed only a handful of technical papers on the subject; at present there are well over 100. Since this program began, the number of nonlinear phenomena known to exhibit phase conjugation has grown from one, i.e. SBS, to several, the most significant of which is degenerate four-wave mixing, DFWM, which is emphasized in this report. The principal thrusts in this program have been directed at answering fundamental questions having to do with the fidelity of the conjugation process and its limitations.

We have quantified the quality of the wavefront compensation that can be achieved with both SBS conjugation and DFWM; and, as described in Chapter 5, we have found the compensation to be essentially perfect - at least two orders of magnitude better than deformable mirrors have demonstrated - when the conjugator is carefully designed and operated under ideal conditions.

However, we have recognized that when operating at high average power levels or under non-standard conditions, in a non-laboratory environment, the actual operation may not produce such complete compensation. Consequently, an important element of this contract has been to identify and quantify potential

error sources. This becomes particularly important once it is recognized that a nonlinear phase conjugator is not adaptive; in a servo sense it is an open loop system, and therefore is not self-correcting.* Most potential error sources stem from causes which are deeply embedded within the physics of the nonlinear phase conjugation process, and we have explored these at considerable length.

Of course, without the availability of a suitable nonlinear material at the desired operating wavelength, a particular application will simply not be feasible. However, conjugation has been demonstrated in many nonlinear materials operating over a wide range of wavelengths as illustrated in Table 1-1. Several new classes of conjugator materials have been identified and experimentally demonstrated under this contract; among these are dyes (e.g., Rhodamine 6G) and semiconductors (e.g., filter glasses). Although the listing in Table 1-1 certainly does not yet cover every laser wavelength of particular interest, it is a rapidly expanding list and there is every reason to believe that a suitable material can be found at any wavelength, given an adequate research effort.

Concurrently with experimental and theoretical work on nonlinear phase conjugation itself, we have explored many system applications. These include many types of oscillator compensation, optical-train and amplifier compensation, and systems wherein compensation of both the laser, the optical train, and an atmospheric path may be achieved. The majority of these applications employ the basic principle illustrated in Figure 1-1. An undistorted reference wavefront enters and propagates through a distorting path; the wave is then conjugated and reflected back through the same distorting path, with the second pass stripping off the wavefront distortions. The beam that exits the path at the end of the second pass is therefore substantially undistorted. If the distorting path includes at least one laser amplifier, and if the reference originates within a laser resonator, then such a concept is called a conjugate resonator. If the clean wavefront is injected via a high-quality oscillator

---

*Phase conjugate systems employing oper-loop conjugators can still be "closed-loop" around the target, in the sense that they may exhibit the classical beam convergence properties on extended targets.

Table 1-1. Summary of Materials in Which Phase
Conjugation Has Been Demonstrated

Wavelength	Laser	Pulsed or cw	Nonlinear Interaction	Nonlinear Medium	Comments
10 μm	CO_2	Pulsed	DFWM	SF_6*	37%, 200kW/cm², 2 cm
			DFWM	HgCdTe*	10%, 100 kW/cm², 0.5 mm
			DFWM	CO_2 (Inverted)	0.5%
			DFWM	Ge	25%, 10 MW/cm², 15 cm
			DFWM	NH_3*	∿1% (Prelim)
			DFWM	$KCl:R_aO_4$	
3.8 μm	DF	Pulsed	DFWM	G_e	
1.06 μm	Nd:YAG	Pulsed	DFWM	Si*	180%, 1 mm, 6 MW/cm²
			SBS	CS_2** CH_4**	10 - 90%
			DFWM	Nd:YAG	∿0.5%
			3 WM	Li Formate	Poor correction
			DFWM	BDN (IR Dye)*	600%, 1 mm, 100 MW/km²
0.69 μm	Ruby	Pulsed	SBS	CS_2**	10-90%
			SBS	CH_4	
			DFWM	Cryptocyanine**	30%
			DFWM	CdS CdSe Glass**	∿5%
			DFWM	CS_2	>100%, 40 cm
5890 Å	Dye	CW	DFWM	Na*	40%, Narrow Band
		Pulsed	DFWM	Na	10⁴%, Narrow Band
5320 Å	Doubled Nd:YAG	Pulsed	DFWM	CdS, CdSe Glasses**	∿30%
			DFWM	Iodine Vapor**	∿0.1%
			DFWM	Rhodamine 6G**	>100%, 1 mm
			DFWM	Rhodamine B**	∿10% (Also 5650 Å)
5100 Å	Dye	Pulsed	DFWM	CdS, CdSe Glass**	∿1%
4880 Å, 5145 Å	Ar⁺	CW	DFWM	Ruby	∿0.2%
			DFWM	BSO	∿1% Slow
			DFWM	$BaTiO_3$	>100% Slow
			DFWM	Liquid Crystals*	∿0.1% Slow

*HRL
**This program.

1-3
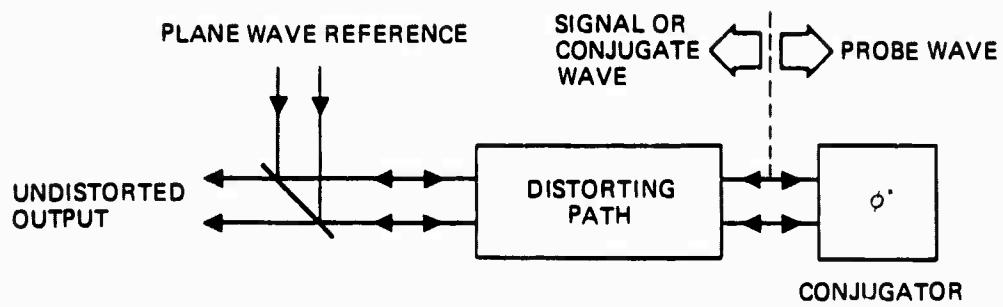
Figure 1-1. Basic compensation principle of most nonlinear phase compensation (NPC) systems.

and the distorting path in Figure 1-1 is a laser amplifier that is double passed, then such a system is called a <u>master-oscillator power-amplifier (MOPA)</u> compensated system.

We have selected two basic classes of such systems for more detailed study in this report: (1) An optical train compensation system with diffraction grating reference injection; and (2) a relay system wherein a large diameter optical beam is transmitted through the atmosphere to a satellite relay. In each application, several types of lasers are considered; and it will be seen that the choice of laser type has a major impact on the key problem areas. Specifically, we will consider optical train compensation for a CW chemical laser (2.7 μm), and a pulsed xenon fluoride laser (0.35 μm). The xenon-fluoride pumped Raman amplifier (operating pulsed) and the xenon fluoride lasers are the lasers that have been considered for the ground-to-satellite relay systems.

1.2 HIGHLIGHTS AND ACCOMPLISHMENTS

The principal accomplishments of this program are listed in Table 1-2. A brief description of the key results and the subjects investigated by chapter is given below.

Chapter 2 discusses the basic DFWM response. The analogy of four-wave mixing and holography is discussed by the now well-known dual grating picture. Formulas are given for predicting the conjugate reflectivity, including the effects of atomic/molecular motion. From this, one finds that to achieve large conjugate reflection coefficients, a large absorption coefficient is required, operation off line-center is necessary, intensities near the saturation intensities of the medium are needed, and the ratio of the characteristic motion time across the grating to the relaxation time of the medium (T_1) should be large. Polarization expressions governing the third-order process are derived. We show that polarization rotation of the conjugated signal can be achieved by appropriate choice of pump polarizations and medium properties. A theoretical development of the behavior of four-level systems is also presented.

Table 1-2. Principal Accomplishments

Experimentally Demonstrated:

Four-wave reflectivity exceeding unity in the green

Complete aberration correction by four-wave mixing and SBS for severely aberrated beams ($\sim$35X diffraction limit)

Viable approaches to angle offset using four-wave mixing

Input/output separation using polarization properties of four-wave mixing

Theory and Analysis:

Developed fundamental theories of four-wave mixing and SBS

Developed viable approach to doppler compensation using DFWM

Established criteria for probe/pump alignment and coherence requirements in DFWM

Showed feasibility of candidate uplink system concepts

Developed model for phase conjugate resonator showing ability to compensate for intracavity aberration

For Chapter 3 an extension of the basic DFWM theory presented in Chapter 2, including the effects of pump attenuation and depletion, is described. The four-coupled wave equations that describe the evolution of the forward pump, backward pump, probe and conjugate signal are solved numerically. The results show that where resonances leading to divergent solutions were predicted in the non-depleted theory of Chapter 2, finite reflectivities are obtained, as would be expected when pump depletion is accounted for. The maximum reflectivity that could be expected when including the depletion of the pump energy is calculated. From these results it is expected that overall efficiencies would not greatly exceed $\sim$20% when the conjugate reflectivity is 50%.

Chapter 4 explores the consequences of deliberately or accidentally introduced modifications to the simple DFWM response. It is shown that geometries which employ small angular separation between probe and pumps lead to reduced sensitivity to pump angular alignment. Further, small tilts and curvatures can be added to one or both pumps and accurately transferred onto the conjugated wavefront as an "override" on the basic conjugated output. The limitations on both types of override are theoretically defined in terms of a loss in conjugator reflectivity and in transfer precision. The reflectivity limitations on a tilt override are also verified experimentally. More importantly, it is shown that if one allows for complete freedom to adjust probe and pump angles in a 3-dimensional geometry, it is possible to achieve tilt overrides without incurring any penalty in reflectivity. That is, phase matching can be maintained for large probe-to-signal offset angles.

Another modification to the basic DFWM system is a frequency offset between the probe and the pumps. Such a nondegenerate operation can again occur from either non-intentional causes - for example Doppler shifts via moving references - or can be deliberately introduced. In all cases the signal wave is offset by an equal frequency shift to the other side of the pump frequency. But its intensity may be appreciably reduced if the probe offset is large. This occurs because (1) the frequency offset typically produces a phase mismatch within the mixer volume, and (2) with two-level systems the dynamic gratings formed within the mixer can only respond to frequency offsets smaller than the inverse of the relaxation rate, T_1. It is shown that the first limitation can be avoided by a proper choice in mixer geometry (for a single

line offset), while the second can be essentially avoided by employing a three-level or two-photon mixing process.

In Chapter 5 we give a detailed discussion of the experimental measurements performed. Measurements of far-field beam profiles indicate that the phase conjugate corrective properties give diffraction limited performance for strongly aberrated beams for moderate reflectivities. We have obtained DFWM signals in several materials in the blue-green wavelength region including dyes, ions in solution, liquids, I_2, and semiconductors. Greater than unity reflectivities are demonstrated. The polarization rotation concept is demonstrated in both dye and semiconductor mixers. The theoretical predictions of amplitude reduction with pump angle misalignment as discussed in Chapter 4, are verified. In addition, the high efficiency large angle offset is demonstrated with 3-dimensional phase matched geometry.

Experiments are also performed in which the probe beam is obtained from one laser, and the pump beam from a second laser. In this case, DFWM signals are obtained only when the frequency difference between the two lasers is less than $1/T_1$ consistent with theoretical predictions of Chapter 4.

Chapter 6 explores many potential applications for (NPC) systems in compensating high energy lasers, and their associated optical trains and transmission paths. These applications fall basically into three categories: (1) local corrections for optical defiguring or local aberrating paths (e.g., laser media); (2) systems for transmitting power to a satellite or a relay satellite with compensation for path distortions up to, but not including, the relay mirror; and (3) compensation for all classes of distortion in target-referencing systems. Key problem areas in these categories are identified. We find that the first two categories of application appear to offer the greatest near-term promise, and we have selected example systems from each category for more detailed investigation. We have concentrated on applications to lasers operating at visible (or shorter) wavelengths, since it is at these wavelengths that the path compensation advantages of NPC systems most strongly dominate those of conventional adaptive optic systems.

Systems that combine nonlinear phase conjugators with one or more Raman amplifiers are discussed in Chapter 7. The most important requirement on the Raman amplifier in these systems is that the amplifier introduce only

reciprocal phase fluctuations that can be cancelled by the phase conjugation. This requirement is shown to restrict pump temporal fluctuations to slower than the inverse of the Raman linewidth, and to restrict pump irradiances to less than a few hundred MW/cm^2. Gain and efficiency considerations for forward Raman amplifiers are shown to require gain coefficient-irradiance-length products of about ten, for good pump-to-Stokes conversion. Saturation and parasitic mode effects are discussed. Finally, illustrative calculations for conversion of excimer pulses to the blue-green wavelength band are given.

CHAPTER 2

RESPONSE OF NONLINEAR MEDIUM

In this Chapter we discuss the basic process of DFWM and examine how DFWM relies on the third-order nonlinearity of the medium (χ^3) to generate the phase conjugate signal that we are interested in. Most of the work discussed in this section was performed under this contract. However, certain aspects were performed with internal funding, but are included to give a complete picture of the processes involved. These will be indicated as the discussion proceeds. We have been primarily interested in resonant processes during this program, and most of the discussions and theoretical developments to follow relate to resonant interactions.

This Chapter is divided into three sections. In the first section a physical description of DFWM and its important properties are given. The second section presents a self-consistent theoretical derivation of the third-order polarization expression, together with density matrix calculations appropriate to DFWM for homogeneously and inhomogeneously broadened systems. This derivation is the foundation for the theoretical considerations that follow in this report, since it presents the basic response of the nonlinear medium. Finally, the third section gives a derivation of the DFWM response to four-level systems.

2.1 PHYSICAL INTERPRETATION OF DFWM

The basic geometry and terminology for four-wave mixing are presented in Figure 2-1 and will be used repeatedly throughout this report. The interaction consists of mixing three input waves to yield a fourth output wave. The three input waves consist of two pump waves (generally in a counterpropagating geometry), E_f, the forward pump, E_b, the backward pump; and a probe wave, E_p, entering at an arbitrary angle to the pumps. These waves couple through the third-order polarization to yield a fourth wave - a signal wave, E_s - that is proportional to the complex conjugate of E_p. A derivation of the polarization follows in Section 2.2. Here we assume the interaction exists and give a simple physical explanation for it.

$\vec{E}_f$

$\vec{E}_b$

NONLINEAR
MEDIUM

$\vec{E}_p$

$\vec{E}_s$
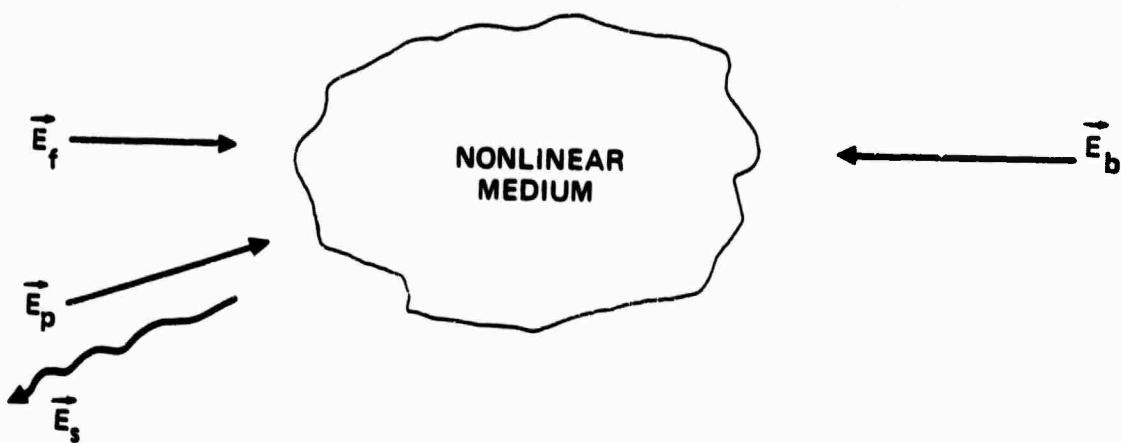
Figure 2-1. The interaction geometry for coplanar
four-wave mixing process.

The physical coupling of the waves stems from the fact that either the refractive index or absorption coefficient of a material changes with light intensity. Consider the effects of saturated absorption or dispersion (other processes such as thermal effects also occur). We assume that E_p, E_f, and E_b are all at the same frequency (consequences of relaxing this requirement are discussed later), and thus they interfere in the nonlinear medium to form a spatial intensity modulation pattern. Saturation of an atomic resonance leads to spatial modulation of the medium complex refractive index, either dispersive, absorptive, or both. This spatial modulation leads to a dual grating or volume hologram picture of DFWM as shown in Figure 2-2. E_p and E_f form a relatively large-period grating exactly spaced (phase-matched) to create Bragg scattering of E_b into E_s. The scattered wave E_s is the phase conjugate of E_p. Thus in the holographic sense, E_b is the readout beam for the hologram formed by E_f and E_p. Similarly, the waves E_p and E_b form a small-period grating with spacing and orientation to precisely scatter E_f into E_s. There is also a third grating resulting from the interference of waves E_f and E_b, which does not contribute to this process since it is not phase matched for scattering of E_s or E_p.

In the figure, the formation and readout processes are shown separately for simplicity, although they occur at the same time. As in conventional holography, the grating planes have a separation given by $D = \lambda/(2 \sin \theta/2)$. It will be shown in Section 2.2 that additional mechanisms lead to DFWM signals that do not have a volume hologram analogy. One such contribution is caused by a two-photon coherent interaction where the pump frequency is adjusted to a two photon resonance in a medium. This type of interaction leads to an interesting system application that will be described later in this report.

For the present discussion, we confine our attention to the volume hologram picture. Most of the observed phenomena discussed in this report are generated by this interaction, but are not always caused by the saturable absorption mechanism.

It is frequently of interest in applications of phase conjugation to obtain a high value of the reflected conjugate signal E_s. Throughout this report we shown derivations that lead to a determination of this reflected signal, as well as experimental investigations of reflectivities. The simplest

FORMATION

(a) (b)

FORWARD PUMP

θ

PROBE

D

BACKWARD PUMP

PROBE

READOUT

CONJUGATE

BACKWARD PUMP

FORWARD PUMP

CONJUGATE

GRATING SPACING D = $\lambda/2$ SIN $\theta/2$
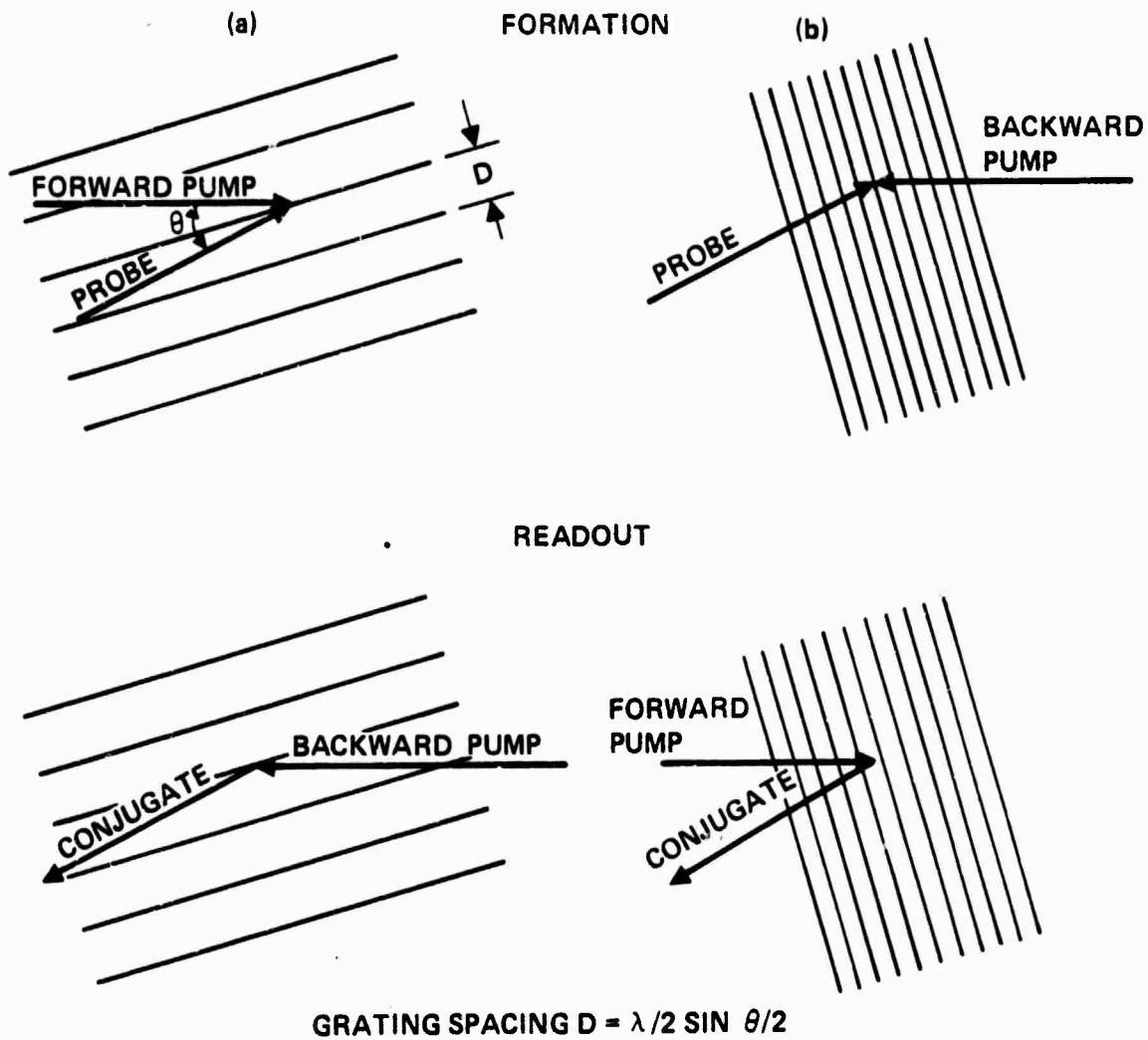
Figure 2-2. Dual grating picture of the four-wave mixer scattering system, (a) forward pump probe grating formation, (b) backward pump probe grating formation.

case, for which an exact solution can be obtained, is for a two-level saturable absorber. In particular, a coupled mode theory for DFWM in a two-level absorbing (or amplifying) system of atoms has been developed,[2-1] wherein the nonlinear medium is a saturable absorber or an inverted (laser) medium with a resonant enhancement at each single-photon step. The solutions indicate that amplified reflection, oscillation, and phase conjugation occur even in the presence of strong absorption. The cited theory shows that the magnitude of the phase-conjugate signal is a function of three parameters: The line-center field absorption or gain (laser media) coefficient-interaction length product, $\alpha_o L$; the ratio of pump intensity to line-center saturation intensity, $I_{f,b}/I_{sat}$, where I_{sat} is proportional to $(1/T_1 T_2)$ and T_1 and T_2 are the longitudinal and transverse relaxation time; and the position in frequency of the pump relative to the line-center frequency of the saturable absorbe $\delta = (\omega - \omega_o)/\Delta\omega$, where $\Delta\omega$ = collision-broadened or natural linewidth. From this work the reflectivity (defined as I_s/I_p) is given as

$$R = \frac{|K \sin \omega L|^2}{|\omega \cos \omega L + \alpha_R \sin \omega L|^2} \quad , \tag{2-1}$$

where

$$K^* = i\alpha_o \left(\frac{1 - i\delta}{1 + \delta^2}\right) \frac{2I/I_{sat}}{\left(1 + 4I/I_{sat}\right)^{3/2}} \quad , \tag{2-2}$$

$$\alpha \equiv \alpha_R - i\alpha_I = \alpha_o \frac{(1 - i\delta)\left(1 + 2I/I_{sat}\right)}{\left(1 + \delta^2\right)\left(1 + 4I/I_{sat}\right)^{3/2}} \quad , \tag{2-3}$$

and

$$\omega = \left(|K|^2 - \alpha_R^2\right)^{1/2} \quad . \tag{2-4}$$

As mentioned, obtaining a high value of reflectivity is generally desired. This is best obtained in a medium characterized by a large line center absorption coefficient and a low saturation intensity. In such a medium, it is advantageous to operate with pump and probe frequencies detuned far from line center, which leads to a dispersive grating in the medium. When there is a population inversion rather than absorption, the optimum operating conditions are significantly altered. In particular, low-intensity operation near line center is preferred. Figure 2-3 shows a representative calculation for an absorption case.

The first extension to this theory[2-2] (performed on this program) which explains motion effects, is a process that can lead to a reduction of the reflectivity. With degenerate operation, the interference patterns between pump and probe waves are fixed in space; if the atoms were stationary, the intensity-induced population gratings would also be fixed. If, because of thermal effects, the atoms can move an appreciable fraction of a grating period during an excited state lifetime, we have a grating wash-out effect that degrades the DFWM signal. The degree of degradation depends on how long it takes an atom to move a grating period, which, in turn, depends on the size of the grating period. Since the grating spacing D varies from $\lambda/2$ for $\theta \to 180°$, to 0 for $\theta \to 0$, we would expect the large-spaced grating (Figure 2-2(a)) to suffer less from degradation caused by atomic motion than the closely spaced grating (Figure 2-2(b)). The contributions from each grating have been separately measured in gaseous media and semiconductors and will be discussed in Chapter 5. The calculated results, verifying this intuitive argument, are given in the following section. In addition, experiments using SF_6 are in agreement with this theory.[2-3]

2.2   THEORETICAL DEVELOPMENT OF DFWM

In this section a self-consistent theoretical development of the third-order polarization responsible for the generation of DFWM signals to be discussed throughout this report is given. Various polarization options are discussed, each of which leads to expanded systems applications. In addition, a derivation of the degradation effects caused by atomic motion is presented.
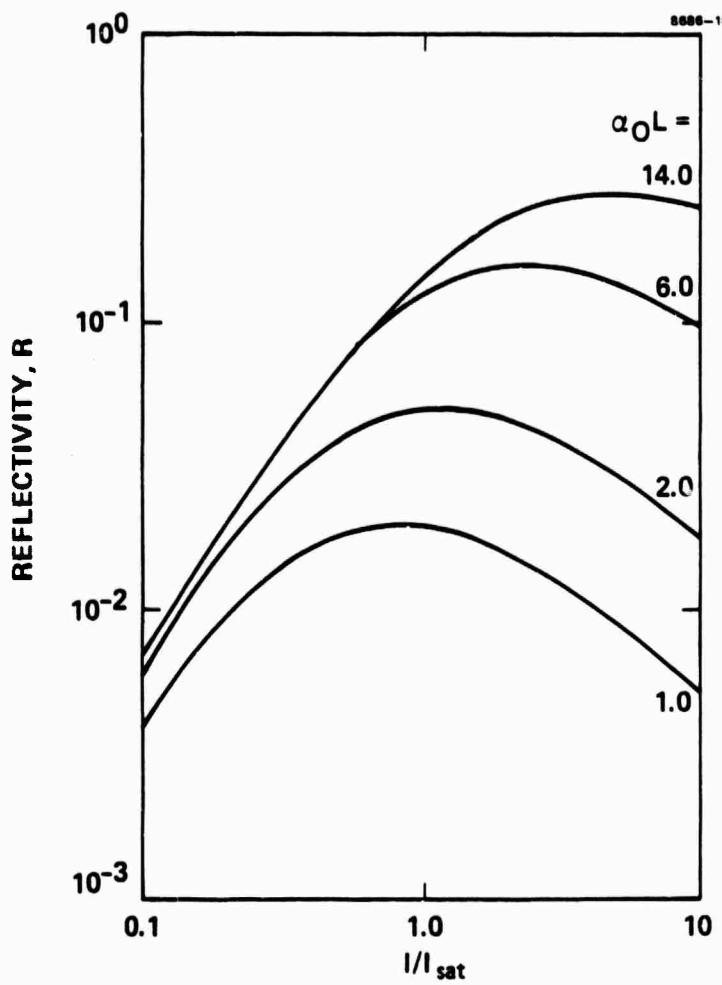
Figure 2-3. Calculated reflectivity versus normalized pump intensity for line-center operation and various values of small signal field absorption.

2.2.1 Polarization Effects in DFWM

The study of the nonlinear response of an optical medium in the presence of applied and generated radiation fields must necessarily take into account the relative orientation of the electric field polarizations, as well as the spatial symmetry of the medium under considerations. A fundamental understanding of the vectorial behavior of the polarization density $\vec{P}$ $(\vec{R},t)$ is intrinsically connected with a characterization of the tensorial properties of the susceptibility $\overleftrightarrow{\chi}$. This section presents a detailed analysis of the response of the medium as applied to DFWM in resonant and nonresonant media. In the case of non-resonant media, we shall apply the well-known spatial symmetry properties of the susceptibility tensor for isotropic and homogeneous media. In the resonant case, we will derive the response from a quantum mechanical calculation via perturbation theory. The results are compiled in a table that describes the electric field polarization of the generated signal as a function of the electric field polarizations of the input fields.

We consider the medium as a collection of harmonic oscillators. For a single harmonic oscillator, having a natural frequency ω_o and a damping rate γ, and acted upon by an external radiation field $E(t)$, the equation of motion is given, by Newton's second law of motion, as

$$\frac{d^2r}{dt^2} + \gamma \frac{dr}{dt} + \omega_o^2 r = \frac{q}{m} E(t) \quad , \tag{2-5}$$

where r is the displacement from equilibrium, q is the electronic charge, and m is the electronic mass. The response of the oscillator is given by

$$r(t) = \int_{-\infty}^{\infty} dt \; G(t-t') \; E(t') \quad , \tag{2-6}$$

where $G(t-t')$ is the Green's function that describes the unit response given by the solution of

$$\frac{d^2G}{dt^2} + \gamma \frac{dG}{dt} + \omega_o^2 G = \frac{q}{m} \delta(t-t') \quad , \tag{2-7}$$

where $\delta(t-t')$ is the Dirac delta function. If we consider an ensemble of N identical harmonic oscillators in the medium subjected to the same radiation field and neglect cooperative effects, we obtain the temporal response of the medium,

$$P(t) = Nqr(t) = \int_{-\infty}^{\infty} dt' \, NqG(t-t') \, E(t') \quad . \tag{2-8}$$

Equivalently, we can obtain the frequency response by introducing a Fourier transform in Equation (2-8). In this case we define the electric field $E(t')$ to be

$$E(t') = \int_{-\infty}^{\infty} d\omega \, E(\omega) \, e^{i\omega t'} \quad . \tag{2-9}$$

Then Equation (2-8) becomes

$$P(t) = \int_{-\infty}^{\infty} d\omega \int_{-\infty}^{\infty} dt' \, NqG(t-t') \, e^{-i\omega(t-t')} E(\omega) \, e^{i\omega t} \quad , \tag{2-10}$$

where we have used the identity $e^{i\omega t} e^{-i\omega t} = 1$. When we introduce a change of variable $t-t' \rightarrow \tau$ and define the frequency response of the medium as

$$\chi(\omega) = \int_{-\infty}^{\infty} d\tau \, NqG(\tau) \, e^{-i\omega\tau} \quad , \tag{2-11}$$

2-9

and the frequency spectrum of the temporal response of the medium is

$$P(\omega) = \chi(\omega)\, E(\omega) \quad . \tag{2-12}$$

Considering that not all media are necessarily isotropic in nature, we define the linear response as

$$P_i(\vec{R},t) = \int_{-\infty}^{\infty} dt'\, R_{ij}(t-t')\, E_j(\vec{R},t') \quad , \tag{2-13}$$

where $R_{ij}(t-t')$ is a second rank tensor describing the linear response of the medium. Its Fourier transform (frequency domain) is called the linear susceptibility $\chi_{ij}(\omega)$. In a similar manner, one can define the third order response to be given by

$$P_i(\vec{R},t) = \int_{-\infty}^{\infty} \int_{-\infty}^{\infty} \int_{-\infty}^{\infty} dt_1 dt_2 dt_3\, R_{ijk\ell}(t-t_1, t-t_2, t-t_3)$$

$$\times\, E_j(t_1)\, E_k(t_2)\, E_\ell(t_3) \quad , \tag{2-14}$$

where $R_{ijk\ell}$ is a fourth-rank tensor describing the nonlinear response of the medium. The frequency spectrum of $R_{ijk\ell}$ is called the third-order susceptibility $\chi_{ijk\ell}$. We assume that the radiation fields are monochromatic, having a common frequency ω, e.g.,

$$E_j(t) = \frac{1}{2}\left\{ E_j\, e^{i\omega t} + E_j^*\, e^{-i\omega t} \right\} \quad . \tag{2-15}$$

The introduction of the electromagnetic field (2-15) into (2-13) and (2-14) yields expressions (in frequency domain) of the form,

$$P_i(\omega) = \chi_{ij}(\omega)\, E_j \quad , \tag{2-16}$$

2-10

$$P_i^{(3)}(3\omega) = \chi_{ijk\ell}(\omega,\omega,\omega)\ E_j\ E_k\ E_\ell \quad , \tag{2-17}$$

$$P_i^{(3)}(\omega) = 3\chi_{ijk\ell}(\omega,\omega,-\omega)\ E_j\ E_k\ E_\ell^* \quad , \ , \tag{2-18}$$

Expression (2-16) describes the physics of linear dispersion and absorption. Expression (2-17) describes the physics of third-harmonic generation. Expression (2-18) describes the physics of DFWM and is the starting point in the description of the vectorial response of the nonlinear medium for optical phase conjugation.

We assume that the macroscopic medium is isotropic in nature. Glasses, liquids, and atomic and molecular gases are typical examples of such media. Then the spatial symmetry of the third-order susceptibility tensor $\chi_{ijk\ell}$ dictates that there are only three independent elements that fully describe the response of the medium to external vectorial fields. These are χ_{1122}, χ_{1212}, and χ_{1221}, so that $\chi_{1111} = \chi_{1122} + \chi_{1212} + \chi_{1221}$. The subscripts 1 and 2 denote either the x, y, or z components of an arbitrary set of three orthogonal axes. Expression (2-18) can be reduced further by expanding the summation over all possible combinations of subscripts, and keeping only those terms that give non-zero contribution to the polarization density $P_i(\omega)$. The result of such algebraic manipulation yields the following expression for the vectorial response of any stationary medium in a general DFWM experiment:

$$\vec{P} = M(\vec{E}\cdot\vec{E}^*)\ \vec{E} + \frac{N}{2}\ (\vec{E}\cdot\vec{E})\ \vec{E}^* \quad , \tag{2-19a}$$

where

$$M = 3(\chi_{1122} + \chi_{1212}) \quad , \tag{2-19b}$$

$$N/2 = 3\chi_{1221} \quad . \tag{2-19c}$$

In DFWM, the electric field envelope E_i consists of three input waves which drive the medium to generate a phase conjugate signal. We write

$$\vec{E} = \vec{E}_f\ e^{-i\vec{k}_f\cdot\vec{R}} + \vec{E}_b\ e^{-i\vec{k}_b\cdot\vec{R}} + \vec{E}_p\ e^{-i\vec{k}_p\cdot\vec{R}} \quad , \tag{2-20}$$

2-11

where $\vec{E}_f$, $\vec{E}_b$, and $\vec{F}_p$ are the slowly varying envelope for the forward pump, backward pump, and input probe waves, respectively. The application of Equation (2-20) into Equation (2-19) yields two distinct contributions to the polarization density. The first one describes the pump-induced and self-induced index changes in the medium. These terms account for nonlinear lensing effects (self-focusing) and nonlinear phase shifts (fidelity problems). We denote such contributions by polarization density as

$$P_{NL} = M \left\{ \left[|\vec{E}_f|^2 + |\vec{E}_b|^2 + |\vec{E}_p|^2 \right] \vec{E}_p \right.$$

$$+ (\vec{E}_p \cdot \vec{E}_f^*) \vec{E}_f + (\vec{E}_p \cdot \vec{E}_b^*) \vec{E}_b \right\} \qquad (2\text{-}21)$$

$$+ \frac{N}{2} \left\{ 2(\vec{E}_p \cdot \vec{E}_f) \vec{E}_f^* + 2(\vec{E}_p \cdot \vec{E}_b^*) \vec{E}_b^* + (\vec{E}_p \cdot \vec{E}_b) \vec{E}_p^* \right\} .$$

The second term describes the effect that gives rise to optical-phase conjugation; it is given by

$$P_{DFWM} = A(\vec{E}_f \cdot \vec{E}_p^*) \vec{E}_b + B(\vec{E}_b \cdot \vec{E}_p^*) \vec{E}_f + C(\vec{E}_f \cdot \vec{E}_b) \vec{E}_p^* . \qquad (2\text{-}22)$$

In the case of non-resonant and stationary media, $A = B = M$ and $C = N/2$. However, in the presence of atomic motion, the effects of Doppler shift and spatial hole burning lead to a distinct values for A and B (as we will explicitly define later in the chapter).

This is one of the two main results of this section. The terms on the right hand side of Equation (2-22) have simple physical interpretations. As discussed previously, it is from these terms (the first two) that the spatial grating or volume hologram picture of DFWM comes. To see this we observe that the term $A(\vec{E}_f \cdot \vec{E}_p^*) \vec{E}_b$ describes a spatial grating generated by the interference of the forward pump and input probe, followed by the coherent scattering of the backward pump from this spatial grating. The term $B(\vec{E}_b \cdot \vec{E}_p^*) \vec{E}_f$ describes a spatial grating generated by the interference of the backward pump and input probe, followed by the coherent scattering of the forward pump from the spatial modulation. The term $C(\vec{E}_f \cdot \vec{E}_b) \vec{E}_p$ has a different interpretation. In a non-resonant or resonant two-level medium, the term describes a tensor grating

2-12

generated by the interference of either of the pump wave and the probe wave, followed by a coherent scattering of the other pump wave. In a resonant two-photon medium, it describes a two-photon coherence generated by the action of the counter-propagating pump waves, followed by a stimulated scattering of the probe wave by an electric dipole allowed coupling to the two-photon coherence (electric quadrupole). Equation (2-22) is valid for any isotropic resonant system.

From Equation (2-22) it can be shown that for different nonlinear optical media, four-wave mixing will exhibit different relationships between the polarizations of the probe and pump waves and the polarizations and amplitudes of the reflected (phase conjugate) wave. Table 2-1 gives examples of the output polarizations and relative efficiencies for different resonant and nonresonant interactions. The arrows and dots indicate all of the nonredundant directions of the linear polarization states of the appropriate beams. The efficiencies indicate which terms contribute to the output, and the subscripts S and T indicate single- and two-photon cases. For the nonresonant case, the first column gives all beams copolarized. Since the dot products are all nonzero, each term contributes to the conjugate output, giving an amplitude of A + B + C. In the second column, the pump and signal are cross polarized, giving a zero dot product, but the pumps are copolarized, giving a nonzero dot

Table 2-1. Effect of the State of Polarization on the Conjugate Output

	Nonresonant			Single-Photon Resonance			Two-Photon Resonance		
Forward pump	↑	↑	↑	↑	↑	↑	↑	↑	↑
Backward pump	↑	↑	⊙	↑	↑	⊙	↑	↑	⊙
Probe	↑	⊙	⊙	↑	⊙	⊙	↑	⊙	↑
Conjugate output	↑	⊙	↑	↑	0	↑	↑	⊙	0
Relative efficiency	$A + B + C$	C	B	$B_S + A_S$	0	B_S	C_T	C_T	0

NOTE: ⊙ = in plane.

   ↑ = perpendicular to plane.

product in the third term. Thus, the C term is the only term left. The remaining columns are determined in the same manner. (The absolute efficiency is larger in the resonant cases.)

Further examination of the table for single-photon resonance shows that the polarization of the output signal is determined by one of the pumps, not by the probe. Thus, one expects to see polarization rotation. This also provides a means of measuring the ratio of one grating to the other or the ratio of B to A. This experiment has been conducted with the results discussed in Chapter 5. To graphically exhibit this polarization rotation concept, the various options available (for an isotropic medium) are given in Figure 2-4. The examples shown are for copolarized and orthogonal pumps.

CO-POLARIZED PUMPS
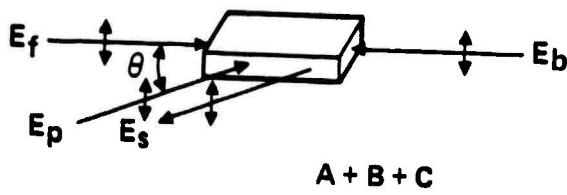
ORTHOGONAL PUMPS
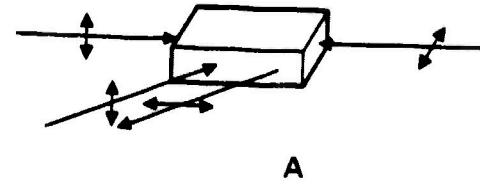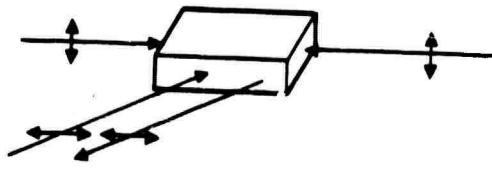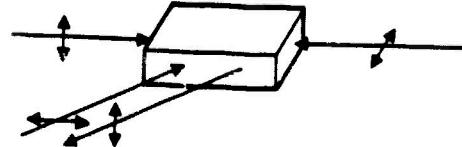
Figure 2-4. Polarization Options in DFWM (isotropic media).

2.2.2 Homogeneous and Inhomogeneous System Response Including Motion Effects

The coefficients A and B can be obtained by using a quantum mechanical calculation. The starting point in the analysis is the quantum mechanical transport equation for the density operator ρ:

$$i\hbar\left(\frac{\partial}{\partial t} + \vec{v} \cdot \nabla\right)\rho = \left[H_o, \rho\right] + \left[V, \rho\right] - i\hbar\{\Gamma, \rho\} + i\hbar\Lambda , \qquad (2\text{-}23)$$

where the convective derivative $\vec{v} \cdot \nabla$ describes the effect of atomic motion (Doppler shifts and spatial hole burning), H_o is the unperturbed electronic Hamiltonian, $V = -\vec{\mu} \cdot \vec{E}$ is the electric dipole $\vec{\mu}$ coupling to the external radiation fields $\vec{E}$, Γ is the decay operator, and Λ is the incoherent pumping operator. $\left[\, . \, \right]$ and $\{ \, , \, \}$ are the commutator and anticommutator, respectively. The third-order response, in the unsaturated regime, is obtained from the perturbation theory and the perturbation chain that describes spatial modulation of the population difference in resonant one-photon systems. Thus,

$$\begin{pmatrix} \rho_{11}^{(0)} \\ \\ \rho_{22}^{(0)} \end{pmatrix} \rightarrow \begin{pmatrix} \rho_{12}^{(1)} \\ \\ \rho_{21}^{(1)} \end{pmatrix} \rightarrow \begin{pmatrix} \rho_{22}^{(2)} \\ \\ \rho_{11}^{(2)} \end{pmatrix} \rightarrow \begin{pmatrix} \rho_{12}^{(3)} \\ \\ \rho_{21}^{(3)} \end{pmatrix} , \qquad (2\text{-}24)$$

where ρ_{11} is the population of the lower quantum state $|1>$, ρ_{22} is the population of the upper quantum state $|2>$, and ρ_{12} and ρ_{21} describe the coherent superposition of states $|1>$ and $|2>$. The superscript denotes the order of the perturbation. The parameter of the perturbation scheme is given by the Rabi flopping frequency $\vec{\mu} \cdot \vec{E}/\hbar$, where $h = 2\pi\hbar$ is the Planck's constant. There are two distinct spatial modulations of the population difference. One is formed by the interference of the forward pump and input probe; the other is formed by the interference of the backward pump and input probe. The calculation of the perturbation chain yields the following results:

Forward Pump-Probe Grating

$$A = i \frac{N_o |\mu_{12}|^4}{4\hbar^3} \int_{-\infty}^{\infty} d\vec{v}\, W(\vec{v}) \frac{1}{\gamma_{12} + i(\Delta + \vec{k}_p \cdot \vec{v})}$$

$$\times \left[\frac{1}{\gamma_{12} + i(\Delta - \vec{k}_f \cdot \vec{v})} + \frac{1}{\gamma_{12} - i(\Delta - \vec{k}_p \cdot \vec{v})} \right] \qquad (2\text{-}25)$$

$$\times \left[\frac{1}{\gamma_1 + i(\vec{k}_p - \vec{k}_f) \cdot \vec{v}} + \frac{1}{\gamma_2 + i(\vec{k}_p - \vec{k}_f) \cdot \vec{v}} \right]$$

Backward Pump-Probe Grating

$$B = i \frac{N_o |\mu_{12}|^4}{4\hbar^3} \int_{-\infty}^{\infty} d\vec{v}\, W(\vec{v}) \frac{1}{\gamma_{12} + i(\Delta + \vec{k}_p \cdot \vec{v})}$$

$$\times \left[\frac{1}{\gamma_{12} + i(\Delta - \vec{k}_b \cdot \vec{v})} + \frac{1}{\gamma_{12} - i(\Delta - \vec{k}_p \cdot \vec{v})} \right] \qquad (2\text{-}26)$$

$$\times \left[\frac{1}{\gamma_1 + (\vec{k}_p - \vec{k}_b) \cdot \vec{v}} + \frac{1}{\gamma_2 + (\vec{k}_p - \vec{k}_b) \cdot \vec{v}} \right] ,$$

where $N_o = \rho_{11}(0) - \rho_{22}(0)$ is the population difference,

$$W(\vec{v}) = (\pi u_o^2)^{3/2} \exp(-v^2/u_o^2)$$

is the velocity distribution function of the resonant medium, $u_o^2 = 2K_B T/m$ is the mean square velocity, K_B is the Boltzmann's constant, T is the equilibrium temperature of the medium, m is the atomic or molecular mass,

$\gamma_{12} = (\gamma_1 + \gamma_2)/2$ is the natural linewidth, and γ_1 and γ_2 are the natural decay rates of states $|1>$ and $|2>$, respectively. $\Delta = \omega - \omega_0$ is the laser detuning from resonance.

There are three distinct regimes of interest: (1) stationary atoms, (2) homogeneously broadened atoms, and (3) inhomogeneously broadened atoms.

The stationary atom regime restricts the velocity of the atom to $\vec{v} = 0$. In this case, $A = B$ and is given by

$$A = i\frac{N_0|\mu_{12}|^4}{4\hbar^3} \left(\frac{1}{\gamma_{12} + i\Delta}\right)\left(\frac{2\gamma_{12}}{\gamma_{12}^2 + \Delta^2}\right) \left(\frac{2}{\gamma_0}\right) \tag{2-27}$$

where $2/\gamma_0 = \gamma_1^{-1} + \gamma_2^{-1}$. In this case, the generated signal achieves a maximum amplitude when the laser detuning is on resonance ($\Delta = 0$). The spectrum of the phase conjugate signal is a Lorentzian.

The condition for homogeneously broadened atoms is such that

$$\gamma_{12} \gg ku_0 \tag{2-28}$$

where ku_0 is the Doppler width. If we neglect the Doppler shift $\vec{k} \cdot \vec{v}$ contribution in all resonance denominators containing the natural linewidth and integrate over all velocity groups, we find

$$A = i\frac{N_0|\mu_{12}|^4}{4\hbar^3} \left(\frac{1}{\gamma_{12} + i\Delta}\right) \left(\frac{2\gamma_{12}}{\gamma_{12}^2 + \Delta^2}\right) \tag{2-29}$$

$$x \left(\frac{1}{i\gamma_1}\right) S_+ Z(-iS_+) .$$

$$B = i\frac{N_o |\mu_{12}|^4}{4\hbar^3} \left(\frac{1}{\gamma_{12} + i\Delta}\right) \left(\frac{2\gamma_{12}}{\gamma_{12}^2 + \Delta^2}\right)$$

$$\times \left(\frac{1}{i\gamma_1}\right) S_- Z(-iS_-)$$

(2-30)

where $S_+ = \gamma_1/2ku_o \sin(\theta/2)$, $S_- = \gamma_1/2ku_o \cos(\theta/2)$, $Z(-iS_{\pm})$ is the Plasma Dispersion function of argument $-iS_{\pm}$, and θ is the angle between the wave vectors of the forward pump and input probe. Equations (2-29) and (2-30) are the solutions obtained by Wandzura[2] in the analysis of atomic motion effects in resonant degenerate four-wave mixing. In the case of fully collinear geometry ($\theta = 0^o$), one notes that the spatial grating A is unaffected by motion, since the periodicity becomes infinite in extent.

If we insert the polarization expression with A and B given by Equations (2-29) and (2-30) into Maxwell's equation, we can obtain an expression for the reduction in amplitude of the reflected signal. For the particular case of resonance operation (i.e., $\Delta = 0$) for a homogeneously broadened system, a plot of the field amplitude reduction versus angle is given in Figure 2-5. The solution is a function of the parameter T_D/T_1, the ratio of a characteristic time constant for motion of the atoms to the relaxation time T_1. In the case of motion, T_D is just the inverse of the Doppler width. For $T_D/T_1 \gg 1$ (i.e., no atomic motion), the solution shows no reduction over the previous case, as expected. For angles greater than $\sim 30^o$, there is a general reduction in amplitude as T_D/T_1 decreases (e.g., as atoms have time to move and wash out the grating). For small angles, the period of the grating becomes increasingly large, increasing the time it takes for the atoms to move one grating period, and thus minimizing the Doppler motion reduction. This is exhibited in the solutions obtained. For small angles, and for $T_D/T_1 \ll 1$, the reduction in amplitude approaches a factor of two. This is because the large-angle grating (smaller period) becomes completely washed out and can no longer contribute to the return.
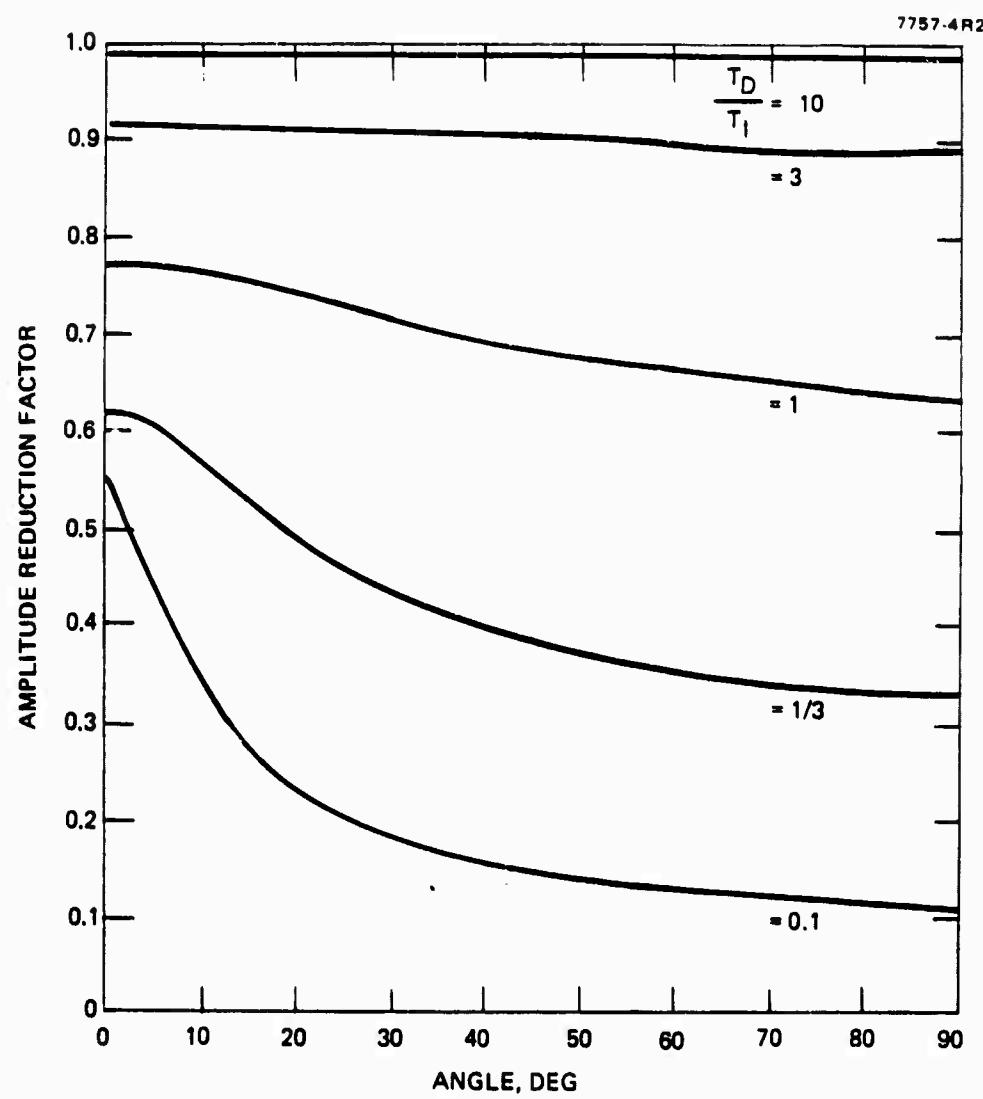
Figure 2-5. The amplitude reduction factor versus angle for a homogeneously broadened system. Note that for large T_D/T_1, motion has no effect. For small T_D/T_1, the curve shows that for θ near zero, the small spaced grating makes almost no contribution.

2.2.3 Inhomogeneously Broadened Atoms

The condition for inhomogeneously broadened atoms is such that

$$\gamma_{12} \ll ku_o \quad . \tag{2-31}$$

The integration over velocities can be achieved easily in the collinear geometry ($\theta = 0^o$) and yields the following expressions

$$A = i\frac{N_o|\mu_{12}|^4}{4\hbar^3} \left(\frac{2}{\gamma_o}\right)\left(\frac{\sqrt{\pi}}{ku_o}\right)\left(\frac{\gamma_{12} - i\Delta}{\gamma_{12}^2 + \Delta^2}\right) \tag{2-32}$$

and

$$B = i\frac{N_o|\mu_{12}|^4}{4\hbar^3} \quad \frac{2\sqrt{\pi}}{(ku_o)^3} \quad . \tag{2-33}$$

Note that the B/A ratio on-line center is given by

$$\frac{B}{A} = \frac{\gamma_o\gamma_{12}}{(ku_o)^2} \ll 1 \quad . \tag{2-34}$$

Hence the contribution from B is negligible compared to the one from A. The spectrum of A is Lorentzian, which reflects the fact that only those atoms having $\vec{v}=0$ interact with all the waves.

The above discussions have been restricted to the case of weak pump waves. However, in the presence of strong pump waves, the resonant two-level medium undergoes saturation effects leading to changes in the third order susceptibility $\chi^{(3)}$ or the coefficients A and B. This was discussed in Section 2.1 for the case of stationary atoms. In this regime, both gratings generate the phase conjugate signal with equal efficiency. The expression for A or B in this case is given by

2-20

$$A = i \frac{N_o |\mu_{12}|^4}{4\hbar^3} \left(\frac{\gamma_{12}}{\gamma_{12}^2 + \Delta^2}\right) \frac{1}{\gamma_{12} + i\Delta} \left(\frac{2}{\gamma_o}\right) \frac{1}{\left\{1 + \frac{\left|\vec{E}_f e^{-i\vec{k}_f \cdot \vec{r}} + \vec{E}_b e^{-i\vec{k}_b \cdot \vec{r}}\right|^2}{I_{sat}}\right\}^2} ,$$

where the frequency-dependent saturation intensity I_{sat} is given by

$$I_{sat} = \frac{\hbar^2 \gamma_o}{\gamma_{12}} \frac{\gamma_{12}^2 + \Delta^2}{|\mu_{12}|^2} . \tag{2-36}$$

These expressions for A and B were used to generate the results given by Equations (2-1) through (2-8) and Figure 2-3.

The dynamical properties of the coefficient C have also been determined for the case of one- and two-photon-resonant systems. In the case of one-photon-resonant systems, conservation of angular momentum permits a strong coupling between two cross-polarized waves by generating an electric quadrupole in the atom or molecule. The induced electric quadrupole is spatially modulated with periodicity $2\pi/|\vec{k}_p - \vec{k}_n|$, where n=f, b. The phase conjugate signal is generated by means of coherent scattering of either pump wave from the electric quadrupole. In the case of two-photon-resonant systems, a two-photon coherent excitation is generated by the simultaneous action of the counterpropagating beams. The excitation in the medium is spatially uniform and oscillates at twice the pump frequency. The phase conjugate signal is generated by an electric dipole allowed coupling to the two-photon coherence. In two-photon excitation, atomic motion plays no role in determing the efficiency of phase conjugation. The theory for effects relating to the C term was not developed on this program. However, the use of two-photon resonant systems for pump-probe detuning will lead to important considerations. A discussion of this application, when considering Doppler shifted systems, was given in the interim report and will not be repeated here.

So far, we have considered the ideal or common DFWM situation. That is, we have taken the pump waves to be counterpropagating, to be plane waves, to be constant in magnitude, and to be of such a magnitude that nonlinear effects caused by the pumps were negligible. We also assumed the probe to be small in magnitude when compared with the pump, and that all waves had the same degenerate frequency.

In most experimental situations and in most applications of interest, these restrictions are not valid. In Chapter 3 and 4, we will examine the results of the DFWM theory when these effects are included.

2.3 FOUR-LEVEL SYSTEMS

We have modeled materials that behave as so-called four-level systems. We will find from the modeling results to be presented that a unique "double-bump" characteristic occurs in the reflectivity vs. pump intensity. This property can lead to the attainment of much higher reflectivity than obtained in simple two-level systems.

In the modeling, we assumed that the four-level system is equivalent to a pair of independent low-level systems. This derivation is a generalization of the work described in Section 2.1; it also provides a basis for the theory which considers the effect of intramolecular relaxation processes tha couple the pair of two-level systems (not described in this report).

The quantum mechanical system we consider is shown in Figure 2-6. Here λ_i and γ_i are the incoherent pumping and decay rates of state $|i\rangle$, respectively. The reservoir acts as a sink of energy. If state $|1\rangle$ is a true ground state, then we can set $\lambda_1 = 0$ and $\gamma_1 = 0$ with λ_1/γ_1 being a constant. In the absence of external radiation fields, the initial population of each state $|i\rangle$ is given by λ_i/γ_i.
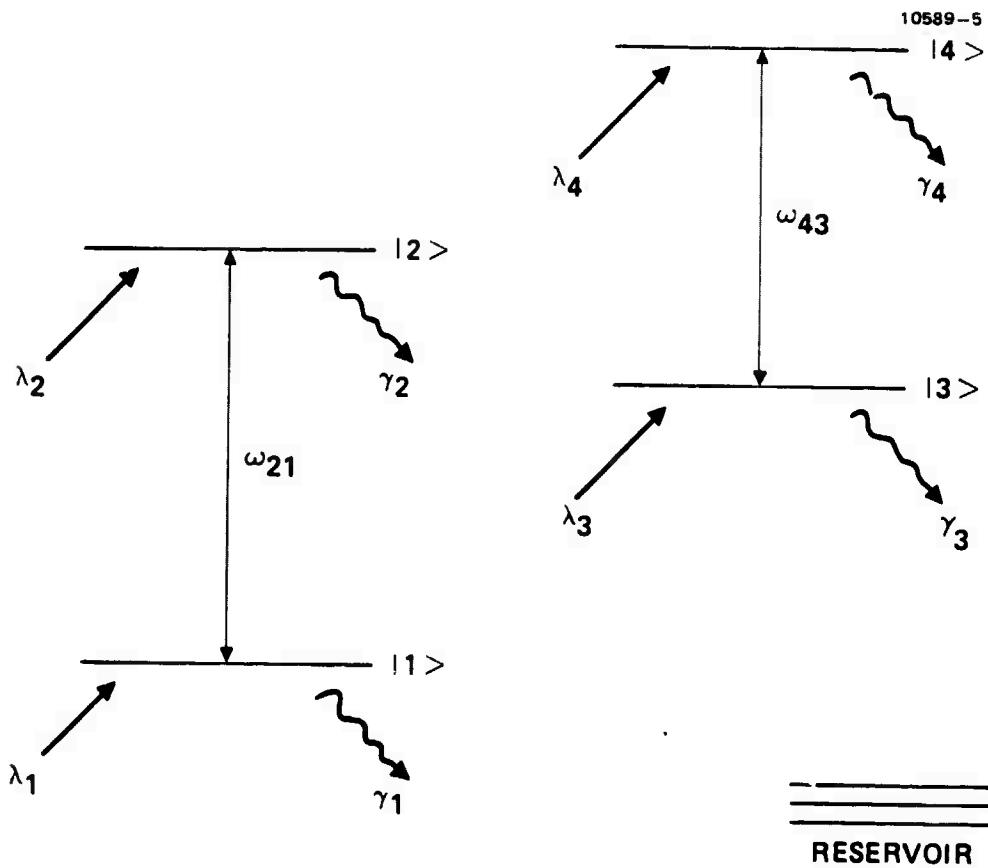
Figure 2-6. Four-level model.

The equations for the reflectivity have been developed and programmed, with an example calculation given in Figure 2.7 showing the double-bump characteristic.

In principle, transition 1→2 has different atomic or molecular parameters from transition 3→4. Indeed, it is the difference in the parameters that permits the double-maximum phenomenon to occur. The physics can be explained as follows. Assume that the saturation intensity (I_1) for the 1→2 transition is lower than the one (I_2) for the 3→4 transition. Then the degenerate four-wave mixing process is more effective in the 1→2 transition for pump intensities below I_1. As

the pump intensity goes beyond I_1 but still below I_2, the 1→2 transition saturates strongly while the 3→4 transition continues to experience the four-wave mixing process in the unsaturated regime. For pump intensities beyond I_2, the 1→2 transition is fully saturated while the 3→4 transition starts reaching the saturation region. This is the basic explanation of the double-maximum effect.
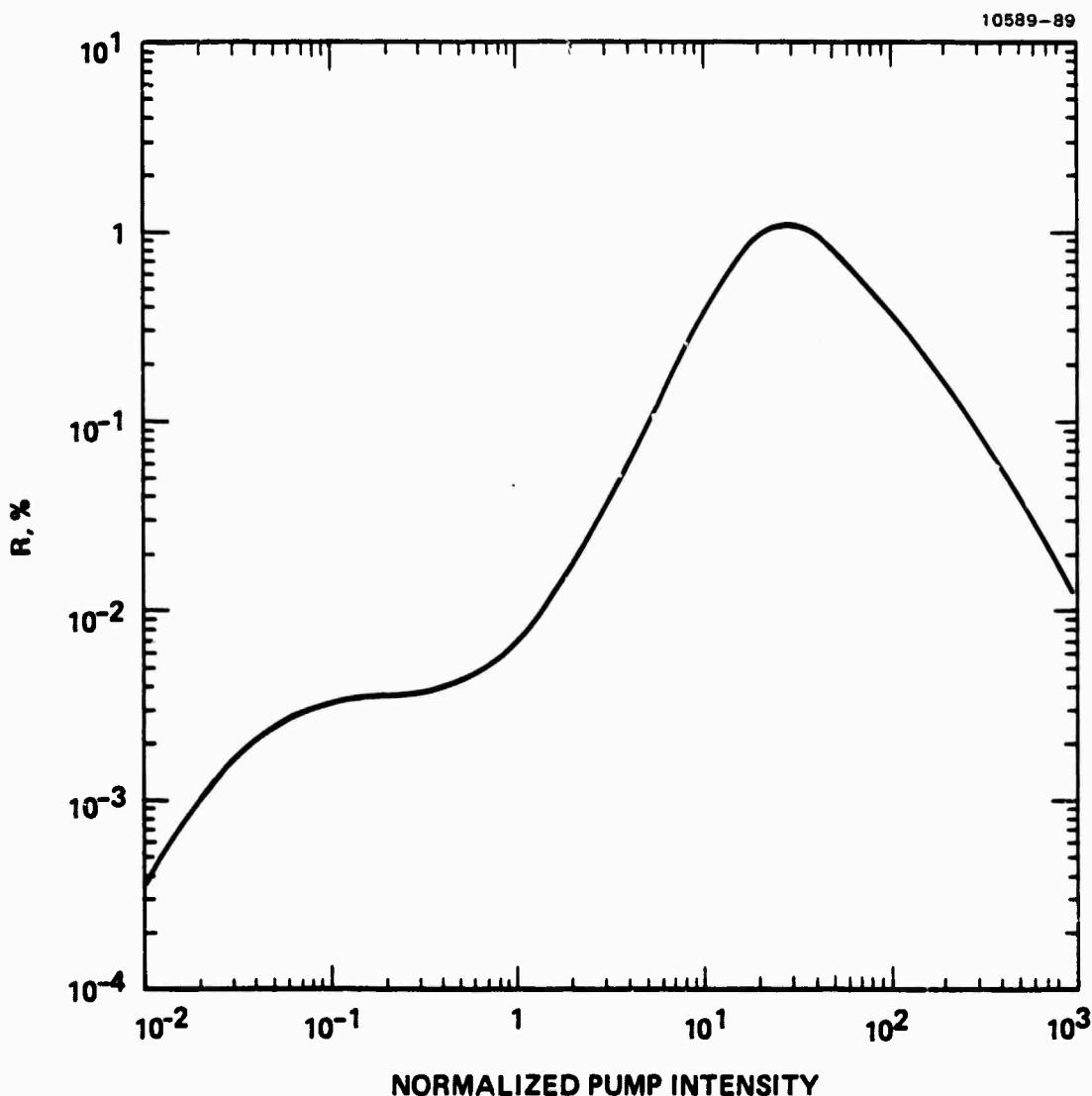
Figure 2-7. Example calculation of four-level model, $\alpha_1 L = 27$, $\alpha_2 L = 4$, $I_2/I_1 = 400$, $\delta_1 = 4$, $\delta_2 = 5$.

REFERENCES

2.1.   Abrams, R. L. and Lind, R. C., Opt. Lett. $\underline{2}$, 94, (1978), $\underline{3}$, 235(E).

2.2.   Wandzura, S. M., Opt. Lett. $\underline{4}$, 208, (1978).

2-3.   Steel, D. G., Lind, R. C. and Lam, J. F., Phys. Rev. A May, 1981.

CHAPTER 3

PUMP ATTENUATION AND DEPLETION EFFECTS ON DFWM

The discussion of phase conjugation by means of DFWM given in Chapter 2 neglects the effects of pump attenuation and depletion. We have performed theoretical and numerical calculations to assess the importance of these effects. The capability to perform these calculations was established using internal funding; specific, pertinent calculations were performed on this program. The results are summarized here for completeness.

We have assumed that the conjugator medium is a two-level saturable absorber of the type considered in Chapter 2. The effects of atomic motion have been neglected. We also have assumed that the pump, probe, and signal waves either are all of the same polarization; or, if they are not, that the angle between the direction of polarization of the forward pump and the probe is small. With these assumptions the four waves satisfy a vector wave equation of the form

$$\nabla^2 \underline{E} - \frac{1}{c^2} \frac{\gamma^2 E}{\partial t^2} = \frac{1}{\varepsilon_o c^2} \frac{\gamma^2 P}{\partial t^2} \quad , \tag{3-1}$$

Where $\underline{E}$ is the electric field vector composed of the sum of the pump, probe, and signal fields, c is the velocity of light in the medium, and $\underline{P}$ is the polarization vector (obtained from Section 2.2.2) in the homogeneous, no motion limit:

$$\underline{P} = \frac{2\varepsilon_o \alpha_o}{K} \frac{i(1 + i\delta)}{1 + \delta^2} \frac{\underline{E}}{1 + \frac{|E|^2}{I_s}} \tag{3-2}$$

The four fields are coupled by means of the quadratic term in the denominator of the polarization vector. In the most general case, in which the four fields have comparable magnitude, these equations yield a set of four coupled equations satisfied by the fields. We refer to this case as the strong probe limit. To calculate the effects of pump depletion, the vector wave equation given in Equation (3-1) must be solved in this limit. In most previous work on DFWM it has been assumed that the probe and signal fields are weak, compared with the pump fields. We refer to this as the weak probe limit (see Chapter 2). In this approximation, the pump fields are decoupled from the probe and signal fields, and, in doing so, the effects of pump depletion are neglected. The four coupled equations reduce to a set of two coupled equations for the pump fields, and another set of two coupled equations for the probe and signal fields.

In both the strong and weak probe limits, the effects of attenuation are sometimes important. For example, Equations (2-1) through (2-4), which neglect attenuation and pump depletion, predict that the probe-wave reflection coefficient increases as the absorption increases. Clearly, this prediction will cease to be accurate when the pump waves have been substantially atten-uated by virtue of the absorption.

Starting from the vector-wave equation given in Equation (3-1), we have derived the appropriate equations for both the strong and weak probe limits and have developed numerical techniques for solving these equations. The results obtained from this analysis are briefly summarized in the following sections.

3.1 PUMP ATTENUATION EFFECTS

The effects of pump attenuation in the weak probe limit have been obtained by first solving the coupled equations satisfied by the pump fields and then using these results in the solution of the coupled equations satisfied by the probe and signal waves. In contrast to the constant pump case considered in Chapter 2, for which an analytical solution was obtained (Equations (2-1) through (2-4)), the equations satisfied by the probe and signal waves in the

case of varying pumps must be solved numerically. Moreover, the solution of these equations is complicated by the fact that both fields are not known a priori at the same ends of the interaction region. One of the fields is known at one end and the other at the other end. We have developed an iterative numerical procedure in which the equations are solved starting from an inital guess for the value of the unknown field, followed by a refinement of the unknown initial field based on the degree to which the trial solution matches the known boundary condition for this field at the other end of the iteration region.

A sample of the results obtained for probe-wave reflectivity in the weak probe limit is given in Figure 3-1. These results apply to a case in which the pump and probe fields have the same polarization and operation on line center (i.e., $\delta = 0$). The dashed curves are the results predicted by the constant pump theory (Equations (2-1) through (2-4), and the solid curves are the results obtained when pump attenuation is considered. Note that the results differ significantly when the pump irradiance is below the saturation value. As might be expected, the effects of attenuation are small when the pump irradiance exceeds the saturation value. The parameter ζ that labels the curves in Figure 3-1 is the value of the product of the small signal (intensity) attenuation coefficient and the length of the interaction region. Increased reflectivity is obtained for larger values of ζ only if the pump irradiance exceeds the saturation value. For values of pump irradiance below saturation the opposite is true; e.g., increased attenuation leads to a decrease in reflection coefficient.

3.2 PUMP DEPLETION EFFECTS

The results obtained in the strong probe limit apply to a situation in which the pump waves are orthogonally polarized. This simplifies the analysis since the probe wave then forms only one grating, not two as it does in the case where the pump waves have the same polarization (Section 2.2.1). Again, we assume in this case that the probe wave is propagating along a collinear direction, or nearly collinear, with the direction of propagation of the forward pump wave.
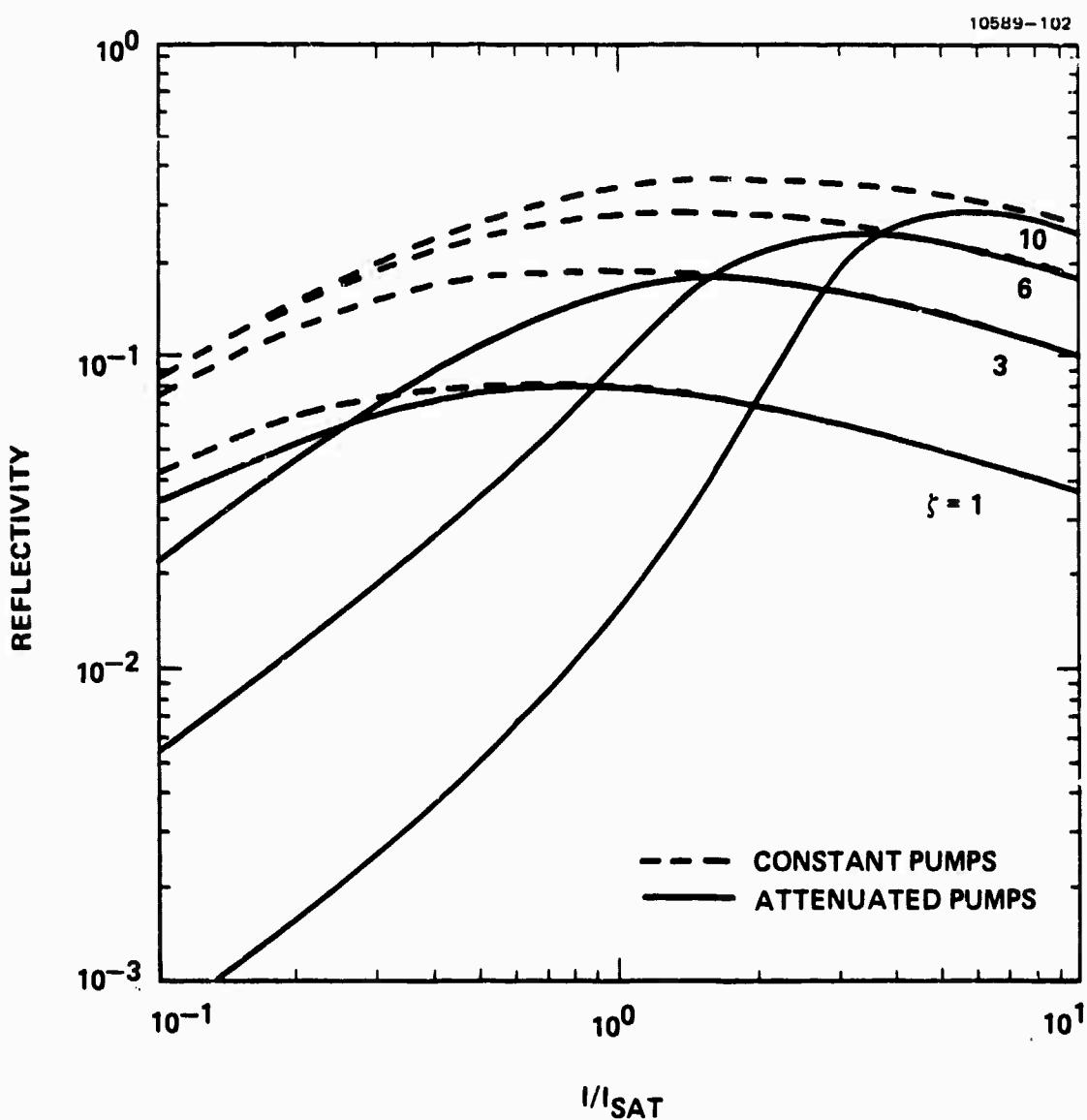
Figure 3-1. Pump attenuation effects on probe wave reflectivity.

The effects of pump depletion are most pronounced when the simpler theory discussed in the previous section predicts large reflectivities. A case of particular interest is provided by the reflectivity resonances predicted by Equations (2-1) through (2-4). We have shown that some of these resonances, which are caused by a resonance of the type that occurs in backward wave oscillators and distributed feedback lasers, occur even in the presence of pump attenuation. It is obvious that pump depletion effects are important in the vicinity of such resonances, since the weak probe theory predicts essentially unlimited power in the reflected field. In reality, the reflected power is finite because the pump fields are strongly depleted under these conditions.

Some results that illustrate these considerations are given in Figure 3-2. These results apply to a case in which the pump and probe fields are detuned from line center by 15 linewidths (i.e., $\delta = 15$). The small-signal absorption coefficient and the length of the interaction region are assumed to be adjusted so that the absorption parameter ζ is equal to 2 for waves at the frequency of the pump and probe fields (which implies that the line-center value of the parameter is $1 + \delta^2 = 226$ times as large). The curves marked A are the results obtained from Equations (2-1) through (2-4). This theory predicts that the reflectivity goes to infinity at two values of probe irradiance. The curves marked B are the results obtained from the variable pump theory discussed in the previous section. Note that this theory predicts that the reflectivity goes to infinity at only one value of probe irradiance. Pump attenuation effects have suppressed the other infinity. The dashed curve marked C gives the results obtained when the effects of pump depletion are taken into account. In this case we must specify the magnitude of the probe irradiance relative to that of the pump. As noted in the Figure, the results shown here apply to a case in which the probe irradiance is 1% as large as that of the pump.

3.3 MAXIMUM ATTAINABLE REFLECTIVITY

To obtain some idea of the maximum amount of energy that can be obtained in the reflected wave, we have solved the equations satisfied by the pump,
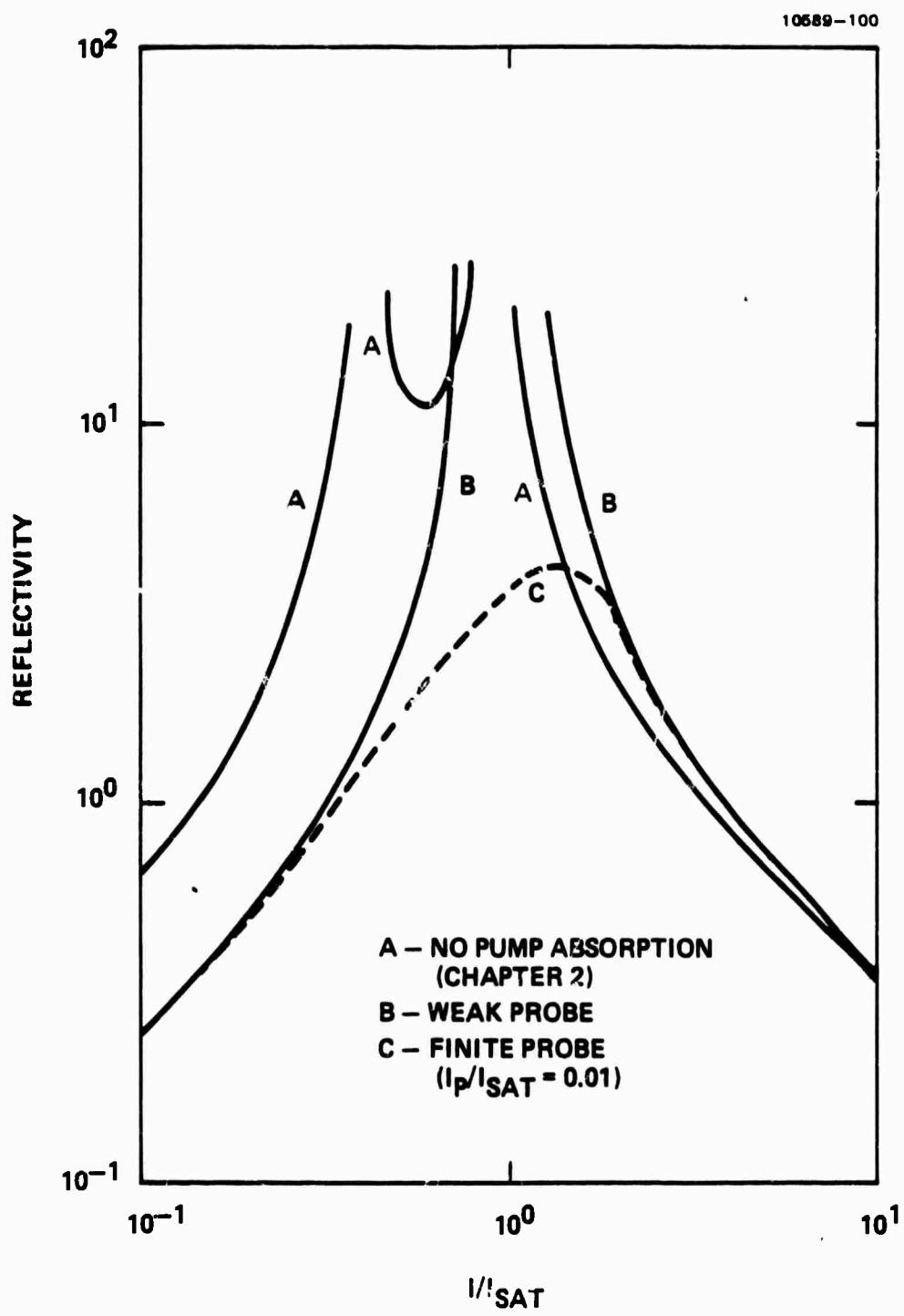
Figure 3-2. Probe amplitude reflectivity in the vicinity of
a backward-wave resonance — $\delta = 15$, $\zeta = 2$.

probe, and the signal fields for the case in which the forward and backward
pumps and the probe field all have equal amplitude on entering the interaction
region. Both pump attenuation and depletion effects are important in this
case. We have assumed that the parameters δ and ζ are equal to the values used
to generate the results in Figure 3-2, $\delta = 15$, and $\zeta = 2$; i.e., we are operating
in the vicinity of the backward-wave resonance discussed in the previous section.

The variation in the irradiance of the reflected (signal) wave as a
function of the magnitude of the pump and probe fields relative to the satura-
tion irradiance . given in Figure 3-3. These results indicate that 50% of the
probe energy is reflected under optimum conditions. This implies that the
maximum overall efficiency is ~17%. No attempt was made to investigate the
effects of distributing the input energy unequally among the pump and probe
waves; thus this result must be considered only is indicative of the attainable
efficiency.
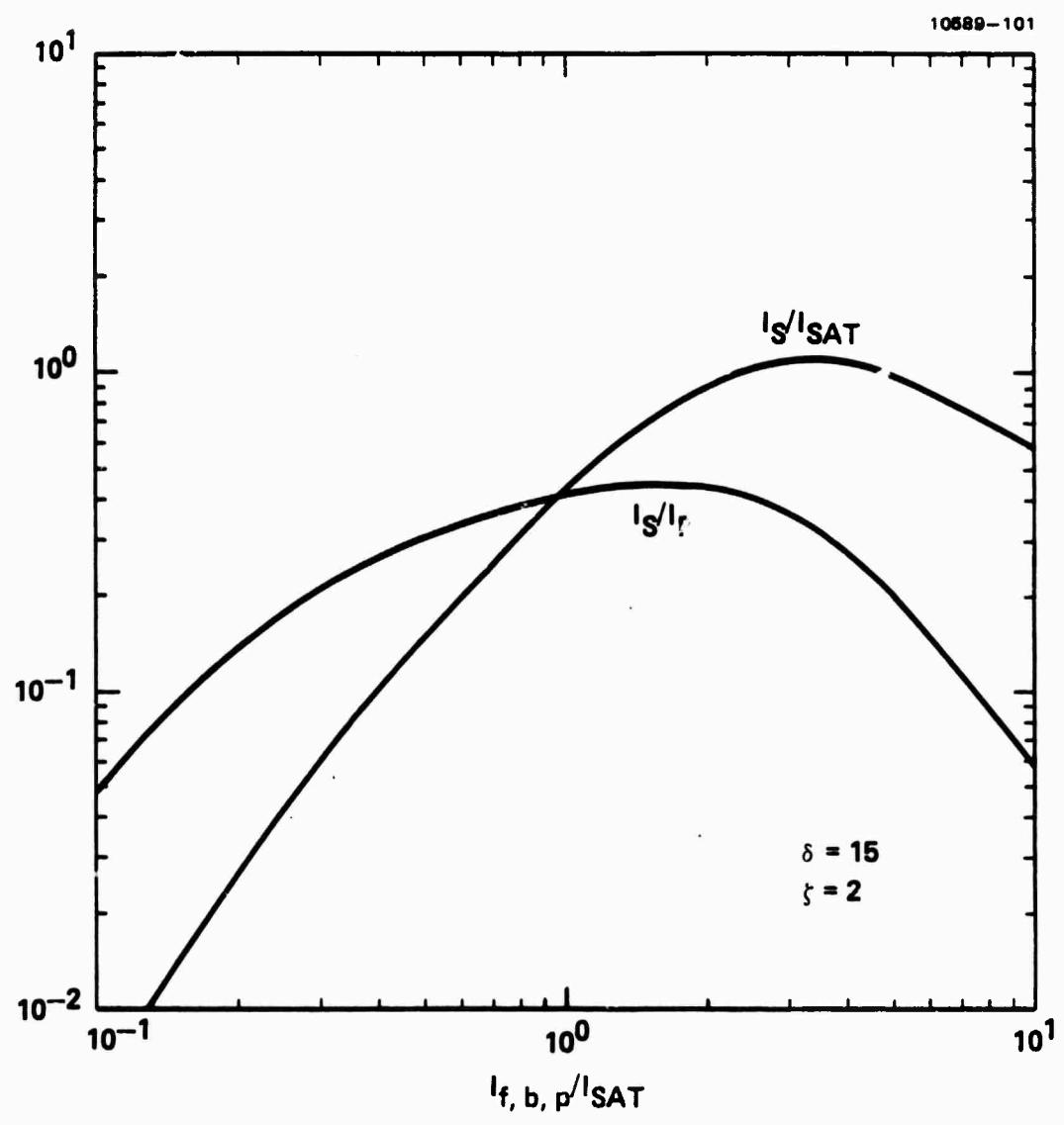
Figure 3-3. DFWM with equal pump and probe amplitudes.

CHAPTER 4

MODIFICATIONS ON THE BASIC DFWM RESPONSE

4.1 OVERVIEW

The previous chapters consider operation of an idealized degenerate four-wave mixer using equal amplitude pumps that are exactly counterpropagating, and that have uniform amplitude profiles and aberration-free wavefronts. This chapter considers two kinds of deviations from the idealized operation: (1) those used to control signal beam output parameters such as frequency, tilt and focus, and (2) those that cause undesirable aberrations in the conjugator output.

In real systems, unavoidable departures from idealized pumps and medium response cause aberrations in the wavefront of the output signal. For example, small errors in pump alignment cause undesired tilts and loss in reflectivity. Doppler shifts induced by target or reference motions may shift the probe frequency away from that of the pumps, again causing a loss in reflectivity as a consequence of phase mismatch. Similarly, remote oscillators employed as reference sources may drift with respect to pump sources. And, in addition, wavefront aberrations can be caused by non-uniform amplitude profiles.

On the other hand, many of the effects which modify the basic operation of the degenerate four-wave mixer can be used to advantage in system operation. For example, a small angular misalignment or offset between the two pump beams produces a corresponding (matching) offset between the mean probe and signal wavefronts as well as possible phase mismatch. This offset can be employed to point the retro beam ahead of the target to effect an intercept at long ranges or to avoid reference burnout.

Another potentially useful offset operation is to shift the pump frequency by a small amount $\Delta\omega_o$ so that (from the frequency matching condition) the signal frequency is offset $2\,\Delta\omega_o$. For instance, this technique might be used to shift a Doppler offset frequency back to the center of the laser amplitude gain line. A third operation uses pump-to-signal wavefront transfer in near collinear geometries to add focus or defocus to a conjugate signal.

4-1

We have employed three basic analysis techniques which lead to closed form expressions describing four-wave mixer operation in these nonstandard modes. These are: (1) a weak scattering analysis; (2) a coupled wave analysis; and (3) a geometric analysis.

The weak scattering analysis treats the four-wave mixer volume as a weak scattering source which radiates a signal field with minimum depletion of the probe field. Such an approach is employed in Section 4.2 to estimate the loss in signal strength resulting from pump-to-pump misalignment, a loss which increases with increasing angular separation of the pump and signal beams. Typically, only a few degrees can be tolerated for pump/signal separations of the order of 5°. There is an experimental demonstration of the predicted signal fall-off.

This same general approach is employed in Section 4.3 to explore the perturbations on the signal beam introduced by accidentally or deliberately introduced phase perturbations on the pump. The first-order effect, with small angular separations between probe and pumps, is a direct transfer of the wavefront perturbation on each pump onto the signal wavefront. However, second-order effects associated with phase mismatch and vignetting are also discussed, which become appreciable for thick four-wave mixers and large-phase perturbations.

Although the weak scattering approach provides an extremely useful first-order estimate of the impact of mixer geometry, it is not a fully accurate description of the four-wave scattering process, since probe depletion is not accounted for. These limitations motivate the second or coupled wave approach of Subsection 4.3, wherein a coupled set of four nonlinear first-order differential equations describes the complete propagation phenomena within the mixer, including the effects of probe depletion.

The four basic nonlinear, first-order differential equations that form a complete description of propagation in the four-wave mixer are introduced in Subsection 4.3.1. Even ignoring diffraction, the equations are complicated and admit closed-form solutions only in special cases. Specifically, the coupled-wave analysis is used for three problems: pump amplitude to signal phase transfer in collinear geometrics; pump-to-probe detuning; and discrete multiline operation.

Although actual systems will probably not be operated with a strictly collinear geometry, we believe that the collinear four-wave analysis should give an excellent first-order quantification of many problem areas. This analysis is employed in Subsections 4.3.2 and 4.3.3 and produces the following key results. One finds that even with strong pumps the reflectivity of the conjugator matches that of the two-coupled-wave theory of Yariv and Pepper, provided that the pumps are of equal intensity. However, the phase of the signal wave contains not only the transferred pump phase (as predicted by the weak scattering theory), but also two additional phase shifts driven by the pump amplitudes — terms not exhibited in the cited theory. One of these "spurious" terms cancels for balanced pumps, but the other generates an (pump) amplitude-to-signal phase coupling whose strength can only be made negligible by employing nonlinear materials with small values of $\chi^{(3)}$. More specifically, we show that the size of the resultant mean-square spatial phase variance depends upon the product of the mixer reflectivity and the variance in the amplitude distribution. The specific case for an amplitude variance associated with truncated Gaussian beams is examined and shown to limit the mixer gain to a factor of five or less for an rms phase error of 0.36 radians (Strehl ratio of 0.73).

The effects of detuning have been investigated and have been shown to differ for two- or three-level systems. Two important effects occur in two-level systems: (1) The atomic system may fail to respond to the moving gratings which generate the conjugated signal. (2) If one retains the usual counter-propagating geometry, a phase mismatch over the mixer length results in a loss in reflectivity.

Reflectivity problems generally dominate in the experimental two-level or "one-photon" mixers employed to date. As discussed in Subsection 4.4.1, the dynamic gratings formed within the mixer decay at approximately the inversion relaxation rate, T_1, and thus there is an appreciable loss of reflectivity for detunings greater than

$$\omega_p - \omega_{f,b} > (T_1)^{-1} \; . \tag{4-1-4}$$

For long mixers (or with low values of T_1), which employ the usual counter-propagating geometry, the phase mismatch associated with a mixer length L, may dominate the frequency response, and there is then appreciable loss in reflectivity for separations such that

$$\omega_p - \omega_{f,b} > \frac{\pi c}{L} \ . \tag{4-1-5}$$

However, this phase mismatch is <u>not</u> a fundamental problem for fixed or measurable frequency offsets, since once these are known the mixer geometry can be modified such that the phase mismatch can be effectively eliminated (see below).

The combined effects from phase mismatch and T_1 (exclusive of the effects of thermal motion within the mixer) are quantified in Subsection (4.4) and the reflectivity vs. frequency offset is illustrated for particular examples which span the parametric space from the regime wherein (4-1-4) dominates, on to where (4-1-5) dominates.

In Subsection 4.4.2 the three-level or "two-photon" responding systems are shown to differ in several important ways. First, atomic motion does not play a role in modifying the refectivity with counterpropagating pumps; thus the bandwicth is almost entirely set by the phase mismatch criterion of Equation (4-1-5). If the pumps are slightly offset in angle (after the manner described in Part 4.5) in order to achieve phase matching, then the effects of Doppler motion are not completely canceled; this will probably thereby determine the limiting bandwidth, although this limitation has not been explored in depth.

Discrete multiline operation is discussed in Subsection 4.4.4 wherein both pumps have the same spectral distribution as the probe. It is shown that, for a pair of probe-wavelengths, three classes of output result, one of which is at the matching input wavelengths with the correct conjugated phase for these wavelengths. The remaining two classes constitute cross-talk terms. One of these arises from intermodulation products, and the other class contains terms

coincident with the probe wavelengths, but with a phase shift corresponding to the wrong wavelength (for complete compensation). The cross terms are all negligible for a frequency separation and/or path length such that (4-1-5) is satisfied. In other cases wherein the optical path difference variance σ_{OPD} is small, specifically for "compensated" Strehl ratios less than 0.7, one requires that

$$ \sigma_{OPD} (\frac{\omega_p - \omega_b}{c}) < 0.05 \quad , \tag{4-1-6} $$

and thus for small frequency separations the compensations may still be quite effective. In other cases (with intermediate frequency separations) it is sometimes beneficial to substitute a single wavelength pump (at the midpoint of the probe spectrum) for a multiwavelength pump.

In Section 4.5 the third class of analysis, a geometrical approach is employed to develop a generalized phase-matching approach for accommodating large frequency and angle offsets in a four-wave mixer. These configurations, which in many cases are noncoplanar, considerably increase the versatility of generating angle and frequency offsets. An angle offset is demonstrated experimentally, which is much larger than could be obtained by simply offsetting a pump angle. We show that the (conjugated) wavefront transfer process under angle offset conditions is very similar to the pump-to-signal wavefront transfer process, and that the dominant error is an amplitude modulation at twice the spatial frequency of the probe-phase variation spatial frequency.

4.2 WEAK SCATTERING ANALYSIS

4.2.1 Introduction

In this Subsection we employ a weak scattering analysis to investigate two important modifications to the basic DFWM response. In Subsection 4.2.2 we investigate the process by which a spatial phase or amplitude variation pattern which is present on one or both pump inputs may transfer onto the

conjugated signal wavefront. In Subsection 4.2.3 we examine the loss of reflectivity which results from pump misalignment.

As examples of applications, consider a focus transfer from the pump to the signal beam. Such a refocus may avoid burning out the reference. Further, if the reference is introduced at an intermediate system location, for example, near a satellite relay, the beam nominal focus on the target may be incorrect because of the difference in ranges.

On the other hand, if a small, uncontrolled focus occurs on the pumps, then the associated focus transfer onto the signal beam can cause a serious loss in Strehl ratio at the intended focal point, an effect that must be allowed for and hence understood. The same potentials and problems hold for more general classes of distortion, which we will represent by Fourier components.

We assume the deleterious distortions are held to reasonably small values by care in design, and similarly we also limit the size of deliberately introduced distortions. For small distortions we will show that with small angles between the forward pump and the probe beam - the usual operating conditions - the first order effect for small distortions is to transfer these distortions directly onto the signal beam.

4.2.2 Pump-to-Signal Wavefront Transfer

It is not difficult to understand the first order pump-to-signal transfer effects with the aid of a few simple pictures, such as illustrated in Figure 4-2-1. From the basic degenerate four-wave mixing equations of Chapter 2 describing the idealized operation, we find that the phase ϕ_s of the scattered wave generated at any point $\vec{r}$ in the four-wave mixer is simply

$$\phi_s(\vec{r}) = \phi_f(\vec{r}) + \phi_b(\vec{r}) - \phi_p(\vec{r}) \quad , \tag{4-2-1}$$

where ϕ_f, ϕ_b, and ϕ_p are the phase shifts of the forward and backward pumps and the probe signals. Thus, if we consider a phase profile on the forward pump, such as exhibited in Figure 4-1, there is a matching phase profile

$$\text{LOCALLY:} \quad \phi_s = \phi_f + \phi_b - \phi_p$$

$\phi_f (x, y)$

$\Delta \phi_m (x, y, z) = 2\phi_f (x, y)$

F

B

$\phi_s (x, y) = 2\phi_f (x, y)$
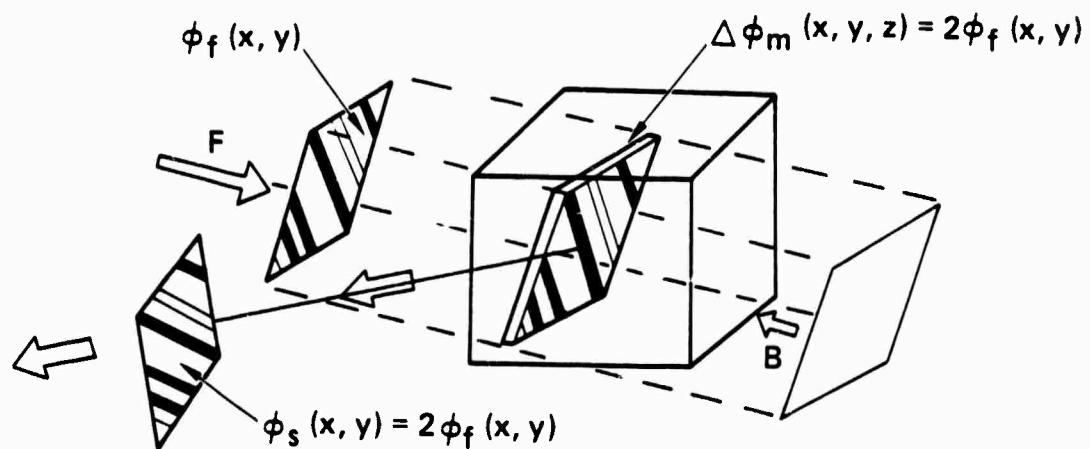
Figure 4-1. Wavefront transfer of pump phase distribution onto the signal (from a scattering viewpoint). Small angles between the probe and pump are assumed.

which is transferred onto the signal being scattered from an interior slab within the four-wave mixer volume, as designated $\Delta\phi_m$ in the figure. If the mixer is a thin slab, oriented approximately normal to the pump beams, and if the offset angle between signal and pump is small, then this same phase distribution is preserved (possibly with a small projective distortion) on the output signal beam. Amplitude patterns on the pumps transfer in much the same manner, except that the patterns are multiplicative rather than additive and saturation effects may modify the transfer process.

As the offset angle becomes large, the projective distortions become larger. Finally, as illustrated in Figure 4-2, at 90% orientation, the phase pattern is accurately transferred to the pump in one dimension and completely "lost" in the other dimension. More precisely, pump phase variations normal to the direction of the probe propagation are transformed into uniform amplitude reductions on the output signal (a consequence of the distributed phase mismatch induced in the mixer volume), as illustrated in the top set of pictures. This sharply contrasts to the transfer process with phase variations which occur in a direction parallel to the probe propagation direction. For the parallel case, such variations transfer directly as phase variations on the output signal as illustrated in the lower set of pictures. In both cases, however, there is a net reduction in (far field) Strehl ratio, which is independent of the orientation of the wavefront error pattern on the pump(s).

In the following paragraphs we will explore the distortion or perturbation transfer in more detail, and examine some of the second order or "parasitic" effects which can limit the utility of an intentional wavefront transfer. Depending upon the geometry, the first order parasitic effects may be a tilt or pointing error introduced on the signal beam (focus errors on the pump), or a (spatial) phase shift in the Fourier component (introduced on the pump). The next order parasitic effect is an amplitude modulation on the signal beam. In addition, there is an elliptical vignetting or apodization on the output beam as a consequence of phase mismatch. Such an apodization is additional to a geometrical apodization which occurs as a consequence of beam displacement. The phase mismatch apodization provides the practical limitation upon the size of wavefront transfer which may be accommodated in a carefully designed system.

LOCALLY: $\phi_s = \phi_f + \phi_b - \phi_p$

$S_{nf} = \exp - \langle 4\phi_f^2(z) \rangle$

$2\phi_f(z)$

$S_{nf} = 1$

$2\phi_f(z)$

$S_{ff} = \exp - \langle 4\phi_f^2(x) \rangle$
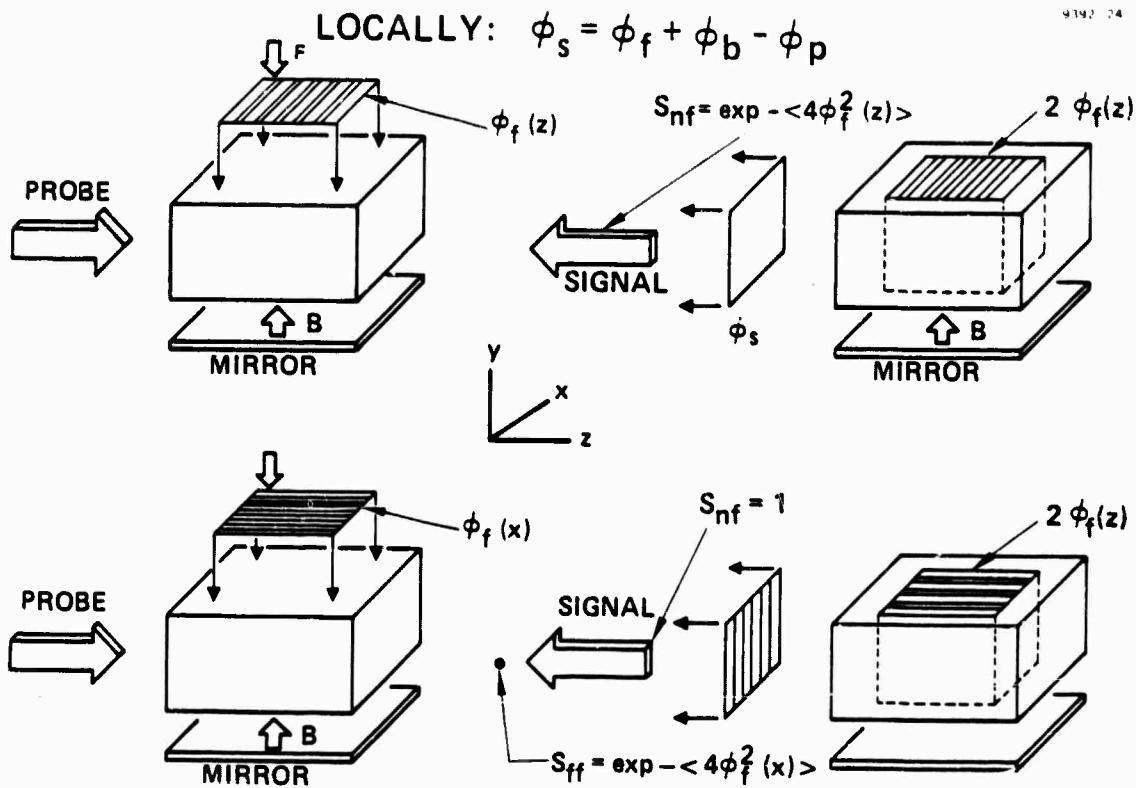
Figure 4-2.   Wavefront error transfer with orthogonal pumping.

4-9

If we desire to employ this wavefront transfer mechanism for useful purposes, for example for focus control, then we must first consider the effect of projective transformations in the mixer volume. We will find that such a transformation can generate an astigmatatic error when attempting a focus override. Consider an infinitesimally thin mixer slab whose face is normal to the probe beam as illustrated in Figure 4-3. Note that the forward pump beam, as projected on the mixer slab, is expanded in the x direction (normal to the plane of the figure) by the projective transformation

$$x = \frac{x'}{\cos\beta} \quad . \tag{4-2-2}$$

For example consider a refocus phase distribution on the forward pump which is

$$\phi_f(x,y) = \phi_{pp} \frac{\left[(x')^2 + y^2\right]}{r_o^2} \quad , \tag{4-2-3}$$

where r_o is the radius of the beam, and ϕ_{pp} is the peak-to-peak phase excursion over the beam. Then, in the plane of the Figure 4-3, Equation 4-2-2 gives a phase on the backward signal wave which is

$$\phi_s(x,0) = \phi_{pp} \left[\cos^2\beta \left(\frac{x}{r_o}\right)^2 + \left(\frac{y}{r_o}\right)^2\right] \quad . \tag{4-2-4}$$

If distribution of (4-2-3) were the desired result, then there is an error from the projective distortion which is

$$\phi_e(x,y) = \phi_{pp} \sin^2\beta \left(\frac{x}{r_o}\right)^2 \quad . \tag{4-2-5}$$

10491-4
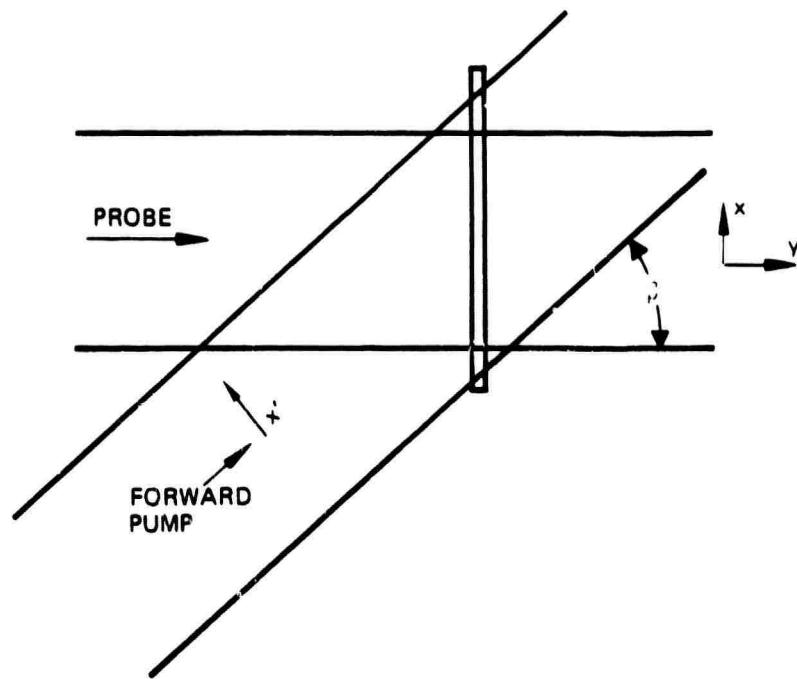
Figure 4-3. A thin four-wave mixer with equal diameter
diameter pump and probe beams, wherein
the mixer face is oriented normal to the
probe beam. The phase pattern on the
pumps is expanded in the x direction as
it propagates onto the mixer slab.

A reasonable measure of the seriousness of this error is the (spatial) mean-squared value which is,*

$$<\phi_e^2> = \frac{\phi_{pp}^2 \sin^4 \beta}{5} \quad . \tag{4-2-6}$$

If, for example, we take $\phi_{pp} = 40\pi$ and $\beta = 0.1$ rad (corresponding to some later examples) then

$$<\phi_e^2> = 0.32 \quad , \tag{4-2-7}$$

which corresponds to Strehl ratio of about 0.73. As $<\phi_e^2>$ further increases (for still larger values of ϕ_{pp}) a serious loss in Strehl ratio occurs.

Of course, one can avoid this projective problem by orienting the faces of the mixer slab normal to the bisector of the probe and forward pump angles as illustrated in Figure 4-4. We choose this geometry for detailed subsequent work. With this orientation, if the slab is of infinitesimal thickness, the phase perturbations on the forward (or backward) pumps are transferred onto the signal wavefront without error. It must be noted, however, that there is some risk in using such a geometry in that the forward pump may couple into the signal direction via reflection off of the slab faces and thereby interfere with the conjugated wavefront.

With thick mixer volumes additional problems arise. In the next section we will provide a simplified explanation of how the overlap geometry of the pump and probe within the thick mixer volue determine whether or not first order parasitic phase aberrations (e.g., tilt) are introduced onto the signal beam. Specifically, we will show that for a beam overlap, which occurs in the central plane of the mixer, this class of parasitic phase distoriton is eliminated.

---

*A square beam cross section is assumed.
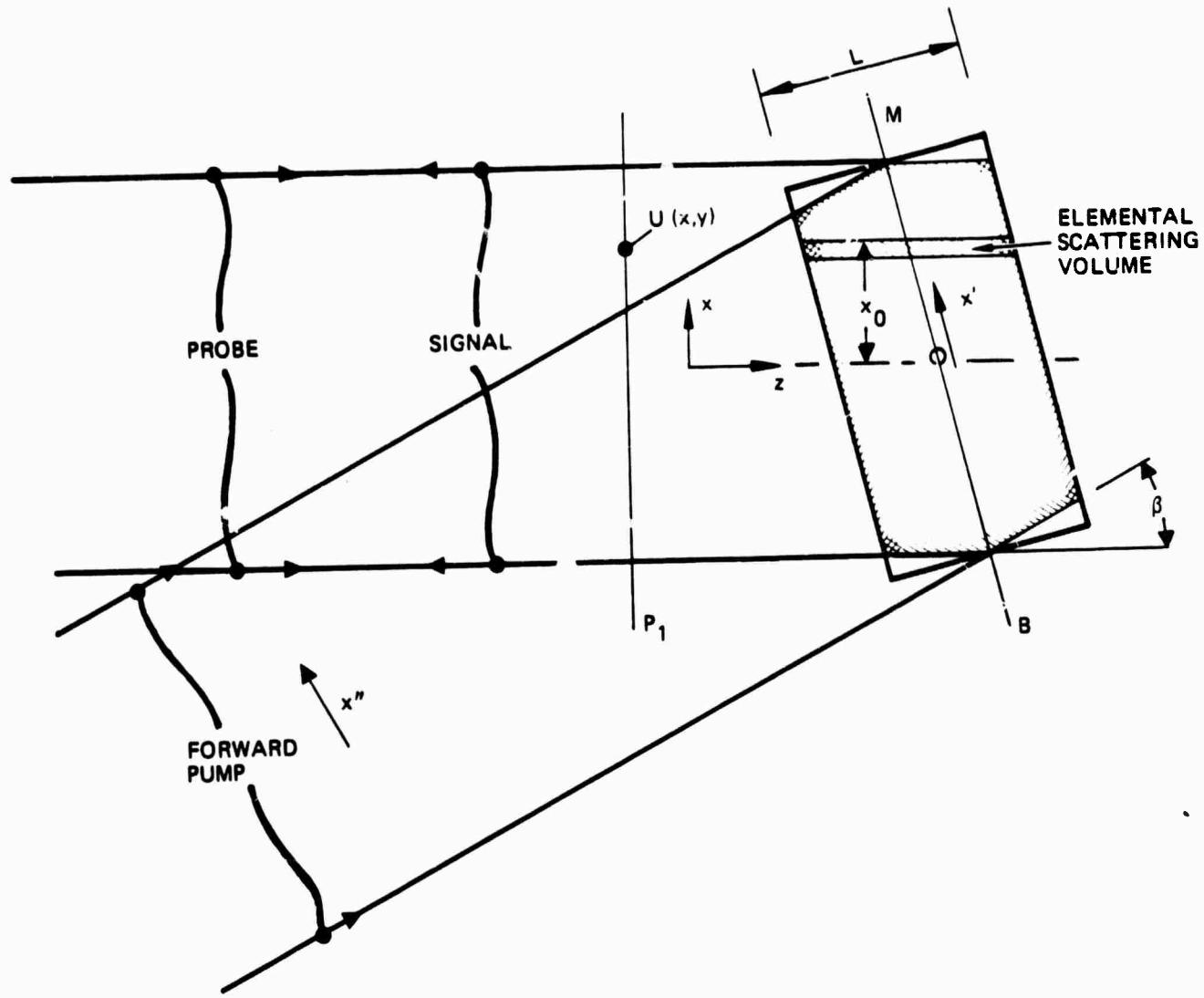
Figure 4-4. A favorable four-wave geometry for pump-to-signal wavefront transfer. The FWM volume within the hatched region is the effective operating volume and within this volume the cylinder, depicted by the cross hatches, centered on coordinates x,y, contributes to the scattered signal field $U(x,y)$ at plane P_1.

Having sele ted a favorable geometry for the mixer slab orientation and
beam overlap, one is left with a class of residual distortions, the foremost
of which is a spatial amplitude modulation on the signal beam as previously
discussed. These distortions depend upon both the width-to-depth ratio of the
mixer slab, and upon the angle between the pump and probe. The distortions
vanish as either approaches zero. The specific analysis for parabolic pump
wavefront errors and for (spatial) sinusoidal distortions is given in 4.2.2.2.

4.2.°.1 The Effect of Beam Cross-Over Location on Parasitic Distortion

In this discussion we assume that the signal and pump wavefronts in the
unperturbed system are uniform-amplitude collimated plane-waves. Further, we
assume that the scale of all wavefront errors and perturbations is sufficiently
large, compared to the depth of the four-wave mixer, that diffraction effects
can be neglected. Initially, we consider a mixer volume whose faces are
parallel and oriented normal to the probe beam as illustrated in Figure 4-5.

In order to keep the treatment as simple as possible, we first consider
the one dimensional problem wherein the pump beam width is narrowed, such that
the beams exactly cross over at the front edge of the mixer volume as illus-
trated in Figure 4-5a or at the center of the slab as in Figure 4-5b. This avoids
the projective distortions discussed in part one (for the two-dimension problem).

One can understand the key effect of the cross-over location by consider-
ing two mixer slabs of infinitesimal width, one at the front edge and one at
the back edge of the mixer. The f ward pump phase perturbation transfers
without further perturbation onto the signal generated in (scattered from) the
forward slab. However, the phase perturbation introduced onto the signal
generated by the rear slab shifts with the beam as it displaces. Thus, at the
back edge of the mixer it is offset by a shift δ where

$$\delta = L \tan \beta \ ,$$

(°-2-8)

BACKWARD
PUMP

δ

PROBE   SIGNAL

x

z

β

x

ϕ_f AS PROJECTED
ON BACK SLAB

ϕ_f AS PROJECTED
ON FRONT SLAB

ϕ_f
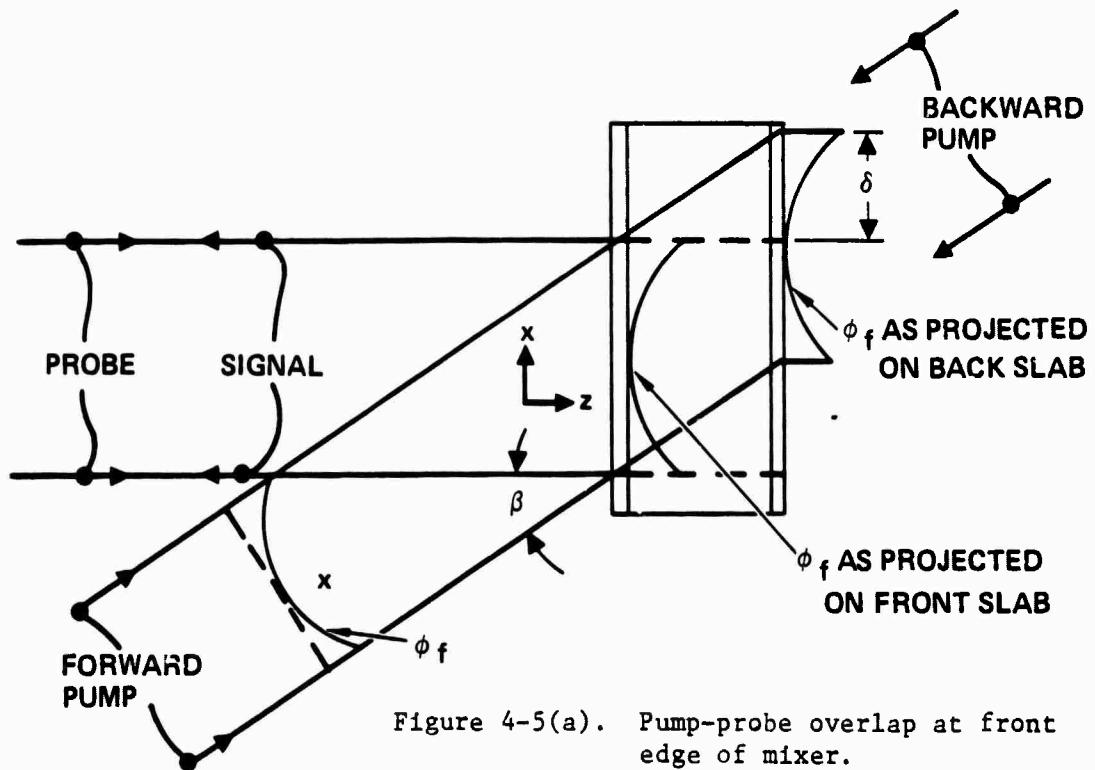
FORWARD
PUMP

Figure 4-5(a).   Pump-probe overlap at front
edge of mixer.

PROBE   SIGNAL

X

Y

ϕ_f AS PROJECTED
ON BACK SLAB

x'

ϕ_f

FORWARD
PUMP

ϕ_f AS PROJECTED
ON FRONT SLAB
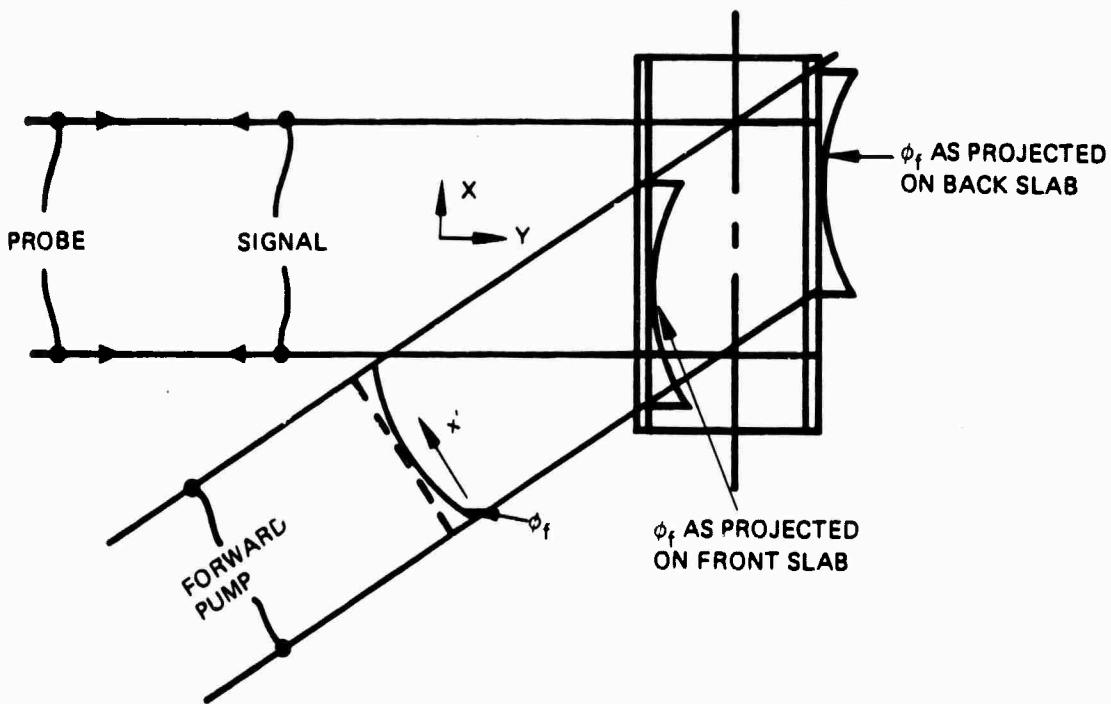
Figure 4-5(b).   Pump-probe overlap at center plane of mixer.

and β is the angle between the forward pump and the probe beams. Specifically for a parabolic perturbation, after (4-2-3) the signal phase produced by the front slab is

$$\phi_s = \phi_f = \phi_{pp} \left(\frac{x}{R_o}\right)^2 \quad , \tag{4-2-9}$$

while the phase perturbation which is transferred onto the signal produced by the rear slab is

$$\phi_s = \phi_{pp} \frac{(x-\delta)^2}{R_o^2} \quad . \tag{4-2-10}$$

The combined signal field produced by both slabs is

$$U_s = H \left[\exp i \, \phi_{pp} \left(\frac{x}{R_o}\right)^2 + \exp i \, \phi_{pp} \frac{(x-\delta)^2}{R_o^2} \right]$$

$$\tag{4-2-11}$$

$$= H \, \exp i \, \phi_{pp} \left(\frac{x}{R_o}\right)^2 \exp i \, \frac{\phi_{pp}}{R_o^2} \left(x\delta + \frac{\delta^2}{2}\right) \cos \frac{\phi_{pp}}{R_b^2} \left(\delta x + \frac{\delta^2}{2}\right) \quad ,$$

where H is a factor dependent on $\chi^{(3)}$, and the pump and signal field strengths. The combined field of (4-2-11) consists of three products. The first factor of the second line represents the direct pump perturbation transfer onto the signal, the second is a parasitic linear phase or tilt component, and the third is a consequence of phase mismatch, resulting from the pump phase perturbation walk off at the back edges. It is not hard to see that when the full mixer volume is operative, L in Equation (4-2-8) is replaced by z, and an integration

over z replaces the simple sum. However, basically the same three types of factors occur, with some changes in the functional form as a consequence of the integration. Similar behavior occurs in the full two-dimensional problem.

This basic behavior is modified if we locate the pump-probe cross-over plane in the center of the mixer as illustrated in Figure 4-5b. In this instance, the pump phase perturbation shift pattern is shifted downwards by $\delta/2$ in the front slab, and upwards by $\delta/2$ in the rear slab giving

$$U_s = H \exp i \phi_{pp} \left(\frac{x+\delta/2}{R_o}\right)^2 + \exp i \phi_{pp} \left(\frac{x-\delta/2}{R_o}\right)^2 .$$

$$(4-2-12)$$

$$= H \left[\exp i \phi_{pp} \left(\frac{x}{R_o}\right)^2\right]\left[\exp i \phi_{pp} \left(\frac{\delta}{2R_o}\right)\right]\cos\left(\frac{\phi_{pp}}{R_o^2} x\delta\right)$$

This contrasts to (4-2-11) in that the tilt component (the second factor in (4-2-11) is eliminated in (4-2-12). Integrating over the full mixer volume produces the same result - elimination of the parasitic tilt term.

Since alignment or experimental error may easily occur, we next address the size of the parasitic tilt component introduced by a "worst case" cross-over of Figure 4-5a. Here we consider the size of the tilt component generated by the full volume. Note that for a general mixer slab at location z Equation (4-2-8) becomes

$$\delta = z \tan\beta , \qquad (4-2-13)$$

and thus the $x\delta$ term in the third factor of (4-2-11) varies linearly with z. Consequently, one expects the average tilt phase ϕ_t introduced by the signal as generated by a full-mixer volume to be one half the value of Equation (4-2-11):

$$<\phi_t> = \frac{\phi_{pp} L \tan\beta}{2R_o} \qquad (4-2-14a)$$

4-17

A more careful analysis verifies that (4-2-14) is correct. As we will discuss subsequently, we expect to be able to employ useful focus offsets corresponding to ϕ_{pp} values of the order 20π, with $\beta = 0.1$ and $L/R_b = 0.25$. For these values, the tilt phase excursion at the beam edges is

$$< \phi_t(\pm R_b) > = \pi/4 \quad . \tag{4-2-14b}$$

This corresponds to a small (Strehl = 0.9) but noticeable degradation in the far field irradiance pattern.

In order to avoid this degradation, we choose the mid-plane crossover of Figure 4-4 as our basic design choice in subsequent analysis, thereby avoiding the tilt problem and simplifying the analysis. Essentially, the same arguments remain valid for slab orientations wherein the face is oriented normally to the forward pump and probe angular bisector (or alternatively for orientations normal to the pump angles).

If we repeat this analysis for a sinusoidal perturbation on the pumps,

$$\phi_f = \phi_m \cos(nx\omega_x + \theta) \quad , \tag{4-2-15}$$

then we find that instead of a parasitic tilt introduced on the signal beam, there is a parasitic sinusoidal component which for the simple two-slab model is

$$\phi_{par} = \frac{1}{2} \phi_m \sin(nx\omega_x + \theta) \quad . \tag{4-2-16}$$

Again, such a component is avoided by locating the beam overlap plane at the midplane of the mixer slab.

4.2.2.2 Analysis of the Parasitic Transfer Effects

The geometry to be analyzed is the bisector angle geometry with cross-over at the center of the mixer volume as illustrated in Figure 4-4. The phase

4-18

perturbation is assumed to occur on the forward pump and the backward pump (although present) is not illustrated. We start our analysis by noting that all phase factors, which vary as $\bar{k} \cdot \bar{r}$ (linear with distance) in the unperturbed geometry, ultimately cancel in a counter-propagating four-wave mixer system and can therefore be ignored. Thus, all of the phase factors to be considered here are perturbations which arise as a direct consequence of the perturbations introduced on the forward pump. The major pump-to-probe transfer problems occur in the plane defined by the probe and pump propagation vectors, the plane illustrated in the cross section of Figure 4-4. Phase variations in the y direction (normal to the paper) are exactly transferred onto the pump independenly of the angle, β, between forward pump and probe. If we define x" as the direction in the plane of Figure 4-14 normal to the forward pump propagation vector, then the phase distortion or perturbation on the forward pump may be described as $\phi_f(x")$. We then ask the question: what is the corresponding phase and amplitude variation on the signal wavefront produced by $\phi_f(x")$? We take the origin to be the center of the mixer slab and designate the mixer bisector plane as MB. The distance from the origin (normal to the y direction) in the MB plane is defined as x. All three x dimensions are related by projective transformations,

$$x" = x' \cos \beta/2 \quad , \tag{4-2-17a}$$

$$x = x' \cos \beta/2 \quad , \tag{4-2-17b}$$

Thus, the phase variation $\phi(x')$ is elongated (in the x" direction) as it propagates to the MB plane and correspondingly foreshortened as it propagates to plane P_1.

Consider a long thin* cylindrical volume of DFWM scattering centers, as illustrated in Figure 4-4 whose centroid is located at distance x above the z axis. The integral of the scattered fields over this volume produces the net

---

*Technically this cannot be an infinitesimal slab since as its dimensions approached λ the assumption of minimal diffraction would be violated.

signal field at point x in plane P_1, under the assumption of minimal diffraction effects. For convenience, we take the z origin in this cylinder to be shifted such that it falls on the central plane (MB) of the mixer. If we consider the phase perturbation in the pump field at a particular point, (x,z) in the shaded cylindrical volume as illustrated in Figure 4-4 we see that it is the same perturbation as occurred at the corresponding (projected) x point,

$$x' = x_o' - \Delta x_o' = x_o' - z \sin\beta \qquad (4-2-18)$$

where x_o is the projected x offset corresponding to the center of the scattering cylinder. Thus the perturbation multiplier of the scattered field from an elemental volume centered at (x,z) produced by a forward pump phase perturbation ϕ_f, is

$$M = \exp i \phi_f (x_o' - z \sin\beta)$$

$$= \exp i \phi_f (x_o z \sin\beta) \qquad . \qquad (4-2-19)$$

The net signal field at plane P_1 is given by the integral of M over the scattering cylinder. In subsequent sections we will evaluate the resultant integral for two specific cases: (A) ϕ_f is parabolic in x, (B) ϕ_f is sinusoidal in x.

Independently of the pump phase distribution, Figure 4-4 illustrates that there is a signal beam apodization, because of the lack of beam overlap causes the scattering cylinders length to shrink from L/cosβ to half this value. Specifically, this occurs for scattering cylinders corresponding to x displacements such that

$$\frac{x}{R_0} > 1 - \frac{L}{2R_0} \sin\beta \qquad . \qquad (4-2-20)$$

The resulting vignetting effect on the signal field is illustrated in Figure 4-6. Note that no vignetting occurs in the y direction; thus the edge isofield amplitude contours are elliptical. As we will see shortly, phase mismatch effects can cause additional vignetting on the signal beam.
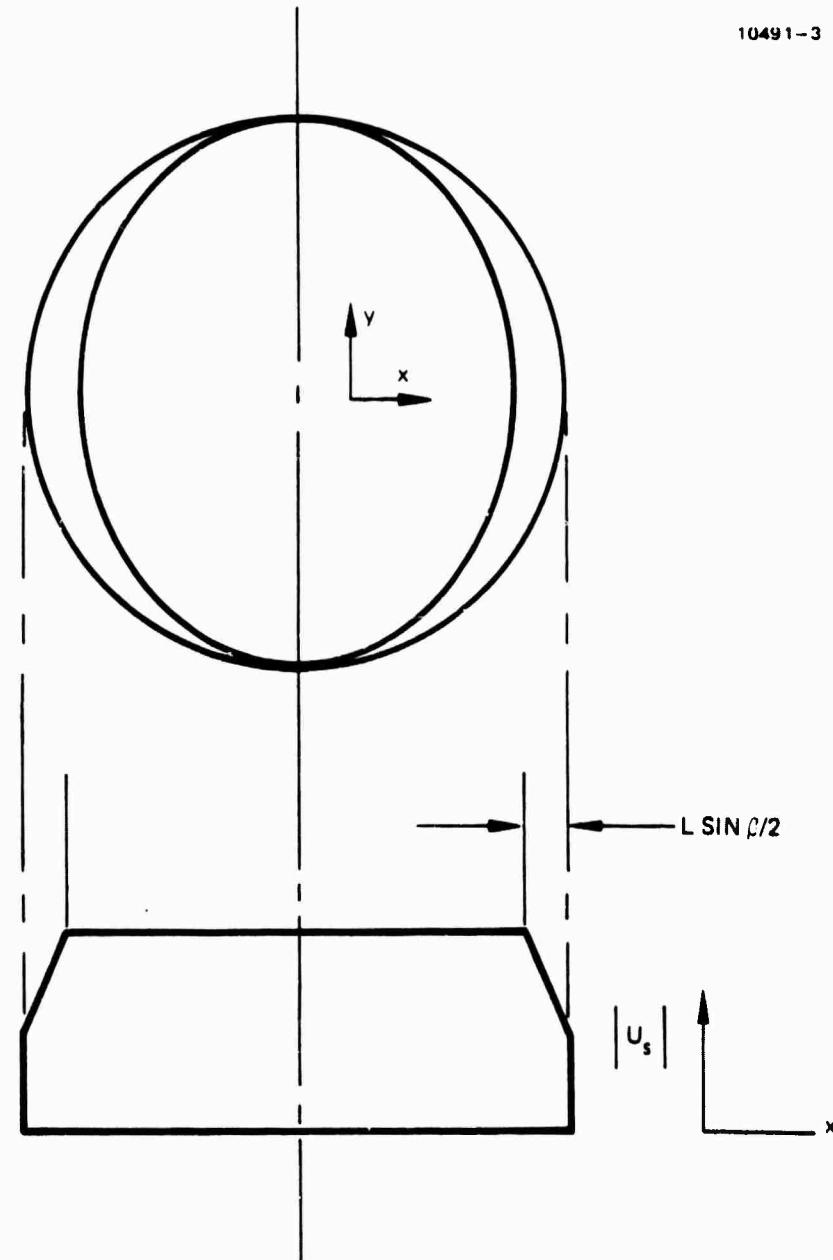
Figure 4-6. Effective amplitude vignetting on the
signal output beam, without pump wave-
front distortions.

4.2.2.2.1 Parabolic or Focus Errors

For this case we take

$$\phi_f(x'') = \phi_{pp}\left(\frac{x''}{R_0}\right)^2 \qquad (4\text{-}2\text{-}21)$$

and the local phase perturbation multiplier, after (4-2-19), on the signal beam is

$$M = \exp\, i\left(\frac{\phi_{pp}}{R_0^{\,2}}\right)(x_0^{\,2} - 2z\,x_0\,\sin\beta + z^2\sin^2\beta) \qquad (4\text{-}2\text{-}22)$$

Since the pump-to-probe angle β and z_{max}/R_s are generally chosen as small, we may neglect the third factor for the moment.* We will later quantify its effect (by way of example) for typical operating conditions.

In the central portion of the beam, the scattering cylinder extends from $-L/2$ to $+L/2$. Consequently, the total scattered field (in this regime) is given by the integral over the cylinder.

$$U_s(x_0) = F\exp\, i\,\phi_{pp}\left(\frac{x_0}{R_0}\right)^2 \int_{-L/2}^{L/2} dz\,\exp\left[i2\phi_{pp}\left(\frac{x_0 z}{R_0^{\,2}}\right)\sin\beta\right]$$

$$\qquad (4\text{-}2\text{-}23a)$$

$$= FL\exp\left[i\phi_{pp}\left(\frac{x_0}{R_0}\right)^2\right]\mathrm{sinc}\,\Gamma$$

where

$$\mathrm{sinc}\,\Gamma = \frac{\sin\Gamma}{\Gamma} \qquad (4\text{-}2\text{-}23b)$$

---

*If the third factor is retained, the integration over z produces fields which are described by error functions of complex argument. This unnecessarily complicates the discussion.

and

$$\Gamma = \phi_{pp}\left(\frac{x_o}{R_s}\frac{L}{2}\right)\sin\beta \qquad (4\text{-}2\text{-}23b)$$

Thus the first order signal (output) field is simply the field which would have been otherwise present, with the pump parabolic phase perturbation transferred onto it. The major deleterious effect results from mixer de-phasing (phase mismatch) over the depth, which produces an amplitude weighting (4-2-23b) or vignetting on the signal beam. This loss is largest at the beam edges, giving an effective apodization of the signal beam. Note that this apodization :curs in the x direction only. For example, if the pump and probe beams are of uniform amplitude, the signal beam is also uniform in the y direction. To quantify the size of the apodization, one must evaluate Γ based upon a focus parameter ϕ_{pp} commensurate with some desired application. Consider a mirror (or radius a) whose output beam focus (nominally at distance f) must be shifted by Δr. The maximum required phase shift $\phi(a)$ is

$$\phi_{pp} = \left(\frac{\pi}{\lambda}\right)\left(\frac{a}{f}\right)^2\Delta f \qquad . \qquad (4\text{-}2\text{-}24)$$

For f = 200 km, λ = 0.5 μm, a = 2 m, Δf = 20 km,

$$\phi_{pp} = 4\pi \qquad (4\text{-}2\text{-}25)$$

This same maximum phase shift is required at the edges of the signal beam out of the FWM. The maximum value of the Γ argument of the sinc apodization function thus becomes

$$\Gamma_{max} = 4\pi\left(\frac{L}{R_0}\right)\sin\beta \qquad . \qquad (4\text{-}2\text{-}26)$$

4-23

For example, if we chose $\beta = 0.1$, $L/R_s = 1/4$, then

$$\Gamma_{max} = \pi/10 , \qquad (4\text{-}2\text{-}27)$$

and the field at the beam edge is reduced in relative magnitude to 98% of its beam center value.

We next return to the neglected third term in the expression (4-2-22) which we now call ϕ_t. Its maximum value in the scattered field integration is at $z = L/2$ giving

$$(\phi_t)_{max} = \frac{\phi_{pp}}{4}\left(\frac{L}{R_s}\right)^2 \sin^2\beta . \qquad (4\text{-}2\text{-}28)$$

For the above example

$$(\psi_t)_{max} = \frac{4\pi}{4}\left(\frac{L}{R_s}\right)^2(0.1)^2 = 0.002 . \qquad (4\text{-}2\text{-}29)$$

If one evaluates the perturbation effect of this term on the integral of (4-2-23), the integrated value is about 1/3 of this value (0.0006), as a consequence of integrating z^2. Similarly, for other applications, with other parameters, L/R_s and K, it appears that the effect of the third term can be neglected for cases where Γ_{max} is small.

Equation (4-2-20) gives the (normalized) ellipticity for the cited example as

$$\frac{x_a}{R_s} = 1 - \left(\frac{1}{4}\right)(0.1) = 0.975 . \qquad (4\text{-}2\text{-}30)$$

4-24

Thus the far field pattern will experience only a minor change from this type of apodization, compared to a uniformly illuminated aperture

4.2.2.2.2 Sinusoidal Phase Errors

In this subsection we consider a wavefront error that is decomposed into its Fourier components. Condiser a particular such perturbation component, on the forward pump, which

$$\phi_f = \phi_m \sin\left(\frac{x'}{R_s} 2N\pi + \theta\right) \quad . \tag{4-2-31}$$

The perturbation field multiplication factor on the signal beam, resulting from this phase perturbation, at an elemental scattering volume centered at (x,y) is obtained by substituting (4-2-18) in (4-2-31) giving

$$M = \exp i \, \phi_n \, \sin\left(\frac{x2N\pi}{R_s} + \theta - \frac{z}{R_s} 2N\pi \sin \beta\right)$$

$$= \exp i \left[\phi_m \, \sin\left(\frac{x2N\pi}{R_s} + \theta\right) \cos\left(\frac{z}{R_s} 2N\pi \sin \beta\right) \right. \tag{4-2-32}$$

$$\left. - \phi_m \, \cos\left(\frac{x2N\pi}{R_s} + \theta\right) \sin\left(\frac{z}{R_s} 2N\pi \sin \beta\right) \right] .$$

The maximum z occurs at

$$z_{max} = L/2 \quad , \tag{4-2-32a}$$

assuming that N and/or β and/or L are sufficiently small that

$$\left(\frac{L}{R_s}\right)\sin \beta \ 2\pi \le 0.5 \tag{4-2-33b}$$

then over most of the cylinder of integration, to an excellent approximation,

$$\cos\left(\frac{z}{R_s} \ 2N\pi \ \sin\beta\right) \doteq 1 \qquad (4-2-34a)$$

$$\sin\left(\frac{z}{R_s} \ 2N\pi \ \sin\beta\right) \doteq \frac{z}{R} \ 2N\pi \ \sin\beta \qquad (4-2-34b)$$

Substituting (4-2-34a) and (4-2-34b) into (4-2-32) gives

$$M \doteq \exp i \ (\phi_m \ \sin B)\left[\exp\text{-}i\phi_m \ \cos B\right]^{Az} \qquad (4-2-35a)$$

where

$$B = \frac{2N\pi x}{R_s} + \theta \qquad (4-2-35b)$$

$$A = \frac{2N\pi}{R_s} \ \sin\beta \quad . \qquad (4-2-35c)$$

Integrating over the cylinder centered at x gives the scattered field received at the plane P_1, which is

$$Ex = F \ \text{sinc}\left[\phi_m\left(\frac{LA}{2}\right) \ \cos\left(\frac{2N\pi x}{R_s} + \theta\right)\right] \exp i(\phi_f) \quad . \qquad (4-2-36)$$

Thus, to this order of approximation, the phase is exactly transferred onto the signal beam. As with parabolic error, the second order effect is an amplitude modulation of the signal beam. In this case the major amplitude modulation occurs at twice the spatial frequency of the phase modulation. The relative peak field excursion is

$$Ex = 1 - \text{sinc}\left[\phi_m\left(\frac{L}{R_s}\right)N\pi \ \sin\beta\right] . \qquad (4-2-37)$$

For example with the equality in (4-2-33b) holding, and $\phi_m = \pi$, Ex = 0.36. Even larger extensions are quite tolerable.

4.2.3 The Effect of Pump Misalignment

Consider a four-wave mixer system in which the backward pump and forward pump are misaligned by an angle β as illustrated in Figure 4-7. The signal wave exits the mixer at some angle θ to be determined, and with some reduced strength because of the resultant phase mismatch, which is also to be determined. The resultant k vector magnitude is given by

$$|\vec{k}_s{}'| = |\vec{k}_f + \vec{k}_b - \vec{k}_p| \quad ,$$

which is not generally equal to ω_s/c. In general, one intuitively expects that the angle of the maximum signal radiation will be at or at least near the angle of $\vec{k}_s'$ which we designate as θ_k. Thus our initial estimation of the angle is angle $\hat{\theta}$, which may be derived by summing the k vector compoinents as

$$\hat{\theta} = \theta_k = \tan^{-1}\left[\frac{-K_f \sin\alpha + K_b \sin(\alpha-\beta)}{K_f \cos\alpha - K_b \cos(\alpha-\beta) + K_p}\right] , \qquad (4\text{-}2\text{-}39a)$$

where

$$K_n = |\vec{k}_n|, \quad n = f, b, p \qquad (4\text{-}2\text{-}39b)$$

We will verify that this estimation is accurate in subsequent paragraphs. For the usual case where the backward and forward pumps and the probe are at the same frequency, and where α and β are small (4-2-39) gives

$$\hat{\theta} = -\beta . \qquad (4\text{-}2\text{-}40)$$
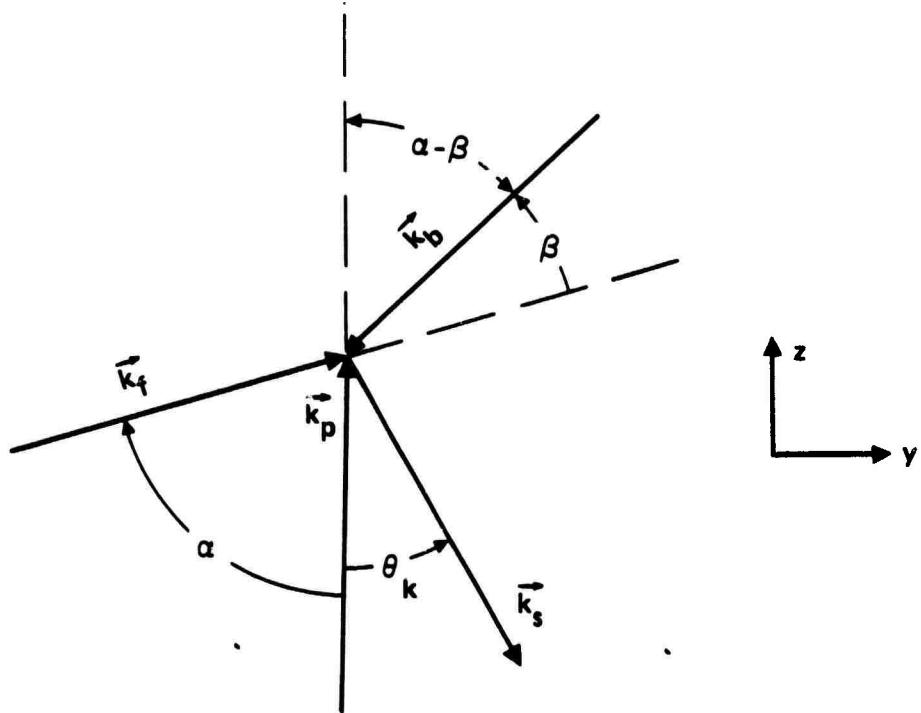
Figure 4-7. Generalized coplanar k vector geometry with pump-to-pump offset.

We have conducted an experiment which verifies this proportionality as indicated in Figure 4-8 (see Section 5.5 for details of the experiment). Clearly, useful signal beam tilt offsets of many milliradians can be obtained in this way, under the conditions cited above. As the pump offset angle becomes large however, we see that the phase mismatch which exists across the mixer volume will reduce the effective reflectivity of the system. To explore this question quantitatively we have employed a parallel piped mixer geometry, as illustrated in Figure 4-9, and computed the far field pattern produced by the mixer volume, treated as a weak scattering system. The far field radiation pattern, which is generated by this scattering process is

$$U(X_o, Y_o) = \left(\frac{F \exp iz_o K_s}{i\lambda_o z_o} \right) \mathrm{sinc}\left[\left(-\Delta + \frac{\theta_k^2 - \theta^2}{2} \right)\left(\frac{L_z}{\lambda_s} \right) \right]$$

(4-2-41)

$$\times \ \mathrm{sinc}\left(\frac{x_o}{z_o} \right)\left(\frac{L_x}{\lambda_s} \right) \ \mathrm{sinc}\left[\left(\frac{y_o}{z_o} - \frac{K_y'}{K_s} \right)\left(\frac{L_y}{\lambda_s} \right) \right] \times \mathrm{Vol}$$

where (x_o, y_o) are the transverse coordinates in the output (far field) plane and z_o is the distance to this plane. The dimensions of the mixer box are L_x, L_y, L_z and λ_s is the wavelength. The angle θ_k is the offset angle of $\vec{k}_s'$ as given in (4.2-39). The angle θ is given by

$$\theta = \frac{\left(x_o^2 + y_o^2 \right)^{1/2}}{z_o} \ ,$$

(4-2-42)

and Δ is given by

$$\Delta \doteq \frac{|k_s'|}{K_s} - 1 \ .$$

(4-2-43)
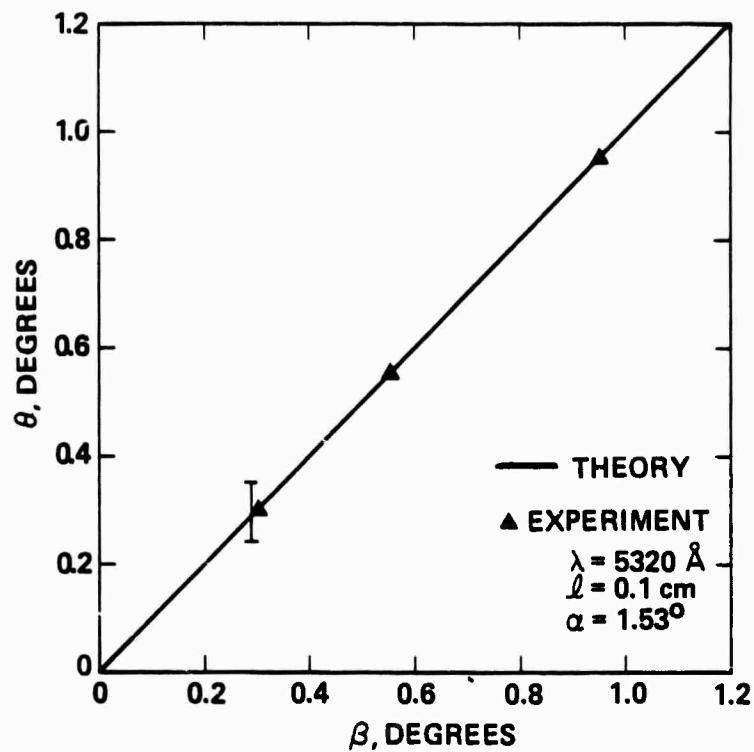
Figure 4-8. Experimental point ahead angle versus
pump-to-pump misalignment angle β.

NON-IDEAL

$$U_s \sim \exp i \, [\bar{k}_s{}' \cdot \bar{r} + \omega_s t]$$

$$-\bar{k}_p$$

$U_s(\omega_s, \phi_s{}')$

$U(x_0, y_0)$
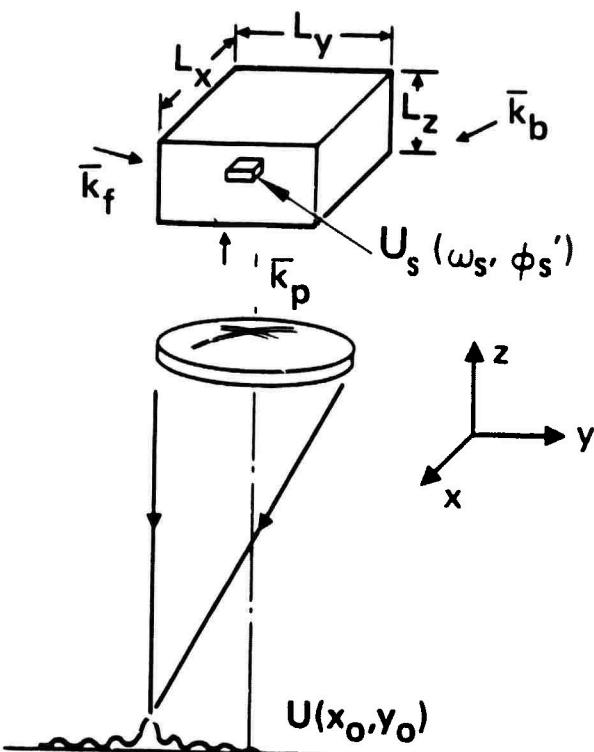
Figure 4-9. Geometry for estimating the far field scattered from a four-wave mixer with pump-to-pump offset.

For small α and β, Δ is well approximated as

$$\Delta \doteq \sin\beta \, \sin\alpha \qquad (4\text{-}2\text{-}45)$$

The parameter K_y' is the y component of k_s'.

In general all three sinc factors contribute an angular dependent weighting to the net radiation pattern. For the case where L_x and L_y become very large, the second two factors approach δ functions, whose narrow width dominates the radiation pattern, and the maximum output occurs at those angles wherein the last two δ function arguments vanish. That is

$$(\Theta_y)_{\text{Peak}} \doteq \frac{y_o}{z_o} = \frac{K_y'}{K_s} = (1 + \Delta) \, \sin\theta_k \qquad (4\text{-}2\text{-}45a)$$

$$(\theta_y)_{\text{Peak}} = \frac{x_o}{z_o} = 0 \quad . \qquad (4\text{-}2\text{-}45b)$$

For the usual cases of interest $\Delta \ll 1$ and θ_k is small, giving the approximation

$$(\theta_y)_{\text{Peak}} \doteq \theta_k \quad , \qquad (4\text{-}1\text{-}46)$$

confirming our initial intuitive feelings about the direction of maximum signal radiation. We have also performed an analysis of a spherical mixer volume which shows that the peak radiation always occurs at angle θ_k.

Substituting from the approximations of (4-2-44) and (4-2-40) for Δ and θ_k in (4-2-41) gives, for the plane $x_o = 0$, a Strehl ratio resulting from the angular mismatch β, which is (for a mixer of square cross-section) given as

$$S \doteq \text{sinc}^2 \left(\frac{\pi\delta}{\theta_w} \right) \text{sinc}^2 \left\{ \frac{\sin\alpha \, \sin\beta + \delta/2 \, [\delta - 2\beta]}{\theta_w} \right\} \qquad (4\text{-}2\text{-}47a)$$

where θ_w is the angular width of the radiation pattern formed from the square mixer aperture. That is,

$$\theta_w = \frac{\lambda}{L_y} = \frac{\lambda}{L_x} \quad , \tag{4-2-47b}$$

and δ is an angular offset variable

$$\delta = \theta_y - \theta_k \quad . \tag{4-2-47c}$$

As a rough guide, the maximum of the far field pattern occurs at approximately $\delta = 0$, giving a simplified approximation to (4-2-47) which is

$$S = \mathrm{sinc}^2 \left[(\sin\alpha)(\sin\beta)\left(\frac{L_z}{\lambda}\right) \right] \quad . \tag{4-2-48}$$

We have plotted the maximum of the complete expression of (4-2-47a) in Figure 4-10 for various values of α as a function of β.

Further, we have conducted experiments for $\alpha = 1.53^\circ$ and compared them to the calculated value in Figure 4-11 (see Section 5.5 for details of the experiment). The agreement is excellent.

4.3 COUPLED WAVE ANALYSIS OF FINITE BEAM EFFECTS IN NON-RESONANT DEGENERATE FOUR-WAVE MIXING

The analysis given in Section 4.2 provides a detailed discussion of the geometrical limitations of finite, spatially varying amplitude and phase of the pump beams on the fidelity of phase conjugation via degenerate four-wave mixing. This section, which complements the previous one, describes the coupled wave approach toward the understanding of finite pump beam effects on phase conjugation.
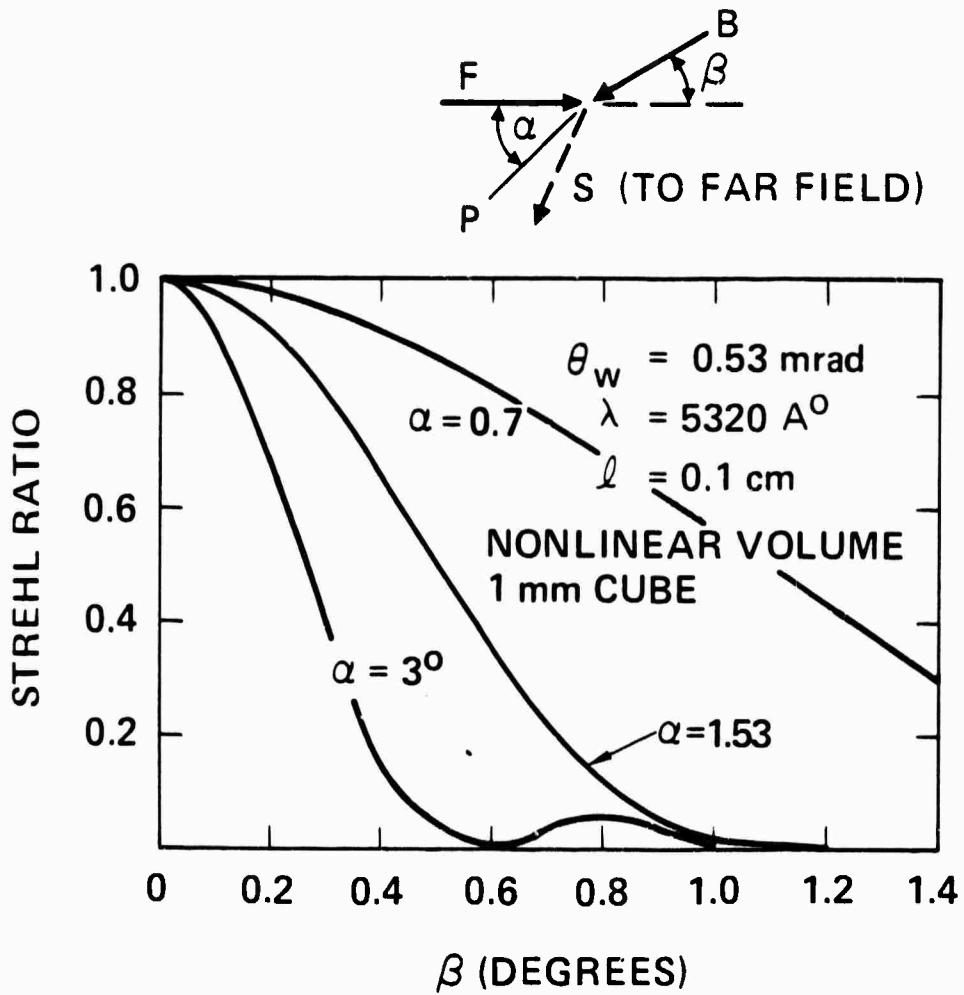
Figure 4-10. Theoretical amplitude reduction in the signal far field as a function of pump-to-pump offset anble β.
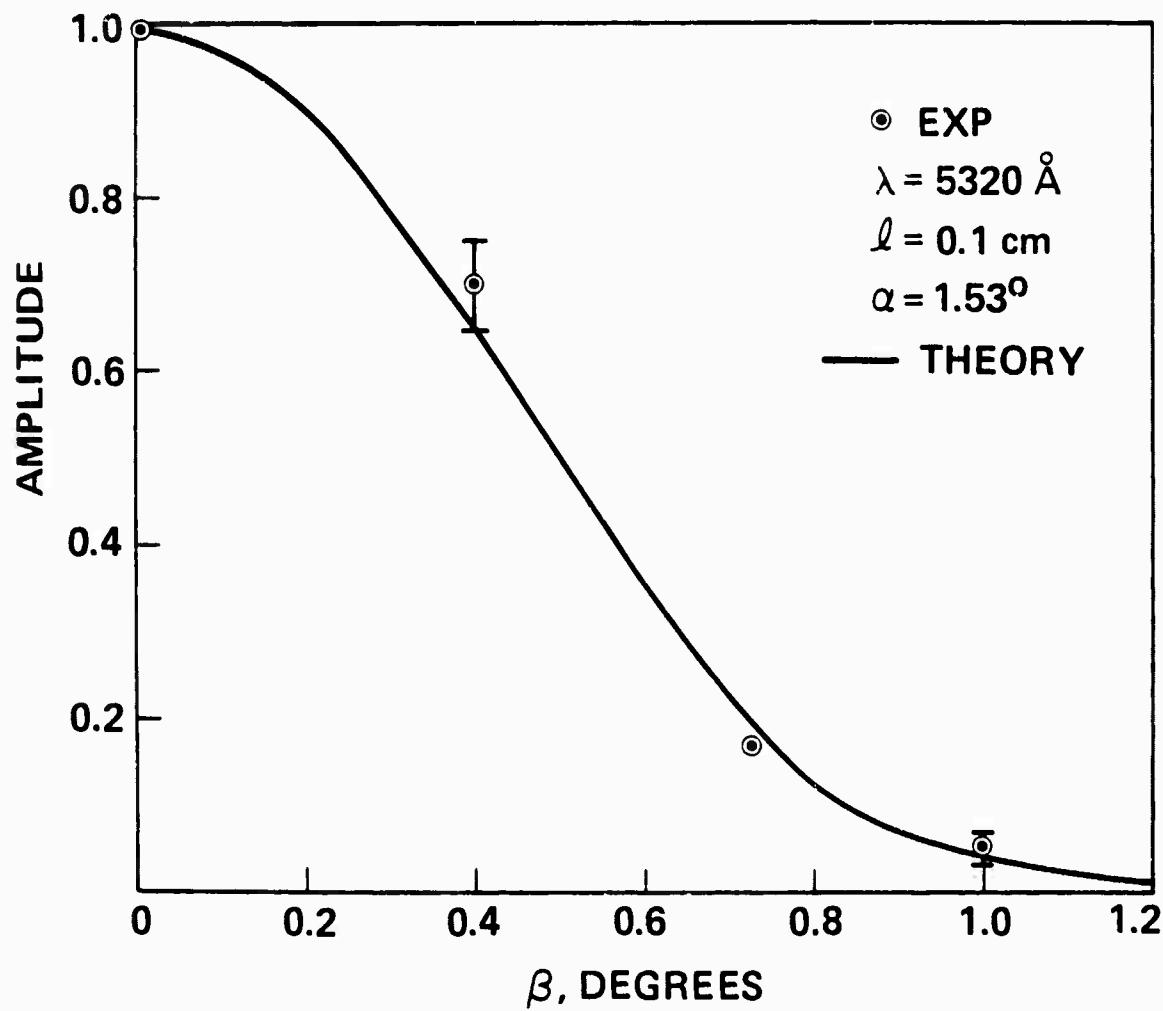
Figure 4-11. Amplitude reduction due to pump misalignment.

4.3.1 Generalized Coupled Wave Equations

We shall assume that the nonlinear polarization density for an isotropic homogeneous medium is given by the expression (2-22). The $\{E_n\}$ are the slowly varying field envelopes and $E_n = \hat{e}_n E_n$. With no pump depletion, but allowing for arbitrarily strong pumps, one obtains the following set of coupled wave equations (also, see Equation 3-1).

$$i\hat{k}_f \cdot \nabla E_f + \frac{1}{2k}\nabla_T^2 E_f = \frac{\omega}{2nc}\left\{M[(I_f+I_b)E_f + (\vec{E}_f \cdot \vec{E}_b^*)\,\hat{e}_f^* \cdot \vec{E}_b]\right.$$

$$\left. + \frac{N}{2}[I_f E_f + 2(\vec{E}_f \cdot \vec{E}_b)\,\hat{e}_f^* \cdot \vec{E}_b^*]\right\} \tag{4-3-1}$$

$$i\hat{k}_b \cdot \nabla E_b + \frac{1}{2k}\nabla_T^2 E_b = \frac{\omega}{2nc}\left\{M[(I_f+I_b)E_b + (\vec{E}_b \cdot \vec{E}_f^*)\,\hat{e}_b^* \cdot \vec{E}_f]\right.$$

$$\left. + \frac{N}{2}[I_b E_b + 2(\vec{E}_f \cdot \vec{E}_b)\,\hat{e}_b^* \cdot \vec{E}_f^*]\right\} \tag{4-3-2}$$

$$i\hat{k}_p \cdot \nabla E_p + \frac{1}{2k}\nabla_T^2 E_p = \frac{\omega}{2nc}\left\{M[(I_f+I_b)E_p + (\vec{E}_p \cdot \vec{E}_f^*)\,\hat{e}_p^* \cdot \vec{E}_f\right.$$

$$+ (\vec{E}_p \cdot \vec{E}_b^*)\,\hat{e}_p^* \cdot \vec{E}_b + (\vec{E}_f \cdot \vec{E}_s^*)\,\hat{e}_p^* \cdot \vec{E}_b + (\vec{E}_b \cdot \vec{E}_s^*)\hat{e}_p^* \cdot \vec{E}_f]$$

$$+ \frac{N}{2}[2(\vec{E}_f \cdot \vec{E}_p)\,\hat{e}_p^* \cdot \vec{E}_f^* + 2(\vec{E}_b \vec{E}_p)\,\hat{e}_p^* \cdot \vec{E}_b^*$$

$$+ 2(\vec{E}_f \cdot \vec{E}_b)\,\hat{e}_p^* \cdot \vec{E}_s^*]\right\} \tag{4-3-3}$$

$$i\hat{k}_s \cdot \nabla E_s + \frac{1}{2k}\nabla_T^2 E_s = \frac{\omega}{2nc}\left\{M[(I_f+I_b)E_s + (\vec{E}_s \cdot \vec{E}_f^*)\,\hat{e}_s^* \cdot \vec{E}_f\right.$$

$$+ (\vec{E}_s \cdot \vec{E}_b^*)\,\hat{e}_s^* \vec{E}_b + (\vec{E}_f \cdot \vec{E}_p^*)\,\hat{e}_s^* \cdot \vec{E}_b + (\vec{E}_b \cdot \vec{E}_p^*)\hat{e}_s^* \cdot \vec{E}_f]$$

$$+ \frac{N}{2}[2\,(\vec{E}_f \cdot \vec{E}_s)\,\hat{e}_s^* \cdot \vec{E}_f^* + 2(\vec{E}_b \cdot \vec{E}_s)\,\hat{e}_s^* \cdot \vec{E}_b^*$$

$$+ 2\,(\vec{E}_f \cdot \vec{E}_b)\,\hat{e}_s^* \cdot \vec{E}_p^*]\right\} \quad , \tag{4-3-4}$$

where M and N are defined by (2-19b) and (2-19c) for resonant media.

The E's are the wave amplitudes as defined in (2-20), the k_n is the unit vector along the direction of propagation of wave. The parameter $\hat{e}_n$ is the electric field polarization unit vector of wave E_n. The expression ∇_T^2 denotes the transverse Laplacian operator, and takes into account diffraction effects. The expressions given above are quite general in the choice of input electric field polarization, as well as direction of propagation of the various waves. The solution of the above equations is extremely difficult with noncollinear geometries and arbitrary polarization. Thus, the analyses that follows starts with a suitable choice of input polarization vectors and interaction geometries in order to effect a simple collinear analysis. In the collinear geometry of Figure 4-12, we shall choose the polarization of the input fields such that $\hat{e}_f = \hat{x}$, $\hat{e}_b = \hat{x}$, and $\hat{e}_p = \hat{y}$. In this case, one sees from Equation (4), that the phase conjugate has the same polarization vector as the input probe field. This interaction geometry allows a clear distinction between all four waves by means of polarization vector and propagation directions. In the noncollinear geometry, any arbitrary choice of polarization vectors yields distinct waves at all times. For sake of consistency, we shall keep the choice of electric field polarizations shown in Figure 4-12. In what follows, we shall discuss the variety of effects arising from the following four cases: a) Degree of phase conjugation in the regime of high reflectivity and finite pump beams. b) Collinear geometry and no diffraction. c) Noncollinear geometry and no diffraction. d) Non-collinear geometry with diffraction.

4.3.2 Coupled-Wave Analysis for Cross Polarized Waves in Collinear Geometry

Initial understanding of phase conjugation via Degenerate Four-Wave Mixing (DFWM) has led to the conclusion that ideal phase conjugation will always occur, provided that the pump beams have planar wavefronts. We will show that perfect operation breaks down under the condition that the reflectivities are larger than one for pump beams having planar wave fronts, with spatially dependent amplitudes and detuned from resonance. The source of the degradation is shown to be the nonlinear phase shifts which are generated by the same third order nonlinearities as the ones giving rise to DFWM.

Let's consider the geometry in Figure 4-12. We assume a collinear geometry in order to simplify the analysis. However, we believe that the conclusions which are reached are equally valid for near-collinear operation — the condition under which we expect most systems to operate.

The f and b beams are assumed to be strong compared to the p and s beams.

First, let us consider the dynamics of the pump beams. The forward pump beam experiences the following physical processes:

1. It self-induces an intensity-dependent change in the index of refraction, i.e., $\Delta n = n_2 |E_f|^2$, where n_2 is the nonlinear index of refraction.

2. It sees an additional change in the index of refraction due to the self-induced intensity-dependent effects provided by the backward b beam, i.e., $\Delta n = n_2 |E_b|^2$.

3. The counter-propagating nature of f and b beams yields a nonlinear spatial phase grating of periodicity $\lambda/2$. The Bragg scattering of the b beam from this grating provides additional phase changes, i.e., $\Delta n = n_2 E_f E_b^* \exp(-2ikz)$ + c.c.

Hence, the net change in the index of refraction as experience by the forward f beam is given by

$$\Delta n_f = n_2 \{ |E_f|^2 + |E_b|^2 + E_f E_b^* e^{-i2kz} + \text{c.c.} \} \quad . \tag{4-3-5}$$

In a similar manner, the backward b beam experiences a net change in the index of refraction given by

$$\Delta n_b = n_2 \{ |E_b|^2 + |E_f|^2 + E_f^* E_b e^{-i2kz} + \text{c.c.} \} \quad . \tag{4-3-6}$$

The wave propagation in the presence of the index perturbation is described by expressions (4-3-5) and (4-3-6) which leads to such phenomena as self-focusing, self-phase modulation, filamentation, and pulse compression.

4-38
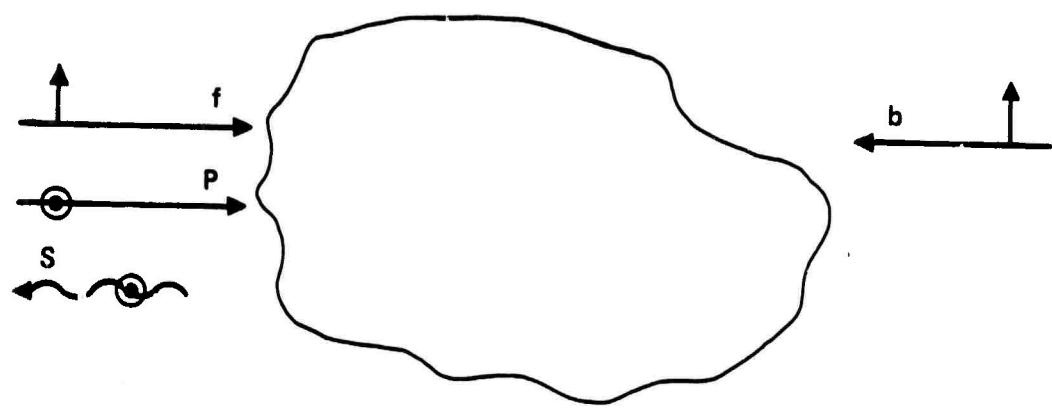
Figure 4-12. Geometry for collinear cross-polarized interaction.

We next consider the particular effects of the nonlinear phase shifts within a DFWM device. First, the probe (p) and signal (s) beams propagate in a medium whose index is modified by the pump beams. This nonlinear index is partially compensated for, provided that the pumps are equal in strength (the medium is symmetrical to the p and s beams). Thus, the fidelity of phase conjugation is determined by the phase of the pump beams and the accumulated nonlinear phase shift experienced by the pump beams. The magnitude of this nonlinear phase shift is in the same order of magnitude as the reflectivity. We will find that phase conjugation will not be diffraction limited even for pump beams with planar wave fronts when the reflectivity exceeds five (see below). And finally, if the pump beams are unbalanced in intensities, then at each point in the medium the net nonlinear phase is given by

$$\frac{\Delta k}{k} = n_2 \left(|E_b|^2 - |E_f|^2 \right) \quad , \tag{4-3-7}$$

which acts effectively as a phase mismatch and leads to a spatially dependent amplitude weighting in the reflectivity.

In order to quantify these effects, we undertake further analysis. In the strong pump beam approximations and neglecting diffraction effects (the interaction length is small compared to the diffraction length), the coupled wave equations of 4-3-1 through 4-3-2 become, for the collinear cross-polarized geometry of Figure 4-12,

$$i \, \frac{dE_f}{dz} = (\alpha + \beta)(I_f + 2I_b) E_f \quad , \tag{4-3-8a}$$

$$- i \, \frac{dE_b}{dz} = (\alpha + \beta)(I_b + 2I_f) E_b \quad . \tag{4-3-8b}$$

and

$$i \, \frac{dE_p}{dz} = 2\alpha(I_f + I_b) E_p + 2\beta \, E_f \, E_b \, E_s^* \quad , \tag{4-3-9a}$$

$$- i \, \frac{dE_s}{dz} = 2\alpha(I_f + I_b) E_s + 2\beta \, E_f \, E_b \, E_p^* \quad . \tag{4-3-9b}$$

4-40

where

$$\alpha = \frac{\omega}{2nc} M \;, \;\; \beta = \frac{\omega}{2nc} N$$

One notes the following conservation laws for the pump beams

$$\frac{d}{dz} |E_f|^2 = 0 \text{ and } \frac{d}{dz} |E_b|^2 = 0 \;,$$

which reflect the assumption of lossless media and non-depleted pumps. The geometry imposes the boundary conditions that $E_f(z{=}0)$, $E_b(z{=}L)$, and $E_p(z{=}0)$ are given quantities, and $E_s(z{=}L) = 0$. Then the solution to the set of equations subject to the prescribed boundary conditions is

$$\frac{|E_s(\vec{r},0)|^2}{|E_p(\vec{r},0)|^2} = \frac{4\beta^2 I_f(\vec{r},0) I_b(\vec{r},0) L^2}{(b_0 L)^2 \cot^2(b_0 L) + \left(\frac{\alpha+\beta}{2}\right)^2 \left[I_f(\vec{r},0) - I_b(\vec{r},0)\right]^2 L^2} \;.$$

$$(4\text{-}3\text{-}10a)$$

The signal phase distribution measured at the plane $z = 0$ is

$$\phi_s(\vec{r},0) = \frac{\pi}{2} + \phi_f(\vec{r},0) + \phi_b(\vec{r},L) - \phi_p(\vec{r},0)$$

$$- (\alpha + \beta)\left[I_b(\vec{r},0) + 2 I_f(\vec{r},0)\right] L \qquad (4\text{-}3\text{-}10b)$$

$$- \tan^{-1}\left\{\frac{\left(\frac{\alpha+\beta}{2}\right)\left[I_f(\vec{r},0) - I_b(\vec{r},0)\right] L}{b_0 L \cot(b_0 L)}\right\} \;,$$

where

$$b_0 = \left\{4\beta^2 I_f(\vec{r},0) I_b(\vec{r},0) + \left(\frac{\alpha+\beta}{2}\right)^2 \left[I_f(\vec{r},0) - I_b(\vec{r},0)\right]^2\right\}^{1/2} \;.$$

$$(4\text{-}3\text{-}10c)$$

$$\vec{r} = \chi \,\hat{i} + y \,\hat{j} \qquad (4\text{-}3\text{-}10d)$$

The first term in Equation (4-3-10b) arises from parametric excitation. The next three terms are just due to the initial input phase of the two counter-propagating pump waves and probe waves. The fourth term is due to nonlinear phase shifts, and the last term arises from the unbalanced pump effects.

The important quantity in Equation (4-3-10b) to consider in the presence of balanced pump beams is the fourth term $\phi = (\alpha+\beta)[I_b+2I_f]L$. We shall determine the effect of this term on the degree of phase conjugation by assuming equal pump intensity for the counterpropagating Gaussian beams, i.e., ($I_f = I_b = I$). For the sake of simplicity we shall assume that $\alpha = \beta$. The tolerance for compensation is determined by the following condition:

$$<(\Delta\phi)^2>^{1/2} < 0.36 \text{ radians} , \qquad (4-3-11)$$

for a Strehl ratio of 0.73, where $\Delta\phi$ is defined to be given by

$$\Delta\phi = 6 \beta L [I - <I>] , \qquad (4-3-12)$$

and the averaging is performed over a circular aperture of radius a_o of the input beam, i.e.,

$$<I> = \frac{1}{\pi a_o^2} \int_o^{2\pi} d\phi \int_o^{a_o} dr\, r\, I(r) . \qquad (4-3-13)$$

A simple calculation shows that for condition (4-3-11) to be satisfied, the reflectivity of the four wave mixing cannot exceed the value of 5 if the root-mean-quare phase variation is to remain less than 0.36 radians. If additional amplitude modulations exist on the pump beams, as could easily occur with high power operation, then the restriction may be still more severe.

To summarize: If the pump beams have a transverse distribution in ampli-tude for planar wave fronts, phase conjugation of the input probe can be achieved for reflectivities of less than five. For higher reflectivities, one expects nonlinear phase shifts to lead to a degradation of phase conjugation. Unbalanced pump beams are undesirable since these cause a reduction in signal, as well as erroneous phase contributions to the phase conjugation process.

4.3.4 Gaussian-Beam Transfer Analysis

We shall assume that the interaction length for degenerate four-wave mixing is much less than the diffraction length ka_o^2, where k is the wave number and a_o is the Gaussian radius of any of the three Gaussian input beams. Furthermore, self-focusing effects are assumed to be non-existent. This assumption can only be satisfied by either keeping the input power levels below the threshold for self focusing, or keeping the interaction length short in comparison to an equivalent self-focusing length. The pump beams are assumed to be described by the following expressions:

$$E_f = A_f \exp\left[-\frac{r^2}{2a_f^2} + i\frac{kr^2}{2R_f}\right] \quad , \quad (4-3-14a)$$

and

$$E_b = A_b \exp\left[-\frac{r^2}{2a_b^2} + i\frac{kr^2}{2R_b}\right] \quad , \quad (4-3-14b)$$

where $r^2 = x^2 + y^2$. Note that we have assumed the medium to be short enough that diffraction of Gaussian beams is not important, i.e., a_f^2, a_b^2, R_f and R_b are independent of z. The solution of this problem then, is the same as the one given in Equation (4-3-10). Also note that in addition to nonlinear phase shifts and unbalanced pump beam effects, the phase of the signal is given by

$$\phi_s = \frac{\pi}{2} - \phi_p (\vec{r},0) + \frac{kr^2}{2R} \quad , \quad (4-3-15)$$

where the effective radius of curvature is given by R, where

$$\frac{1}{R} = \frac{1}{R_f} + \frac{1}{R_b} \quad . \quad (4-3-16)$$

In addition, it is interesting to note that if $R_b = -R_f$, (i.e., the counterpropagating pumps are the conjugate of each other), then the phase of the generated signal is the negative of that of the incoming probe. However, more generally one can arrange an appropriate focus on the pump beam to give rise to a focusing or defocusing affect in the generated signal. For example, if $R_f = R_b = R$, and the input probe has a plane wavefront, then the generated signal wavefront has a radius of curvature given by $R_s = R/2$, which is represented as a focusing action.

The solution of Equation (4-3-9), subject to the 2-point boundary conditions, yields an expression of the form for the generated signal,

$$E_s(z=0) = 2i\beta \, E_f(r,0) \, E_b(r,0) \, E_p^*(r,0) \left\{ \frac{1}{i \frac{(\alpha+\beta)}{2}(I_f - I_b) - b_0 \cot b_0 L} \right\},$$

$$(4-3-17)$$

and in the weak coupling (small reflectivity) regime (Equation (4-3-17) reduces to

$$E_s(z=0) = 2i\beta \, E_f(r,0) \, E_b(r,0) \, E_p^*(r,0) \ . \qquad (4-3-18)$$

Observe that if E_p^*, E_f, and E_b are Gaussian beams, then the generated signal is also a Gaussian beam, with mean square radius given by

$$\frac{1}{a_s^2} = \frac{1}{a_f^2} + \frac{1}{a_b^2} + \frac{1}{a_p^2} \ , \qquad (4-3-19)$$

where a_p^2 is the mean square radius for the probe beam. This verifies the weak scattering results of Section 4.2.

4.4 THEORY OF NEARLY DEGENERATE FOUR-WAVE MIXING

The discussion in the previous sections of the physics and limitations of optical phase conjugation has been devoted to the cases of resonant and non-resonant degenerate four-wave mixing. It was assumed that all frequencies were equal in the analyses. However, there are practical situations where the input probe may be a wave oscillating at a slightly different frequency from the pump waves (or from a different laser). One can cite such examples as Doppler shifts arising from the translational motion of either the receiver or transmitter, or both. Off pump line center response could occur with the laser system and drift in frequency during operation, etc. These practical considerations have led us to carry out a detailed study of the frequency response of a phase conjugate mirror for a case where the input probe frequency is different from that of the counterpropagating pump waves. We have considered the response of resonant isotropic media such as alkali vapors and molecular gases, approximating such media by simple models, such as 2- and 3-level systems shown in Figures 4-13 and 4-14.

The interaction process for nearly degenerate operation is shown in Figure 4-15. ω, Ω and $2\omega-\Omega$ are the frequencies of the counter-propagating pump waves, input probe, and phase conjugate signal, respectively. Before proceeding to the rigorous formulation of the problem, it is helpful to provide a more intuitive understanding of the various physical phenomena involved.

First, consider the interaction of the pump and probe waves with the 2-level system. The interference of the forward pump wave, f, and input probe wave p no longer generates a spatial modulation in the population difference. Instead it produces a traveling wave excitation in the population with frequency $\omega-\Omega$ and phase speed $(\omega-\Omega)/|\vec{k}_p-\vec{k}_f|$. The direction of propagation of the traveling wave is given by $\hat{k}_p-\hat{k}_f$, where $\hat{k}_n$ denotes a unit vector of wave n. The scattering of the backward pump (b) wave from this traveling wave excitation yields a phase conjugate signal* having frequency $\omega-\Omega$. In a similar manner, the backward pump b wave and input probe p wave generates a traveling wave excitation. The direction

---

*That is, the spatial phase distribution on the input wave is reversed.
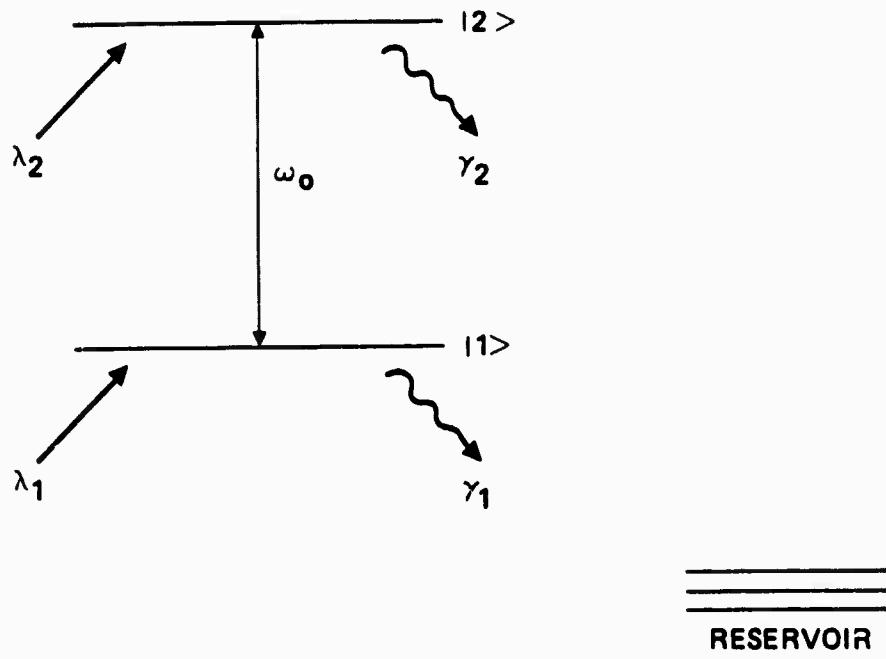
Figure 4-13.   2-level system. λ_n and γ_n are the
incoherent pumping and decay rates of
level $|n\rangle$ respectively.
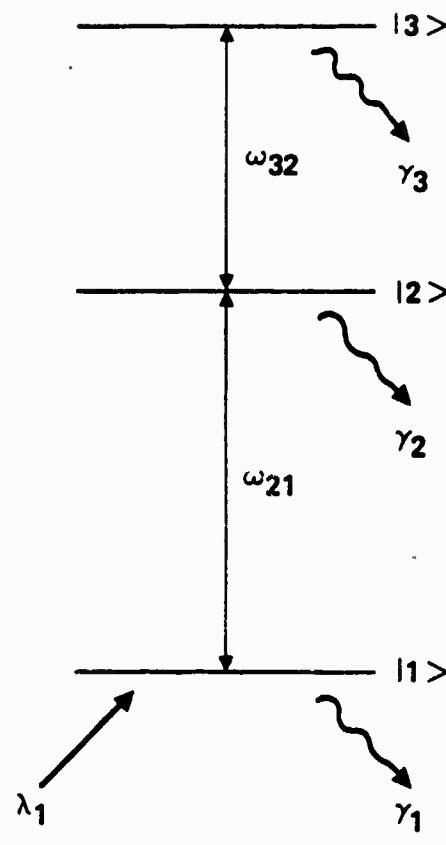
Figure 4-14. 3-level system as a model for 2-photon processes.

f(ω)

b(ω)

**ISOTROPIC
RESONANT
MEDIUM**

p(Ω)

s ($2\omega - \Omega$)
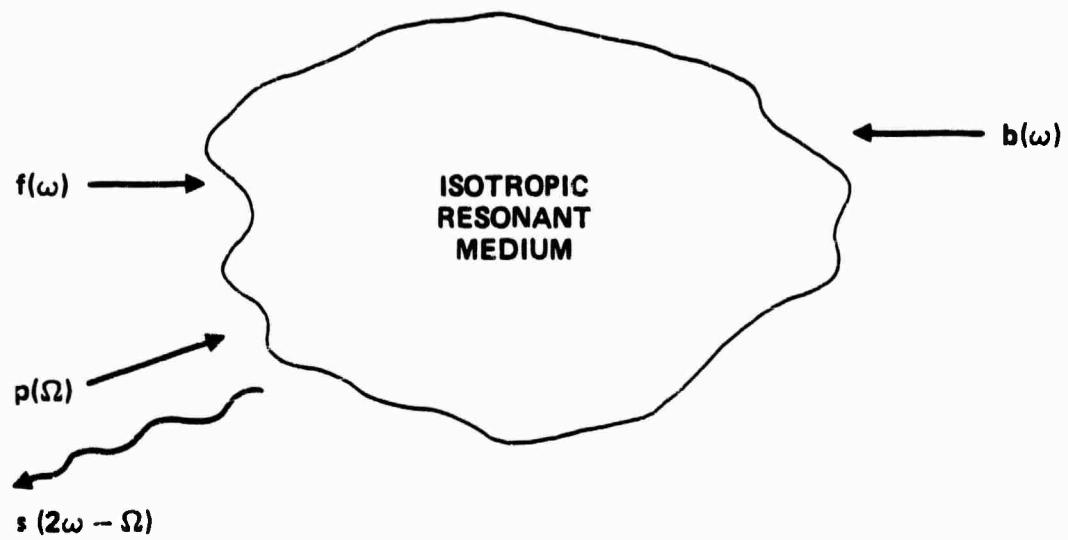
Figure 4-15.   Interaction geometry for nearly degenerate four-wave mixing.

of the traveling wave excitation is given by $\vec{k}_p-\vec{k}_b$. The scattering of the forward pump f wave generates a phase conjugate signal. The efficiency of the signal generation is determined in part by the amount of phase mismatch that arises in the four-wave mixing process, i.e., if a counterpropagating geometry is maintained, then there is a k vector mismatch.

$$\Delta\vec{k} = \vec{k}_f+\vec{k}_b-\vec{k}_p-\vec{k}_s \neq 0 \quad , \tag{4-4-1}$$

which occurs as a consequence of the probe wave p differing in frequency from generated signal s. In this case one defines a coherence length L_c given by

$$L_c = \frac{\pi}{|\Delta\vec{k}|} \quad , \tag{4-4-2}$$

which is the critical length of the interaction region L such that if L exceeds L_c, generation of phase conjugate signal becomes markedly inefficient.

Next consider the interaction of the counter-propagating and probe waves with the three-level system shown in Figure 4-14. The effect of the counter-propagating waves on the three-level system is to generate a coherent super-position of states $|1\rangle$ and $|3\rangle$. This coherent excitation is spatially uniform and oscillates at twice the pump frequency ω. The action of the input probe wave is to stimulate a phase conjugate signal via an electric dipole coupling to the two-photon coherent excitation. Again, phase matching consideration yields the important requirement that the interaction length be less than the coherence length L_c in order to generate phase conjugate signals in an efficient fashion.

In spite of this common feature, the bandwidths of the phase conjugate reflectivity (as a function of the difference between pump and probe frequencies) for the two- and three-level systems are different. If we assume that phase mismatch is compensated via angular orientation, or is negligible,

the bandwidth of the phase conjugate signal in two-level systems is then
determined by the energy relaxation rate $1/T_1$, where T_1 is the time it takes
an atom to achieve thermal equilibrium with the environment. This is because
at exact resonance a traveling wave excitation is generated in the excited
state of an atomic species. The excited state has a finite duration, which
is given precisely by T_1 if the initial state of the system is in the ground
state. Hence, for times much longer than T_1, the atom effectively returns
to the ground state via spontaneous decay, which is an incoherent process.
Thus, only for pump-probe detuning greater than $1/T_1$ the reflectivity will
decrease. In contrast, the bandwidth of the phase conjugate signal in a
three-level system is frequently determined by the degree of phase mismatch
rather than $1/T_1$ because the stimulated process, that produces the phase
conjugate signal, is achieved away from any intermediate atomic resonance
line. It is the counterpropagating pumps that generate the two-photon
coherence; the probe wave is not involved in this generation.

Yet the above discussion is oversimplified, since stationary atoms are
assumed. The effect of moving atoms modifies the reflectivity in two-level
systems in a subtle manner, due to Doppler effects (this work was performed
under Hughes· R&D). But due to the Doppler-free nature of the two-photon
processes, atomic motion does not play a similar role in modifying the
reflectivity in three-level systems.

4.4.1 Pump/Probe Detuning Effects in Two-Level Systems

The starting point in our analysis of the problem is again the solution
of the quantum mechanical transport equation in the perturbation regime.
The third order polarization density is calculated and provides the source
terms in Maxwell's equations. The electric field is written as

$$\vec{E} = \frac{1}{2} \sum_{n=f,b,p,s} \vec{E}_n \, e^{i(\omega_n t - \vec{k}_n \cdot \vec{r})} + \text{c.c.} \,, \tag{4-4-3}$$

such that E_f and E_b are constants in the interaction region, $\omega_f = \omega_b = \omega$, $\omega_p = \Omega$ and $\omega_s = 2\omega - \Omega$, $\vec{k}_f + \vec{k}_b = 0$. The polarization density has the general expression

$$\vec{P} = \varepsilon_o \chi^{(1)} E + \varepsilon_o \chi^{(3)} E_f E_b E^\star \quad \exp \quad i(\vec{k}_f + \vec{k}_b - \vec{k}) \cdot \vec{r} \qquad (4-4-4)$$

where $\chi^{(1)}$ and $\chi^{(3)}$ are the linear and four-wave mixing susceptibilities, respectively. In the slowly varying envelope approximation, the Maxwell equations yields a set of scalar coupled wave equations for E_p and E_s. They are given by

$$\frac{dE_s}{dz} = \alpha_s E_s + i\beta_s E_f E_b E_p^\star \, e^{i\Delta kz} \qquad (4-4-5a)$$

$$\frac{dE_p}{dz} = -\alpha_p E_p - i\beta_p E_f E_b E_s^\star \, e^{i\Delta kz} \qquad (4-4-5b)$$

where the absorption coefficients α_n are given by

$$\alpha_s = - \frac{2\omega - \Omega}{2n_s c} \left[\chi_s^{(1)} \right] \qquad (4-4-6a)$$

$$\alpha_p = - \frac{\Omega}{2n_p c} \left[\chi_p^{(1)} \right] \, , \qquad (4-4-6b)$$

and the four-wave mixing coupling constants are given by

$$\beta_s = \frac{2\omega - \Omega}{2n_s c} \left[\chi_s^{(3)} \right] \qquad (4-4-7a)$$

$$\beta_p = \frac{\Omega}{2n_p c} \left[\chi_p^{(3)} \right] \, . \qquad (4-4-7b)$$

4-51

n_s and n_p are the indices of refraction for E_s and E_p, and the phase mismatch is $\Delta k = |\vec{k}_p| - |\vec{k}_s|$. The boundary conditions are such that $E_p(z=0)$ is a given complex quantity and $E_s(z=L)$ is zero. Subject to these boundary conditions, the solution of Equations (4-4-5) yields the following expression

$$E_s(z=0) = i\beta_s E_f E_b E_p{}^*(z=0) \left\{ \frac{1 - e^{(\lambda_1 - \lambda_2)L}}{(\lambda_1 - \alpha_s) - (\lambda_2 - \alpha_s)\, a^{(\lambda_1 - \lambda_2)L}} \right\} \qquad (4\text{-}4\text{-}8)$$

where

$$\lambda_1 = -\frac{1}{2}(\alpha_s + \alpha_p - i\Delta k) + \frac{1}{2}\sqrt{(-\alpha_s + \alpha_p - i\Delta k)^2 - \left[4\,\beta_s\beta_p{}^* I_f I_b - \alpha_s(\alpha_p - i\Delta k)\right]}$$

$$(4\text{-}4\text{-}9a)$$

$$\lambda_2 = -\frac{1}{2}(\alpha_s + \alpha_p - i\Delta k) - \frac{1}{2}\sqrt{(\alpha_s + \alpha_p - i\Delta k)^2 - 4\left[\beta_s\beta_p{}^* I_f I_b - \alpha_s(\alpha_p - i\Delta k)\right]} \ .$$

$$(4\text{-}4\text{-}9b)$$

We have used the notation that $I_n = |E_n|^2$. The phase conjugate reflectivity is given by

$$R = \frac{|E_s(z=0)|^2}{|E_p(z=0)|^2} \qquad . \qquad (4\text{-}4\text{-}10)$$

A perturbation calculation of the response of the medium yields the following expression for the linear and four-wave mixing susceptibilities:

Two-Level Systems (Homogenously-Broadened)

$$\chi_s^{(1)} = +\frac{\Delta N_o}{i\hbar\varepsilon_o}|\mu_{12}|^2\left[\frac{1}{\gamma_{12} + i(\Delta + \delta)}\right] + \frac{\Delta N_o}{4i\hbar^3\varepsilon_o}|\mu_{12}|^4\left[I_f + I_b\right]\frac{2}{\gamma_o}\left[\frac{1}{\gamma_{12} + i(\delta + \Delta)}\right]\left[\frac{2\gamma_{12}}{\gamma_{12}^2 + \Delta^2}\right]$$

$$(4\text{-}4\text{-}11)$$

$$\chi_s^{(3)} = -\frac{N_o}{2ih^3\varepsilon_o}|\mu_{12}|^4\left[\frac{1}{\gamma_{12}+i(\Delta+\delta)}\right]\left[\frac{1}{\gamma_{12}+i\Delta}+\frac{1}{\gamma_{12}+i(\Delta-\delta)}\right]\left[\frac{1}{\gamma_1+i\delta}+\frac{1}{\gamma_2+i\delta}\right]$$

$$(4\text{-}4\text{-}12)$$

$$\delta \rightarrow -\delta: \quad \left\{ \begin{array}{c} \chi_s^{(1)} \rightarrow \chi_p^{(1)} \\[2ex] \chi_s^{(3)} \rightarrow \chi_p^{(3)} \end{array} \right\} \qquad (4\text{-}4\text{-}13)$$

where γ_{12} is the atomic linewidth, γ_n is the energy decay rate of state $|n>$, the pump detuning from atomic resonance is given by $\Delta=\omega-\omega_o$, and the pump-probe detuning is given by $\delta=\omega-\Omega$. ΔN_o is the population difference between lower and upper states. Figures 4-16, 4-17, and 4-18 show the functional dependence of the phase conjugate reflectivity as a function of pump-probe detuning parameter δ/γ_{12}, for various interaction lengths L. It is seen that the reflectivity increases in magnitude as the interaction length increases. This result stems from the physical consequence of a larger amount of atoms interacting with the radiation fields. The density was chosen to be equal to 10^{14} atoms/cc, with pump intensities of 10^4 W/cm^2. and a linewidth γ_{12}, with a decay rate γ of 1200 MHz. The dipole movement. are representative of typical alkali vapor, such as Na. One notes that the bandwidth of the reflectivity is given by γ_{12} or γ, in agreement with the physical interpretation given earlier.

4.4.2 Pump/Probe Detuning Effects in Three Level Systems

The calculation of the response of the three-level system proceeds along the same line as in the last section. The results are

$$\chi_s^{(1)} = \frac{N_o}{i\hbar\varepsilon_o}|\mu_{12}|^2\frac{1}{\gamma_{12}+i(\Delta+\delta)} \qquad (4\text{-}4\text{-}14)$$
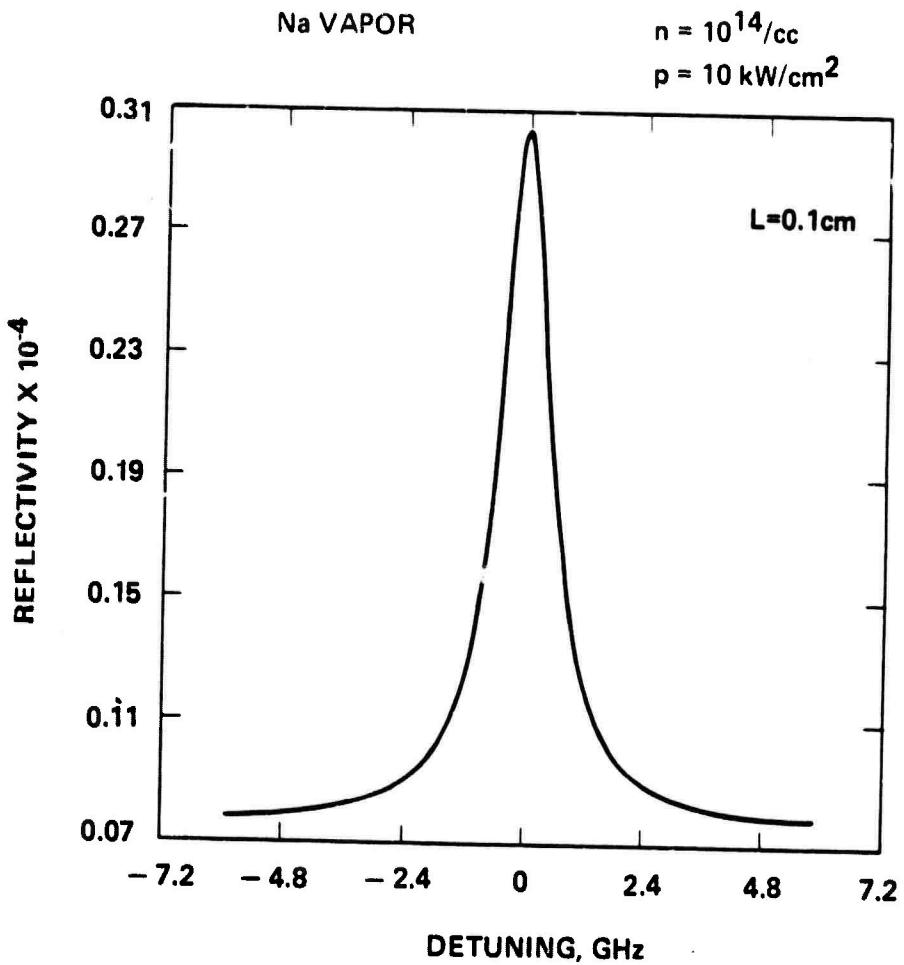
Figure 4-16. Probe-pump detuning for 1-photon resonance in
a cell of length 0.1 cm.
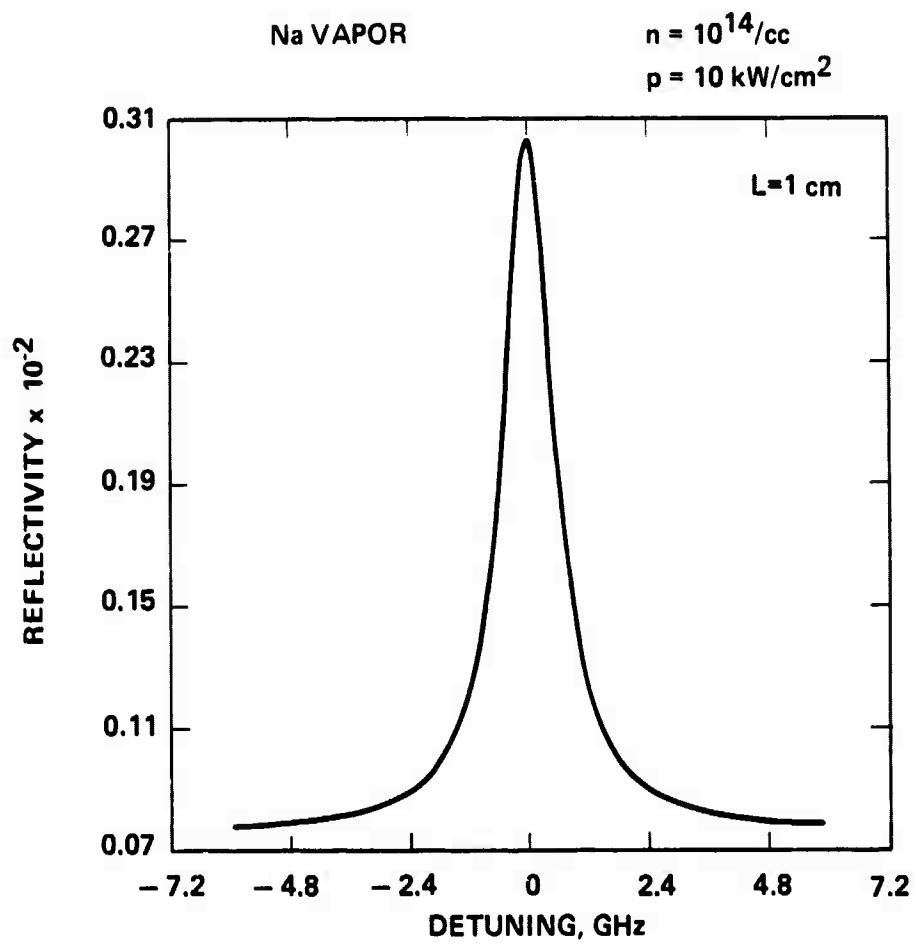
Figure 4-17. Probe-pump detuning for 1-photon resonance in a cell of length 1 cm.

Na VAPOR

$n = 10^{14}/cc$

$p = 10 \text{ kW/cm}^2$
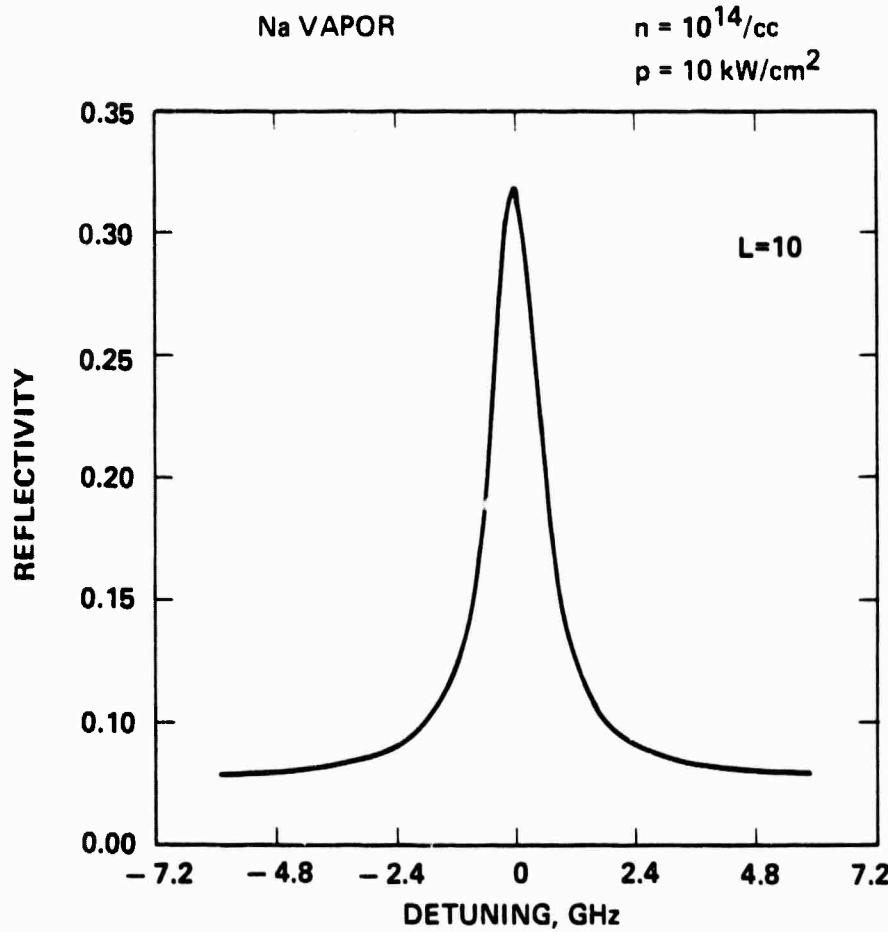
Figure 4-18.   Probe-pump detuning for 1-photon resonance in a cell of length 10 cm.

$$\chi_s^{(3)} = -\frac{N_o}{2ih^3\varepsilon_o} |\mu_{12}|^2 |\mu_{34}|^2 \frac{1}{\gamma_{12}+i\Delta_{21}} \frac{1}{\gamma_{13}+i\Delta_{31}} \left\{ \frac{1}{\gamma_{12}+i(\delta+\Delta_{21})} - \frac{1}{\gamma_{23}+i(\delta+\Delta_{32})} \right\}$$

(4-4-15)

$$\delta \rightarrow -\delta: \quad \left\{ \begin{array}{c} \chi_s^{(1)} \rightarrow \chi_p^{(1)} \\ \\ \chi_s^{(3)} \rightarrow \chi_p^{(3)} \end{array} \right\}$$

(4-4-16)

where $\Delta_{ij}=\omega-\omega_{ji}$ is the pump detuning from the resonance frequency ω_{ji}. γ_{ij} is the linewidth of transition line $|i\rangle\rightarrow|j\rangle$. Figures 4-19 through 4-22 show the functional dependence of the reflectivity as a function of normalized pump-probe detuning δ/γ_{13}. Again, the density of atoms is 10^{14}/cc and pump intensities of 10^4 watts/cm^2. The 2-photon linewidth γ_{13} is taken to be 1200 MHz. Note that for short interaction length the bandwidth exhibits a broad spectrum. As the interaction length L increases, the effect of coherence appears to take over, leading to interference effects of Figure 4-21 in the wings. Hence, it leads to an effective narrowing of the bandwidth. This fact is reflected in Figure 4-22 where the interaction length is 100 cm.

To show the relative importance of optical phase conjugation in 2- and 3-level systems, Figure 4-23 depicts the reflectivities for both systems. Note the broadband effect of a 2-photon resonance compared to 3-photon resonances.

4.4.3 Theory of Multiline Effects on Phase Conjugation

In the previous discussions, we have devoted all the analyses to the interesting case of phase conjugation via single mode coherent sources. However, the majority of high power laser systems operate on the multimode basis, i.e. the output radiation contains more than one frequency. The question arises as to whether the fidelity of phase conjugation is modified in a multimode operation. We present here a detailed study of multiline effects on phase conjugation. In particular, to reduce the complexity of the study, we shall restrict the discussion to the case of 2-line effects. We shall show that optical phase conjugation in multimode systems can only be achieved under certain conditions.

Na VAPOR
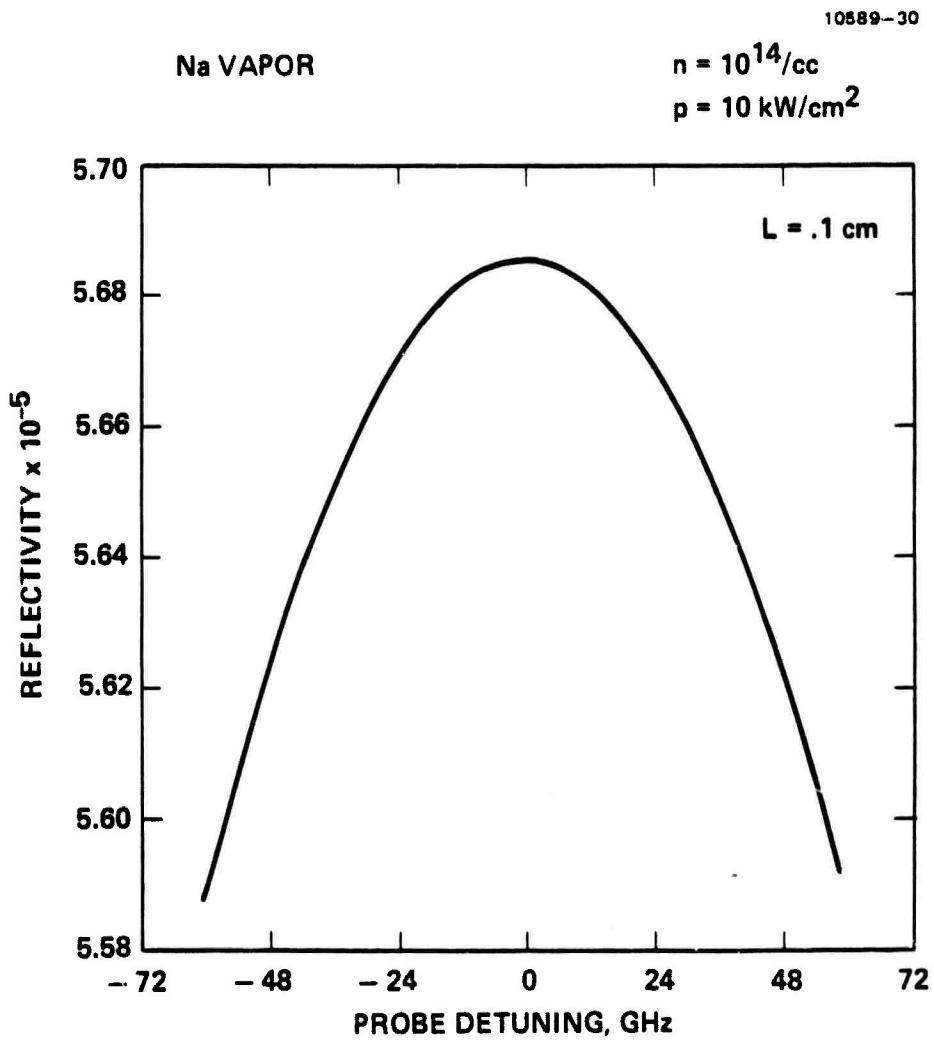
$n = 10^{14}/cc$

$p = 10 \text{ kW/cm}^2$

Figure 4-19. Probe-pump detuning for 2-photon resonance
in a cell of length 0.1 cm.
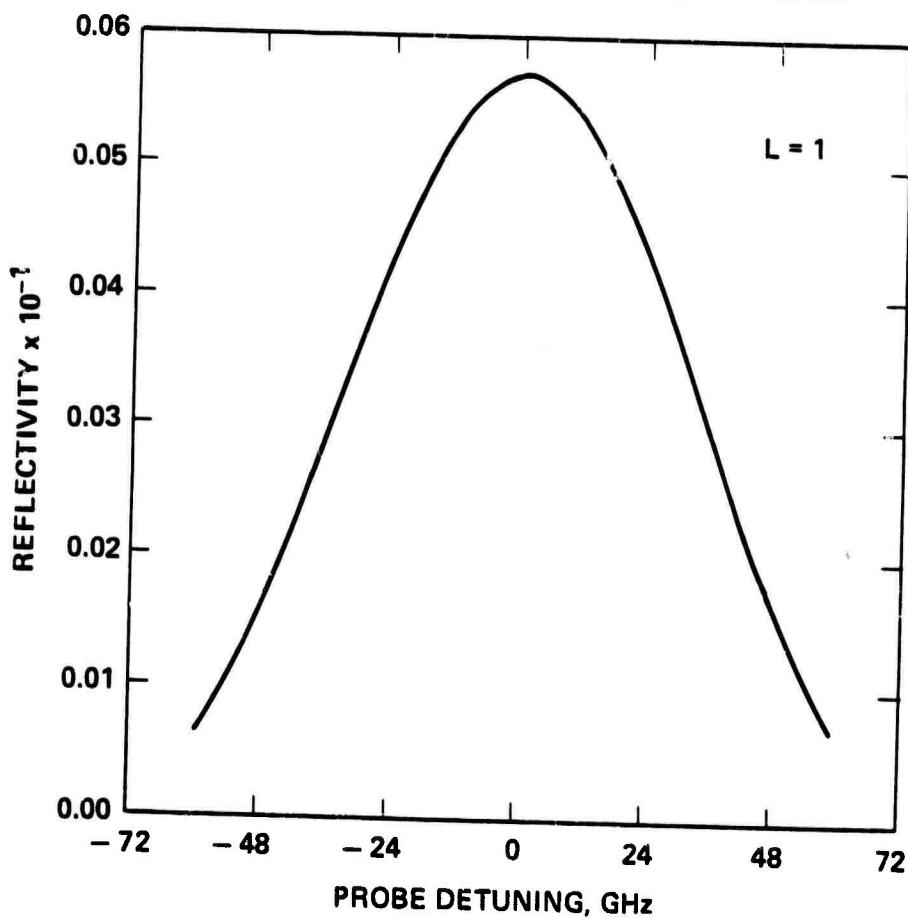
Figure 4-20.   Probe-pump detuning for 2-photon resonance
in a cell of length 1 cm.

Na VAPOR
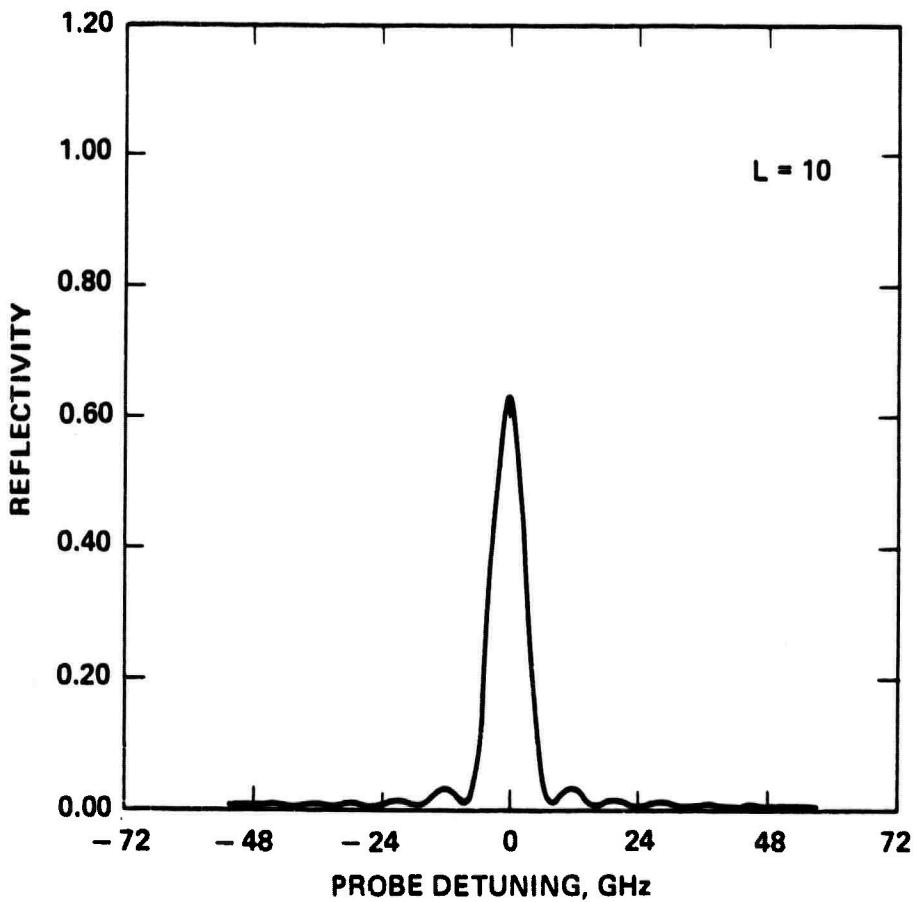
$n = 10^{14}/cc$

$p = 10 \text{ kW/cm}^2$

Figure 4-21. Probe-pump detuning for 2-photon resonance
in a cell of length 10 cm.

Na VAPOR $n = 10^{14}/cc$

                            $p = 10 \text{ kW/cm}^2$
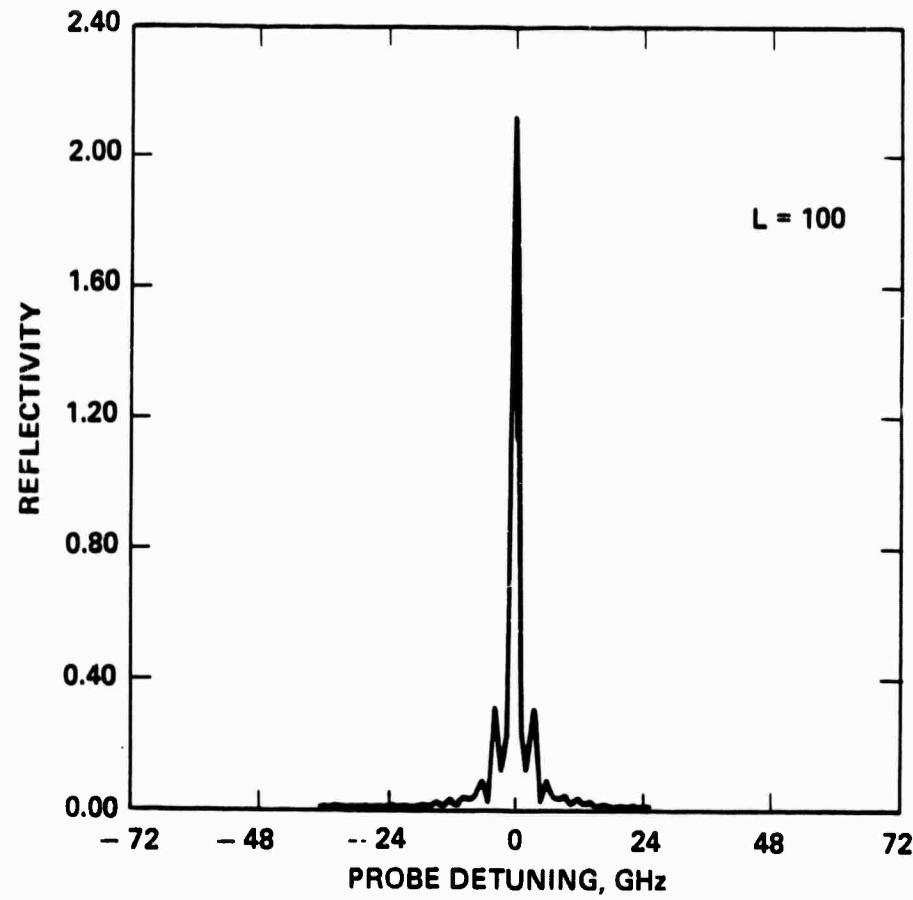

Figure 4-22. Probe-pump detuning 2-photon resonance
in a cell of length 100 cm.
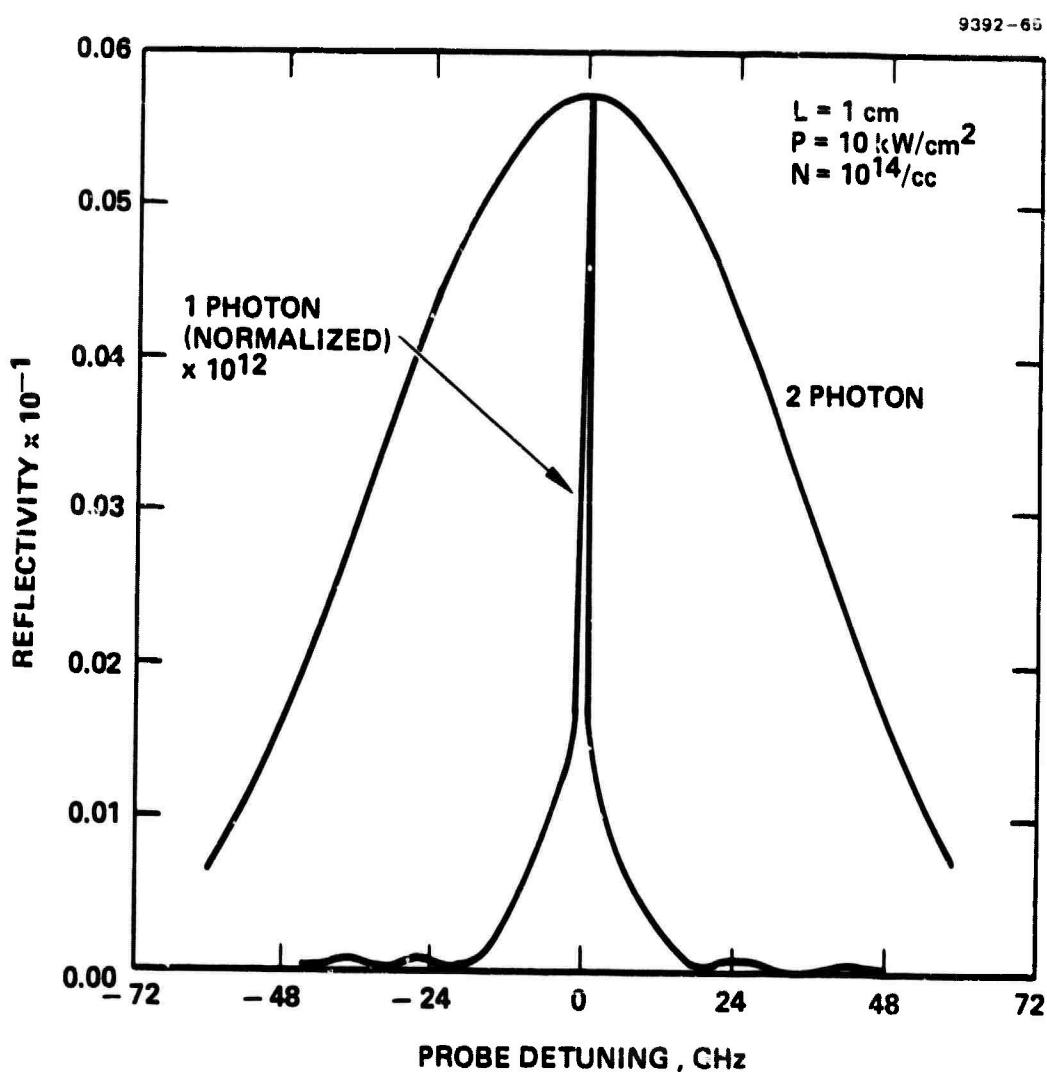
Figure 4-23. Probe-pump detuning characteristics for Na vapor.

The interaction geometry is shown in Figure 4-24. ω_1 and ω_2 are two distinct frequencies. We shall assume that the radiation fields interact with a resonant 2-level system. In this case, there are two types of interaction. The first one arises from the spatial grating that is formed by the interference of a pump and probe waves of the same frequency. The second one arises from the traveling wave grating that is formed by the interference of pump and probe waves having different frequencies. The complexity of such interaction processes is shown in Table I and Figure 4-25, which represent a four wave mixing process of the form

$$\vec{P} = A_1(\vec{E}_f \cdot \vec{E}_p^*)\vec{E}_b \quad . \tag{4-4-17}$$

In a similar manner, Table II shows the complexity given by the interaction

$$\vec{P} = A_2(\vec{E}_b \cdot \vec{E}_p^*)\vec{E}_f \quad . \tag{4-4-18}$$

Furthermore, note that even in the absence of thermal motion, the efficiency of generation depends on the response of the medium. One expects that the spatial grating will have different magnitude of response from the traveling wave grating. A quantum mechanical calculation via perturbation theory shows the following third order susceptibilities for Table I.

$$\chi(-\omega,\omega,\omega,-\omega) = M\left[\frac{1}{\gamma_{12}+i(\omega-\omega_o)}\right]\left[\frac{1}{\gamma_{12}+i(\omega-\omega_o)} + \frac{1}{\gamma_{12}-i(\omega-\omega_o)}\right]\left(\frac{2}{\gamma_o}\right) \tag{4-4-19}$$

$$\chi(\omega_2,\omega_2,\omega_1,-\omega_1) = M\left[\frac{1}{\gamma_{12}+i(\omega_2-\omega_o)}\right]\left[\frac{1}{\gamma_{12}+i(\omega_1-\omega_o)} + \frac{1}{\gamma_{12}-i(\omega_1-\omega_o)}\right]\left(\frac{2}{\gamma_o}\right) \tag{4-4-20}$$
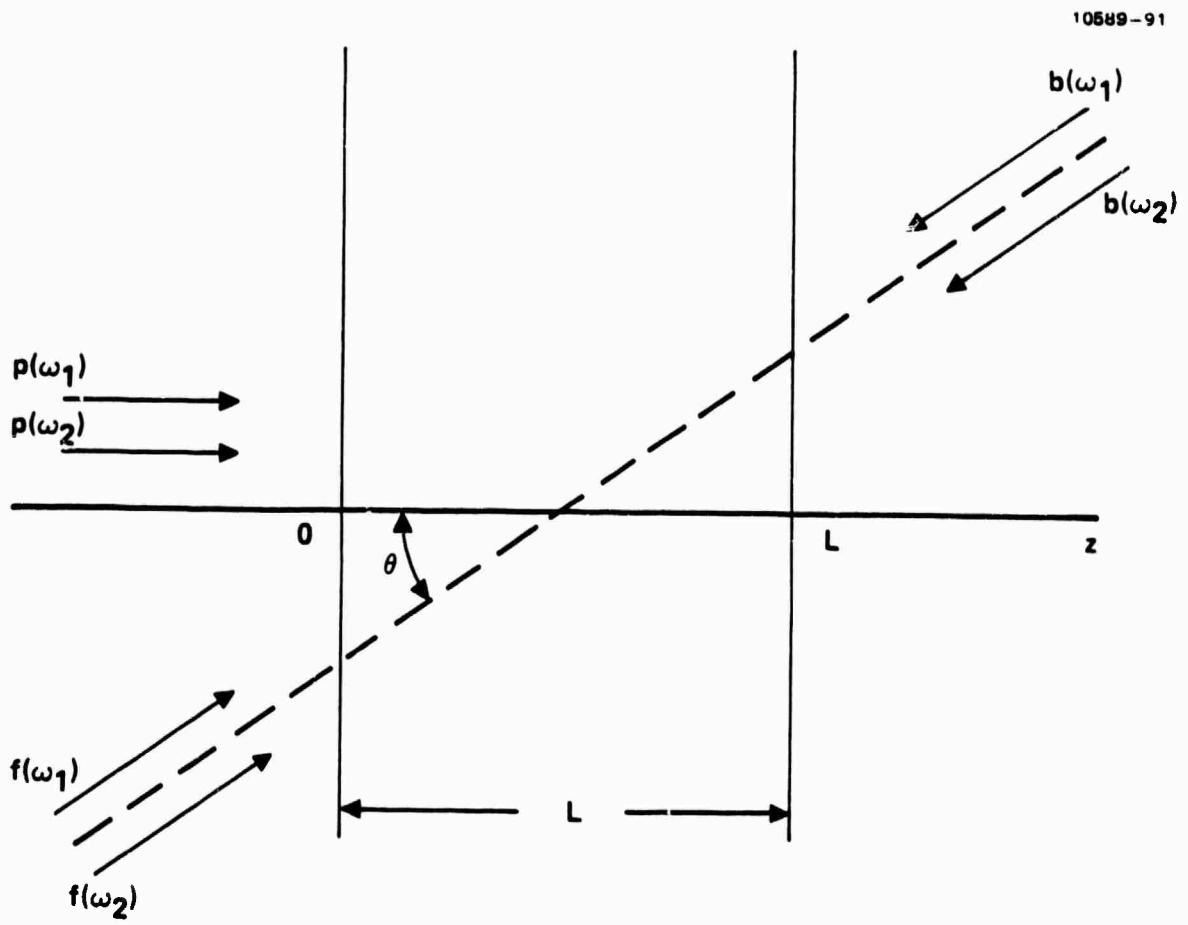
Figure 4-24.   Interaction geometry for 2-line phase conjugation.
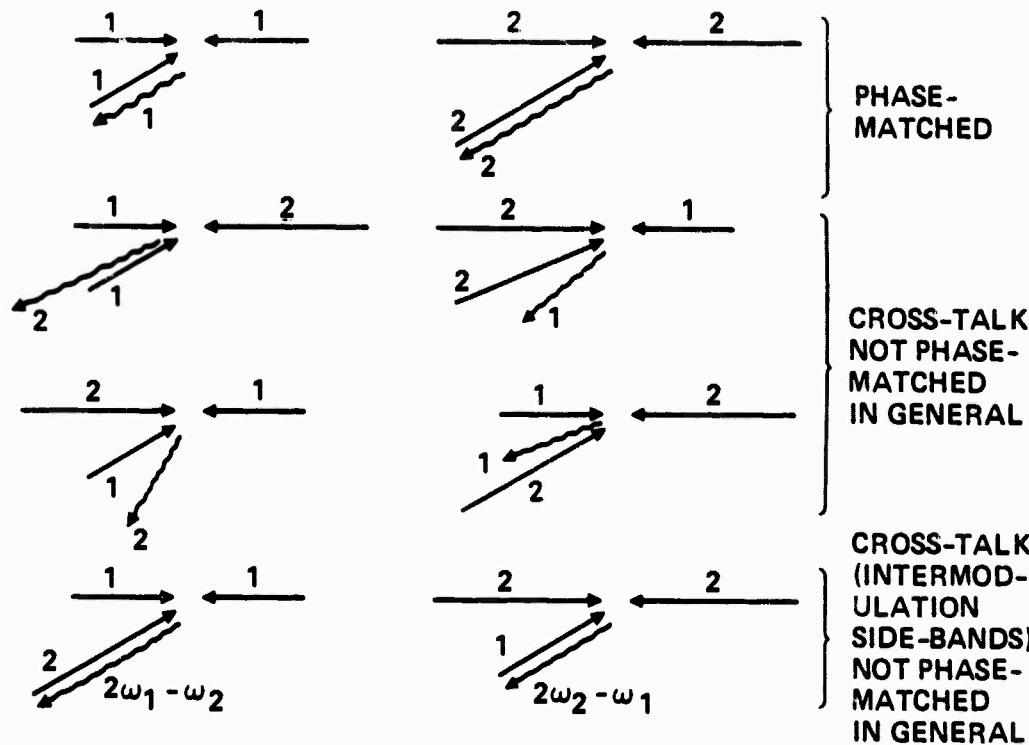
Figure 4-25. Classification of signal products in a four-wave mixer output when operating with 2-line pumps and probes.

Table I. Four-Wave Mixing Processes Giving Rise to DFWM and cross talk

Grating Forming Terms		Type of Grating	Read-out Wave	Phase Conjugate Signal S	Class of Signal
f	p				
ω_1 $\vec{K}_{f_1}$	ω_1 $\vec{K}_{p_1}$	Fixed	ω_1 $\vec{K}_{b_1}$	ω_1 $-\vec{K}_{p_1}$	DFWM
ω_1 $\vec{K}_{f_1}$	ω_2 $\vec{K}_{p_2}$	Traveling	ω_2 $\vec{K}_{b_2}$	ω_1 $\vec{K}_{f_1}+\vec{K}_{b_2}-\vec{K}_{p_2}$	cross talk
ω_2 $\vec{K}_{f_2}$	ω_2 $\vec{K}_{p_2}$	Fixed	ω_1 $\vec{K}_{b_1}$	ω_1 $\vec{K}_{f_2}+\vec{K}_{b_2}-\vec{K}_{p_1}$	cross talk
ω_1 $\vec{K}_{f_1}$	ω_1 $\vec{K}_{p_1}$	Fixed	ω_2 $\vec{K}_{b_2}$	ω_2 $\vec{K}_{f_1}+\vec{K}_{b_2}-\vec{K}_{p_1}$	cross talk
ω_2 $\vec{K}_{f_2}$	ω_1 $\vec{K}_{p_1}$	Traveling	ω_1 $\vec{K}_{b_1}$	ω_2 $\overline{K}_{f_2}+\overline{K}_{b_1}-\overline{K}_{p_1}$	cross talk
ω_2 $\overline{K}_{f_2}$	ω_2 $\overline{K}_{p_2}$	Fixed	ω_2 $\overline{K}_{b_2}$	ω_2 $-\vec{K}_{p_2}$	DFWM

$$\chi(\omega_1,\omega_2,\omega_1,-\omega_2) = M\frac{1}{\gamma_{12}+i(\omega_1-\omega_o)} \times \left[\frac{1}{\gamma_{12}-i(\omega_2-\omega_o)} + \frac{1}{\gamma_{12}+i(\omega_1-\omega_o)}\right]$$

$$\times \left[\frac{1}{\gamma_1+i(\omega_1-\omega_2)} + \frac{1}{\gamma_2+i(\omega_1-\omega_2)}\right] \qquad (4\text{-}4\text{-}21)$$

$$\chi(\omega_2,\omega_1,\omega_2,-\omega_1) = M\frac{1}{\gamma_{12}+i(\omega_2-\omega_o)} \times \left[\frac{1}{\gamma_{12}+i(\omega_2-\omega_o)} + \frac{1}{\gamma_{12}-i(\omega_1-\omega_o)}\right]$$

$$\times \left[\frac{1}{\gamma_1+i(\omega_2-\omega_1)} + \frac{1}{\gamma_2+i(\omega_2-\omega_1)}\right] \qquad (4\text{-}4\text{-}22)$$

$$\chi(\omega_2,\omega_1,\omega_2,-\omega_1) = M\frac{1}{\gamma_{12}+i(\omega_2-\omega_o)} \times \left[\frac{1}{\gamma_{12}+i(\omega_2-\omega_o)} + \frac{1}{\gamma_{12}-i(\omega_1-\omega_o)}\right]$$

$$\times \left[\frac{1}{\gamma_1+i(\omega_2-\omega_1)} + \frac{1}{\gamma_2+i(\omega_2-\omega_1)}\right] \qquad (4\text{-}4\text{-}23)$$

Notation for the argument of the susceptibility is as follows:

$$\chi(\omega_s,\omega_b,\omega_f,-\omega_p) \quad .$$

and the constant M is given by

$$M = N_o(\mu_{12})^4/(2ih)^3\varepsilon_o \quad .$$

Hence, in the case of the interference formed by the forward pump and input probe wave, the following equations for the combined signal wave, neglecting nonlinear phase shifts apply.

$$\frac{dE_{s_1}}{dz} = i \frac{\omega_1}{2n_1 c} \left\{ \chi(\omega_1, \omega_1, \omega_1, -\omega_1) E_{f_1} E_{b_1} E_{p_1}^* \right.$$

$$+ \chi(\omega_1, \omega_2, \omega_1, -\omega_2) E_{f_1} E_{b_2} E_{p_2}^* e^{i\Phi z} \qquad (4-4-24)$$

$$\left. + \chi(\omega_1, \omega_1, \omega_2, -\omega_2) E_{f_2} E_{b_1} E_{p_2}^* e^{i\Theta z} \right\}$$

$$\frac{dE_{s_2}}{dz} = i \frac{\omega_2}{2n_2 c} \left\{ \chi(\omega_2, \omega_2, \omega_2, -\omega_2) E_{f_2} E_{b_2} E_{p_2}^* \right.$$

$$+ \chi(\omega_2, \omega_1, \omega_2, -\omega_1) E_{f_2} E_{b_1} E_{p_1}^* e^{i\alpha z} \qquad (4-4-25)$$

$$\left. + \chi(\omega_2, \omega_2, \omega_1, -\omega_1) E_{f_1} E_{b_2} E_{p_1}^* e^{i\beta z} \right\}$$

Resulting phases are such that

$$\Phi = \left[\left(k_{f_1} - k_{b_2} \right) \cos\theta - k_{p_2} + k_{s_1} \right] \qquad (4-4-26a)$$

$$\Theta = \left[\left(k_{f_2} - k_{b_1} \right) \cos\theta - k_{p_2} + k_{s_1} \right] \qquad (4-4-26b)$$

$$\alpha = \left[\left(k_{f_2} - k_{b_1} \right) \cos\theta - k_{p_1} + k_{s_2} \right] \qquad (4-4-26c)$$

$$\beta = \left[\left(k_{f_1} - k_{b_2} \right) \cos\theta - k_{p_1} + k_{s_2} \right] \qquad (4-4-26d)$$

In the weak scattering limit (i.e., the input probe waves do not experience significant change in the interaction region), the Equations (4-4-24) and (4-4-25) can be integrated to yield the following:

$$
\begin{aligned}
E_{s_1} = i\,\frac{\omega_1}{2n_1 c} \Bigg\{ &-\chi(\omega_1,\omega_1,\omega_1,-\omega_1) E_{f_1} E_{b_1} E_{p_1}^{*}\, L \\
&+ \chi(\omega_1,\omega_2,\omega_1,-\omega_2) E_{f_1} E_{b_2} E_{p_2}^{*} \left(\frac{1-e^{i\phi L}}{i\phi} \right) \\
&+ \chi(\omega_1,\omega_1,\omega_2,-\omega_2) E_{f_2} E_{b_1} E_{p_2}^{*} \left(\frac{1-e^{i\theta L}}{i\theta} \right) \Bigg\}
\end{aligned}
\tag{4-4-27}
$$

$$
\begin{aligned}
E_{s_2} = i\,\frac{\omega_2}{2n_2 c} \Bigg\{ &-\chi(\omega_2,\omega_2,\omega_2,-\omega_2) E_{f_2} E_{b_2} E_{p_2}^{*}\, L \\
&+ \chi(\omega_2,\omega_1,\omega_2,-\omega_1) E_{f_2} E_{b_1} E_{p_1}^{*} \left(\frac{1-e^{i\alpha L}}{i\alpha} \right) \\
&+ \chi(\omega_2,\omega_2,\omega_1,-\omega_1) E_{f_1} E_{b_2} E_{p_1}^{*} \left(\frac{1-e^{i\beta L}}{i\beta} \right) \Bigg\}
\end{aligned}
\tag{4-4-28}
$$

Equations (4-4-27) and (4-4-28) are the main results at this section. The interaction process, given by expression (4-4-18) and Table II, follows a similar line. As pointed out earlier, the right hand sides of Equations (4-4-27) and (4-4-28) contain terms proportional to the conjugate wave as well as cross-talk contributions. Cross-talk, which represents a transfer of information from line to line, will be important only if

$$
|\Delta k|\quad L < 2\pi \;,
\tag{4-4-29}
$$

Table II. Four-Wave Mixing Processes Giving Rise to DFWM and Cross Talk

Grating Forming Terms		Type of Read-out Wave		Phase Conjugate Signal S	Class of Signal
b	p	Grating	f		
ω_1 $\vec{K}_{b_1}$	ω_1 $\vec{K}_{p_1}$	fixed	ω_1 $\vec{K}_{f_1}$	ω_1 $-\vec{K}_{p_1}$	DFWM
ω_1 $\vec{K}_{b_1}$	ω_2 $\vec{K}_{p_2}$	traveling	ω_2 $\vec{K}_{f_2}$	ω_1 $\vec{K}_{f_2}+\vec{K}_{b_1}-\vec{K}_{p_2}$	cross talk
ω_2 $\vec{K}_{b_2}$	ω_2 $\vec{K}_{p_2}$	fixed	ω_1 $\vec{K}_{f_1}$	ω_1 $\vec{K}_{f_1}+\vec{K}_{b_2}-\vec{K}_{p_2}$	cross talk
ω_1 $\vec{K}_{b_1}$	ω_1 $\vec{K}_{b_1}$	fixed	ω_2 $\vec{K}_{f_2}$	ω_2 $\vec{K}_{f_2}+\vec{K}_{b_1}-\vec{K}_{p_1}$	cross talk
ω_2 $\vec{K}_{b_2}$	ω_1 $\vec{K}_{p_1}$	traveling	ω_1 $\vec{K}_{f_1}$	ω_2 $\vec{K}_{f_1}+\vec{K}_{b_2}-\vec{K}_{p_1}$	cross talk
ω_2 $\vec{K}_{b_2}$	ω_2 $\vec{K}_{p_2}$	fixed	ω_2 $\vec{K}_{f_2}$	ω_2 $-\vec{K}_{p_2}$	DFWM

4-70

where $\Delta K = \alpha, \beta, \phi, \Theta$. In this situation a coherence length for cross-talk becomes important:

$$L_{coh} = \frac{2\pi}{|\Delta k|} \quad . \qquad (4\text{-}4\text{-}30)$$

But if $L \gg L_{coh}$, no cross-talk will take place, because L_{coh} depends on the angle between the forward pump and input probe.

Now consider the coherence requirement for all the distinct wave vector mismatches α, β, ϕ and Θ. The coherence lengths are defined to be given by

$$L_n = \frac{c}{\Delta \nu \, |\cos\theta - 1|} \quad n = \alpha, \phi \qquad (4\text{-}4\text{-}31)$$

and

$$L_m = \frac{c}{\Delta \nu \, |\cos\theta + 1|} \quad n = \beta, \Theta \qquad (4\text{-}4\text{-}32)$$

where $\Delta \nu$ is the difference in frequencies between the two lines. For angles $\theta = 2^o$ and $\Delta \nu = 0.16 \times 10^{14}$ Hz (experimental conditions, see Section 5.6) one obtains

$$L_n = 3 \times 10^{-2} \qquad (4\text{-}4\text{-}33)$$

and

$$L_m = 9.37 \times 10^{-6} \text{m} \quad . \qquad (4\text{-}4\text{-}34)$$

Thus, for interaction length L, such that

$$L > L_n \text{ and } L_m \, , \qquad (4\text{-}4\text{-}35)$$

cross-talk will not be significant.

Furthermore, there exists an additional interaction process which generates side-band frequencies at $2\omega_1 - \omega_2$ and $2\omega_2 - \omega_1$. The physical mechanism is shown in the two diagrams at the bottom of Figure 4-13. Note that it is not a phase matched interaction.

4-71

4.5 GENERALIZED-OFFSET AND PHASE-MATCHING WITH 3-DIMENSIONAL GEOMETRY

This section presents a generalized analysis of many possible phase-matched, three-dimensional geometries for FWM which achieve a frequency and/or angle offset between the input (probe) and the "conjugated" return signal. We will show both theoretically and experimentally that it is possible to achieve useful offsets and still retain the propagation path corrections that are the desired output of a nonlinear phase conjugator.

There are many applications of such frequency and angle offset techniques. (1) Since the pumps may be arranged to be non-counterpropagating with angle offset techniques, feedback of the pump into the laser oscillator can be avoided. (2) In high power systems one can avoid damaging a glint reference or a cooperative reference system (corner reflector or source) by offsetting the conjugator to refocus the high-power beam at one side of the reference. (3) Doppler shifts can be compensated for, without any loss in conjugator efficiency resulting from phase mismatch.

These advantages are not obtained without some sacrifice. We will show that the phase-matched condition strictly holds for only one set of probe and pump angles, which restricts the field of view over which good conjugation is obtained. However, for normal atmospherically-spread beams, the loss in performance is negligible. The major performance loss caused by angular offset is expected to result from atmospheric anisoplanatism and not from loss in conjugator performance, when propagating over atmospheric paths.

4.5.1 The Generalized Phase-Matching Conditions

We ignore polarization effects while recognizing that certain modes at certain angles combined with bad choices of polarization will not work. Further, we assume that the nonlinear medium can instantaneously respond at the offset frequencies and is isotropic.

The basic geometry and nomenclature is illustrated in Figure 4-26 where, however the k vectors are not necessarily coplanar. The frequency and k-vector matching relationships, which result from the "conjugation term" in the
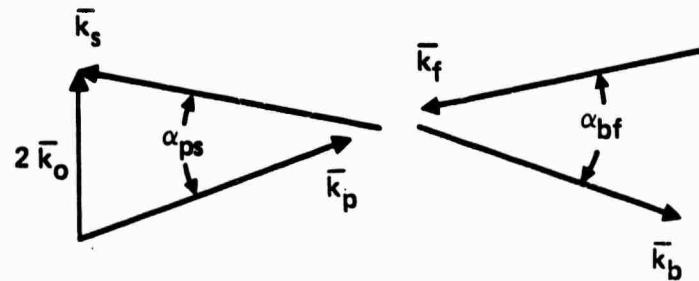
$\bar{k}_p$ = PROBE k VECTOR

$\bar{k}_s$ = SIGNAL k VECTOR

$\bar{k}_b$ = "BACKWARD" PUMP k VECTOR

$\bar{k}_f$ = "FORWARD" PUMP k VECTOR.

Figure 4-26. A generalized FWM geometry. The k vectors are in general neither collinear nor coplanar.

third order nonlinear susceptibility expansion, are conveniently expressed* as

$$\omega_f + \omega_b = \omega_p + \omega_s \qquad (4\text{-}5\text{-}1a)$$

$$\vec{k}_f + \vec{k}_b = 2\vec{k}_o = \vec{k}_p + \vec{k}_s \quad , \qquad (4\text{-}5\text{-}1b)$$

where, in a non-dispersive medium,

$$\vec{k}_n = \frac{\omega_n}{c} \hat{e}_n \qquad (4\text{-}5\text{-}1c)$$

where $n = f, b, p, s$ (for forward, backward, probe and reference), and $\hat{e}_n$ is a unit vector in the direction of the k vector. Equation (4-5-1a) states that the mean frequency of the pumps equals the mean frequency of the two signal components. If we call this mean frequency ω_o, then the most general offsets (in symmetrical form) are, for the pumps,

$$\omega_f = \omega_o + \Delta_p \qquad (4\text{-}5\text{-}2a)$$

$$\omega_b = \omega_o - \Delta_r \quad . \qquad (4\text{-}5\text{-}2b)$$

For the signal components they are

$$\omega_p = \omega_o + \Delta_s \qquad (4\text{-}5\text{-}2c)$$

$$\omega_s = \omega_o - \Delta_s \quad . \qquad (4\text{-}5\text{-}2d)$$

---

*We are exclusively concerned with those terms which lead to the so-called conjugated waveforms scattered out of the system. With minor offsets, these terms give back nearly the same frequency as the signal and pump frequencies.

In similar fashion we can rewrite the $\bar{k}$ vector relations of (4-5-1b) in symmetrical form as

$$\vec{k}_f = \vec{k}_o + \vec{\delta}_p \tag{4-5-3a}$$

$$\vec{k}_b = \vec{k}_o - \vec{\delta}_p \tag{4-5-3b}$$

$$\vec{k}_p = \vec{k}_o + \vec{\delta}_s \tag{4-5-3c}$$

$$\vec{k}_s = \vec{k}_o - \vec{\delta}_s \tag{4-5-3d}$$

If we square the magnitude of Equations (4-5-1a) and (4-5-1b) the results are

$$\omega_f^2 + \omega_b^2 + 2\omega_f\omega_b = \omega_p^2 + \omega_s^2 + 2\omega_p\omega_s \tag{4-5-4a}$$

$$\omega_f^2 + \omega_b^2 \quad \omega_f\omega_b \, \hat{e}_f \cdot \hat{e}_b = \omega_p^2 + \omega_s^2 + 2\omega_p\omega_s \, \hat{e}_p \cdot \hat{e}_s \quad . \tag{4-5-4b,}$$

Subtracting (4-5-4a) from (4-5-4b) gives

$$\omega_f\omega_b(1-\cos\theta_{fb}) - \omega_p\omega_s(1-\cos\theta_{ps}) \quad , \tag{4-5-5a}$$

where θ_{ps} and θ_{fb} are the pump-to-pump and the signal-to-signal angles. Since θ_{ps} and θ_{fb} are typically near a retro angle ($\theta = \pi$), it is convenient to let

$$\theta_{ps} = \pi - \alpha_{ps} \quad , \tag{4-5-6a}$$

and

$$\theta_{fb} = \pi - \alpha_{fb} \quad , \tag{4-5-6b}$$

4-75

giving, in place of (4-5-5a),

$$\omega_p \omega_s \, \cos^2 \frac{\alpha_{ps}}{2} = \omega_f \omega_b \, \cos^2_b \frac{\alpha_{fb}}{2} \; . \tag{4-5-7}$$

If we substitute Equations (4-5-2) in (4-5-7), the result is

$$\left[1 - \left(\frac{\Delta_s}{\omega_o} \right)^2 \right] \cos^2 \frac{\alpha_{ps}}{2} = \left[1 - \left(\frac{\Delta_p}{\omega_o} \right)^2 \right] \cos^2 \frac{\alpha_{fb}}{2} \tag{4-5-8}$$

Equation (4-5-8) indicates the required angular separation between the pumps and signal components, while Equations (4-5-1b) and (4-5-3) describe the center-line behavior of each of these k-vector sets.

As we will see, there are many different ways to satisfy the Equation (4-6-8), and these lead to quite different four-wave geometries.

4.5.2 Representative Geometries

Representative geometries that may be used to produce desired signal frequency or angle offsets are shown in Table III. One way of classifying the geometries is with a truth table for coplanarity and frequency degeneracy, as illustrated. Another way employs the offset transfer mode as illustrated by the last column in the table. Thus, the A geometry represents the conventional coplanar, degenerate four-wave system in which

$$\Delta_s = \Delta_p = \alpha_{ps} = \alpha_{fb} = 0 \tag{4-5-9}$$

With the B geometry, a pump angular offset α_{fb} produces (or compensates for) an equal angular offset between probe, signal, and frequency degeneracy wherein

$$\Delta_s = \Delta_p = 0 \tag{4-5-10a}$$

$$\alpha_{ps} = \alpha_{fb} \; . \tag{4-5-10b}$$

Table III. Representative Geometries for Generalized Offset Operation

COPLANAR?	DEGENERATE?	OFFSET ERROR COMPENSATION MODE
YES	YES	NONE AVAILABLE
NO	YES	PUMP ANGLE → SIGNAL ANGLE
YES	NO	PUMP ANGLE → SIGNAL FREQ
NO	NO	PUMP ANGLE → SIGNAL ANGLE PUMP FREQ → SIGNAL FREQ

This approach has been experimentally verified, as discussed in Section 5.5. With the C geometry, a pump angular offset α_{fb} is compensated by an associated frequency offset, so that

$$\Delta_p = \alpha_{ps} = 0 \qquad\qquad (4-5-11a)$$

$$\frac{\Delta_s}{\omega_o} = \sin \frac{\alpha_{fb}}{2} \quad . \qquad\qquad (4-5-11b)$$

With the D geometry, a pump angular offset is compensated by a corresponding signal angular offset, while a pump frequency offset is compensated by a corresponding signal frequency offset, such that Equation (4-5-8) may be decomposed to

$$1 - \left(\frac{\Delta_s}{\omega_o}\right)^2 = 1 - \left(\frac{\Delta_p}{\omega_o}\right)^2 \qquad\qquad (4-5-12a)$$

$$\cos^2 \frac{\alpha_{ps}}{2} = \cos^2 \frac{\alpha_{fb}}{2} \quad . \qquad\qquad (4-5-12b)$$

Note that Equations (6d) and (6e) disclose a method for achieving simultaneous and _independent_ angular and frequency offset in the conjugated wavefronts by matching frequency offsets and angle offsets. We call such a design a "match mode." The rules for this mode may alternately be described by Equations (6d) and (6e), or the following construction rules using an arbitrary $\bar{k}_s$ and $\bar{\Gamma}_p$. (1) construct $\bar{k}_o$ (or $2\bar{k}_o$), (2) rotate the plane containing $\bar{k}_s$ and $\bar{k}_p$ about the line containing $\bar{k}_o$ by an arbitrary angle, and (3) designate the new positions of $\bar{k}_s$ and $\bar{k}_p$ as pump vectors $\bar{k}_b$ and $\bar{k}_f$. Of course, Figure 4-5-2d illustrates only one of many such choices.

Although the match mode is sufficient for simultaneous angle and frequency offset, Equation (4-5-8) suggests other possibilities. Specifically, we can also satisfy (4-5-8) if

$$1 - \left(\frac{\Delta_s}{\omega_o}\right)^2 = F_c \cos^2\left(\frac{\alpha_{fb}}{2}\right) \tag{4-5-13a}$$

$$1 - \left(\frac{\Delta_p}{\omega_o}\right)^2 = F_c \cos^2\left(\frac{\alpha_{ps}}{2}\right) . \tag{4-5-13b}$$

For the case F_c = unity,

$$\sin^2\left(\frac{\alpha_{fb}}{2}\right) = \left(\frac{\Delta_s}{\omega_o}\right)^2 \tag{4-5-14a}$$

$$\left(\frac{\Delta_p}{\omega_o}\right)^2 = \sin^2\left(\frac{\alpha_{ps}}{2}\right) . \tag{4-5-14b}$$

If we choose the sign of α_{fb} to satisfy Equation (4-5-3), we can again achieve independent angular and frequency offsets. In this case, the angular effects are cross-coupled to frequency offsets, so we call this a cross mode. One of the most attractive features of this mode is that it allows us to compensate a Doppler shift without requiring pump frequency perturbaticns. Again, the same geometrical approach defines the class of geometrical construction: (1) choose a desired $\overline{k}_p$ and $\overline{k}_s$, (2) construct $\overline{k}_o$ (or $2\overline{k}_o$), (3) in the plane defined by $\overline{k}_p$, $\overline{k}_s$ (and $\overline{k}_o$) construct a $\overline{k}_f$ and $\overline{k}_b$ which satisfies (4-5-14b), and (4) rotate this plane by any arbitrary angle about $\overline{k}_o$.

A "degenerate" case occurs with this mode for angle only offset in the sense that only one pump orientation is permitted (Figure 4-27). For an offset of 180° in the conjugated wavefront, the system becomes fully degenerate

with collinear signal and pump k vectors. Figure 4-27 is the same as Table IIIc in the sense that the pump and signal roles are interchanged. Figure 4-28 provides another example of a cross-mode which is coplanar.

In the most general case, (4-6-8) can be satisfied by letting

$$\left[1 - \left(\frac{\Delta_p}{\omega_o} \right)^2 \right] = K \left[1 - \left(\frac{\Delta_s}{\omega_o} \right)^2 \right]^{1/2} \cos \frac{\alpha_{ps}}{2} \qquad (4\text{-}5\text{-}15a)$$

$$\cos^2 \frac{\alpha_{fb}}{2} = \frac{1}{K} \left[1 - \left(\frac{\Delta_s}{\omega_o} \right)^2 \right]^{1/2} \cos \frac{\alpha_{ps}}{2} \qquad (4\text{-}5\text{-}15b)$$

where K is a constant constrained to fall between

$$K_{min} = \left[1 - \left(\frac{\Delta_s}{\omega_o} \right)^2 \right]^{1/2} \cos \frac{\alpha_{ps}}{2} \qquad (4\text{-}5\text{-}16a)$$

and

$$K_{max} = \left\{ \left[1 - \left(\frac{\Delta_s}{\omega_o} \right)^2 \right]^{1/2} \cos \frac{\alpha_{ps}}{2} \right\}^{-1} \qquad (4\text{-}5\text{-}16b)$$

by the requirement that the left sides of (4-6-15a) and (4-6-15b) be less than unity. In general, we call these "mixed modes."

For the particular case

$$K = \left[1 - \left(\frac{\Delta_s}{\omega_o} \right)^2 \right]^{1/2} \cos \left[\frac{\alpha_{ps}}{2} \right]^{-1} , \qquad (4\text{-}5\text{-}17a)$$
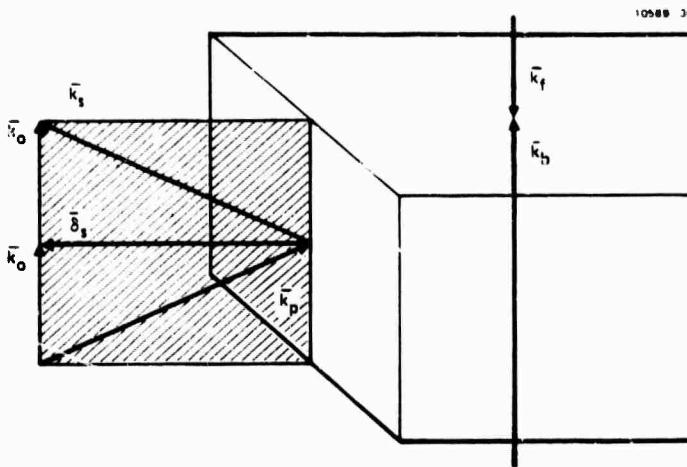
Figure 4-27. Example of a Cross Mode Angle (only)
offset since there is no frequency
offset, $\alpha_{12} = 0$ and the pumps are
collinear (the geometry is degenerate).
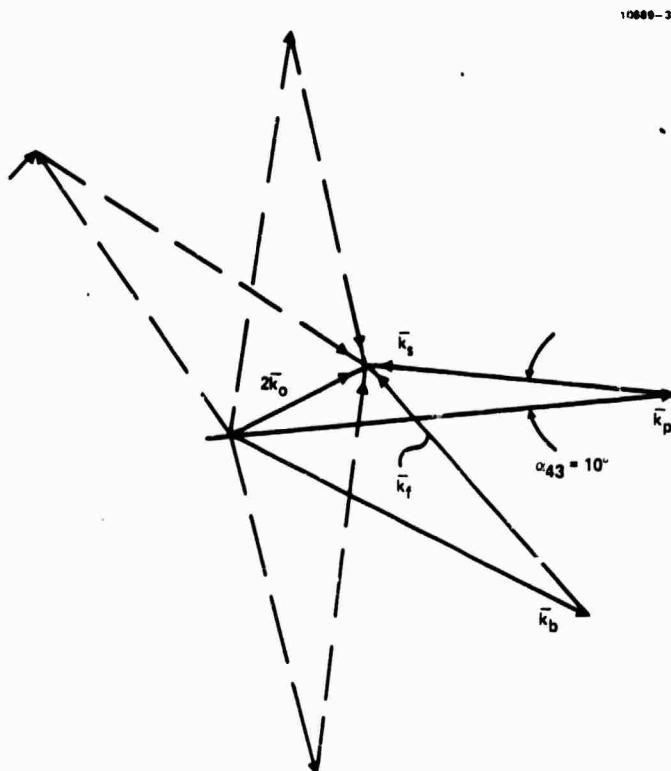
Figure 4-28. Example of a
coplanar cross mode with both
angle and frequency offset,
where $\alpha_{43} = 10°$ and Δ_s/ω_o
= 0.2. Even within the same
plane, four different pump
orientations are allowed, as
illustrated by the dashed
lines. Half of these cor-
respond to 180° rotations of
the pump plane about $\bar{k}_o$.

we obtain the match modes A (wherein frequency and angular offsets match), while for the particular case

$$K = \left[1 - \left(\frac{\Delta_s}{\omega_o} \right)^2 \right]^{1/2} \cos \frac{\alpha_{ps}}{2} \quad , \tag{4-5-17b}$$

the result is a cross mode. For $K = K_{min}$ we employ pure frequency offsets in the pumps, while for $K = K_{max}$ we employ pure angular offsets in the pumps. We will call these "frequency only" and "angle only" modes.

The case $K = 1$ minimizes the sum of the fractional pump frequency separation, and the angular separation that is required to produce a given signal frequency and angular offset. It is thus in a sense of a "minimum departure" from normal non-offset operation.

All of these choices, in K above as well as in intermediate values, can be achieved by the same constructional techniques described in the preceding sections. Clearly (4-5-15a) and (4-5-15b) are redundant and it is sufficient to solve Δ_p/ω_o in (4-5-15a) since the pump vector triangle is determined from the base $(2\bar{k}_o)$, along with the two sides $\omega_o + \Delta_p$ and $\omega_o - \Delta_p$.

4.5.3 Conjugation Fidelity with Offset Operation

The basic degenerate four-wave mixer system accurately conjugates over a very wide range in acceptance angle. However, as one might suppose, the modes discussed in this subsection, which accommodate either frequency or angle offset on the signal, have restrictions on the classes of probe signals which can be accurately conjugated. We will discuss the limitations on frequency offset in Subsection 6.4.2, a discussion which is independent of the mixer geometry; hence, we need not repeat it here. The angle effects are another matter.

The effect of angular offset can be considered from two viewpoints: (1) one assumes a given phase distribution on the probe beam and asks how accurately

this distribution is transferred to the signal beam under offset conditions. (2) And, one can represent a distorted wavefront by a set of plane waves distributed over some angular span and ask how accurately any one of the signal component wave k vectors is displaced from the nominal output direction (e.g., taken as the centroid), relative to the displacement of the corresponding probe component k vector, relative to its nominal input direction.

We pursue the first approach here, since the problem then becomes closely analogous to the problem of pump-to-signal wavefront transfer already discussed in Section 4.2.2. We will borrow directly from those results. In particular, we find that in order to avoid projective transfer errors, a thin slab mixer should be employed with its faces oriented normal to the bisector of the probe and signal beam angles. If the depth of the mixer volume is small compared to the scale of the wavefront variations, the signal phase is the negative of the probe phase, and the signal is an accurate conjugate. More specifically, for the Nth order Fourier term, the phase transfer process is accurate for any geometry for which

$$\left(\frac{L}{R_o} \sin\alpha_{ps}\right) N\pi < 0.5 \quad , \tag{4-5-18}$$

where R_o is the signal beam radius, α_{ps} is the probe-to-signal angular separation, and 2L is the mixer depth. As with the pump transfer cases, the first order residual effect is an amplitude modulation of the signal beam at second and higher harmonies of a Fourier component in the probe phase decomposition. In particular, the field multiplier is approximately of the form

$$M(x) = \text{sinc}\left(\frac{\phi_m LA}{2}\right) \cos\left(\frac{2N\pi x}{R_o} + \theta\right) \quad , \tag{4-5-18a}$$

where ϕ_m is the peak phase excursion of the Nth spatial harmonic and mixer depth and

$$A = \frac{2N\pi}{R_o} \sin \alpha_{ps} \quad . \tag{4-5-18b}$$

CHAPTER 5

EXPERIMENTAL MEASUREMENTS OF DFWM

In this chapter a detailed description of the experimental measurements made on the program are given. Not included however, is a discussion of the detailed measurements of SBS made during the early portion of this program, which were summarized in the interim report.

The objectives of the experimental studies undertaken were basically threefold: First - investigate materials with potential for use in the blue-green wavelength region; second - determine the ability of DFWM to correct highly aberrated beams; and third - demonstrate certain of the basic properties unique to DFWM such as polarization rotation, pump misalignment, general three-dimensional offset geometries, and non-degenerate operation.

The results of these measurements are described in the seven sections of this chapter. At the outset, the basic apparatus is described which was used to make the measurements. Then, the materials investigated are described with measurements of the conjugate efficiencies presented. Several useful materials for blue-green work are identified such as dyes, filter glass semiconductors, and others. In Section 5.3, the detailed far-field measurements of aberrated and unaberrated beams are presented. These measurements were made using several of the materials identified above. Diffraction limited correction was achieved for moderate conjugate efficiencies, while deviations from diffraction limited performance occurred near unity efficiencies. In Section 5.4 the polarization rotation concept is demonstrated. The two-dimensional in the plane and three-dimensional general geometries are described in Section 5.5. The effects of phase-mismatch on amplitude reduction is demonstrated. Further, the phase-matched result showing no amplitude reduction is also demonstrated. In Section 5.6 nearly degenerate four-wave mixing is discussed. Two-wavelength experiments were performed. And, an important experiment to establish coherence requirements of four-wave mixing was also performed. Here one laser was used for the probe and a separate laser for the pumps. A signal was obtained only when the frequency difference between the two lasers was kept within the criteria

established in Chapter 4. Finally, in Section 5.7 a discussion of criteria used to choose materials for blue-green operation is presented. These criteria were used in material selection for certain of the experiments performed in 5.2 above.

5.1 BASIC APPARATUS

During this program two different laser systems were employed to make the measurements to be discussed - a pulsed ruby laser, and a pulsed doubled or tripled Yag tunable dye laser system. The ruby system has been described in detail in the interim report and will not be discussed here. The Yag-dye system (used for the bulk of the measurements) is a custom design from Quantel. The Yag laser (see Figure 5-1) consists of an oscillator, followed by two amplifiers. The oscillator is passively Q-switched by a BDN saturable absorber mixture. The passive Q-switch, augmented by the etalons in the oscillator cavity, produce a transform limited single-longitudinal-mode ~ 10 nsec pulse of about 15 mJ energy. The pinhole in the cavity restricts oscillation to several modes, with most of the energy in the TEM_{oo} mode. This beam is focused with a concave mirror of 2.5m focal length, and spatially filtered before being amplified. The amplified beam is doubled or tripled as desired and can be sent to a Quantel dye laser when needed. Typical output characteristics for the laser are 800 mJ at 1.06 μm, 320 mJ at 5320Å, and 120 mJ at 3550Å. The dye laser operates between 4100-7600Å with a maximum output of about 50 mJ in the yellow. The system was typically operated at 5Hz. A temporal pulse shape is shown in Figure 5-2. This entire laser system was mounted on a 4' x 10' optical table. Some experiments employed two simultaneous wavelengths; the doubled-Yag output was used as one wavelength, with the tunable dye as the second. These two beams were taken from the system as shown in Figure 5-1.

The basic experimental configuration for DFWM measurements is shown in Figure 5-3. Other variations of this set-up were used, and will be discussed as necessary. The beam is first expanded and spatially filtered to give plane wave pumps, then collimated to a diameter of ~ 0.7 mm and is used at this diameter in the "canonical" four-wave mixing geometry. The probe beam is split
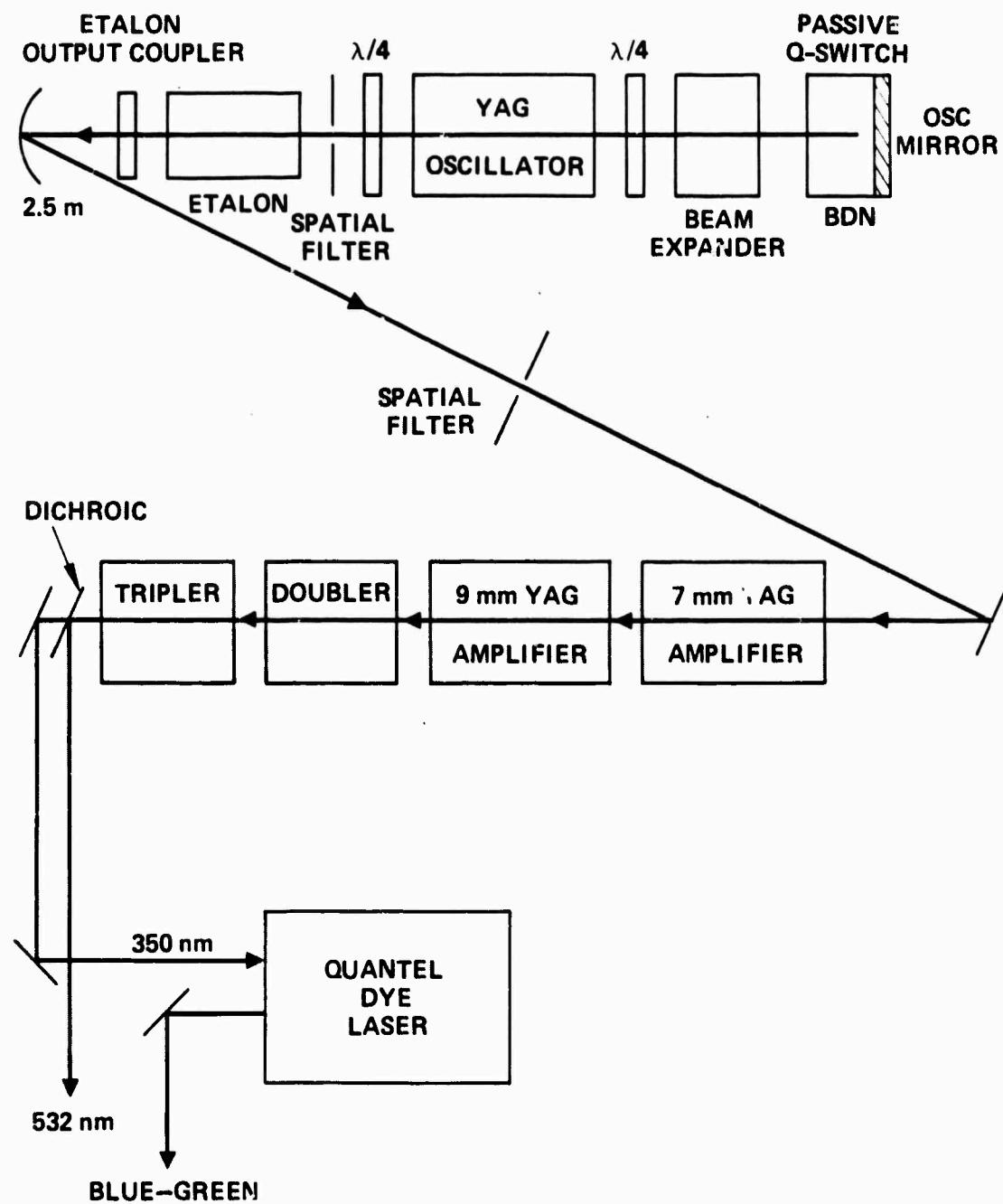
Figure 5-1. Quantel Yag-dye laser system.
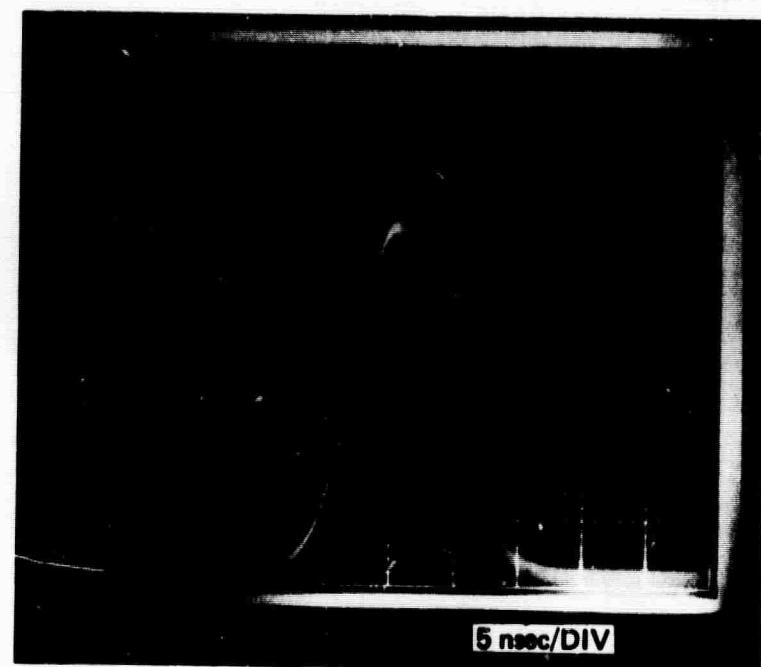
Figure 5-2. Temporal pulse shape of Yag laser
output.
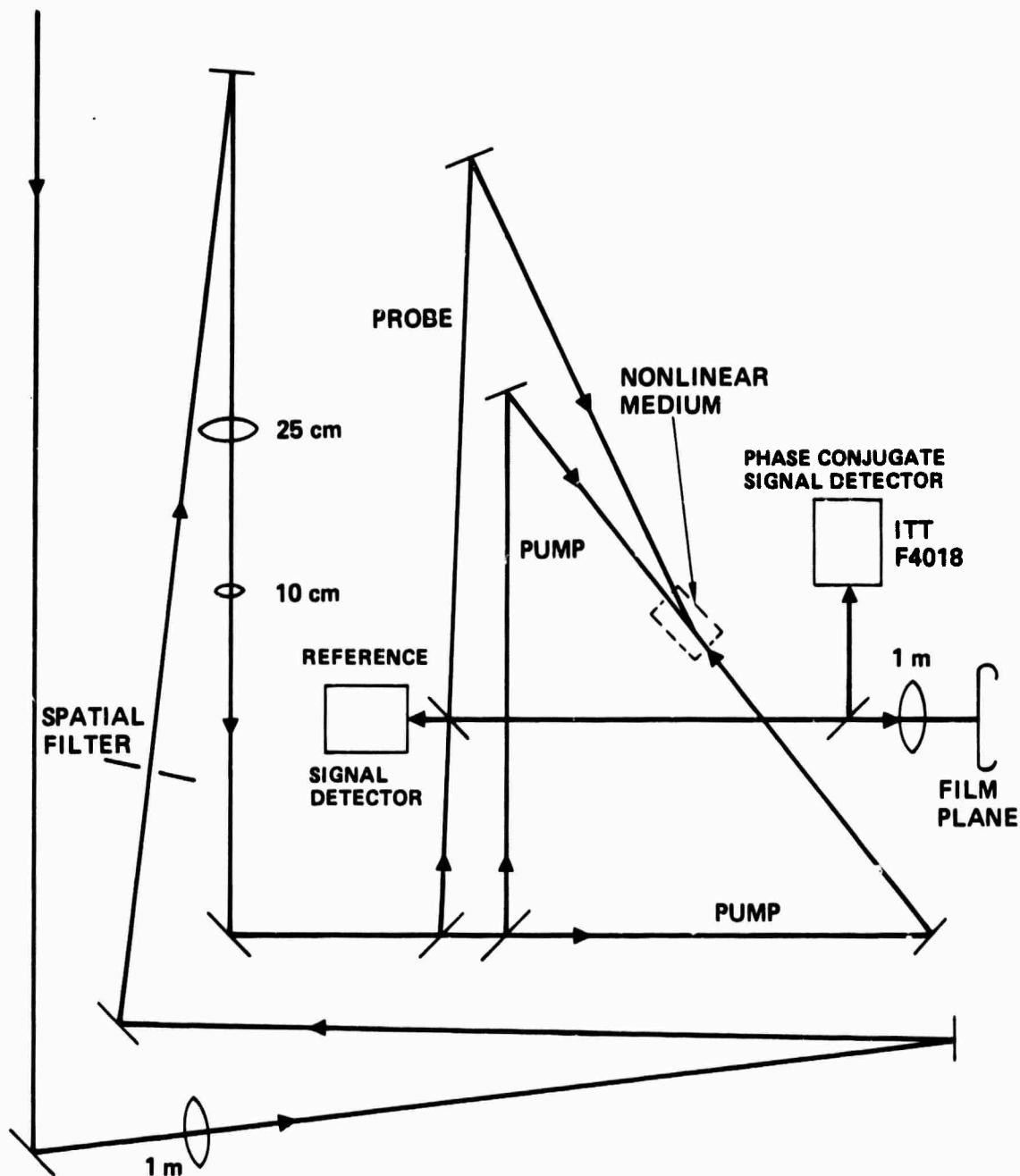
Figure 5-3. Apparatus for DFWM experiments.

off by a 5% beam splitter and enters the nonlinear medium at an angle of less than one degree. The pumps are equal in magnitude and enter the medium in a counterpropagating geometry as shown. A part of the reference signal is split out as shown and monitored with an ITT fast photodiode. The phase conjugate signal is also monitored with a fast photodiode. In addition, far-field photographs of the spatial intensity pattern of the beam are taken at the focal point of a high quality 1m focal length lens of 2 in. diameter.

5.2 MATERIALS INVESTIGATION AND PHASE-CONJUGATE EFFICIENCY MEASUREMENTS

A large number of materials have been examined on this program. The goal was to examine their suitability as nonlinear media primarily in the blue-green region of the spectrum. (A detailed discussion of criteria used to choose materials is given in Section 5.7 below.) Examples of some of the materials investigated are given in Table 5-1 with an indication of the wavelengths examined. Primarily solids and liquids were used, and each is discussed in detail below.

As a means of reference for later results, temporal pulse shapes for the DFWM signals are given in Figure 5-4. Figure 5-4(a) gives the retro-mirror (remove the nonlinear medium and replace it with a regular mirror) with full-width-half maximum (FWHM) of 5.2 nsec; 5-4(b) shows the DFWM signal in R6G with a 3.8 nsec FWHM; and 5-4(c) shows the DFWM signal in Corning #3-68 filter with ~4 nsec FWHM. The narrowing of the pulse of the DFWM signal relative to the retro-signal due to the nonlinear process is observed. Also, a somewhat different pulse shape is observed for R6G and the filter glass, indicating different mechanisms responsible for the generation of the signal. This is, in fact, the case, and will be discussed below.

5.2.1 Semiconductor - Doped Glasses

Several workers at HRL and elsewhere have recently reported[5-1,2,3,4,5,6,7,8] the usefulness of near-band-gap semiconductors for degenerate four-wave mixing and optical bistability. For DFWM, high reflection coefficients (and gain) have been reported. For a given wavelength, factors determining the selection of the semiconductor for high DFWM efficiencies, including the bandgap and sample

TABLE 5-1. Materials Studied for DFWM Returns at Visible Wavelengths

Class	Material	Wavelength (Å)
Solid	CdS	5320
	CS 3-68 (Corning filter)	5320
	CS 2-73	5800
	RG 695 (Schott filter)	6943
Liquid	Cryptocyanine	6943
	R6G/Methanol	5320, 5200, etc.
	R500/Methanol	4900-5300
	Potassium-dichromate/water	5320
	Potassium-permanganate/water	5320
Gas	I_2 vapor	blue-green-yellow

thickness, have also been discussed. In practice, the selection of an appropriate semiconductor for a given wavelength for high DFWM efficiency is complicated by the difficulty of growing crystals of suitable dimensions with precisely the desired band-edge, optical absorption, and overall optical quality. In this program, we have made a convenient implementation of near-band-gap semiconductors by the use of commercially available glasses doped with crystallites of mixed composition; the band gap is varied by varying the composition. Glasses are isotropic, and thus avoid problems associated with the birefringence of anisotropic semiconductors. With appropriate choice of the semiconductor-doped glasses, we have demonstrated moderate efficiency DFWM (reflection returns of ∿1-10%) for several wavelengths in the 500 nm - 700 nm wavelength range.

The most commonly studied mixed semiconductor-doped glass appears to be the one based on the CdS/CdSe mixture. This colored glass, called selenium ruby glass, can be made in colors ranging from deep yellow (x > 0.8) to deep red (x < 0.2), corresponding to a gradual decrease in the band gap with

(a)

REFERENCE   RETRO MIRROR,
SIGNAL   5.2 nsec FWHM

(b)
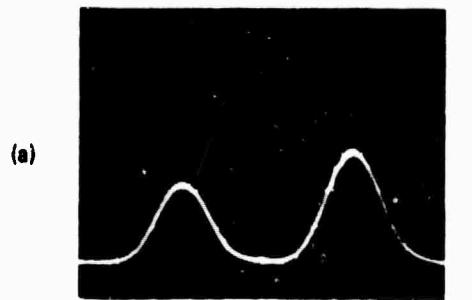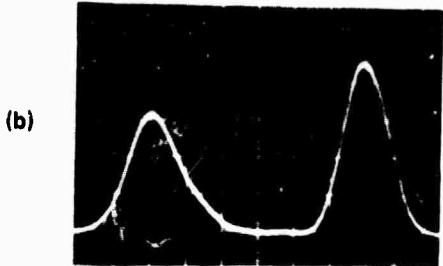
REFERENCE   DFWM SIGNAL
SIGNAL   IN R6G,
                  3.8 nsec FWHM

(c)
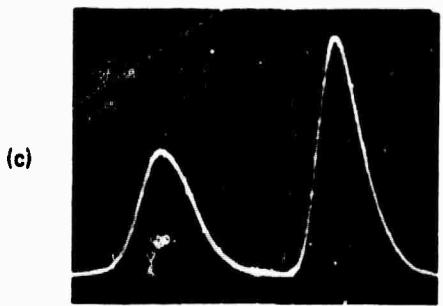
REFERENCE   DFWM SIGNAL IN 3-68
SIGNAL   CORNING FILTER,
                  4.0 nsec FWHM

Figure 5-4.
Temporal pulse shapes (a) retro-mirror,
(b) R6G, (c) 3-68 corning filter, 2.9 nsec/
dim.

increasing selenium concentration. The glasses used here were obtained from Corning Glass and Schott Glass.[5-9,10] Typical transmission data for these sharp cut-off color glasses is given in Figure 5-5. The filters chosen were the ones giving about 25-50% transmission at the wavelength of interest.

The presence of tiny mixed semiconductor crystals in such glasses was noted as early as 1932 by Rooksby,[5-11] via x-ray diffraction. Optical studies of the basic kinetics of the mixed crystal formation were reported by Schmidt[5-12] in 1967. An approximately linear dependence of the absorption edge of the mixed crystals as a function of the selenium fraction $(1-x)$ was noted, indicating only a small variation in the composition of the crystallites for a given colored glass sample. With the use of light scattering studies and electron microscopy, it was estimated that the sizes of the crystallites were typically in the 100Å to 1000Å range. Thus, these "doped" glasses consist essentially of microcrystals of semiconductor material, completely isolated from one another by the amorphous glass matrix in which they are imbedded; the microcrystals themselves appear to be of one uniform composition throughout the entire glass and are oriented randomly. The glass itself is insulating, and thus very little is known about the electrical semiconductor parameters of the microcrystals.

As a point of reference, the first experiments were performed with a material that is much better characterized. These experiments were performed at 5320Å on a high resistivity n-type single crystal sample of CdS, whose optical and electrical properties are well known. This 3.5 mm crystal was oriented with its c-axis perpendicular to the electric field of each of the co-polarized pump and probe beams. Figure 5-6 shows a log-log plot of the DFWM reflectivity versus pump intensity for this sample. Here 40-50% reflectivities could routinely be achieved. From the low-intensity (slope of 2) portion of this plot, we estimate an experimental value of 3.4×10^{-9} esu for the experimental effective third-order susceptibility. Assuming that the nonlinearity is due to plasma generation[5-1,3,5,6] and noting that the ∿7 nsec laser pulses are significantly shorter than the ∿1 microsecond lifetime[5-13] of
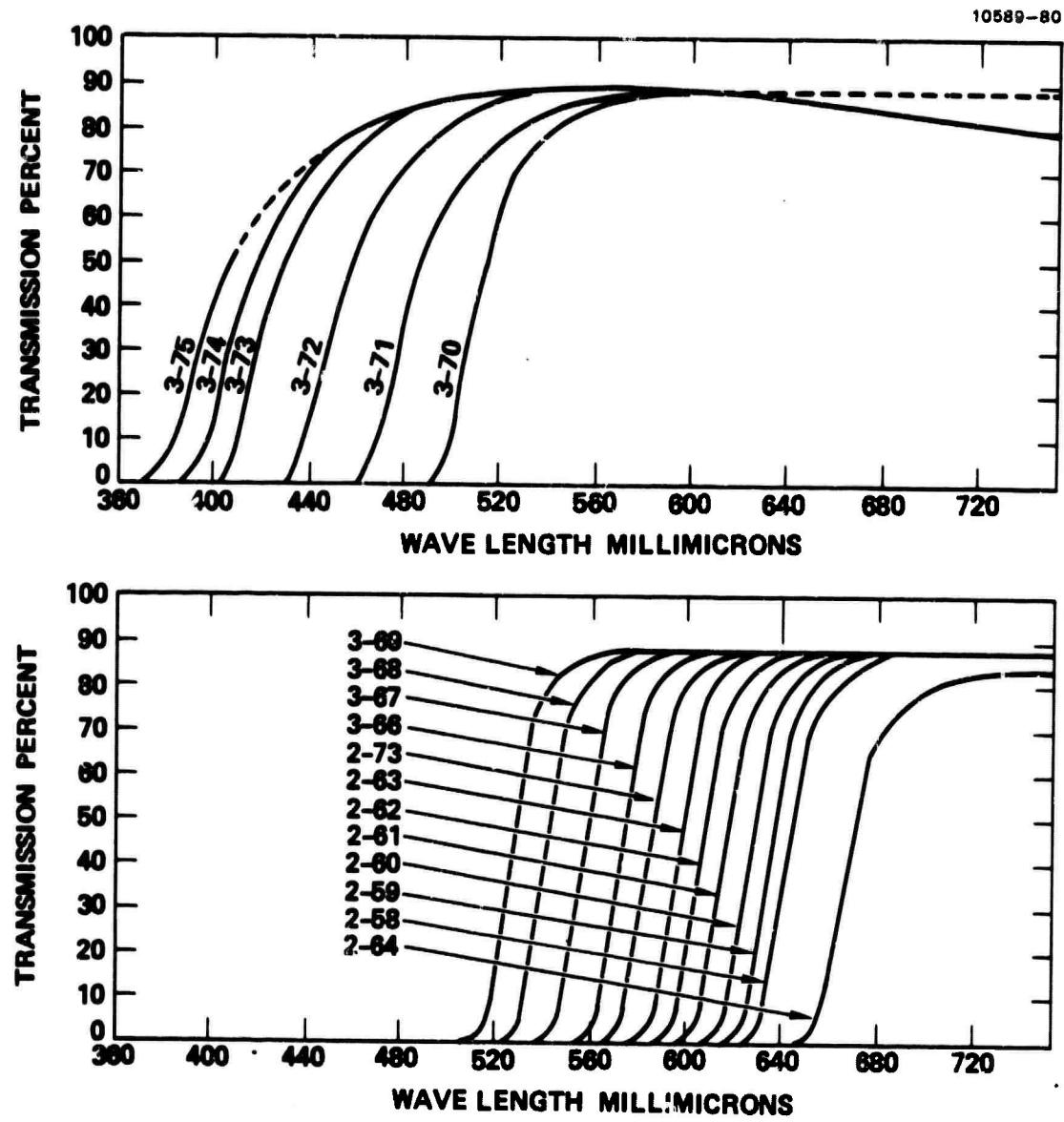
Figure 5-5. Transmission spectra of various corning "sharp cut yellow and red filters" taken from corning glass color filter catalog, Corning, New York.
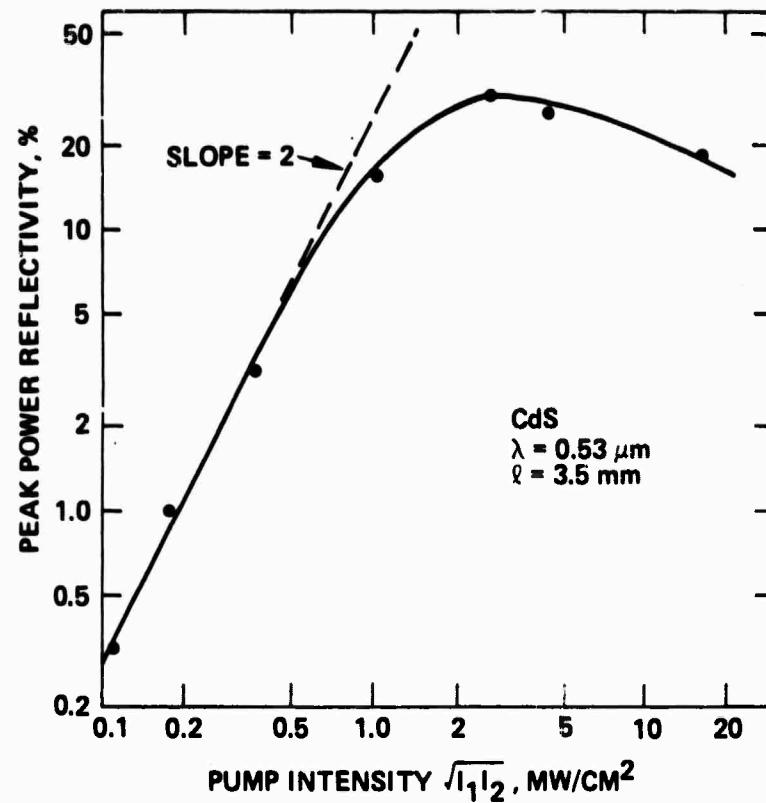
Figure 5-6.   Phase conjugate reflectivity versus intensity for CdS.

the electron-hole plasma, this experimentally observed value is found to be in good agreement with the value of $\sim 4 \times 10^{-9}$ esu calculated[5-1,14] from

$$\chi^{(3)}(\omega,T) = \frac{\eta(T)\alpha(\omega,T)ce^2\tau(T)}{8\pi\, m_{eh}^*\hbar\omega^3}\left[\frac{\omega_g^2}{\omega_g^2-\omega^2}\right],$$

and experimental data on the semiconductor parameters of CdS.[5-15,16.17,18,19] In this equation ω is the laser frequency η is the quantum efficiency of carrier generation, α is the frequency dependent absorption coefficient, m_{eh}^* is the reduced effective mass of the electron-hole pair and τ is the temperature-dependent recombination time.

Figure 5-7 shows the log-log plot of the DFWM reflectivity versus pump intensity obtained when the CdS sample is replaced by a 2 mm thick sample of a CdS_xSe_{1-x}-doped glass with x = 0.9 (Corning glass filter #3-68). The fact that the initial slope of this plot is only 0.9 (i.e., much lower than the anticipated value of 2) implies that either the DFWM signal is saturating (due to effects such as nonlinear absorption), or that the nonlinearity has saturated; or even that a third order nonlinearity is not adequate to explain the observed DFWM signal. However, in contrast to other workers,[5-10,20] in our work the photon energy (2·33 eV) was significantly smaller than the $\sim 2\cdot4$ eV estimated band gap energy (the low intensity transmission of our sample = 30%) and, we did not observe any saturation of absorption in this glass sample (or in CdS). Assuming that the DFWM signal is saturated at our intensity levels, and that the origin of the nonlinearity is similar to that in CdS, we estimate an experimental third order nonlinearity of at least $1\cdot3 \times 10^{-8}$ esu from the data of Figure 5-7. A calculation similar to that for CdS cannot be performed because of the lack of data on the semi-conductor parameters of the CdS_xSe_{1-x} doped glasses. For comparison, Figure 5-7 indicates a measurement of the efficiency of I_2 vapor at 121°C. We see that it is several orders of magnitude lower than the results for 3-68.
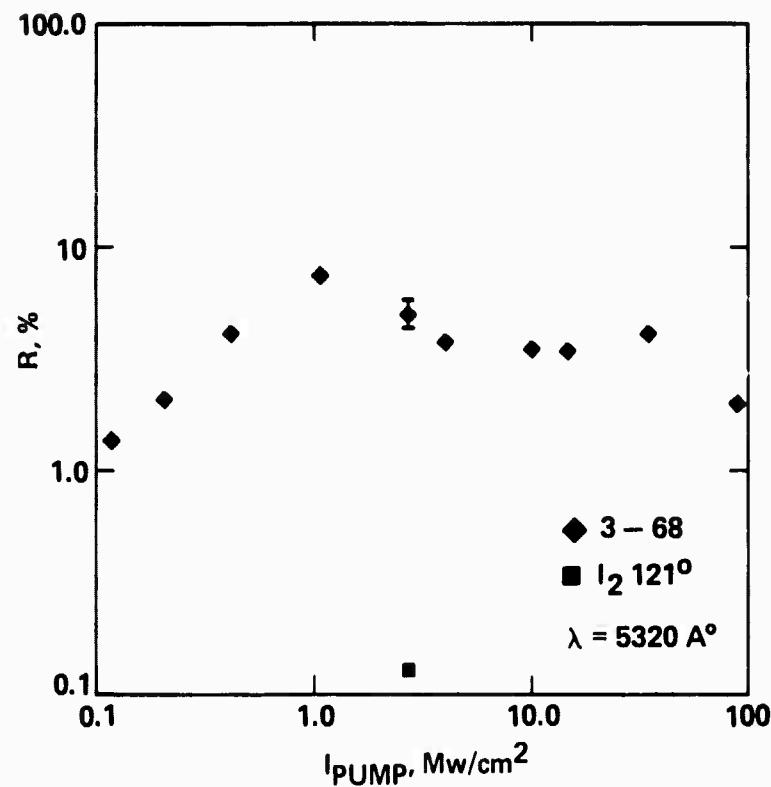
Figure 5-7. Phase conjugate reflectivity versus
intensity for corning filter glass 3-58
and I_2 vapor.

To verify the applicability of the glasses to other wavelengths, we performed experiments using the tunable dye laser. Appropriate semiconductor glasses were chosen for each of these wavelengths, and $\sim$1-10% peak DFWM reflectivities were observed for each of these cases at pump powers of $\sim$1 MW/c.^{2}. Representative results are presented in Table 5-2. At the wavelengths outside the 0.5 μm – 0.7 μm range, it should be possible to use glasses of other mixed crystal compounds, such as those represented by Corning filters #CS 3-70 to CS 3-75. Polarization rotation experiments have been performed with 3-68 glass, and the results of these experiments are described in Section 5.4. Experiments were performed at 6943Å in Schott filter glass RG 695. The reflectivity results for this material are given in Figure 5-8. The behavior is different from the other glasses and is not understood at this time.

Table 5-2. Various Semiconductors and Estimated Nonlinear Susceptibilities Near Their Bandgap

CdS_xSe_{1-x} Glass (Filter)	X	λ, μm	$\chi^{(3)}_{eff}$ esu
Corning #CS 3-68	$\sim$0.9	0.532	$\sim$1.3 x 10^{-8}
Corning #CS 2-73	$\sim$0.7	0.580	$\sim$5 x 10^{-9}
Schott RG 695	$\sim$0.1	0.694	$\sim$3 x 10^{-9}

5.2.2 Saturable Absorbers/Liquids

As shown in Table 5-1, various saturable absorber dyes in various liquid solvents have been investigated in this program. As we will show below, the phase conjugate return can result from a nonlinear response in the dye, depending upon the intensity regime you are in, namely, saturable absorption as discussed in detail in previous chapters, or from a different mechanism in the liquid solvent producing the well known thermal grating effect,[5-21,22,23] or from both.
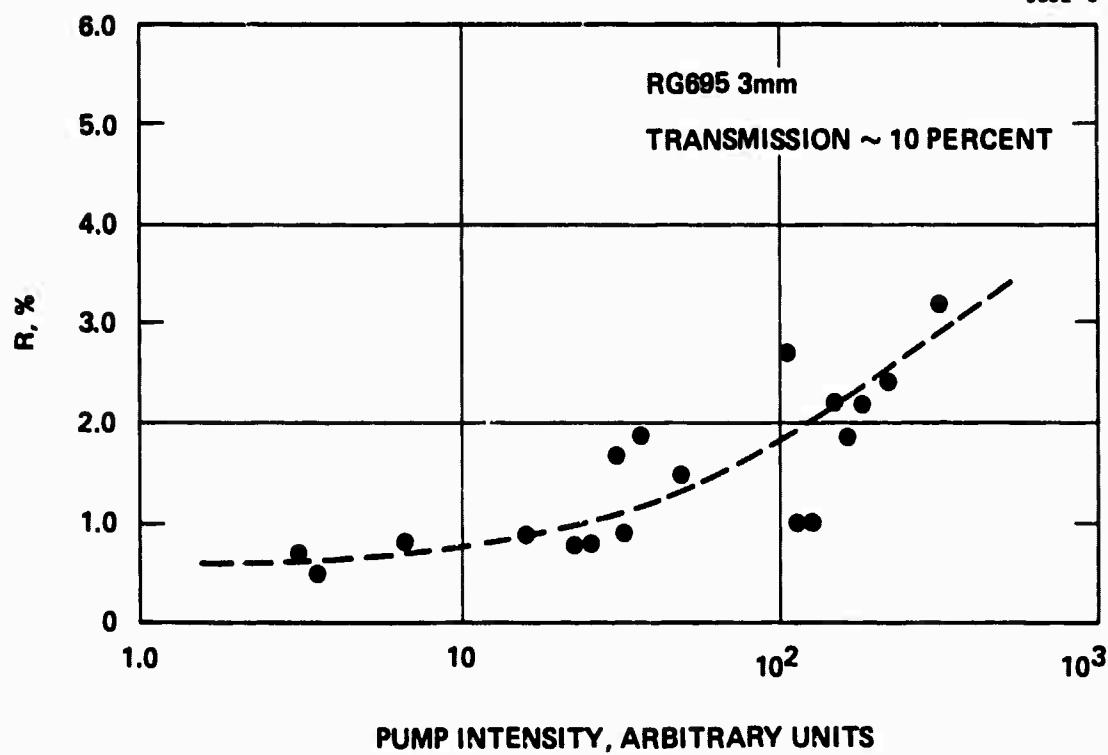
Figure 5-8. Phase conjugate return versus intensity for RG695 filter.

All of the processes, however, employ a dye as the medium which absorbs light. Thus, as in the case for solids, the appropriate dyes are selected on the basis of their absorption spectrum for the wavelength of interest. Examples of candidate dyes for various wavelengths are shown in Table 5-3. Rhodamine 6G (R6G) has the largest absorption cross section of most dyes, with a peak occurring at 5320Å; thus, it became a convenient material to study with our doubled-Yag system.

In Figure 5-9 we show a log-log plot of the phase-conjugate reflectivity vs. pump intensity (where the pump intensity is normalized to the saturation intensity of the $S_0 \to S_1$ transition, $I_{sat} = 3$ MW/cm^2) for a R6G/Methanol mixture in a cell 1 mm in length for a small-signal absorption length product $\alpha_0 L = 1$. Several points emerge from this data. We see the lower portion of the curve clearly saturates at approximately the saturation intensity of R6G. In fact, a simple calculation of the reflectivities based on the two-level model discussed in Chapter 2 (Eqtns 2-1-1 - 2-1-4) predicts this lower portion exactly. Typically, 1% reflectivities are obtained in this region. The upper portion of the data points (where greater than 100% reflectivities were easily achieved) is due to the thermal grating effect which is well known to occur in liquids,[5-1,5-2,5-3] and in this case is due to thermal transfer to the methanol solvent. This was established thorugh a series of separate measurements which will be described below. At first, from the functional dependence of this upper portion, and from similar experiments[5-4] performed at 1.06 μm in the saturable absorber dye DCN in dichlorethane, it was speculated that an excited state process, such as the four-level type models described previously, could account for this region of the data. Or that a coherent 2-photon process could lead to the result. The elimination of the two-photon process as a contributor was made through appropriate cross-polarization experiments to be described in Section 5.4 below. When known (or measured) cross sections and saturation intensities of excited states in R6G were put into the four-level model of Chapter 2, this theory was not able to predict the results obtained.

Table 5-3. Possible Dyes To Be Used
At Different Wavelengths

Dye	Wavelength (Based on Absorption Peak) (nm)
Cryptocyanine	694
Rhodamine 6G (590)	530
Rhodamine 560	506
Coumanin 540	458
Coumanin 500	392
Stilbene 420	340

A sequence of photographs is given in Figure 5-10 where we show the DFWM temporal response as the intensity is gradually increased from a region of the lower portion of the reflectivity curve to the higher portion of the reflectivity curve. What is shown in each photograph is the reference signal (see Figure 5-1) on the left and the DFWM detector signal on the right. We see that at low reflectivity a DFWM signal with a FWHM of 3.2 nsec occurs at 14 nsec delay from the reference signal (the absolute delay is not important, but the relative delay of this signal with respect to the delay of the higher intensity signals will be). As the intensity is increased, we see that at 5.4 MW/cm^2 a new signal is starting to appear, delayed in time from this first signal. As the intensity increases, the contribution of this signal increases, until at $\sim$11 MW/cm^2 both signals are equal in magnitude with the new signal delayed from the first by $\sim$4.4 nsec. With further increase in intensity, the delayed signal begins to dominate the return (the first signal saturates and then decreases, as shown in Figure 5-9), while the new signal is continually increasing until finally, at about 27 MW/cm^2, this signal - with a FWHM of $\sim$3.5 nsec, and delayed from the reference by $\sim$15.5 nsec - is completely responsible for the returns observed.
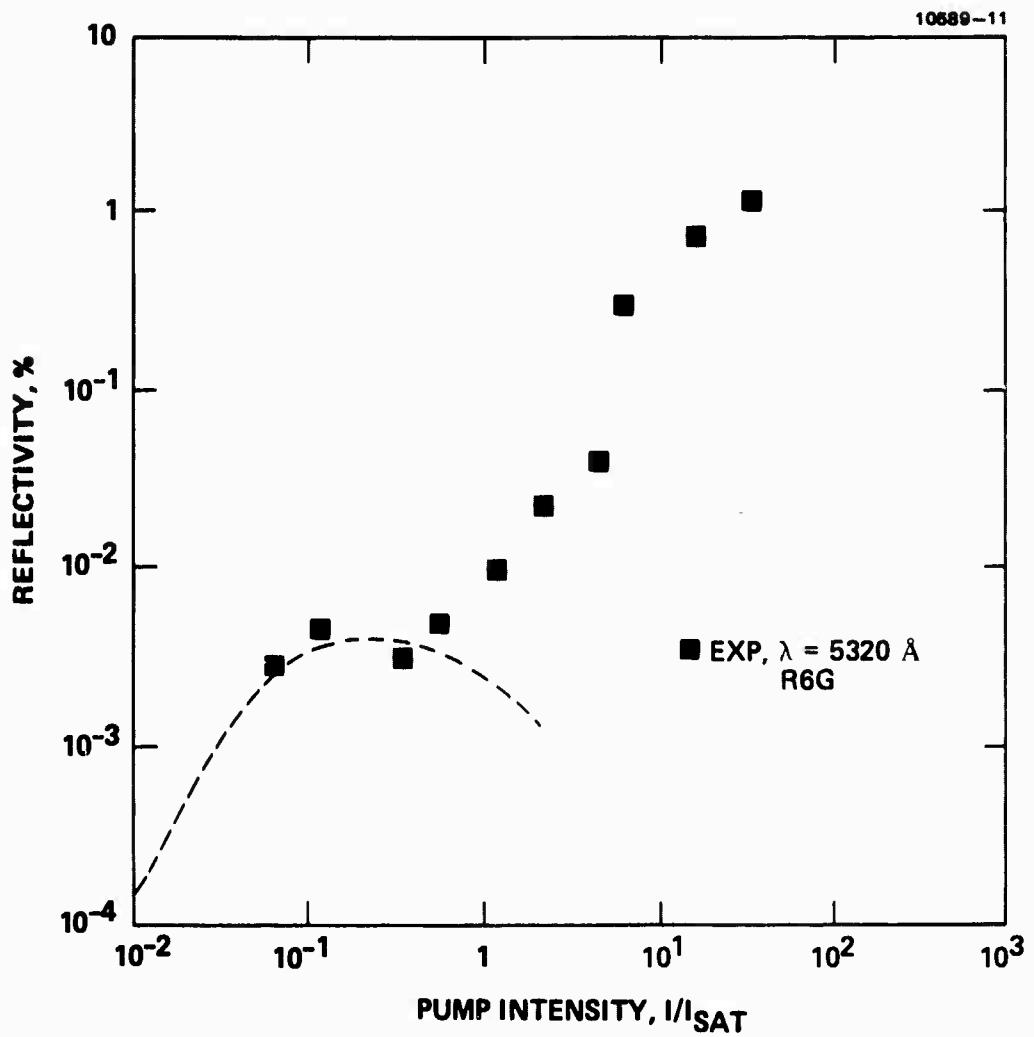
Figure 5-9. Phase conjugate reflectivity versus pump intensity for R6G.

PUMP POWER
(REFLECTIVITY)

0.3 MW/cm^2
(0.9 %)

11
(1.5 %)

1.8

12

5.4

18

7.2

27
(20 %)

REF   DFWM   REF   DFWM
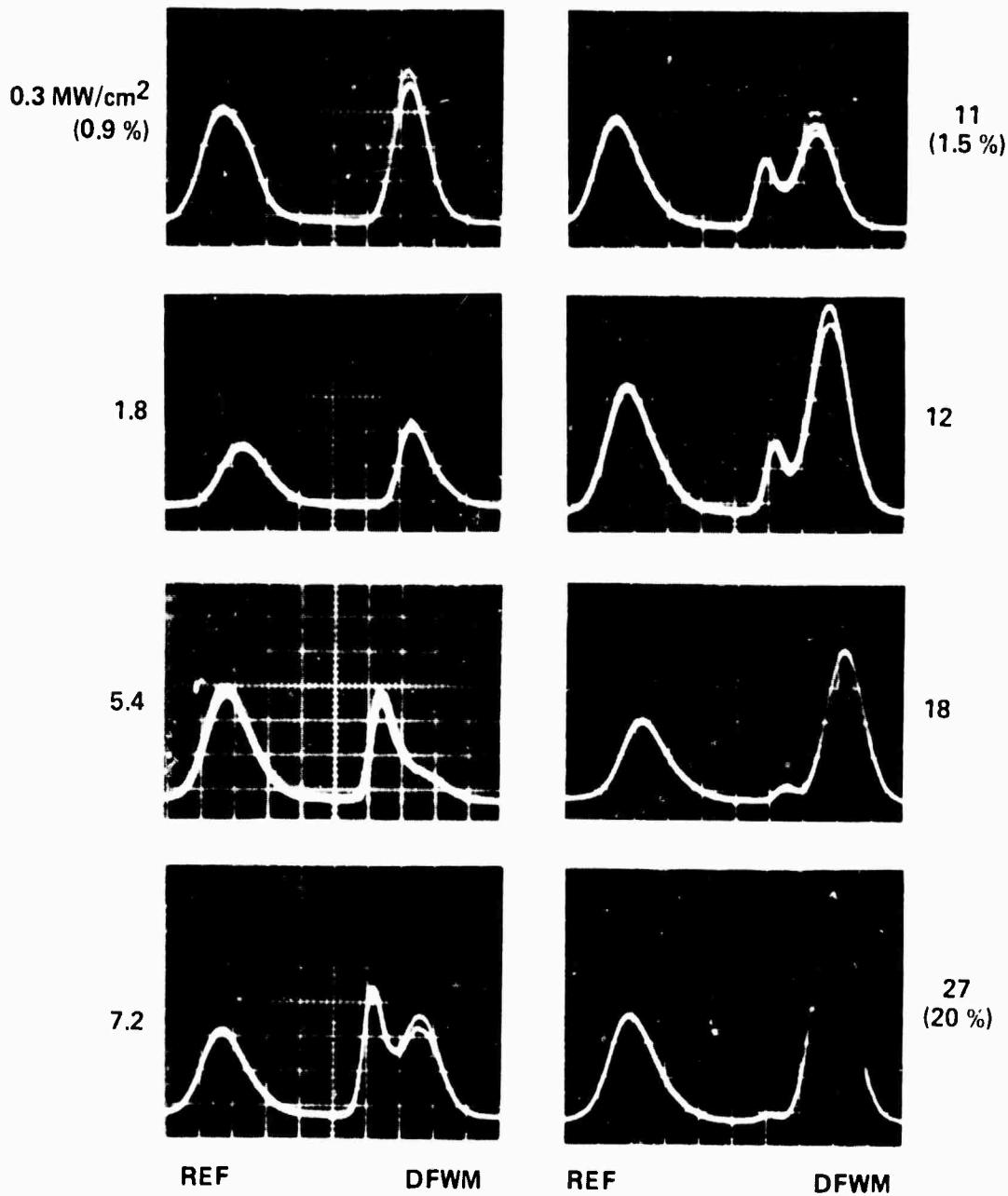
Figure 5-10.   Temporal pulse shapes for R6G for various pump powers (reflec-
tivities) giving input reference beam and DFWM signal showing
development of thermal grating.

It was demonstrated by a time delay experiment that this signal is due to a thermal grating in the methanol. Thermal gratings have long-time constants, typically on the order of microseconds, a concequence of the acoustic-type process involved. The light is first absorbed in the dye, setting up E.M. standing waves which heat the methanol and produce density gradients; and hence, refractive index gratings from which the probe is scattered. Because these thermal distributions have long-time constants, the gratings can be formed and read out at a much later time, as compared to conventional gratings.

An experiment was performed in which the forward pump and probe entered the cell simultaneously and formed a grating. The backward pump was then delayed by up to $\sim$30 nsec and the DFWM signal observed stayed essentially constant. Since the laser pulse was about 7 nsec, the readout (backward pump) beam was scattering from a slowly decaying grating that was formed at an earlier time, strongly suggesting a thermal grating as the scattering source. In contrast, the saturable absorption process, which has time constants appropriate to the radiative lifetime of the S_1 state (lifetimes of the order of a few nsec), requires all three beams to be present simultaneously to generate a DFWM signal. Thus, in the delayed experiment we would expect no contribution from the earlier signal as generated by saturable absorption in the sequence of Figure 5-10 (the lower portion of the reflectivity curve of 5-9) at the lower intensities. This is, in fact, what is observed, and these results are given in Figure 5-11. Shown here is the DFWM signal at reflectivities of $\sim$0.1%, 1%, and 10% with the backward pump, delayed by 30 nsec from the forward pump and probe. We see that only one signal occurs for all intensities, with the time delay the same for all intensities, and, in fact, equal to that obtained at the high intensities.

By using the results from Reference[5-3], we can show that for the given parameters of the experiment the reflectivities achieved are consistent with those expected from thermal gratings. The reflectivity is given by (Eqtn 6 of Ref 5-3)

$$R_{T.G.} = TD^2 \, U_f U_s n \quad ,$$

PHASE CONJUGATE
REFLECTIVITY

(a)

REF   DFWM

0.1 %

(b)

REF   DFWM

1.0 %

(c)

REF   DFWM

10 %
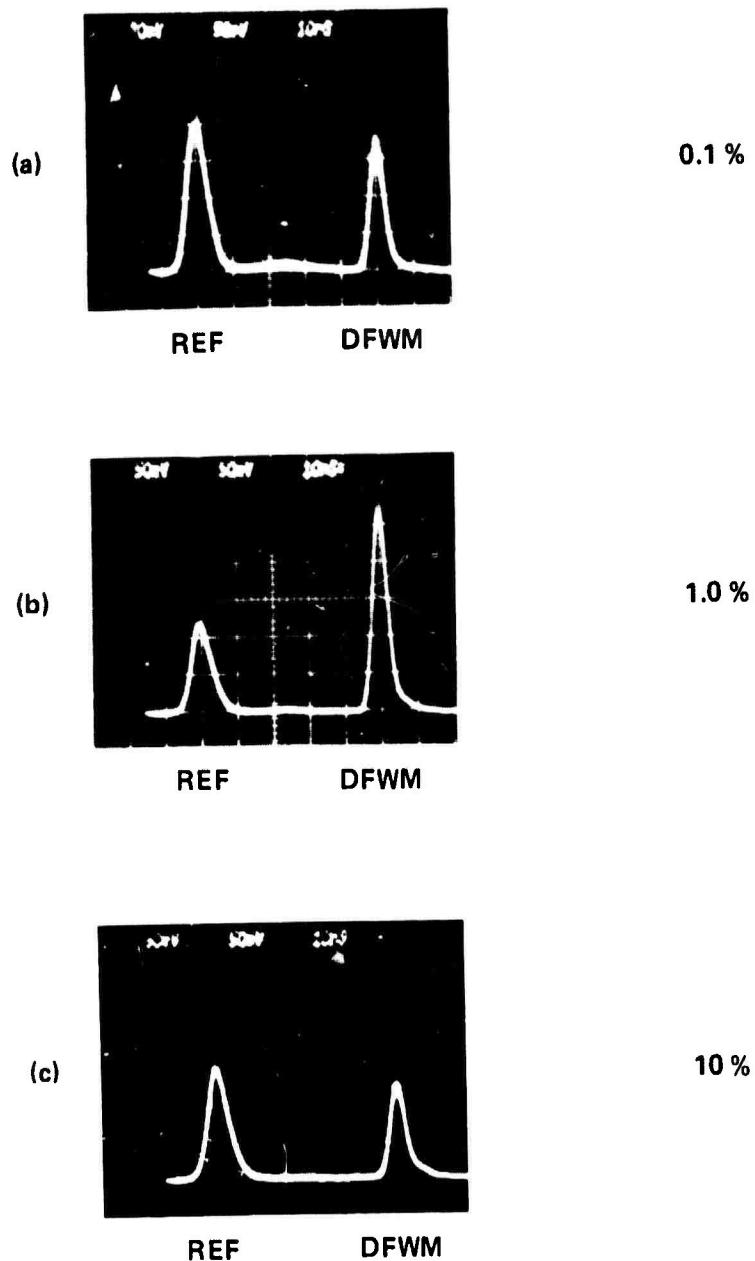
Figure 5-11.   Temporal pulse shapes for R6G with backward
pump delayed by 30 nsec from the forward pump
and probe for phase conjugate efficienies
of (a) 0.1%, (b) 1.0%, and (c) 10%.

where

$$T = \exp(-\alpha_o L) \quad ,$$

$$U_f = \text{energy density in forward pump,}$$

$$U_p = \text{energy density in probe,}$$

and

$$D = \text{coupling coefficient indicating the strength}$$
$$\text{of the thermal grating} = 16 \text{ for methanol}$$

where

$$n = 1 \text{ for } \alpha_o L > 1$$

Using appropriate numbers from the present experiment, we find that $R \simeq 10\%$, consistent with the measured values. Unfortunately, although thermal gratings can lead to high reflectivities, as we will see in Section 5.3 below, accurate conjugation is not always achieved in this regime due to self-focusing or thermal blooming effects in the liquid.

A measurement of the reflectivity as a function of concentration of the R6G is shown in Figure 5-12. We see that regardless of the mechanism responsible for the DFWM returns the dye is required.
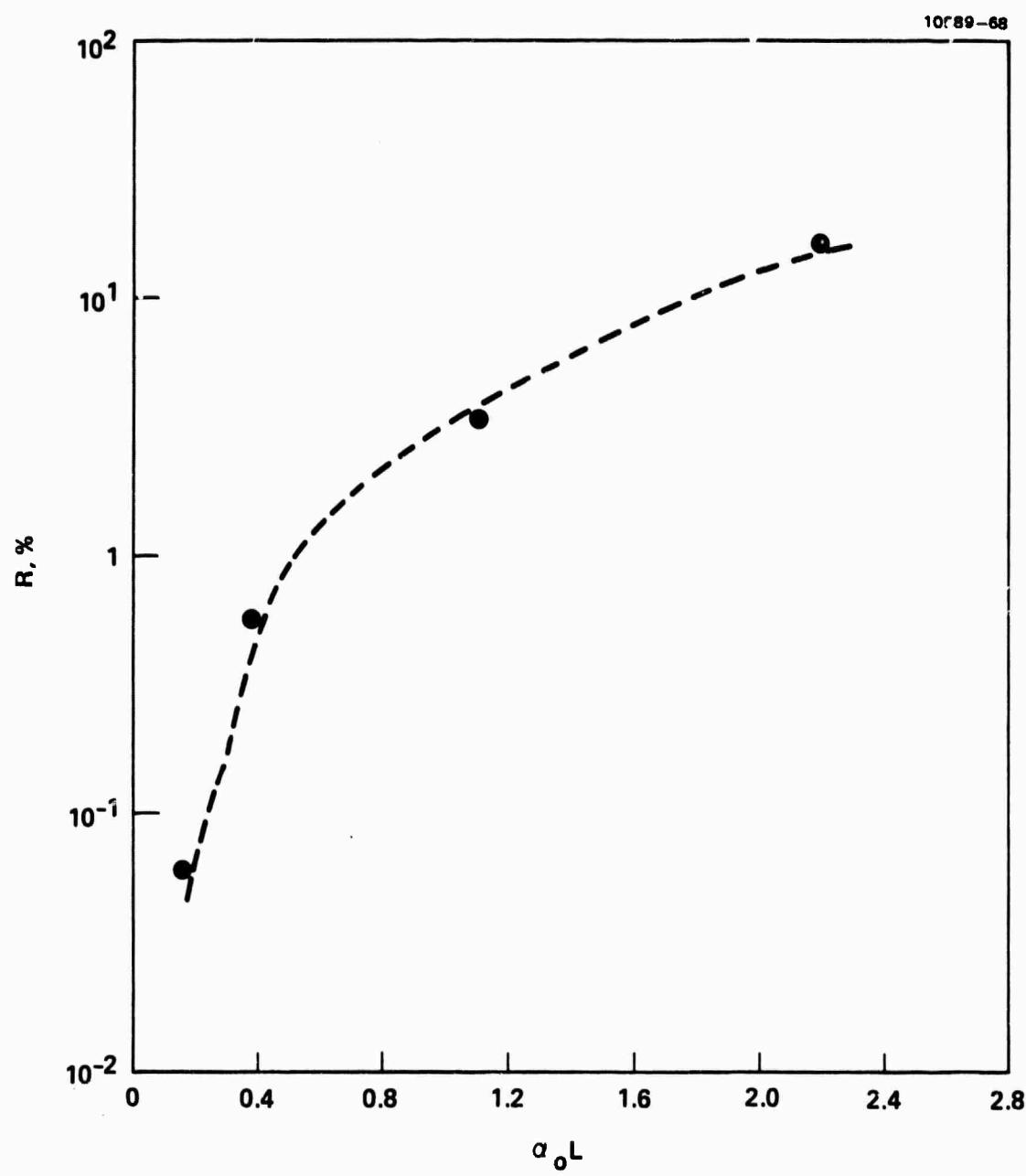
Figure 5-12. Reflectivity versus $\alpha_o L$ for R6G.

5.3 DETAILED FAR-FIELD INTENSITY PROFILES

One of the primary experimental accomplishments of this program is the measurement of far-field beam profiles to determine the corrective properties of DFWM. The far-field intensity distributions are measured at the focal point of a 1 m lens by a photographic technique using high-contrast film in a series of exposures at differing attenuations. In this way, the actual profile of the original, aberrated, and corrected beams can be determined independently of film linearity. The details of this procedure are described in the interim report where similar results have been obtained using SBS. We present here only the results obtained for DFWM.

The uncompensated and unaberrated beam quality is first monitored by removing the nonlinear medium, placing a reflecting mirror in that position, and reflecting the light back into the 1 m focal length camera through the beam-splitter. The degree of aberration introduced by the aberrator is next measured by placing the aberrator in the indicated position. The aberrator is a microscope slide etched in HF. A reference reflector is again substituted for the four-wave mixer, which causes the light to double-pass the aberrator. The precision of the DFWM correction process is then monitored, leaving the aberrator at the position shown in Figure 5-1. Thus, the quality of the aberrated and compensated beam is again measured at the focal plane, with the light passing the aberrator into the nonlinear medium, conjugating, and retraversing the aberator, ideally cancelling the aberrations, and producing a diffraction limited focal spot.

In contrast to the SBS experiments, where the aberrator was simply placed in the beam path before entering the SBS cell, the DFWM experiments require the effective imaging of the abberator at the nonlinear medium. The need for this can best be explained by examining Figure 5-13. The aberrator could most simply be located in front of the four-wave mixer, as shown in Figure 5-13a. However, care must be taken to avoid locating the aberrator in the pump path, since the fidelity of conjugation would be severely reduced with aberration introduced onto the pump beams. (See Chapter 4). However, if the
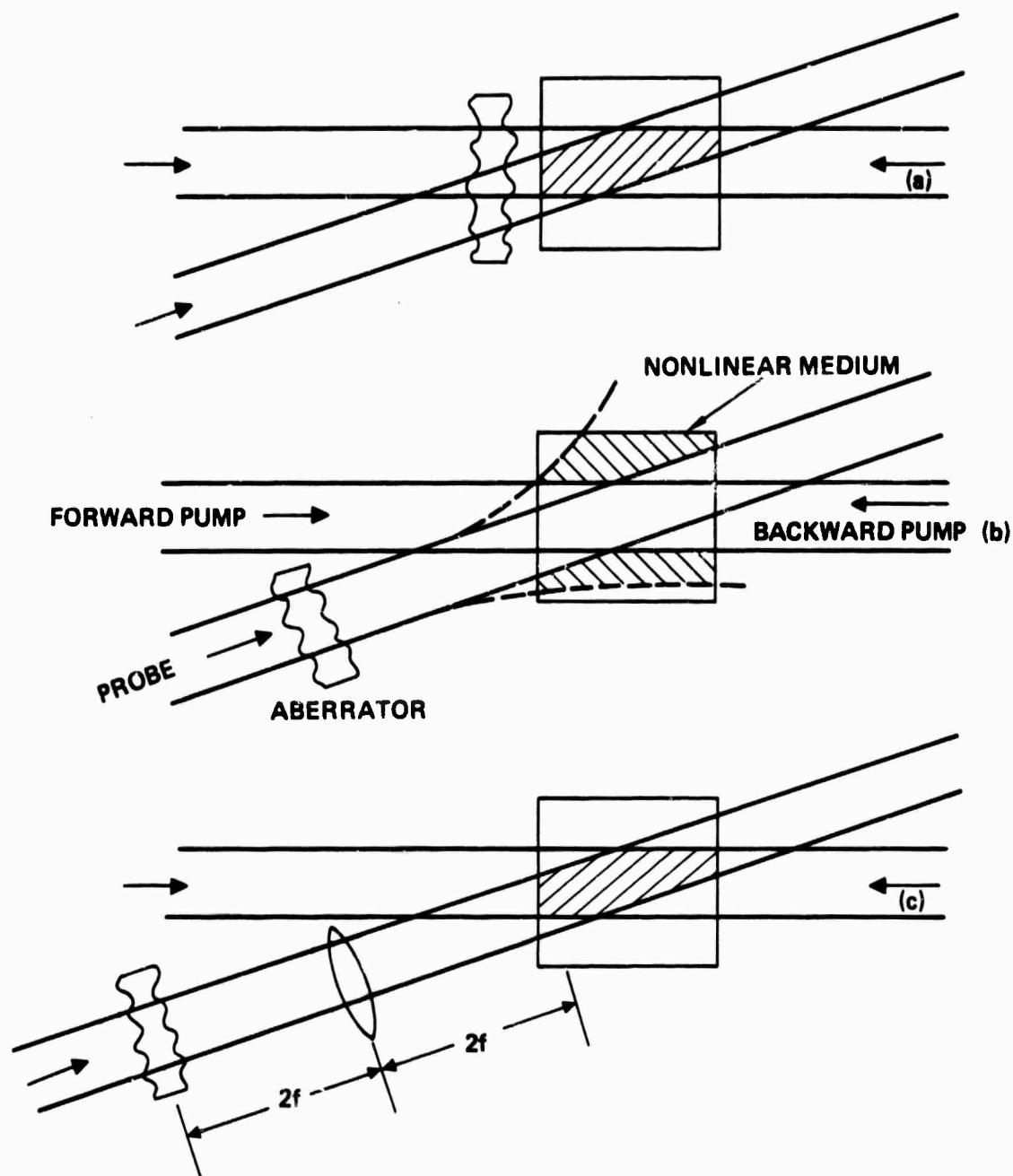
Figure 5-13. Imaging of aberrator.

aberrator is well spaced (as indicated in Figure 5-13b) to avoid pump interference, diffraction spreading of the aberrated beam then causes much of the probe beam to fall outside the pump region, as shown by the crosshatched region. This portion of the beam is, of course, not conjugated, and the correction process is incomplete. This was experimentally verified. To avoid this problem the aberrator must be imaged at the nonlinear medium position, as shown in Figure 5-13c. It is not necessary to maintain a 1:1 image (as shown), since the beam can be reduced in size from the pump diameter as long as the intensity in the probe beam is still well below the pump beam intensity. All the conjugation data to be discussed however, employed a 1:1 imaging scheme.

A qualitative example of the correction capability of DFWM is shown in Figure 5-14. This illustration shows the input laser signal, or probe beam, with reference mirror and no aberrator. The second picture gives the double-passed aberrator (aberration about 11λ diffraction limited) with reference mirror and the corrected signal after passing through the aberrator-conjugator-aberrator. From this we imply that the DFWM corrected beam has a far-field divergence nearly equal to that of the input laser beam. This correction capability is quantitatively demonstrated in the following figures, giving intensity profiles of the far-field spatial pattern for several situations of interest. Note that when referring to "lens" in these figures we imply that the imaging lens itself represents a fixed aberration which the conjugation process also removes.

The first example chosen for DFWM experiments used the saturable absorber cryptocyanine in methanol at 6943Å (using the Ruby laser). The intensity profiles shown in Figure 5-15 are for the following cases: reference or input beam, the aberrated reference beam-lens only, the aberrated reference beam-lens and aberrator, the phase conjugate beam with no aberration, the phase conjugate beam with lens aberration, and the phase conjugate beam with lens and aberrator. We see that in all cases the profiles essentially overlap the input reference beam down to an intensity $\lesssim 10^{-4}$ of the peak intensity. This indicates quantitatively that the correction is perfect. In addition to

CORRECTED
SIGNAL

ABERRATED
INPUT SIGNAL

INPUT
LASER SIGNAL
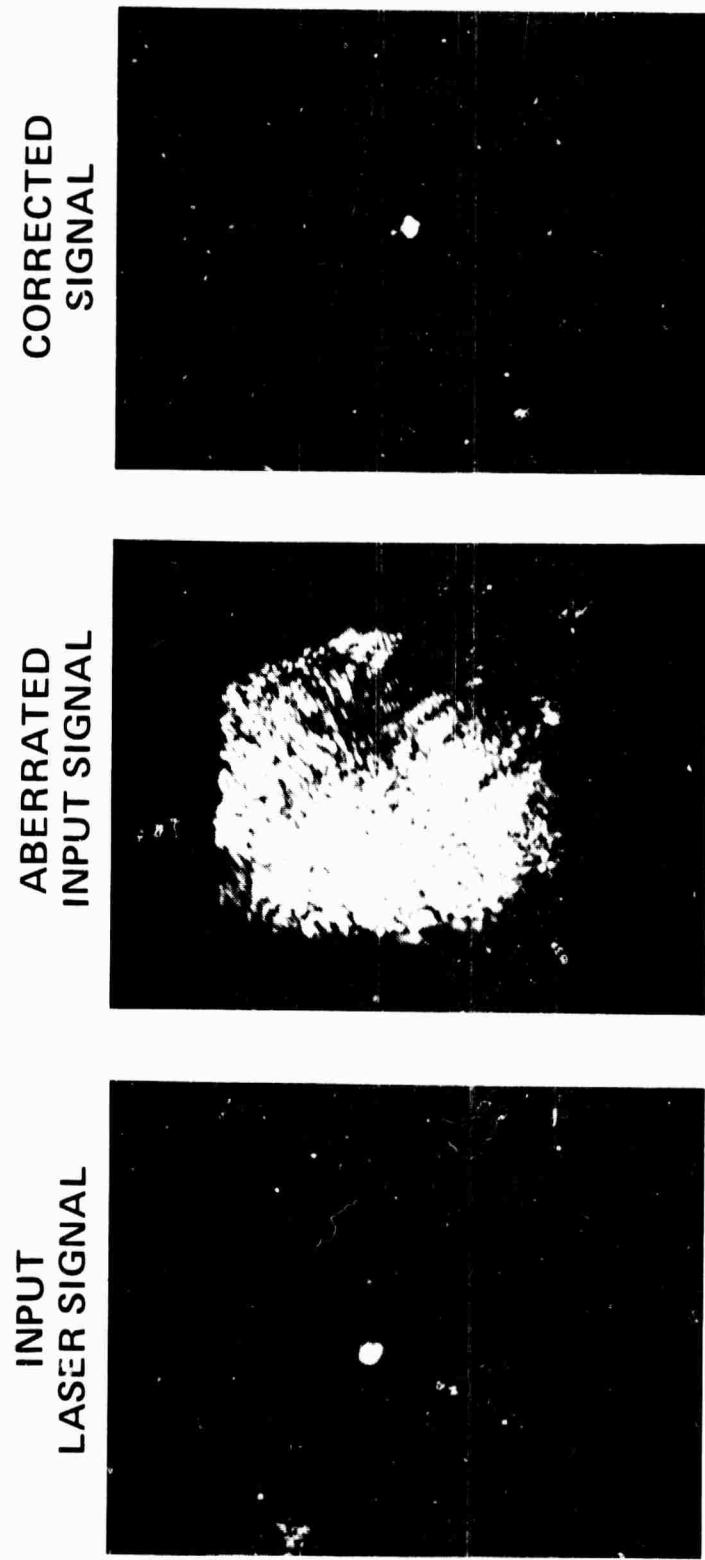
Figure 5-14.   DFWM phase conjugation — far-field photographs.
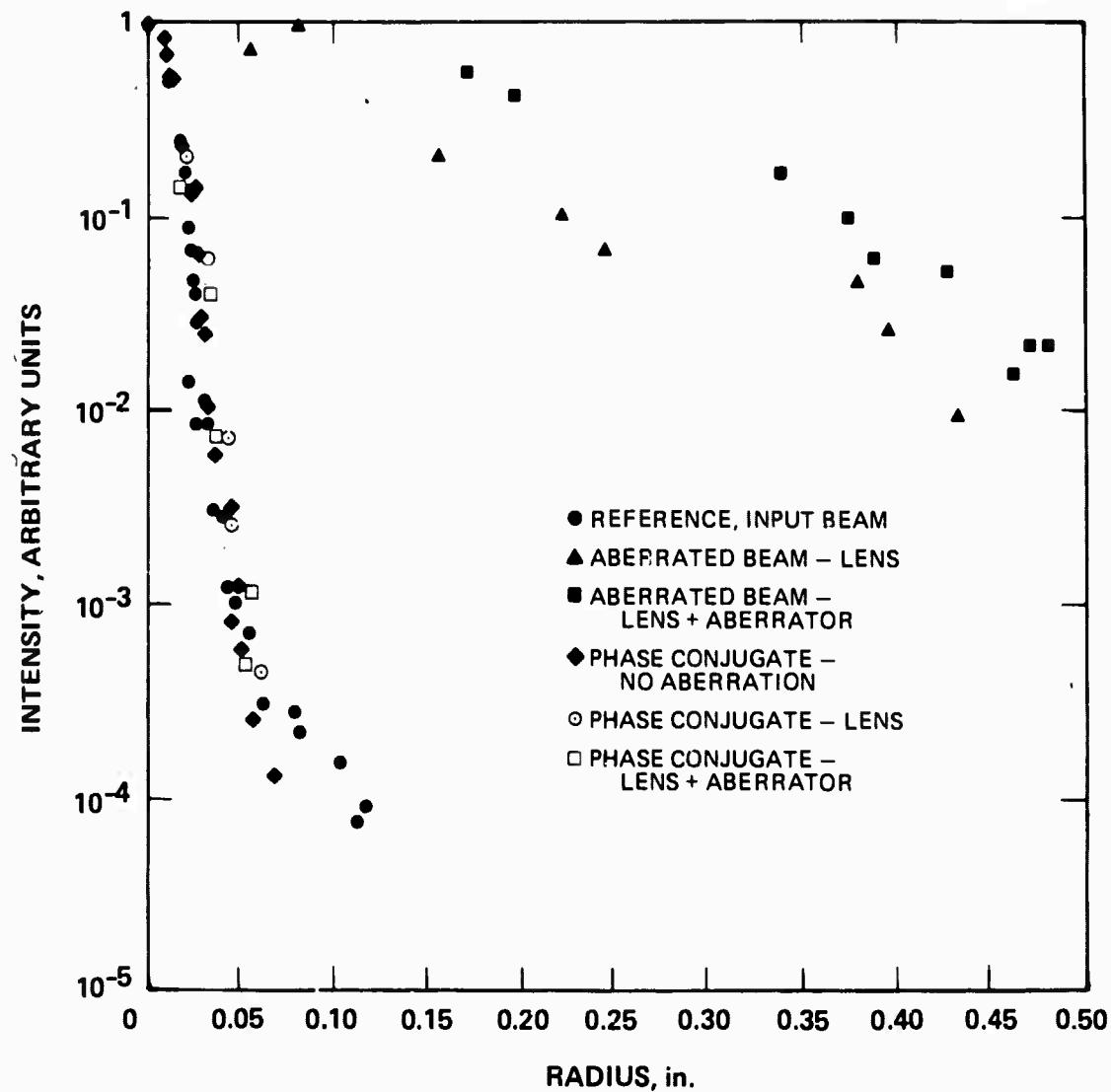
Figure 5-15. Intensity profiles using cryptocyanine ($\alpha_o L=2$) as nonlinear medium at λ = 6943A.

this detailed profile measurement, a power-in-the-bucket measurement was made to confirm if any energy could be found in the profile wings that might appear below the 10^{-4} value. Such measurements indicated that the fraction of nonconjugated return produced is immeasurably small. That is, energy that could contribute to a return that deviates from the profiles shown (e.g., non-phase-conjugate) is zero to within the experimental error (estimated to be <10%). A similar set of results was obtained using the semiconductor materials. An example of the data for the Schott glass RG 695 at $\lambda=6943\text{Å}$ is given in Figure 5-16. Again essentially perfect correction is achieved.

We next examined blue-green absorbing materials using the doubled-Yag apparatus and R6G dye in methanol as the nonlinear medium. Intensity profiles have been determined for several reflectivities to examine the fidelity of the conjugation process as the return efficiencies approach 100%. We were interested in determining whether nonlinear processes associated with the pump itself or other processes begin to play a role at the higher efficiencies. Effects, such as self-focusing or thermal blooming, were expected to be important, and our experimental results indicated that this was the case. (See Chapter 4). In Figure 5-17 the intensity profiles are shown for a conjugate efficiency of $\sim 0.5\%$ (where the return is due to a saturable absorption of the R6G). Again, as in the cases already discussed, the profiles essentially overlap down $\sim 10^{-5}$ of the peak intensity. Power-in-the-bucket measurements were also performed, indicating no energy in the wings as before. However, in Figure 5-18, taken at an efficiency of 35% (where thermal grating is dominant) we see that the conjugate signal (not aberrated) shows a deviation from the input reference signal (taken at high power also). This deviation is traceable to either self-focusing of the pump beams (individually) or thermal blooming effects as the intensity was raised to achieve the higher reflectivities. This can be seen by examining photographs of the DFWM signal in the far-field, and of the pump beam directly after passing through the cell, which are shown in
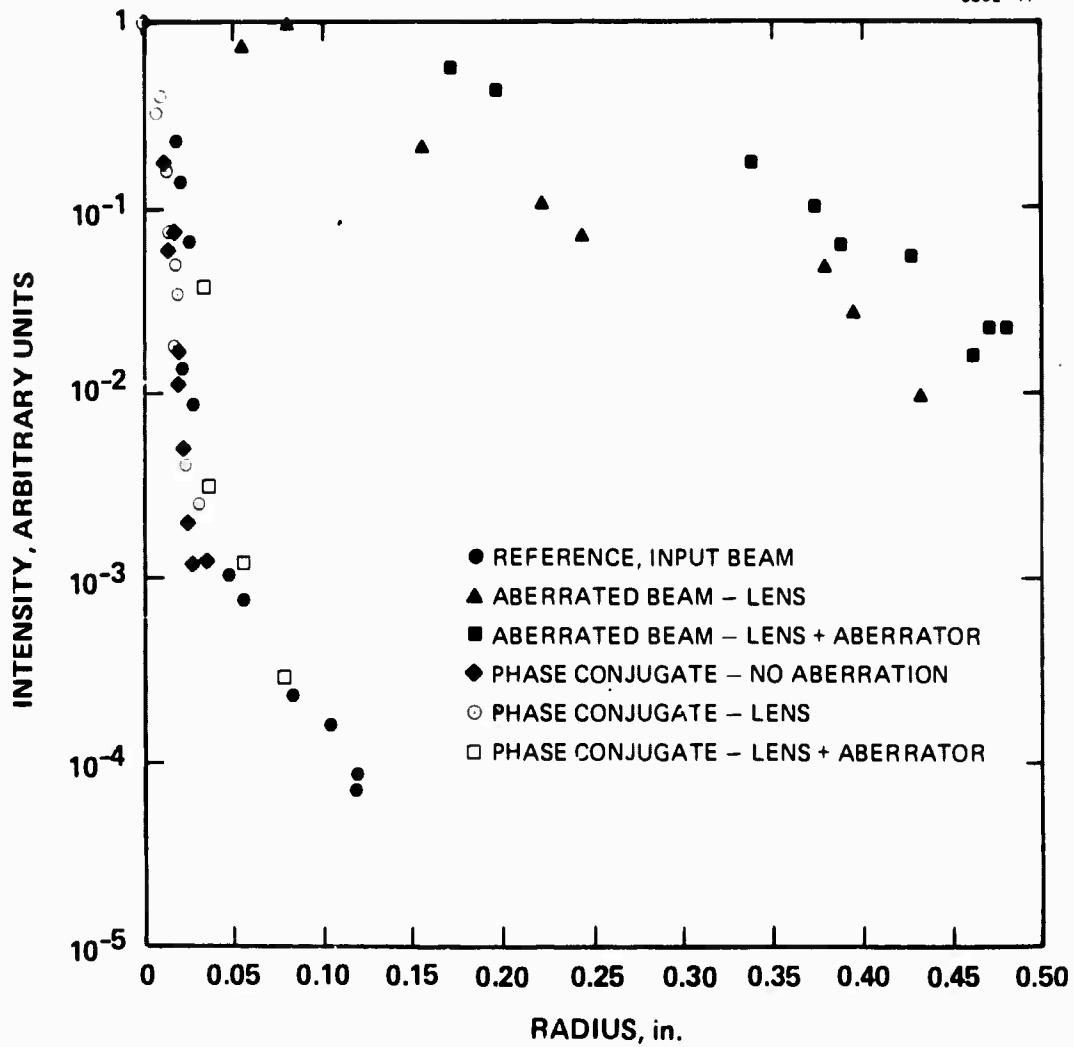
Figure 5-16. Intensity profiles using RG 695 filter glass as nonlinear medium at $\lambda = 6943\text{Å}$.
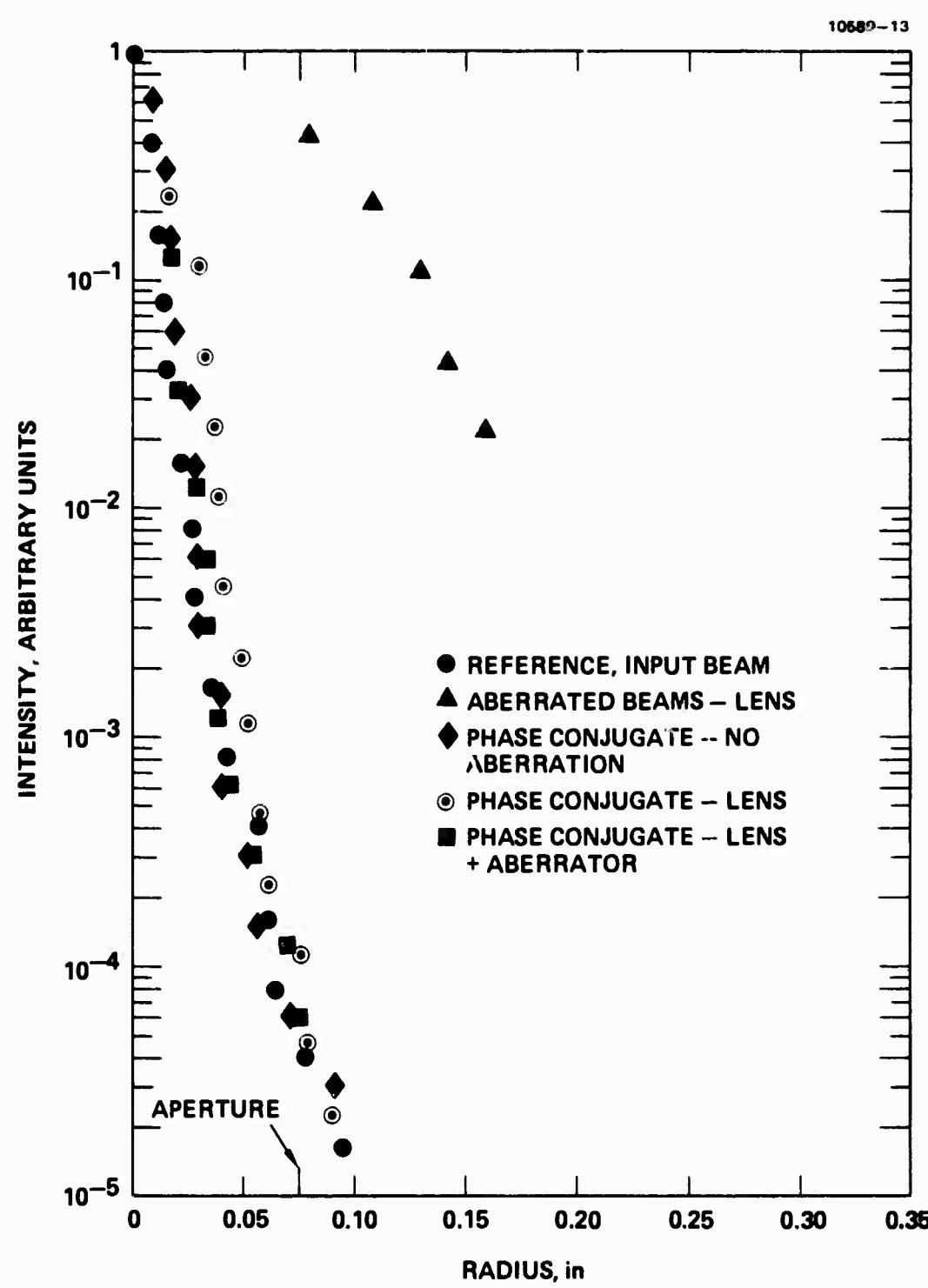
Figure 5-17. Intensity profiles using R6G at $\lambda=5320\mathring{A}$ reflectivity = 0.5%.
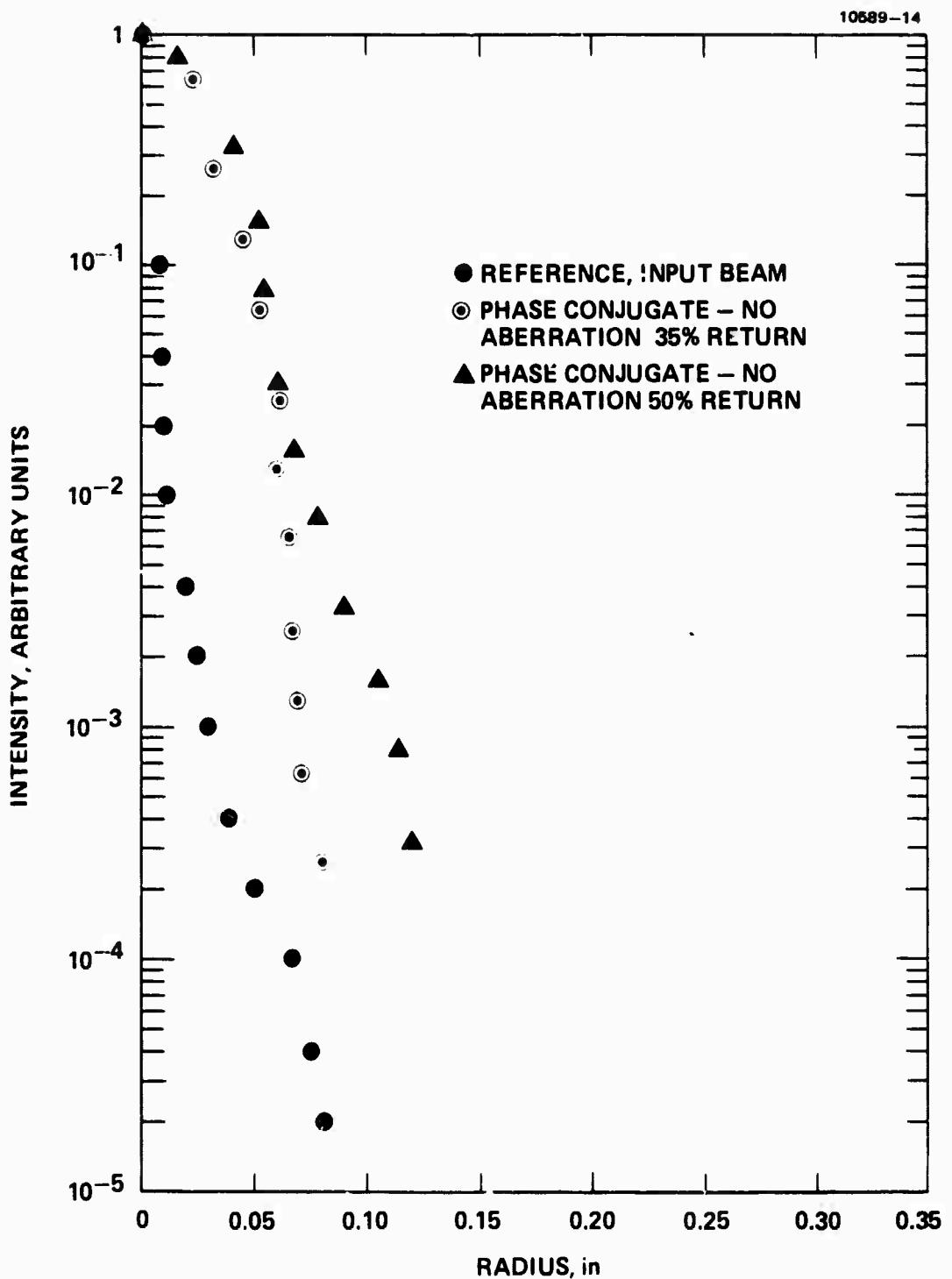
Figure 5-18. Intensity profiles for R6G at $\lambda=5320\text{Å}$, reflectivity = 35% and 50%.

Figure 5-19 for efficiencies of 0.5% and 35%. In Figure 5-20 we show the growth of the spot size with reflectivity. From this illustration we can estimate that the DFWM beam is aberrated to about 2.5X diffraction limited at 100% efficiency (the 0.5% reflectivity point is diffraction limited). In spite of this increase in spot size, however, the aberration correction is still reasonable, as seen from Figure 5-21 where the intensity profiles for the aberrated conditions at 35% reflectivity are given.

5.4 POLARIZATION SELECTION

The purpose of these experiments was to examine the contribution of each term in the polarization expression (Chapter 2, Equation 2-18) to the DFWM conjugate signal observed in R6G and the semiconductor glasses. Thus, we will measure the relative efficiencies of the three key terms in (2-18): the A term-forward pump-probe grating; the B term-backward pump-probe grating; and the C term-coherent contribution. The experimental technique makes use of the cross polarization concept shown in Figure 2-4. The experimental configuration used for these experiments is shown in Figure 5-22. The polarization rotation is accomplished by using a $\lambda/4$ plate-polarizer combination put in each beam as appropriate.

The experiments were performed in the intensity regime where saturable absorption was responsible for the DFWM signal in R6G. This is necessary in order to compare the results with the theory of Chapter 2. We first demonstrated polarization rotation by leaving E_f and E_p S-polarized, and rotating E_b to P-polarization. Using a polarization analyzer in front of our signal detector, we dtermined that the signal was P-polarized with no measurable S component. The experiment was repeated setting E_b and E_p to S-polarization, and E_f to P-polarization. Again, the signal was P-polarized with no measurable S component. If all beams were S-polarized, the signal was also S-polarized with no measurable P component (all data discussed in sections 5-2 and 5-3 above were taken with S-polarization). Finally, E_p was rotated to P-polarization, while leaving E_b and E_f as S-polarized. In
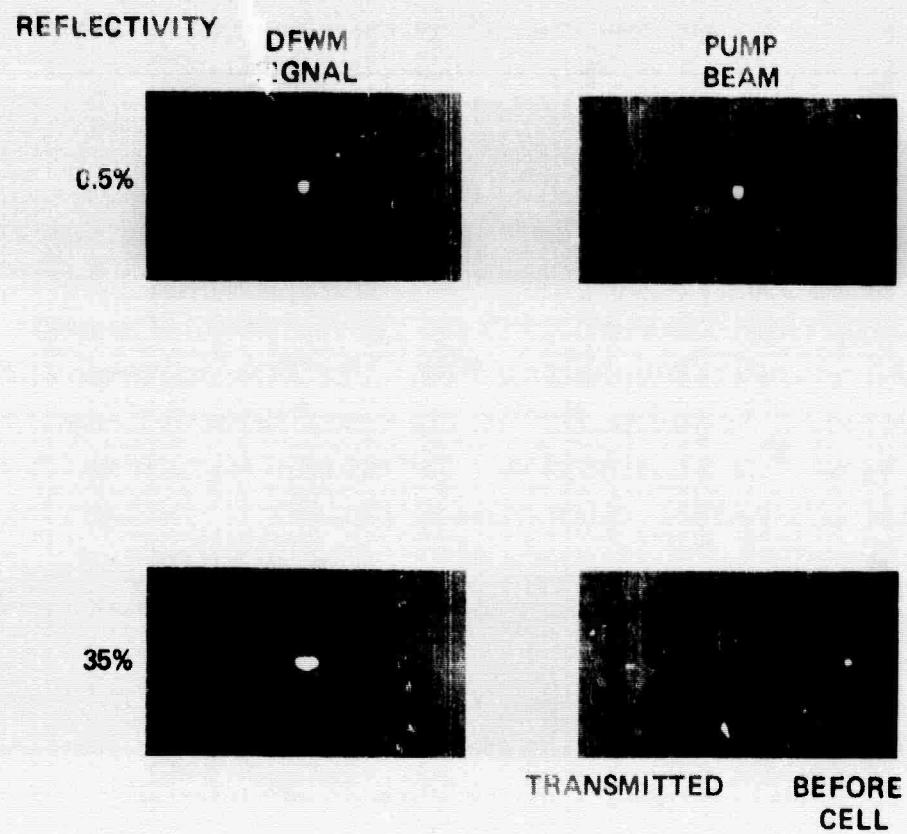
Figure 5-19. Photographs of transmitted pump and DFWM signal at 0.5% and 35% efficiency.
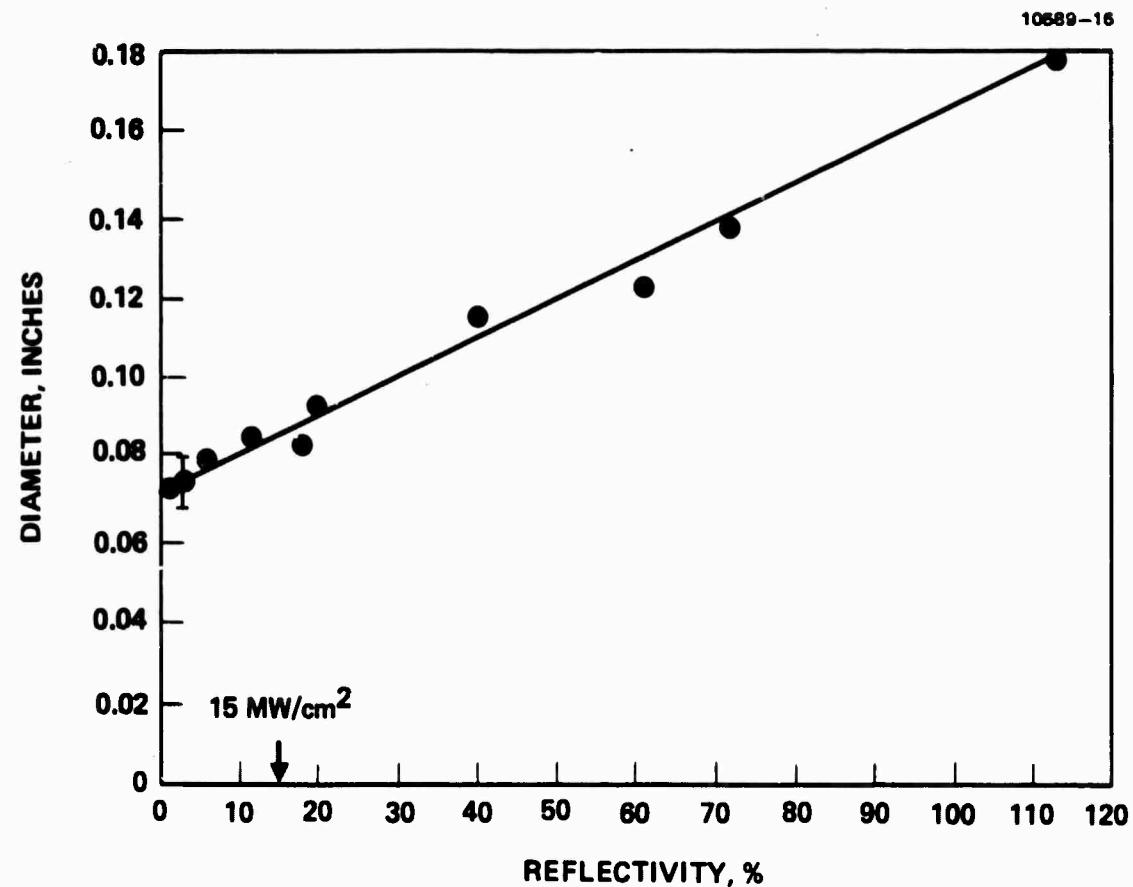
Figure 5-20. Diameter at a fixed intensity on film in far-field versus
phase conjugate reflectivity.
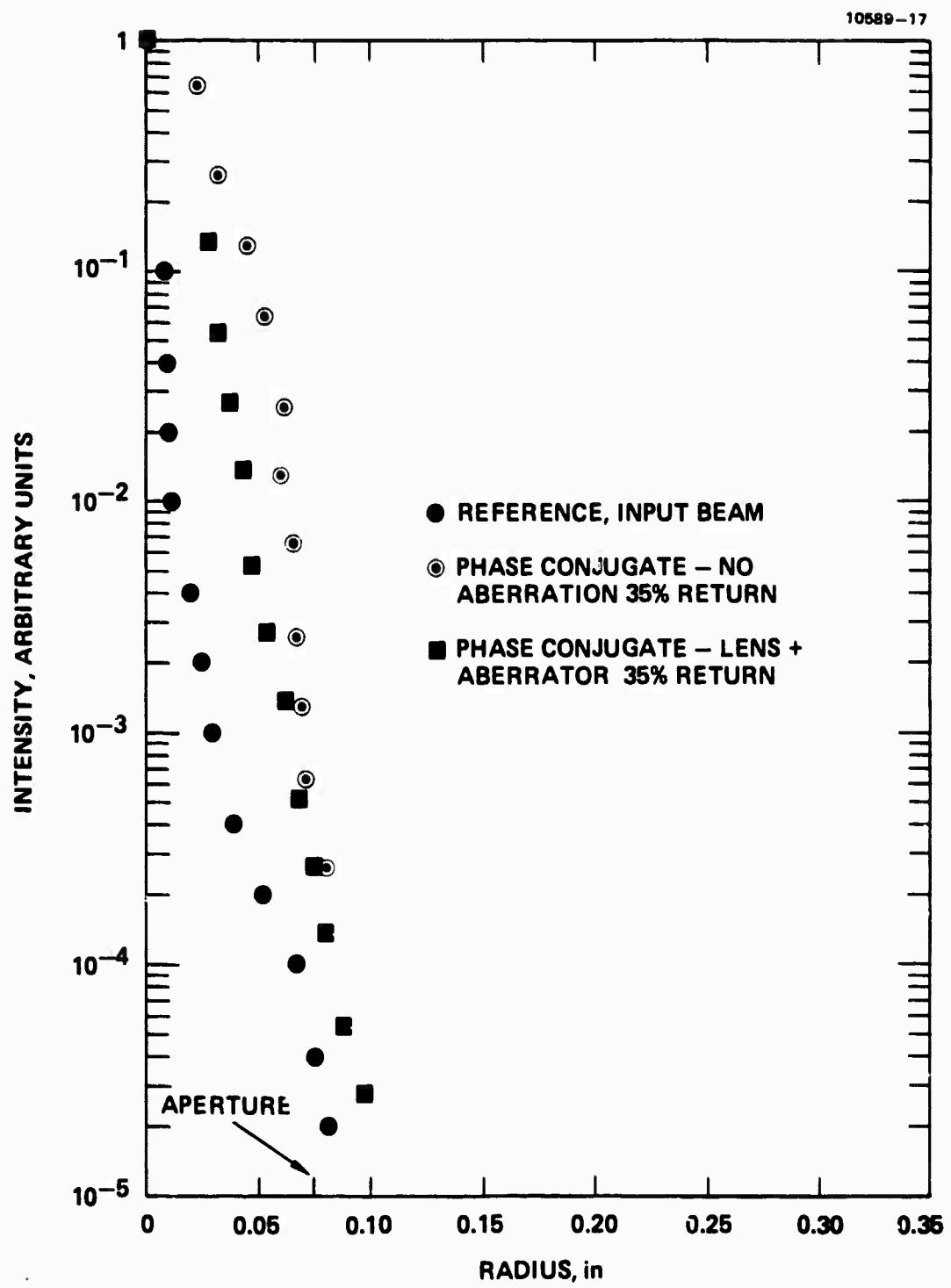
Figure 5-21.   Intensity profiles for R6G at $\lambda = 5320\overset{\circ}{A}$ reflectivity = 35%.
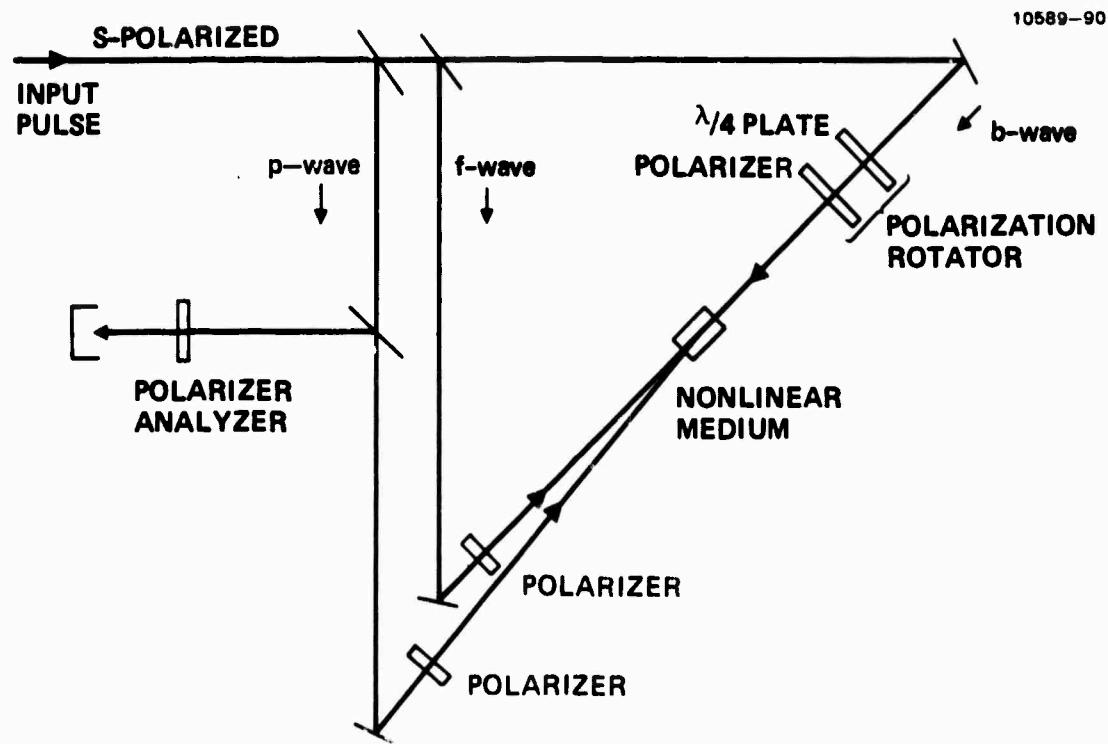
Figure 5-22. Optical configuration used for polarization rotation experiments (here E_b is P-polarized, E_p, E_f are S-polarized).

this case, no measurable signal was observed for either S- or P-polarization. The results of these experiments are summarized in Figure 5-23. The signal magnitudes observed are also shown in the Figure. To within the experimental error, the A and B terms are equal for R6G. This is easily understandable by noting that for R6G, a characteristic mean-free path for collisions is much shorter than either grating spacing, which means that thermal motion effects are dominated by diffusion. ($\lambda_{mfp} \sim 1\text{Å}$ $D_{fp} \sim 20,000\text{Å}$, $D_{bp} \sim 2000\text{A}$). The time for diffusion is $T_D = \lambda^2/D$, which leads to $T_D/T_1 >> 1$ for both gratings. Hence, from Figure 2-5 we expect no degradation in the signal from motion effects. And thus, both gratings would result in the generation of comparable signals.

Further experiments were performed in the high intensity regime (R>10%) to see the polarization behavior when the thermal grating dominates. In this case, again there was no contribution from the C term. However, with both gratings giving a signal magnitude of 2 we find that A = 0.36 and B $\geqslant$ 0.20. We see that the large angle grating gives a smaller contribution to the signal than the small angle grating. This is clearly shown in Figure 5-24 where the pulse shape is given for the signal with all beams copolarized, and for the small angle, and large angle gratings. It is not clear at this time why the signals do not add up to the total observed except that some type of coherent addition might be occurring, or that it is necessary for E_f and E_b to interfere. One would not expect the latter, since the signal is not Bragg phase-matched along the probe direction.

Experiments were also performed using the Corning #3-68 filter glass. We found that in this case the signal due to the large-angle grating is comparable, and about 50% larger than the signal due to the small angle grating. This is because most of the semiconductor crystallites are generally much smaller (100Å-1000Å) than even the $\sim$1030Å period of the small-period grating; thus, unlike the situation in bulk semiconductors, the free carrier plasma is effectively confined to these isolated pockets, and plasma diffusion does not reduce the diffraction efficiency of the small-period grating. In our experiments, with a $\sim 2^\circ$ external angle between the forward pump and the probe beams, the small and large gratings have periods of $\sim$1030Å and 3 µm, respectively.

POLARIZATION CONDITION		DETECTOR POLARIZER SETTING	SIGNAL MAGNITUDE	
f—wave →S—pol→ ‖ ←S—pol b—wave p—wave /S—pol/ s—wave /S—pol/		S—pol P—pol	(A + B) (0.01)	2 ± 0.1 NOISE
f—wave →S—pol→ ‖ ←P—pol b—wave p—wave /S—pol/ s—wave /P—pol/		S—pol P—pol	(0.01) A	NOISE 1 ± 0.2
f—wave →P—pol→ ‖ ←S—pol b—wave p—wave /S—pol/ s—wave /P—pol/		S—pol P—pol	(0.01) B	NOISE 0.7 ± 0.3
f—wave →S—pol→ ‖ ←S—pol b—wave /P—pol/ NO SIGNAL		S—pol P—pol	C (0.01) (0.01)	NOISE NOISE
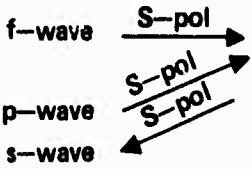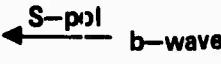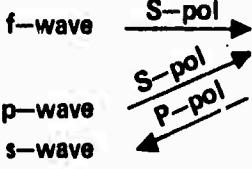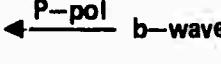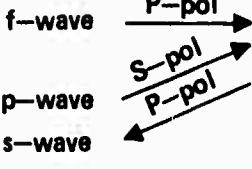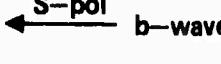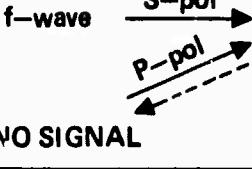
Figure 5-23. Polarization selection experiments in R6G in the low intensity regime.
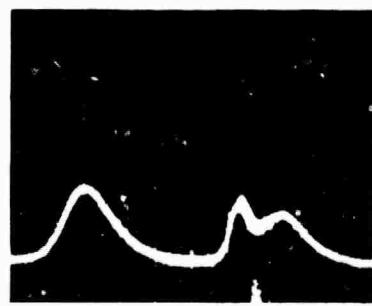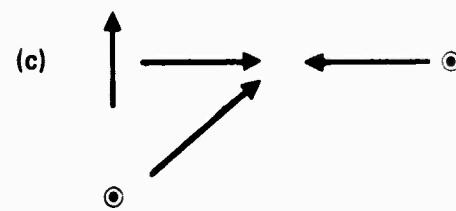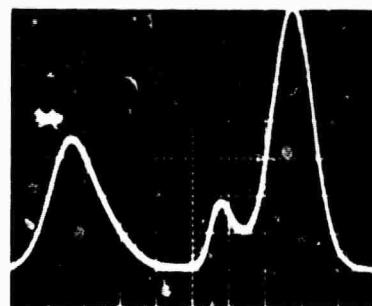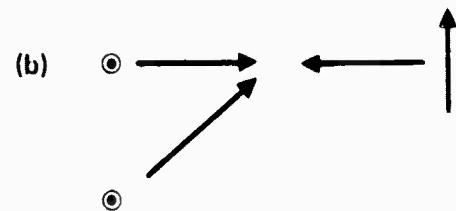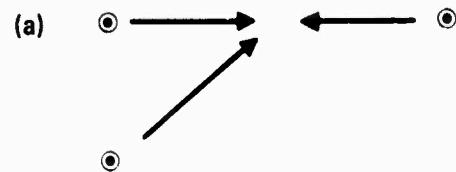
Figure 5-24. Crossed polarized sequence in R6G (a) both,
(b) small angle, (c) large angle, 2.9 nsec/div.

5.5 NON-COLLINEAR GEOMETRY EXPERIMENTS

These experiments fall into two categories - (1) in-the-plane experiments, where phase mismatch occurs leading to signal reduction, and (2) out-of-the-plane experiments where phase matching is maintained and no signal reduction is expected. The results from these experiments have already been discussed in Chapter 4. Here we want to indicate the various configurations used for these experiments.

Figure 5-25 shows the in-the-plane geometry. The angle β is varied (where β is measured from the counterpropagating direction) and the angle θ, between the input probe and resulting phase conjugate signal is then measured. In addition, the amplitude of the resulting conjugate signal is also determined. The results of this experiment are shown in Figure 4-8 where we see excellent agreement between the theory developed and these experimental measurements.

We have experimentally verified, in one case, the generalized-offset concept using the 3-D geometry discussed in Section 4-5. In particular, we performed the degenerate non-coplanar experiment pictured in Figure 4-27a. For ease of explanation of the experiment, a two-dimensional layout of the apparatus is shown in Figure 5-26. For the experiment performed, the backward pump and forward pump were offset (by α_{fb}) 4.6° from each other. The probe was then brought in at 3° to the plane of the pumps. The four-wave signal that was observed occurred exactly (within the experimental error) at the angle expected from above, i.e., at $\alpha_{ps} = \alpha_{fb}$. More importantly, the magnitude of the observed signal was within 30% of that measured in the standard, coplanar on-offset geometry where $\alpha_{fb} = \alpha_{ps} = 0$. We have also performed the experiment in the plane with a $\beta = 4.6^\circ$ offset in the pumps, and found the magnitude to drop to $\sim 1\%$ of the counterpropagating case using the configuration of Figure 5-25. Thus we have verified the operation of one useful phase-match offset geometry.
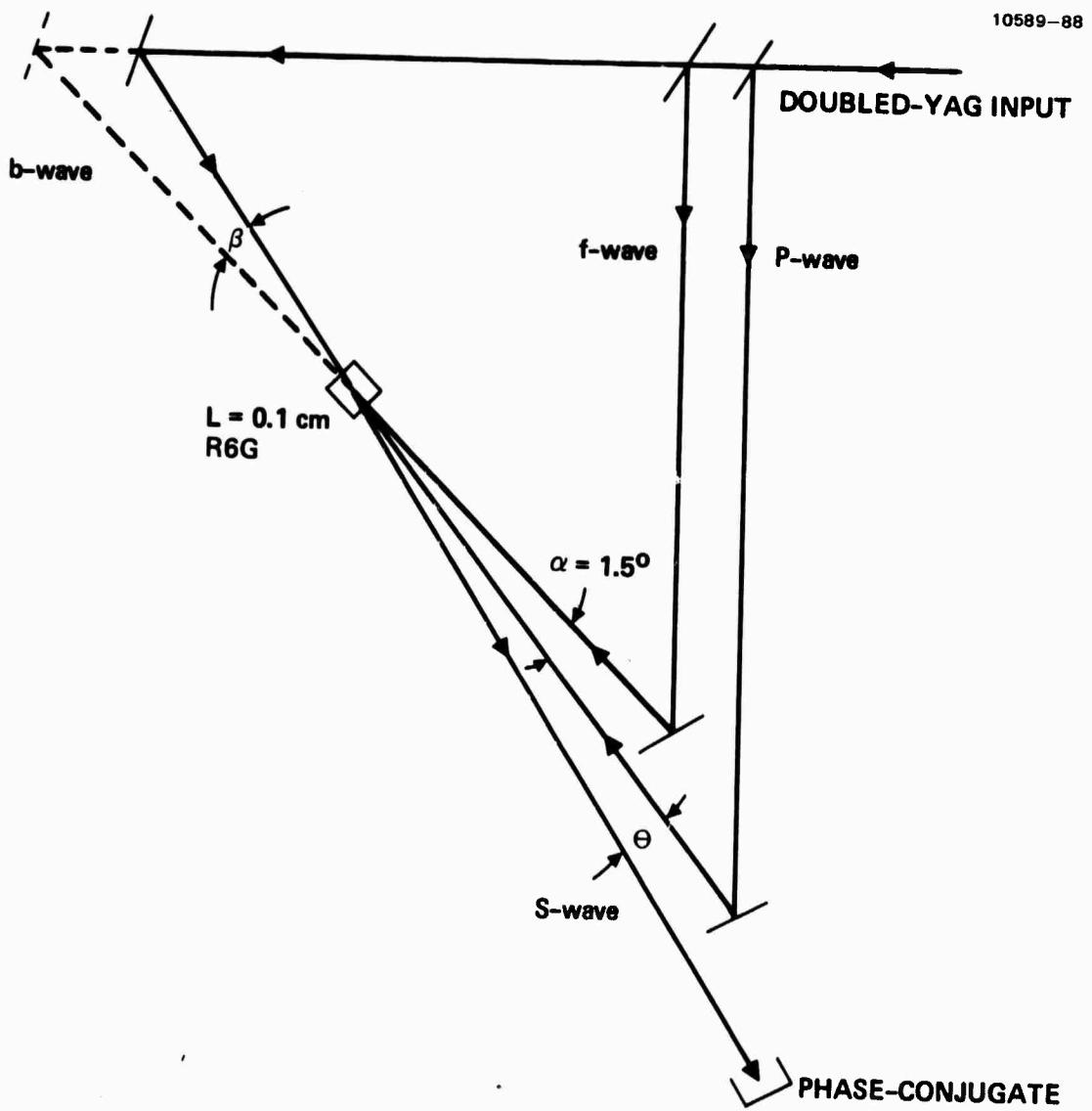
Figure 5-25.   In-the-plane noncollinear pump geometry configuration.
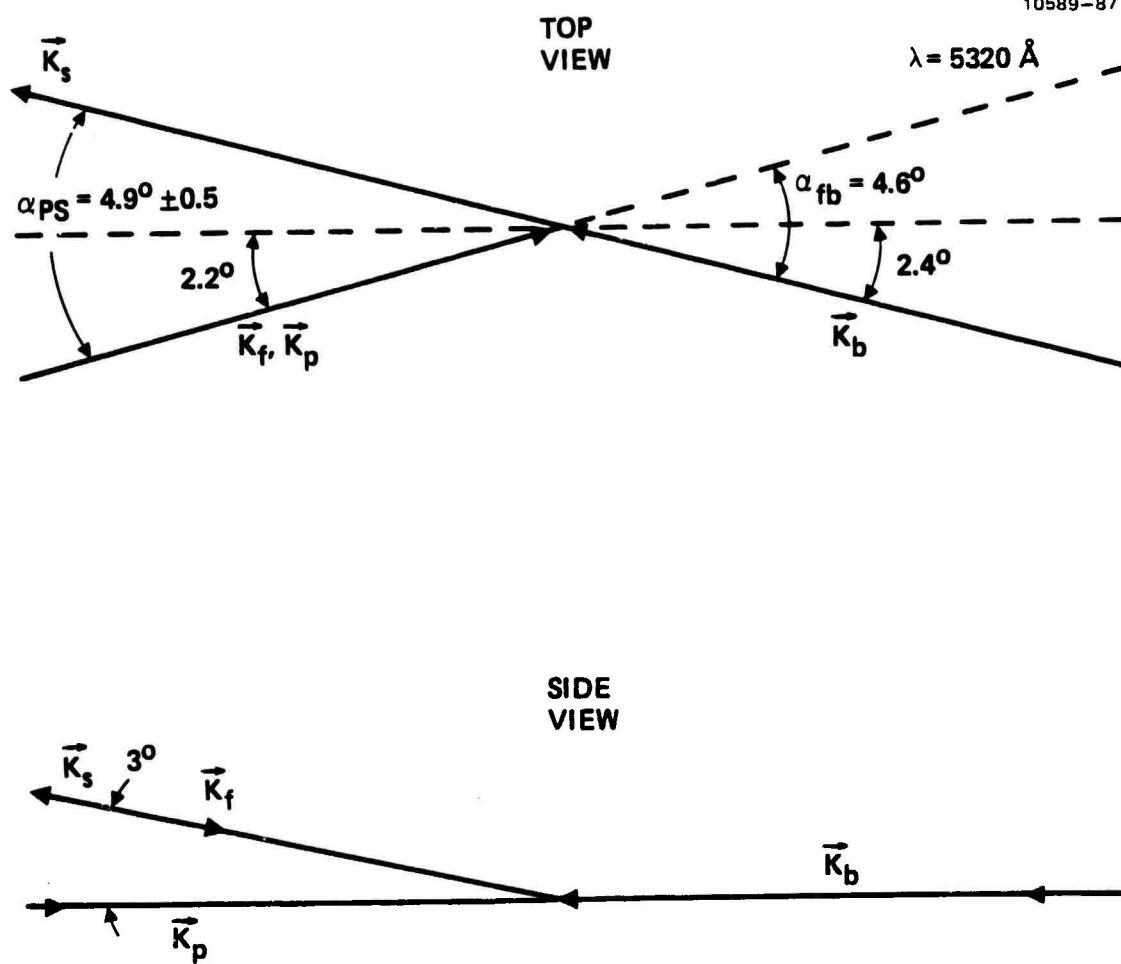
Figure 5-26. Out of the plane experimental arrangement.

5.6 NEARLY-DEGENERATE FOUR-WAVE MIXING

(1) Two-Wavelength Experiments

For these experiments two wavelengths were employed for all beams in the four-wave setup. That is, each pump and the probe had two frequencies present simultaneously. The doubled-Yag laser (λ_1 = 5320A) and the dye laser produced the two frequencies (see Figure 5-1). The two frequencies entered the four-wave mixing apparatus as shown in Figure 5-27. R6G was used as the nonlinear media. The signal was detected using detector 1, which recorded both wavelengths simulataneously, and detector 2, which recorded either λ_1 or λ_2, depending upon where the spectrometer was set. The experiment consisted of the following sequence:

- both λ_1 = 5320 and λ_2 = 5200 present in the R6G simultaneously
- λ_1 only, λ_2 blocked
- λ_2 only, λ_1 blocked

The relative signals obtained in each case are shown in Figure 5-28. From these results we see that each wavelength acts independently of the other. The λ_1 and λ_2 wavelengths employed were sufficiently separated so that we would not anticipate seeing the third order intermodulation products (see bottom of Figure 4-25) discussed in Section 4.4.3. Measurements at these wavelengths gave inconclusive results. Conjugation data was not taken, but similar type experiments performed in the IR at HRL showed no crosstalk or degradation in conjugation.

(2) Pump-Probe Coherence

For these experiments the pump beams were obtained from the doubled-Yag laser, while the probe beam was obtained from the dye laser (see Figure 5-29). First, experiments were performed using the 5320Å probe (see dashed line) to establish baseline performance levels. This path was then blocked and the probe was obtained from the dye laser only. The wavelength of the dye laser was adjusted in frequency until a signal was observed. A signal was obtained only when the probe frequency was tuned adjacent to the pump frequency. We note from 4.4.3 that this frequency difference can be no greater than
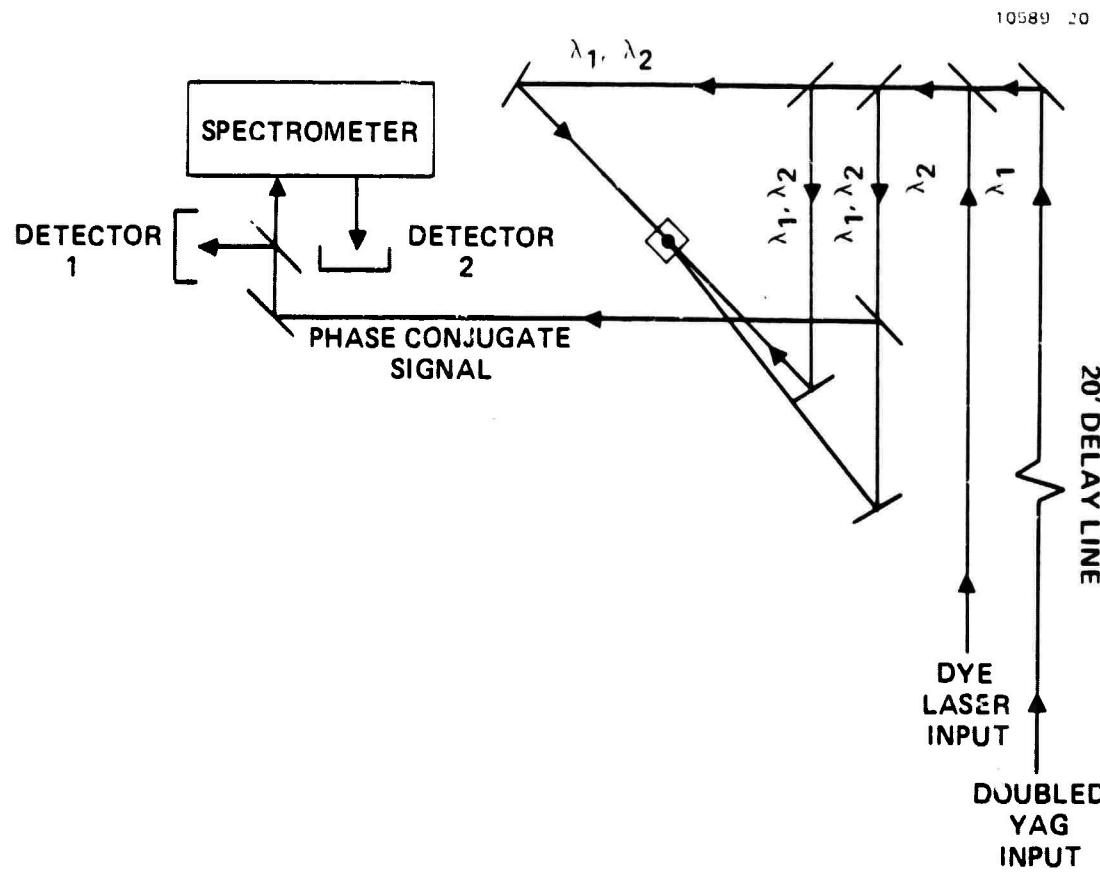
Figure 5-27.   Two wavelength four-wave mixing set-up.

WAVELENGTH, Å		RELATIVE SIGNAL		
		DETECTOR 1	DETECTOR 2 SET AT	
			5320	5200
$\lambda_1 + \lambda_2$ 5320 + 5200		2	1	1
λ_1 5320		1	1	0
λ_2 5200		1	0	1

Figure 5-28.   Two wavelength experiments in R6G.

10689—22
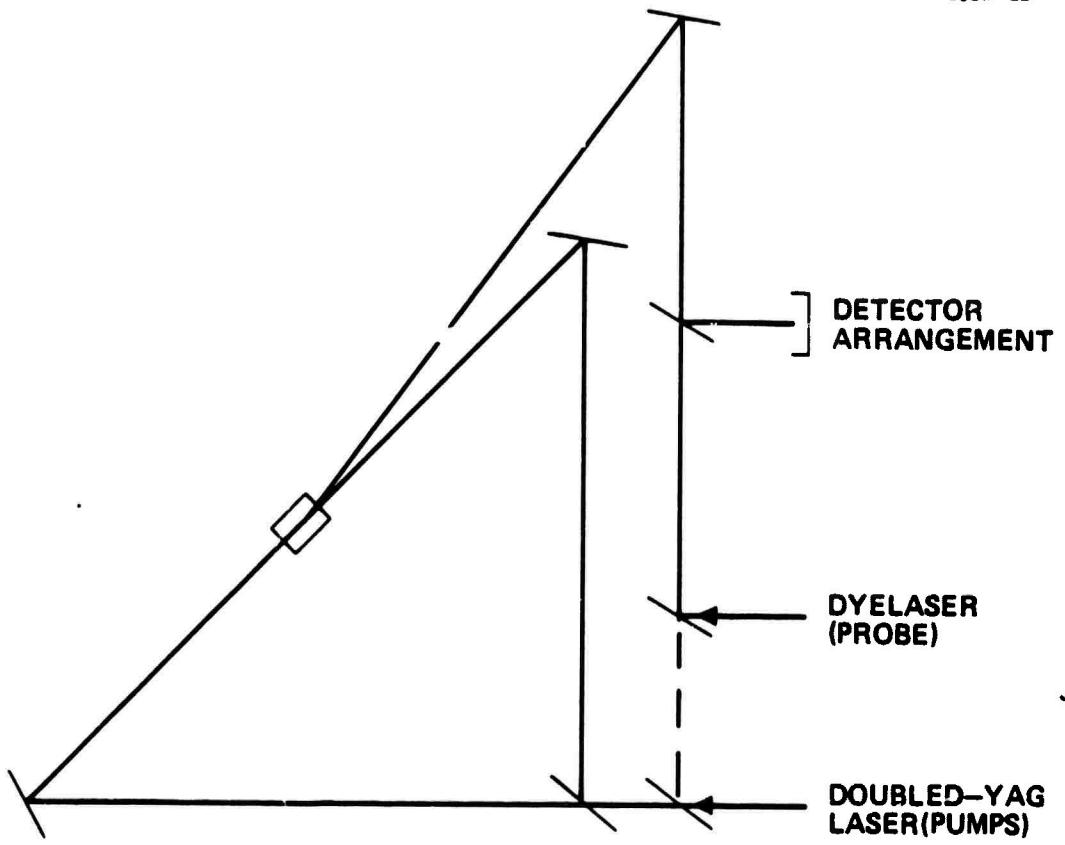
Figure 5-29. Pump/probe coherence experimental set-up.

$\Delta\nu = \nu_{pump} - \nu_{probe} = 1/T_1$. For R6G, this corresponds to $\Delta\nu \approx 200$ MHz, which is less than the mode spacing for the Yag laser itself. To establish this frequency coincidence a combination of a Fabry-Perot interferometer and a one-half meter Ebert monochromator was used. Light from the doubled output of a Nd:YAG laser and from the dye laser also operating at 5320Å was simultaneously passed into a Hilger Fabry-Perot interferometer equipped with a 15.07 mm spacer and aluminum coated flats. The resulting ring pattern was then focused onto the entrance slit of the one-half meter monochromator. At the output plane of the monochromator, a microscope viewed the image, which for a single input wavelength was a pattern defined by the intersection of the entrance slit with a series of Fabry-Perot rings (see Figure 5-30). For two wavelengths differing in wavelength by an amount larger than the spectrometer resolution capability, two independent patterns are produced (see in Figure 5-23b). By adjusting one of the laser wavelengths, the slit profiles can first be made to overlap, and finally also the circle patterns when $\lambda_1 = \lambda_2$. The free spectral range of the Fabry-Perot interferometer was about 10 GHz; and for a finesse of 50, it was possible to establish the laser frequencies to be equal within about 200 MHz uncertainty, which is required for R6G. The key point that comes from these experiments is that DFWM signals can be obtained using separate lasers for pump and probe, but that careful control of the frequency difference must be maintained. The absolute value of the signal obtained in this case varied considerably, since the Yag laser mode could drift (the Yag laser, while running single mode, can drift modes, since it is not locked to a stable source). However, the signal level approached the value obtained for single laser pump/probe operation on occasions. Thus, if a stable single longitudinal mode source was used, the signal strength would be expected to remain constant at the one frequency level.

5.7 MATERIALS CONSIDERATIONS FOR WIDE WAVELENGTH RANGE OPERATION IN THE VISIBLE AND NEAR U.V.

The selection of a material for use as the nonlinear medium for degenerate four wave mixing (DFWM) capable of operating over a wide range of frequencies

10 GHz

λ_1

a

$\lambda_1 \neq \lambda_2$

b

$\lambda_1 \simeq \lambda_2$

c
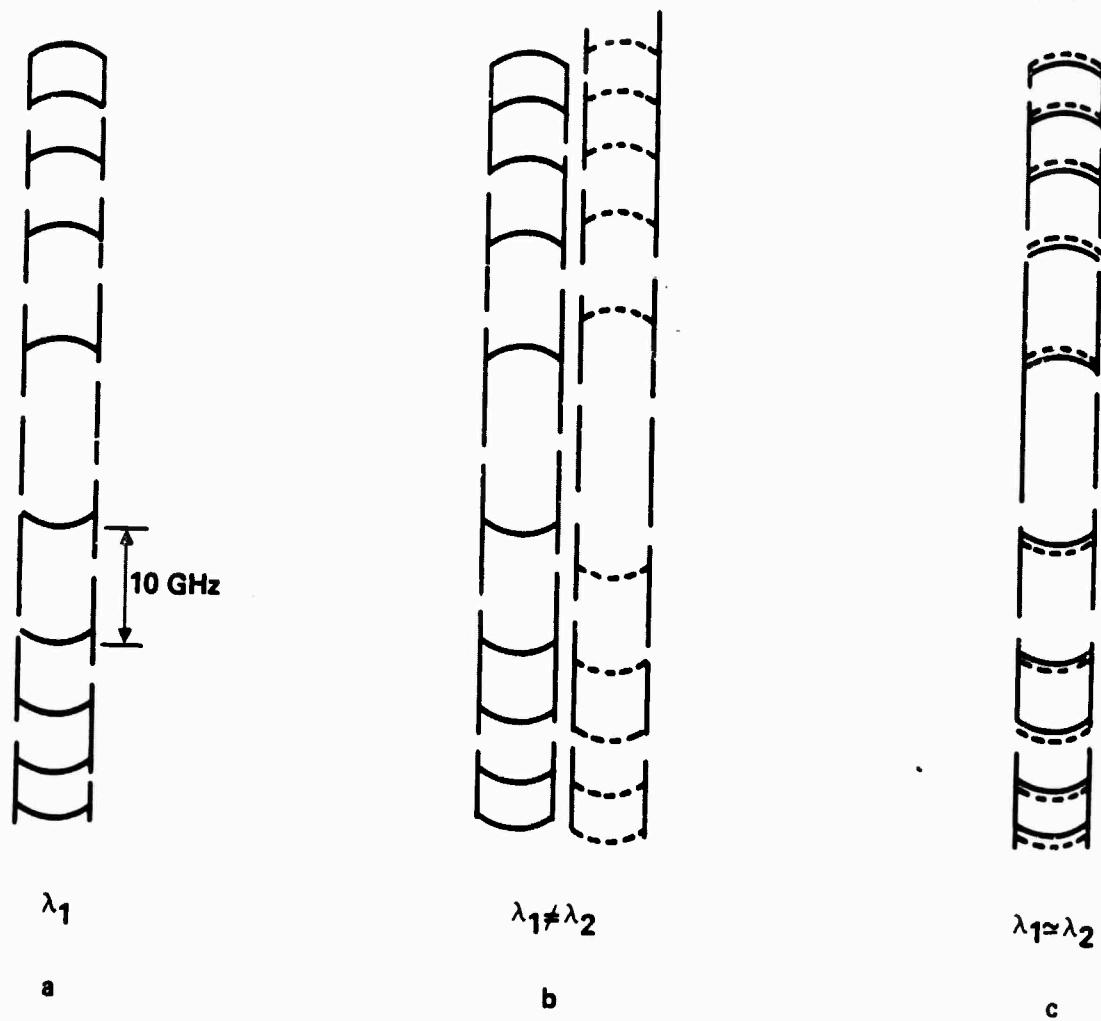
Figure 30.   Fabry-Perot ring pattern at spectrometer exit slit.

in the visible region of the spectrum can be made from two spectral types. Materials such as organic dyes and doped glasses provide absorption bands which are essentially continuous over selectable regions, which can be several hundred Angstroms wide. A second category of spectral profile that can be employed is a very dense collection of individual absorption features separated by more than the individual natural linewidth. Such latter materials have been employed to date mostly in the infrared where DFWM has been obtained on V-R transitions in SF_6 and in NH_3. This latter type has the advantage of resonance enhancement of the nonlinear susceptibility, if the operating wavelength is appropriately positioned near a particular absorption feature. For UV-visible operation we require electronic transitions, and we find the required line structure and density resulting fron not only vibration-rotation structure, but possibly additional fine structure due to higher order interactions involving nuclear properties of the constituent atoms.

A candidate for visible operation is the I_2 molecule; a preliminary observation on this system has been made in this program using pulsed laser excitation. One report has appeared in the literature (5-25) of CW DFWM in I_2 using an Argon ion laser. Iodine has an extremely dense spectral structure, exhibiting strong absorption from below 4500Å to beyond 6500Å, with individual rotational lines closer than about 0.1Å. This structure is further complicated by hyperfine interactions which split a given rotational line into 15 or 21 components distributed over a range of approximately 1 GHz. Using conventional spectroscopic methods, these components are not completely resolved within the Doppler width of about 470 Mhz at room temperature. But they can be isolated using DFWM because of the velocity selective nature of the process.

By this is meant that for a Maxwellian distribution of atomic or molecular velocities in our gaseous medium, only a limited number of atoms or molecules having velocities near zero can simultaneously interact with both pump waves and the incident probe wave. Any otner velocity group will be Doppler shifted with respect to the forward pump or probe, requiring a different frequency for resonance to take place. That same velocity group

will be Doppler shifted in the other direction for the backward pump, and consequently will not be in resonance simultaneously, except for zero velocity atoms or molecules. The interaction can take place over a frequency range on the order of the power-broadened homogeneous linewidth centered at the transition frequency ν_o that corresponds to an atom or molecule at rest. This linewidth is typically one to two orders of magnitude smaller than the Doppler width.

The origin of the hyperfine structure in I_2 is somewhat more complex than for atomic sodium, which has been used at HRL principally for CW DFWM experiments. Kroll[5-26] has explained the observed hyperfine structure in the visible iodine absorption spectrum as a combination of a nuclear electric quadrupole interaction in both the ground $X\ ^1\Sigma_g^+$ state, and in the excited $B\ ^3\pi_{ou}^+$ electronic state, and a magnetic hyperfine interaction in the B state. As a function of B state excitation, Levenson[5-27] has shown that variations occur in the difference between electric field gradients in the B and X states associated with the nuclear electric quadrupole term in the Hamiltonian, and has also demonstrated a variation in the spin rotation coupling constant, defining the magnetic hyperfine interaction magnitude. The net result is a distribution of hyperfine lines over ~ 1 GHz which is quite unique for a given rotational line. Line shifts due to both tensor and scalar spin-spin interactions, and a nuclear magnetic octupole have been reported;[5-28] but these are on the order of a few kilohertz and would probably have little consequence for any real applications.

A detailed analysis of the $I_2\ B \leftrightarrow X$ spectrum has been made[5-29] of sufficient accuracy to permit the computation of rotational line positions to approximately 10^{-2}Å, neglecting hyperfine structure. Data also exists to permit a computation of the small signal absorption coefficient:

$$\alpha = \frac{2\pi^2}{3h\varepsilon_o\lambda}\ N_{v''J''}\ |R_e|^2\ q_{v'v''}\ \frac{S_{J'J''}}{(2J''+1)}\ g(\nu)\ ,$$

where

$N_{v''j''}$ is the number of molecules in level v"J",

R_e is the electronic contribution to the dipole moment,
very close to one Debye for I_2 B-X,

$S_{J'J''}$ is the Hönl-London rotational line strength[5-30],
$S_{J'J''} \sim J''/4$ for large J",

$q_{v'v''}$ is the Franck-Condon factor[5-31] for which
tabulations are available,

and $g(\nu)$ is the normalized lineshape function.

Line broadening in I_2 is complex, arising from radiative decay processes, predissociation of the B $^3\pi_{0u}^+$ state via a nearby repulsive $^1\pi_u$ state, and from pressure dependent collision mechanisms. The zero pressure homogeneous linewidths depend upon the exact details of the predissociation, which is dependent both on v' and J'. Typical values are on the order of 100 kHz. For conditions likely to be appropriate for DFWM applications, the homogeneous linewidth will be largely determined by collision broadening, which is on the order of 3.5 Mhz/Torr. At room temperature 22°C, the vapor pressure of iodine is 0.24 Torr, leading to a contribution to the homogeneous width of about 840 kHz, and a resulting upper state lifetime of ~170 nsec. Room temperature saturation parameter determinations are on the order of 10 Watts/cm^2, and are in reasonable agreement with theoretical estimates[5-32]. In designing an experimental cell, lengths of 1 to 10 cm and temperatures of 20 - 50°C will provide adequate absorption ($\alpha L>1$) for the spectral range of the B - X spectral system.

A number of questions remain to be answered in connection with the use of I_2 molecules for DFWM purposes. Specifically, the exact dependence of the saturation parameter on the temperature through the density variation must be established. The effects of optical pumping need to be examined in the light of the complex hyperfine structure and possible V-V relaxation bottlenecks in the ground electronic state. Optical pumping is the process by which molecules are removed from the lower energy level being accessed by the incident laser

beams, and transferred via spontaneous emission pathways from the upper level
to energy levels near the lower level being excited, but not in resonance with,
the incident frequency.
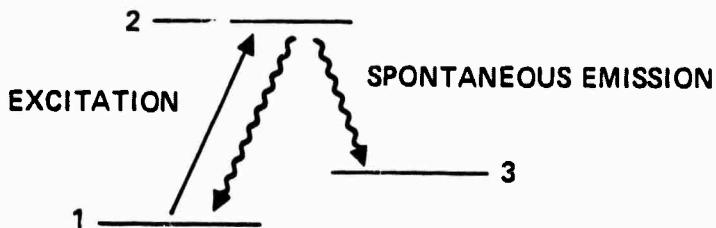
In effect, molecules are transferred from level 1 to level 3, and so long as
no process exists to move them from 3 back to 1 at a rate comparable to the
excitation rate, the consequence is to empty level 1 and stop all interaction
with the incident waves. The splitting of energy levels 1 and 3 can arise
from hyperfine structure, or on a larger scale, simply from the quantized
vibrational or rotational energies of the lower electronic state. Nevertheless,
the strong absorption and broad spectral coverage suggest molecular I_2 could
be an attractive candidate for DFWM purposes.

There are a number of other convenient gas phase materials that have
potential for wide spectral coverage as the active medium of a four-wave
mixer. In general, the spectroscopy and related photochemical kinetics are
not as well established for these systems as for iodine, and substantial work
is required to define parameters such as line positions, natural and collision
determined linewidths, saturation intensities, and hyperfine structure, as
well as unequivocal identification of the relevant electronic states. For
operation in the visible and near ultraviolet, several candidates are available
for investigation. We will briefly examine NO_2, glyoxal, and other halogens.

Figure 5-31 shows data by Hsu, Mants and Zare[5-33] of the absorbance of
NO_2 from 3600Å to 6800Å, when individual line features are not resolved. The
maximum absorption coefficient occurs near 4100Å, and has a value of about
$0.02 \ cm^{-1}Torr^{-1}$. With a path length of several cm. and a cell fill pressure
of several tens of Torr, sizable absorptions can be obtained over the entire
spectral range.
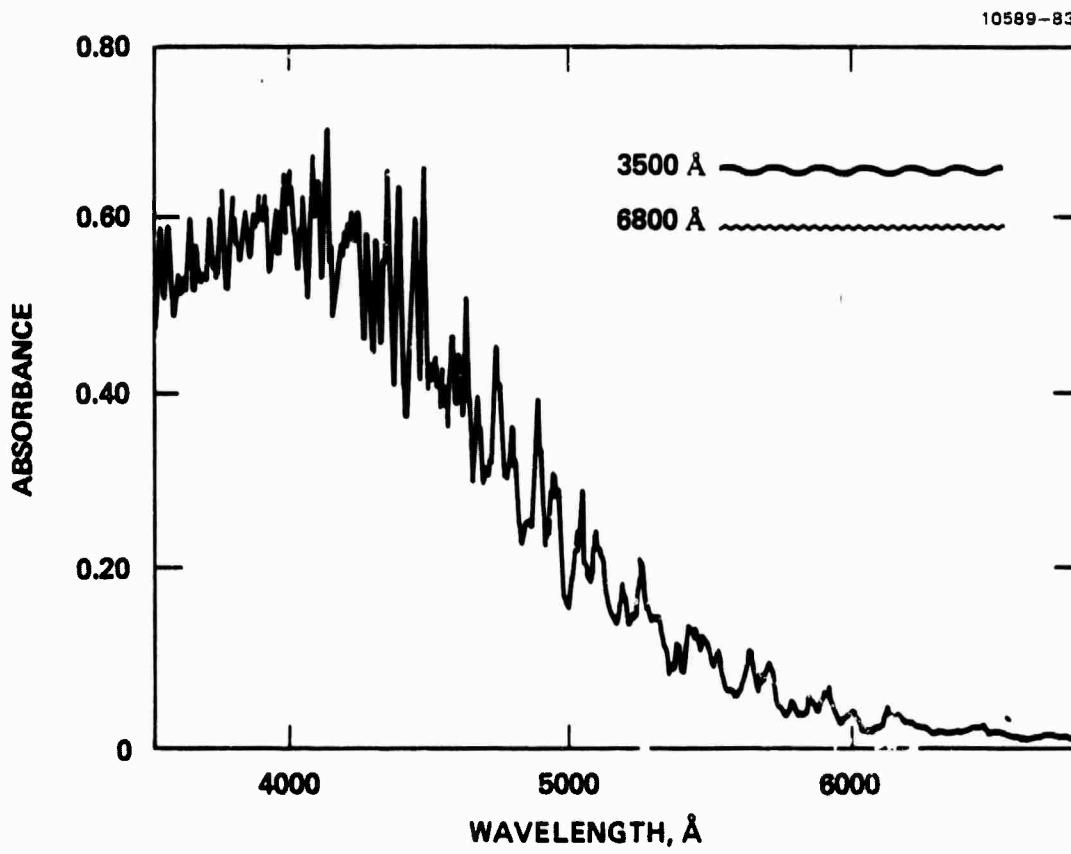
Figure 5-31. Spectrophotometer trace[2] of the NO_2 3600Å-6800Å region (9.70 torr, 7.5-cm path length, room temperature). Pen drift at 3500Å and at 6800Å is shown.

The understanding of the spectroscopy of NO_2 is far from complete. There are believed to be four electronic states of the molecule that may participate in the absorption process and these interact with each other directly or indirectly in complex ways. This interaction not only gives rise to spectral structure much more complicated than that expected from a simple symmetric top, but also leads to a large variation in radiative lifetimes which in some regions are at least two orders of magnitude longer than the lifetime inferred from the integrated absorption coefficients.[5-34] Lifetime measurements range from 0.5 μsec[5-35] to 260 μsec[5-36] and can be associated with nonexponential decay processes.

The predominant isotopic form of the molecule is $^{14}N\,^{16}O_2$, in which the ^{14}N nucleus has a nuclear spin 1, and ^{16}O a nuclear spin 0. Coupling of the total nuclear spin I = 1 with the other angular momenta causes the appearance of hyperfine structure, in this instance a triplet feature, with splittings of 10^{-3} to 10^{-4} cm^{-1}. Only a very limited amount of work on this structure has been reported,[5-37] but the Doppler-free nature of DFWM means that such spectral features will be evidenced in DFWM return signals.

At the present time, there is inadequate data to specify the saturation intensity expected at any given wavelength. As with the other materials being examined, this and the other important parameters await experimental determination.

A further possible gaseous candidate for DFWM applications, which possesses broadband absorption structure between 5000Å and 2300Å, is the molecule glyoxal $C_2H_2O_2$.[5-38,39] At 150°C, an extinction coefficient $\alpha = 3 \times 10^{-3}$ cm^{-1} $Torr^{-1}$ has been reported[5-39] near 3130Å. The ^1A_u-^1A_g band exhibits well developed line structure[5-40] between 3900Å and 5400Å, and this system in glyoxal and its mono- and dideuterated derivatives has been the most thoroughly studied.[5-41,42] Extensive rotational analysis has been carried out, particularly near 4550Å where absorption features are available every few hundredths of an Angstrom. Very limited kinetic studies are available for this molecule with a collision-free upper state lifetime of 2.2 μsec having been reported.[5-43,44] No data on hyperfine structure or saturation intensities are available for detailed evaluation of expected DFWM performance.

Before leaving gaseous materials, we should remark on the possibility
of using other halogens (see Figure 5-32). Bromine and chlorine have an
electronic energy level structure similar to iodine, but somewhat reduced
absorption on bound-bound transitions. At wavelengths longer than about 5100Å,
Br_2 absorbs by excitation to the A $^3\pi_{1u}$ or the B $^3\pi_{ou}^+$ states. The extinction
coefficient is about 1.4×10^{-3} cm^{-1} $Torr^{-1}$ at 5700Å, and decreases at longer
wavelengths where the spectrum consists of a well-resolved line structure.
At wavelengths shorter than 5100Å, the absorption increases to twice the above
value near 4000Å. But the photon energy exceeds the dissociation energy of
the B state, and it would appear to be an inappropriate wavelength region
for DFWM because of molecular photodecomposition. Operation with Cl_2 near
its absorption maximum at 3300Å is similarly not possible. However, signif-
icant changes occur in the absorption features for diatomic interhalogens,[5-45]
and these may also be useful for DFWM applications.

When the specific wavelengths are appropriate, another general class of
materials that could merit further investigation are electrically excited
gases in which sizeable metastable level densities can be built up. Absorption
from these levels could then be exploited in the usual manner. Discharges in
the noble gases can lead to sizeable populations in such levels; and in the
case of neon, numerous transitions out of the metastable levels occur in the
5400Å - 7400Å region. In Paschen notation these are transitions from the
four 1s level to the ten 2p levels, and correspond to the characteristic red
neon emission. Two of the four 1s levels are metastable against electric
dipole transitions to the ground state, but radiation trapping at pressures
greater than 0.5 Torr essentially makes all four levels metastable and avail-
able for visible absorption. A similar possibility exists in electrically
excited molecular nitrogen. Absorption may be possible from metastable
$A^3\Sigma_u^+$ molecules on the First Positive band system which is in the near IR.

A final class of materials deserving further investigation involves the
absorption associated with ions in solution or in crystalline hosts. The
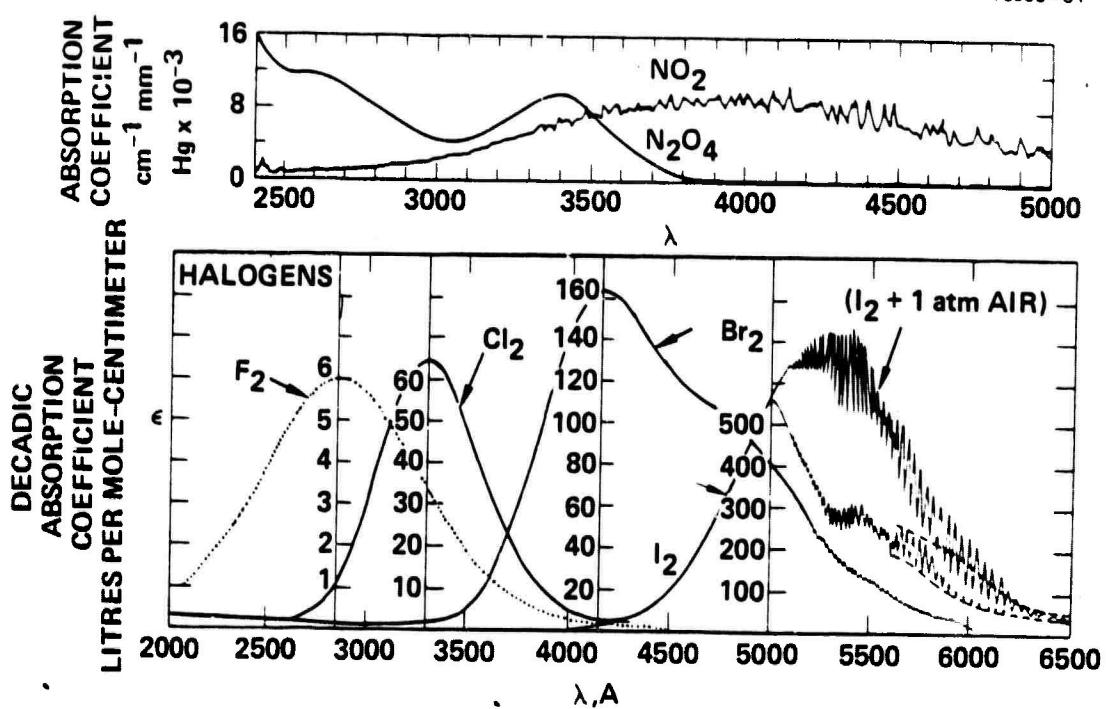
Figure 5-32.   Absorption sperta of the halogens.

MnO_4^- ion absorbs strongly between 4200Å and 7000Å (f = 0.03), and CrO_2^{2-} absorbs strongly between 3100Å and 4500Å (f = 0.09)[5-39] Relaxation of these species in solution is expected to be very fast, and this might imply impractically large values of saturation intensity. Controlled environments for these ions in chelate structures might prove useful. Preliminary experiments have yielded strong DFWM signals in solutions of potassium permanganate and potassium dichromate (see Section 5.2). Doped crystals of Sm^{2+} ions in NaCl represent another candidate for DFWM.

REFERENCES

CHAPTER 5

5- 1. R.K. Jain and M.B. Klein, Appl. Phys. Lett. $\underline{35}$, 454 (1979).

5- 2. H.M. Gibbs et al, Appl. Phys. Lett. $\underline{35}$, 451 (1979).

5- 3. R.K. Jain, M.B. Klein, and R.C. Lind, Optics Ltters $\underline{4}$, 328 (1979).

5- 4. D.A.B. Miller, S.D. Smith, and A. Johnston, Appl. Phys. Lett. $\underline{35}$,
        658 (1979).

5- 5. V. Kreminitskii, S. Odoulov, and M. Soskin, Phys. Stat. Sol. $\underline{(a)\ 57}$,
        K71 (1980).

5- 6. K.K. Jain and D.G. Steel, Appl. Phys. Lett. $\underline{37}$, 1 (1980).

5- 7. M.A. Khan, F.W. Kruse, and J.F. Ready, Optics Letters $\underline{5}$, 261 (1980).

5- 8. D.A.B. Miller, R.G. Harrison, A.M. Johnston, C.T. Seaton, and
        S.D. Smith, Optics Comm., $\underline{32}$, 478 (1980).

5 -9. Corning Glass Industries, Corning, New York; Schott Optical Glass Inc.,
        Duryea, Penn.

5-10. Similar glasses were used by Eichler, et al. for transient holography;
        however, they used saturation of absorption, which does not appear to
        occur in our work. No connection with semiconductor plasmas was made
        by these authors: H. Eichler, G. Enterlein, P. Glozbach, J. Munschau,
        and H. Stahl, Appl. Opt. $\underline{11}$, (1972).

5-11. H.P. Rooksby, J. Soc. Glass Tech. $\underline{16}$, 171 (1932).

5-12. G. Schmidt, in International Congress on Glass, Symposium on Colored
        Glasses, Prague, 1967, pp. 114-129.

5-13. R.W. Smith, Phys. Rev. $\underline{105}$, 900 (1957).

5-14. D.H. Auston, S. McAfee, C.V. Shank, E.P. Ippen, and O. Teschke,
        Sol. St. Electronics $\underline{21}$, 147 (1978).

5-15. For this calculation, we assumed an absorption coefficient of 3 cm^{-1}
        (measured, also see Ref. 16), a reduced effective electron-hole mass
        of 0.16 η_o (see Ref. 17), a refractive index of 2.6 (Ref. 18), and a
        band gap of 2.41 eV (Ref. 19).

5-16. D. Dutton, Phys. Rev. <u>112</u>, 785 (1958).

5-17. J.J. Hopfield, J. Appl. Phys. <u>32</u>, 2277 (1961); J.J. Hopfield and
D.G. Thomas, "Intl. Conf. on Semiconductor Phys., Proceedings, Prague,
1960, (New York, Acad. Press, 1961), pp. 332-334.

5-18. S.J. Czyak, et al, J. Opt. Soc. Am. <u>47</u>, 240 (1957).

5-19. M. Balkanski and R.D. Waldkon, Phys. Rev. <u>112</u>, 123 (1958).

5-20. G. Bret and F. Gires, Appl. Phys. Lett. <u>4</u>, 175 (1964);   ,
C.R. Acad. Sc. Paris 258, <u>3469</u> (1964).

5-21. P.Y. Key, R.G. Harrison, V.I. Little, and J. Katzenstein, IEEE Quantum
Electron. <u>QE-6</u>, 641 (1970).

5-22. H. Eichler, G. Enterlein, P. Glozbach, J. Munchau, and H. Stahl,
Applied Optics, <u>11</u>, No. 2 (1972).

5-23. G. Martin and R.W. Hellwarth, Appl. Phys. Lett. <u>34 (a)</u> (1979).

5-24. E.I. Moses and F.Y. Wu, Opts Letts., <u>5</u>, #2 (1980).

5-25. R.K. Raj, D. Beach, J.J. Snyder, G. Camy and M. Ducloy,
Phys. Rev. Lett <u>11</u>, 1251, 1980.

5-26. M. Kroll, Phys. Rev. Lett <u>23</u>, 631, 1969.

5-27. M.D. Levenson and A.L. Schawlow, Phys. Rev. <u>A6</u>, 10, 1972.

5-28. L.A. Hackel, K.H. Casleton, S.G. Kukolich and S. Ezekiel,
Phys. Rev. Lett. <u>35</u>, 568, 1975.

5-29. J. Wei and J. Tellinghuisen, J. Molec. Spectrosc. 50, 317, 1974.

5-30. G. Herzberg - Spectra of Diatomic Molecules, Van Nostrand N.Y. 1950.

5-31. J. Tellinghuisen, J. Quant. Spectrosc. Radiat. Transfer <u>19</u>, 149, 1978.

5-32. T.W. Hänsch, M.D. Levenson and A.L. Schawlow, Phys. Rev. Lett. <u>26</u>,
946, 1971.

5-33. D.K. Hsu, D.L. Monts and R.N. Zare, Spectral Atlas of Nitorgen
Dioxide 5530 to 6480 Å Academic Press NY, 1978.

5-34. A.E. Douglas, J. Chem Phys. <u>45</u>, 1007, 1966.

5-35. P.B. Sackett and J.T. Yardley, Chem. Phys. Lett <u>9</u>, 612, 1971.

5-36. V.M. Donnelly and F. Kaufman, J. Chem. Phys. <u>66</u>, 4100, 1977.

5-37.   R. Schmiedl, I.R. Bonilla and W. Demtroder, J. Mol. Spectrosc. $\underline{67}$, 1978.

5-38.   G.W. King, J. Chem. Soc. (London) 5054, 1957.

5-39.   J.G. Calvert and J.N. Pitts Jr., Photochemistry, John Wiley and Sons, New York, 1966.

5-40.   G. Herzberg, Electronic Spectra and Electronic Structure of Polyatomic Molecules. D. Van Nostrand Co. New York, 1966.

5-41.   J. Paldus and D.A. Ramsay, Can. J. Phys. $\underline{45}$, 1389, 1967.

5-42.   F.W. Birss et al, Can. J. Phys $\underline{48}$, 1230, 1970.

5-43.   J.T. Yardley, G.W. Halleman and J.I. Steinfeld, Chem. Phys. Lett. $\underline{10}$ 266, 1971.

5-44.   J.T. Yardley, J. Chem. Phys. $\underline{56}$, 6192, 1972.

5-45.   M.S. Child and R.B. Bernstein, J. Chem. Phys $\underline{59}$, 5916, 1973.

CHAPTER 6

SYSTEMS OVERVIEW AND SCOPE

6.1 SYSTEMS OVERVIEW

Before discussing system operating principles, it is useful to review the basic properties of the high energy laser (HEL) systems in which nonlinear phase conjugation (NPC) may find a role. We have emphasized operation at visible wavelengths for two reasons, although one of our example systems employs a multi-line chemical laser. First, assuming that the required laser development is forthcoming, visible operation will offer a major potential for improved overall system operation in future long-range systems, since the shorter wavelengths have both smaller diffraction-spreading and smaller atmospheric-nonlinear effects than the mid-IR chemical lasers or the 10 μ-band CO_2 lasers. Second, at the visible and near UV wavelengths, the path compensation advantages of NPC systems strongly dominate those of conventional adaptive-optic systems. For example, a 4-meter visible ground-to-space system requires on the order of 3000 wavefront error sensors, control systems, and deformable mirror actuators for good turbulence correction; while a 3.8 μm system requires less than 100 (Ref GBBC final report). Thus, NPC, which offers the potential of replacing a very complex system with a single correcting device, offers a major technology payoff at visible wavelengths.

We have examined many potential applications for NPC systems in compensating the phase distortions of high-energy lasers and their associated optical trains and propagation paths. These applications fall basically into three categories: (1) Local corrections for optical defiguring or locally aberrating paths (e.g., laser media); (2) Systems for transmitting power to a satellite or a relay satellite with compensation for path distortions up to the relay mirror; and (3) Compensation for all distortions in target-referencing systems. A brief overview of the operating principles common to these categories is given in Section 6.2.

Our initial investigations were of broad scope but as the program proceeded we have concentrated upon the first two categories of application as offering the

greatest near-term promise, and have selected example systems from each category for more detailed investigation. Category (3), target-referencing systems, will not be discussed because of the severe technological problems that we believe will postpone this class of application. Some of these problems are shared in common with conventional adaptive optics systems, and others are unique to nonlinear phase conjugation systems.

6.2 GENERAL CONCEPTS

The majority of these concepts employ the basic principle illustrated in Figure 6-1. An undistorted reference wavefront enters and propagates through a distorting path; the wave is then conjugated and reflected back through the same distorting path, with the second pass stripping off the wave-front distortions. The beam that exits the path at the end of the second pass is therefore substantially undistorted. If the distorting path includes at least one laser amplifier, and if the reference originates with a laser reso-nator, then such a concept is called a conjugate resonator. If the clean wave-front is injected by means of a high-quality oscillator, and the distoring path in Figure 6-1 is a laser amplifier that is double-passed, then such a system is called a master-oscillator power-amplifier (MOPA) compensated system.

MOPA systems may be designed with the simple objective of removing optical distortion present in the high energy laser gain chamber; or by moving the reference injection further down the optical train, they may also be designed to compensate one or more additional path elements in the optical train. The general rule is that any optical element which is traversed by the reference wave is included within the distorting path box of Figure 6-1 and can, in principle, be compensated. Of course, if these systems are to function efficiently at high power levels, one must employ somewhat more sophisticated structures than illustrated in Figure 6-1. Some of these will be discussed subsequently, and some key problem areas will be defined.

6.2.1 Oscillator Compensation Systems

An important application of nonlinear phase conjugation to local correction is in the internal compensation of oscillators. Internal NPC compensation

PLANE WAVE REFERENCE

SIGNAL OR CONJUGATE WAVE

PROBE WAVE

UNDISTORTED OUTPUT

DISTORTING PATH

Q'

CONJUGATOR
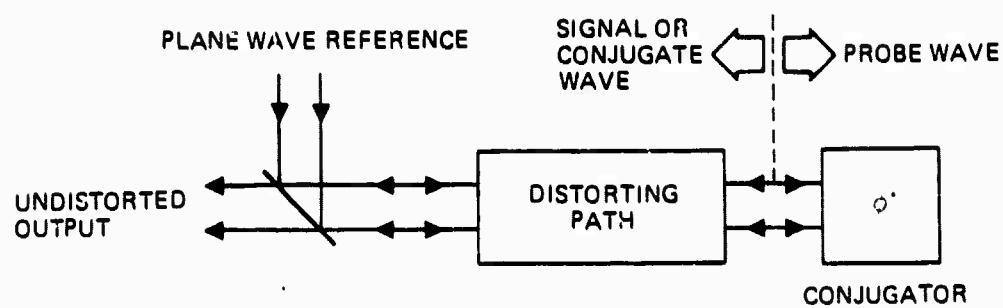
Figure 6-1. Basic compensation principle of most nonlinear phase compensation (NPC) systems.

offers several potential advantages over conventional intracavity adaptive-optics systems: (1) simultaneous correction on N laser lines, each with its own distortion, appears feasible; (2) much higher spatial-frequency distortions can be corrected; (3) higher bandwidth corrections can be achieved; and (4) ultimate cost should be lower because the system is intrinsically simple.

One basic approach to oscillator compensation is illustrated in Figure 6-2. In a general sense, three key elements are included: (1) a plane-wavefront generator, (2) a lasing medium, and (3) a nonlinear phase conjugator. In the system illustrated, the plane wavefront is produced by a pinhole spatial filter, and the phase conjugator is an SBS system. To facilitate the discussion, we will use transmission optics and low-power implementations. In some cases, we will also discuss implementations and problems appropriate to high-power applications.

There are several fairly basic problems with the system depicted in Figure 6-2. First, there are pinhole losses and the potential for pinhole burnout. Second, there is a start-up problem, since initially there is no right hand mirror to set up oscillation conditions. Third, there are problems with the beam splitter: (a) a large portion of the plane wavefront returning from the pinhole is lost* by downwards reflection off of the splitter, and (b) as a result, the power density on the pinhole is higher than need be. Fourth, the frequency offset produced in a basic SBS conjugator progressively accumulates and eventually walks off the gain line of the lasing medium. Fifth, there is a potential problem with scattering-off of the spatial-hole-burning diffraction gratings formed within the laser medium.

In Figure 6-3, we have corrected some of these defects by incorporating a polarization switching phase conjugator using the polarization rotation schemes discussed in Chapter 2. Thus, the wavefronts reflected off the conjugator are polarized parallel to the splitter (normal to the plane of the paper), and the polarization of the wavefront transmitted back via the pinhole system

---

*The lost energy can, of course, be largely recovered by adding a mirror which redirects the beam back in the direction of the output wavefront. Such a recovery system must act like an interferometer so that the correct phasing and angular orientations must be carefully maintained.

OUTPUT
P_O

DIFFRACTION
LIMITED PINHOLE

PLANE WAVE
GENERATOR

GAIN
MEDIUM

ϕ^*

LASING MEDIUM

NONLINEAR PHASE
CONJUGATOR
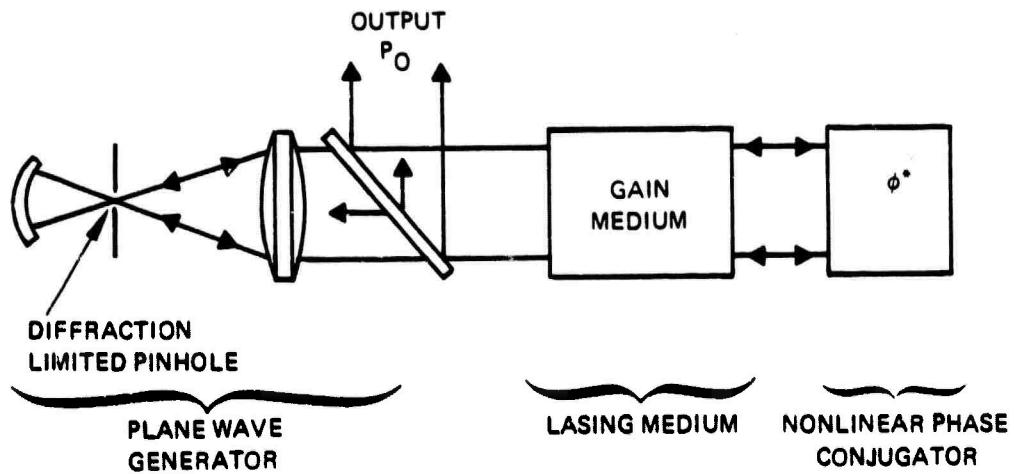
Figure 6-2.   A basic approach to oscillator compensation. The beam
splitter would be replaced by a diffraction grating at
high power levels, and the illustrated splitter ratio
gives about 10% feedback.

QUARTER
WAVE PLATE

P_O

90%

10%

DIFFRACTION
LIMITED PINHOLE

GAIN
MEDIUM

$\lambda/4$
PLATE

ϕ^*
(4 WAVE)
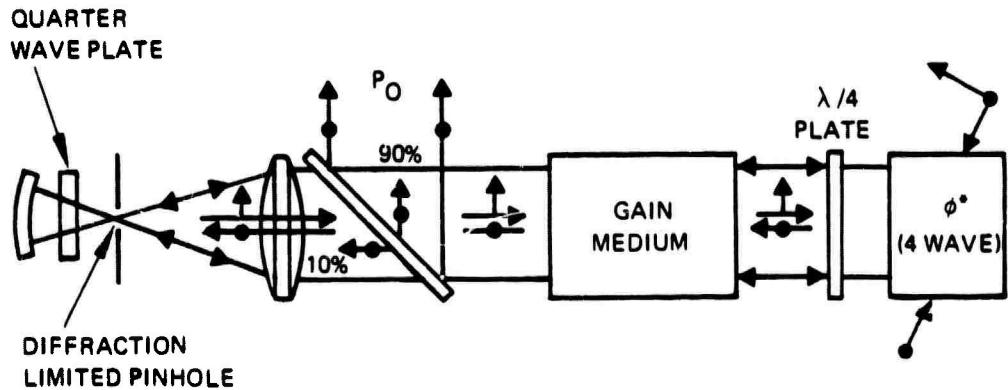
Figure 6-3.   A more efficient approach to oscillator compensation.
By employing a phase conjugator which rotates the plane
of polarization and a polarization-sensitive beam
splitter, the power lost by the splitter is largely
avoided and the power density on the pinhole is reduced
by a factor of three (for the same feedback).

is rotated 90° by a double pass through a quarter-wave plate. The polarization plate is chosen to pass this polarization substantially without reflection. For example, it may be an interference filter operated near Brewster's angle for the filter, or it may be a diffraction grating chosen to give high efficiency at this polarization. Thus, as an example, for 10% feedback the beam splitter can be designed to transmit 10% of its incident energy to the pinhole, as contrasted to the 33% transmitted by the system shown in Figure 6-2. Further, the "lost" energy from the second pass of the splitter in Figure 6-2 is eliminated.

Figure 6-4 shows a pump supply to the system shown in Figure 6-3 wherein the sustained pump is achieved via oscillator feedback. Since the pump supply will not function during initial start-up, we have added a one-pulse oscillator, which supplies the required pump power during the start-up. We have taken advantage of the degeneracy of the four-wave mixing system to isolate the two types of pump by angular separation.

In addition to the technology problems presented by the phase conjugator, the pinhole, spatial filter, and the splitter elements, there are the conventional mode filling problems associated with the confocal resonator configuration.

Note that the spatial filters employed within these structures may be implicit in the sense that the cumulative diffraction effects occurring over many (perhaps hundreds) of passes can conceivably fulfill the required spatial filter function. In fact, we have some evidence based on computer simulations (W.P. Brown, private communication) that this is the case.

Nevertheless, there are strong advantages to the use of spatial filters (including high-order mode suppression), and we have searched for filters which could fulfill this role at high average powers. Clearly, with short-focal-length pinhole systems, as illustrated in Figures 6-2 and 6-3, the pinhole stop would not survive operation at high-power levels and the irradiance at the focus may exceed the air breakdown threshold. Accordingly, we have conceived of approaches that minimize the power density on the spatial filter stop. The approach to be discussed employs one or both of two elements.
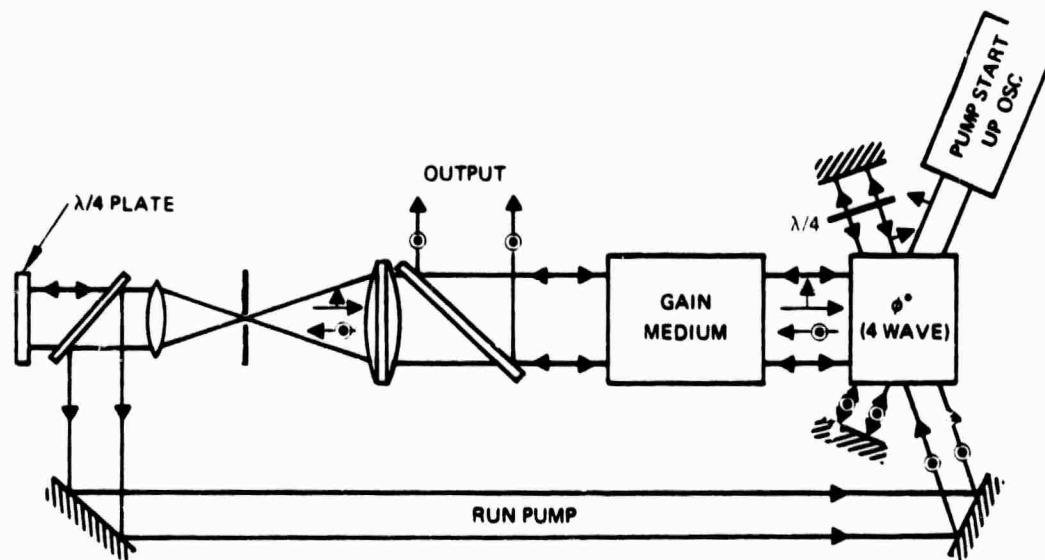
Figure 6-4. One approach to obtaining the pump waves. A pump start-up oscillator initially supplies the pump source. One strong oscillations are initiated, the pump oscillator shuts off and the pump is supplied by feedback from the oscillator itself.

First, the f/number of the spatial filter focusing optics is kept high by employing small diameter input optics ($\sim$0.5 cm) and long (folded) paths ($\sim$20m). The stops, which are essentially in the far field of input optics, have diameters which become about the same size ($\sim$0.3 cm) as the input/output optics. This equalizes the power density loading and minimizes the worst case loading. Second, the loadings on those optical elements may be further lowered by using rotating systems. The rotary pinhole illustrated in Figure 6-5 provides one example. In this approach, rotary metal disks distribute the pinhole peripheral heating over a wide area. The pinhole system should be somewhat canted so that reflected energy from the periphery of the pinhole does not re-enter the oscillator.

We have also explored several possible ring-resonator oscillator configurations; the most promising one to date is illustrated in Figure 6-6. Basically, the feedback follows a figure-eight path. The upper loop of the "8" is the usual optical feedback loop, while the lower loop is a double-pass loop in which the polarization state of the wavefront propagating through the amplifier is first normal to the plane of the loop. The wavefront reflects off the output polarization filter to the phase conjugator, reflects again as a conjugated wavefront, has its polarization state rotated to the plane of the loop, passes the amplifier once more, and then exits through the exit polarizer. Two optically active rotators are required to set up the double pass of the lasing media. Note that the phase conjugator is operating off-axis in a mode contrary to its natural functioning. This operation can be obtained in a four-wave conjugator, as described in Subsection 4.5.

6.2.2 Master-Oscillator Power-Amplifier (MOPA) Compensation Systems

Systems which are configured as MOPAs are more versatile than oscillators, with respect to the classes of path error which can be compensated. Although most of the MOPA systems to be considered employ the basic two-pass configuration (illustrated in Figure 6-1), in some cases there are advantages to multipass or iterated operation. In such systems, the fields produced by successive
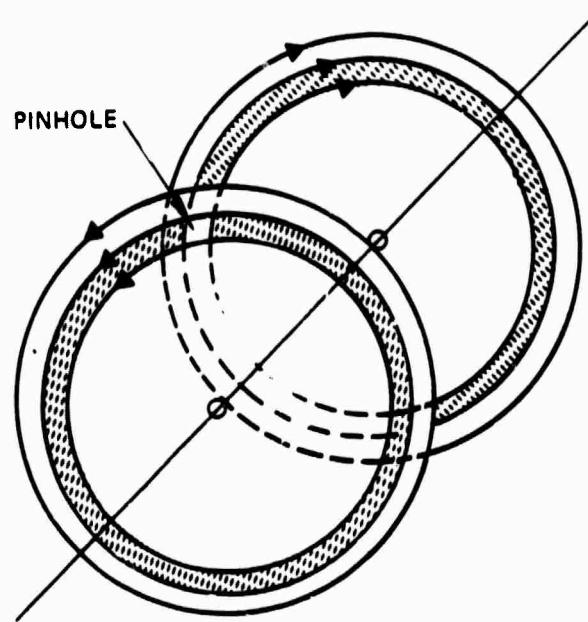
PINHOLE

Figure 6-5.
The "rotary" pinhole system. A pair
of rotating wheels with an annular hole
in each wheel forms a pinhole with rotary
edges. In this way, heating at the pinhole
edges is distributed over an area hundreds
of times greater than with a conventional
pinhole.
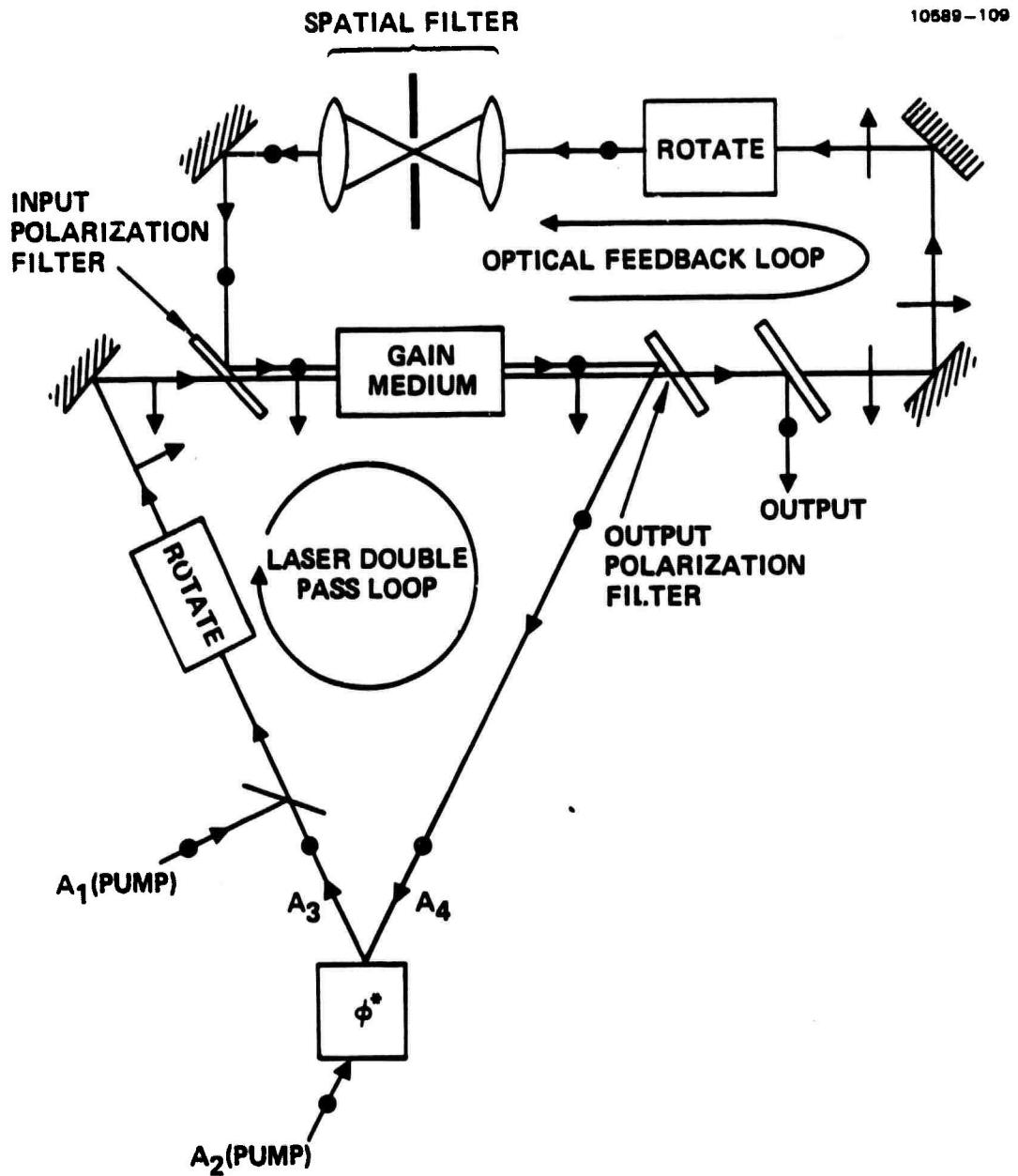
Figure 6-6. A "figure-eight" ring laser oscillator with a phase con-
jugator for gain medium compensation. The gain medium
is double passed in the same direction in two differing
polarization states before exiting the output polariza-
tion separation system.

passes typically do not overlap in the gain medium, and we designate them as "iterated" MOPAs. These may be contrasted to oscillators or phase conjugate resonators in which the fields overlap and superimpose.

Figure 6-7 illustrates one class of two-pass MOPA systems in which the basic system of 6-1 is expanded to include a two stage amplifier. With pulse operation, an isolator or saturable absorber may be included between stages to improve the system stability. Thus, in the event that the laser amplifiers are pumped ahead of the arrival of the oscillator pulse, such an isolation system inhibits the buildup of spurious oscillation or superflourescence. As in the oscillator systems, polarization rotation is employed to efficiently couple in and out of the system. In the MOPA system of Figure 6-7, the oscillator is injected with a polarization which is efficiently reflected back into the system via a diffraction grating on a flat mirror, and after passing the amplifier the polarization is rotated (by 90°) within the four-wave mixer by the use of orthogonally polarized pumps, as described in Chapter 2. The returning conjugated wavefront is of the correct polarization and (ideally) ignores the diffraction grating, and reflects off of the under-lying mirror with minimal loss (to the diffraction orders).

We have found that it is helpful to stage the amplifier chain in order to improve the extraction efficiency, as will be described in the next section. That is, the beam should expand by a factor of between 1.5 and 2 in passing from amplifier 1 to amplifier 2 on the outward path.

The problems which may occur in this class of system are of two kinds: (1) Engineering problems, having to do with the laser train design, and conjugator performance; and (2) Compensation problems, having to do with potential limitations on amplifier optical train compensation, even assuming that the conjugator functions perfectly.

The engineering problems as defined above attempt to exclude the more common or routine design considerations. These are typically component problems and may involve the basic physics describing the operation of the amplifier or conjugator. However, some design problem such as laser amplifier extraction efficiency discussed in Subsection 6.3 may involve the ensemble interaction of the conjugator and the amplifiers, as well as a number of
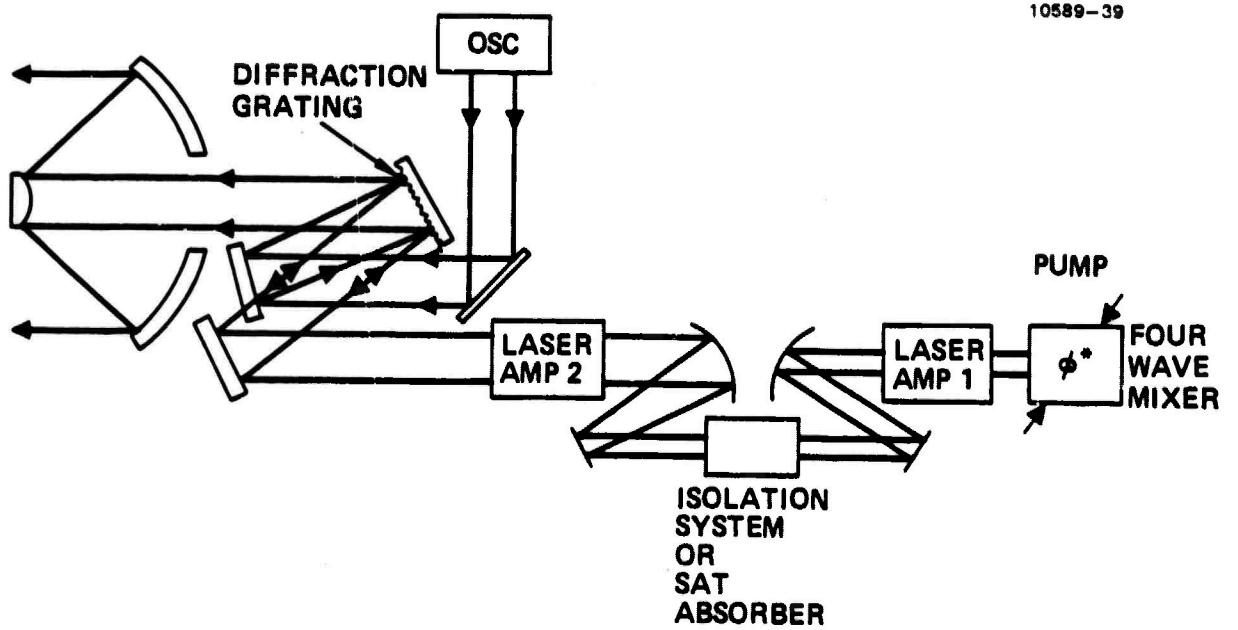
Figure 6-7.   One example of a MOPA system with a four-wave mixer for amplifier and partial optical train compensation.

components in the optical train. As further examples of engineering problems, there is the availability of the conjugator itself (material questions), the operation at the required high average power levels, and the problem of supplying high power pumps of good quality. Similarly, there may be a problem in achieving adequate two-way amplifier gains. For example, simultaneous backwards and forwards operation of SRS amplifiers is not well understood, as discussed in Chapter 7.

In addition, there are fundamental compensation issues having to do with laser amplifiers, which are concerned with field or intensity induced index changes occurring in the laser medium.

One basic issue stems from pulse operation in which the pulses do not overlap in the laser medium. Specifically, laser media may have an index spatial pattern impressed on them by a pulse with transversely varying amplitude. Thus, a problem may occur if the probe pulse does not overlap the amplified signal output pulse and if the decay time of these patterns is short compared to the delay between the signal and probe pulses. Under such circumstances, a probe pulse will not measure the medium phase errors induced by the output pulse, except under the impractical conditions wherein the signal and probe pulses have equal amplitudes. Two examples are thermally induced index changes as nonlinear dispersive effects.

If the signal and probe waves overlap in the medium, then this class of problem is minimized. But another arises: when operating with copolarized probe and signal waves, an index grating is formed in the laser medium (much as in a four-wave mixer) which gives rise to spurious scattered waves whose character is not correct for proper compensation. This general class of problem is discussed by Yariv and Pepper,[6-1] and their analysis will not be repeated here. It should be noted that the solution cited in their paper, equal amplitude probe and signal waves, is not a practical solution to the amplifier problem.

This problem is minimized, and in most cases avoided, by the polarization rotation illustrated in Figure 6-7. However, some lasers will exhibit a quadrupole polarization cross-coupling, such that a "quadrupole spatial grating" is formed, which may generate similar problems to the index gratings.

This class of problem appears to be troublesome only in gas lasers operating at low pressures and without substantial buffer gases.

To summarize, we do not expect to encounter any amplifier compensation problems for those systems wherein probe and signals overlap in the amplifier and are cross-polarized.

6.3 EXTRACTION EFFICIENCY, LASER GAIN AND CONJUGATOR LOADING

We next review three important (and conflicting) objectives in the integration of a conjugator into a laser system: (1) We want low-to-modest average power probe signals into the conjugator in order to minimize thermal loading problems. In the case of four-wave mixers this low power loading requirement becomes more demanding, since the required pumps must have good beam quality, and the pump powers typically exceed the probe power by an order of magnitude or more. Similarly, in many systems the power loading on internal spatial filters may present a major design consideration. (2) Good extraction efficiency from the laser amplifier is desired. This requires operation at optical intensities greater than the saturation intensity. More explicitly, the overall gain-length product of the amplifier should be sufficiently large to permit a weak field from the conjugator to build up to high spatial average values over most of the amplifier length. (3) The required laser gains must be held to reasonable values in order to avoid stability problems. Further, the available gain may be more simply limited in many systems by the availability of space.

We have explored this problem by computing the extraction efficiency vs. small-signal gain, $G_0 = \exp g_0 L$, for a number of oscillator and master-oscillator power-amplifier (MOPA) systems. We will find that extraction efficiency is also a function of the ratio of the power (cw) or energy (pulse) loading on the conjugator to the amplified output power or energy. This ratio is a key parameter, which typifies the average power handling requirements of the conjugator. Similarly, this parameter drives the pump-power requirements in a four-wave mixer.

Since we are concerned with both pulse and cw operation, the extraction efficiency must be separately defined for each case. For cw oscillators, as illustrated in Figure 6-8a it is defined as

$$\eta_{ext} = \frac{P_{out}}{P_{stored}} = \frac{P_{of}(1-R_o)}{P_{stored}} \qquad (6\text{-}3\text{-}1a)$$

and as

$$\eta_{ext} = \frac{W_{out}}{W_{stored}} = \frac{W_{of}(1-R_o)}{W_{stored}} \qquad (6\text{-}3\text{-}1b)$$

for pulsed operation, where P_{stored} and W_{stored} are the powers and energies stored in the inverted populations*, and R_o is the output mirror reflectivity. For MOPA systems $R_o = 0$, as illustrated in Figure 6-8b and the efficiency is defined as

$$\eta_{ext} = \frac{P_{of} - P_{osc}}{P_{stored}} \qquad (6\text{-}3\text{-}2a)$$

for CW operation and

$$\eta_{ext} = \frac{W_{of} - W_{osc}}{W_{stored}} \qquad (6\text{-}3\text{-}2b)$$

for pulsed operation. The stored power for CW operation is*

$$P_{stored} = g_o L\, I_{sat} A \qquad (6\text{-}3\text{-}3a)$$

---

*One way of computing the stored powers of energies is to employ the nonlinear output/input transfer characteristic of the system and let the driving fields become infinite.

where g_o is the small-signal gain coefficient, I_{SAT} is the saturation irradiance, L is the length and A is cross-sectional area of the laser gain chamber.

For pulsed operation

$$W_{stored} = g_o \, E_{SAT} \, LA \qquad (6-3-3b)$$

where E_{SAT} is the saturation energy density (joules/cm^2).

In order to obtain the extraction efficiency one must compute (in principle at least) the key intensity levels in and out of the amplifier, while operating under steady-state saturated conditions. The saturation models which were employed are classical cw and pulse models. For example see 6-5-3. The steady state intensity levels were computed in two differing ways: (1) closed-form solutions were employed if these were available from the literature; (2) a series of minicodes called CO TRIP [for conjugator-triple (staged) amplifier] were employed where closed-form analysis was impractical. The minicodes and closed-form analyses were also employed as cross checks on each other in many cases.

As an example, consider a CW MOPA such as illustrated in Figure 6-8a, where the conjugator reflectivity is unity, and the ratio of the incident power on the conjugator $(P_{if} = P_{ob})$ to the output power P_{of}, which we designate as F, is 10%. That is, the conjugator power loading factor is

$$F = \frac{P_{if}}{P_{of}} = 0.10 \qquad (6-3-4)$$

For amplifiers of uniform cross section, the extraction efficiency is plotted as the dashed curve of Figure 6-9 (one or two-way CW). Note that as the gain increases - presumably by employing longer amplifiers - the extraction efficiency improves; however, the efficiency increases rather slowly with increasing gain.

$$P_{out} \quad \longleftarrow \quad P_{of} \quad \longleftarrow \quad P_{ib} \quad \boxed{\begin{array}{c} \text{LASER AMP} \\ G_0 = \exp g_0 L \end{array}} \quad P_{if} = F P_{of} \quad \boxed{\phi^*} \quad P_{ob}$$

**MIRROR
REFLECTIVITY
R_0**

(a) CW OSCILLATOR

**LASER
OSC**

$$P_{out} = F_{of} \quad \boxed{\begin{array}{c} \text{LASER AMP} \\ G_0 = \exp g_0 L \end{array}} \quad P_{if} \quad \boxed{\phi^*} \quad P_{ob}$$

P_{ib}
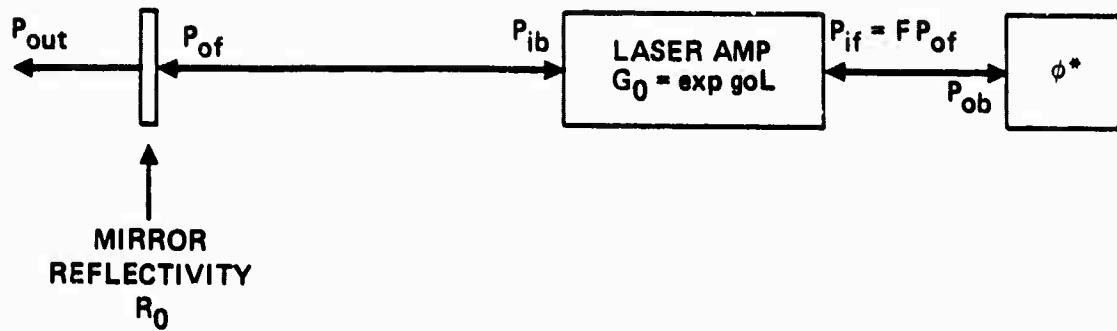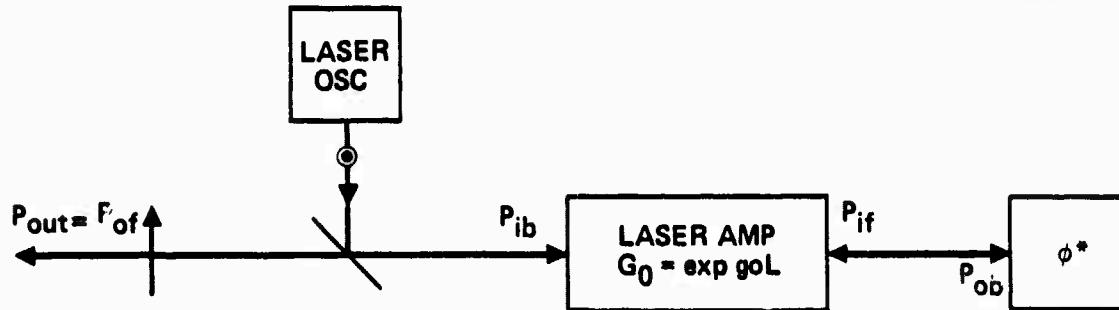
(b) CW MOPA

Figure 6-8. Equivalent oscillators and MOPA systems. If the steady state feedback power P_{ib} of 6-8a equals the injected oscillator power of 6-8b then extraction efficiencies are identical.
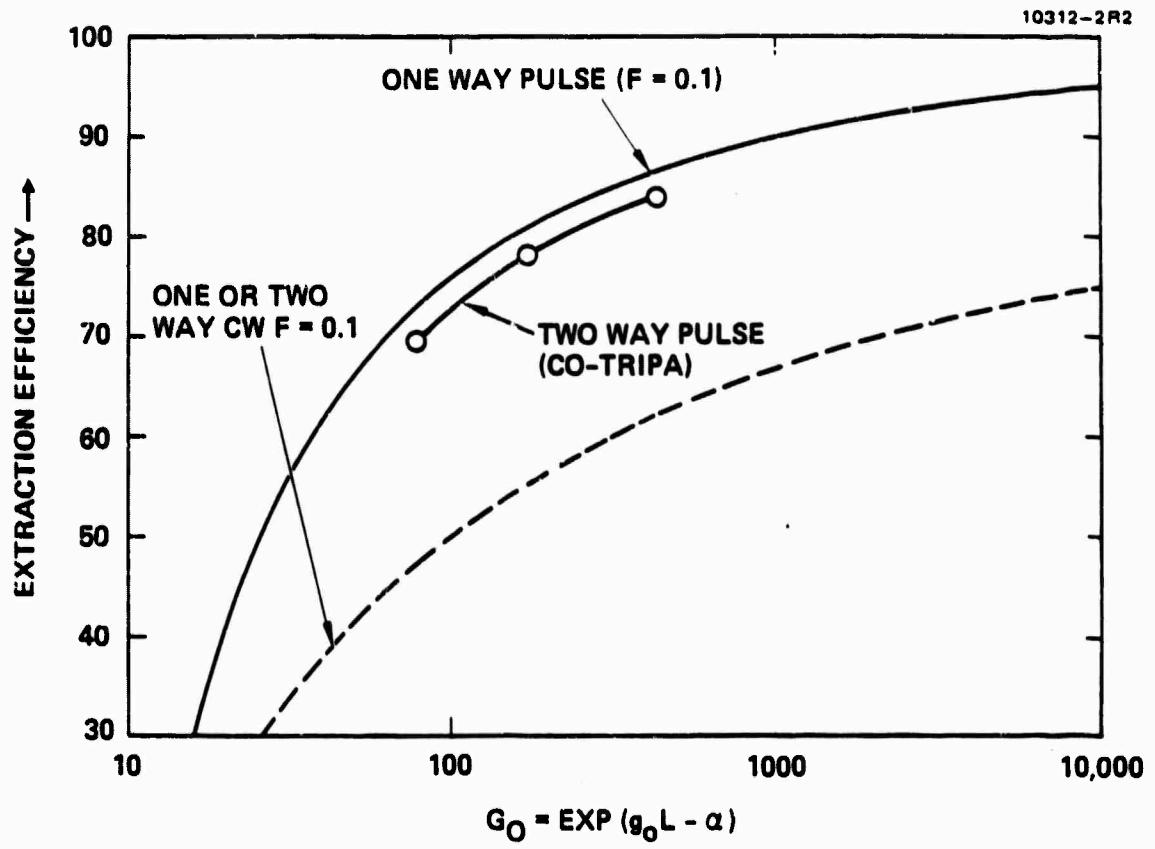
Figure 6-9a. Extraction efficiency versus gain for uniform cross section laser.

Next consider the CW oscillator of Figure 6-9b with the same laser amplifier as employed in the oscillator and the same intensity cross-section distribution (assumed uniform). If the steady-state input power P_{ib} is the same as in the oscillator system, and the conjugator reflectivity is the same, then the internal fields are the same and the same extraction efficiency curve describes both MOPA and oscillator operation.

The curves for pulse operation are different, however, because the assumed saturation characteristics of the amplifier change under pulse operation. A closed-form parametric solution for extraction efficiency and G_o is simply derived for one-way* (conjugator to output) operation as described in Appendix G. For the example previously considered, with

$$F = \frac{W_{if}}{W_{of}} = 0.1 \tag{6-3-5}$$

where W_{if} and W_{of} are the input and output pulse energies, the resulting extraction efficiency is plotted as the top solid curve of Figure 6-9a (one-way pulse). This efficiency is appreciably better than the comparable cw behavior. Two-way pulse operation is treated by a minicode to give ($F = 0.1$) results indicated by the dot-dashed curve. The extraction efficiency falls just below the one-way curve.

Since the cited examples have high (10%) average power loading on the conjugator device, it becomes advantageous to operate with lower values of F. Accordingly, the extraction efficiencies for $F = 0.033$ and $F = 0.01$ are also illustrated in Figure 6-8b, with both pulse and cw operation. We see considerable reduction in extraction efficiency associated with the lower values of F. This stems from conditions at the end of the laser gain chamber nearest the conjugator, which is typically operating at an intensity level appreciably lower than the medium saturation value. This means that the optical fields

---

*In some of the systems to be discussed (as in Subsection 6.4.4, for example) there is a frequency translation associated with the conjugator which may reduce the backwards (left-to-right) gain to very small values. In the extreme limit, this gives substantially one-way operation.
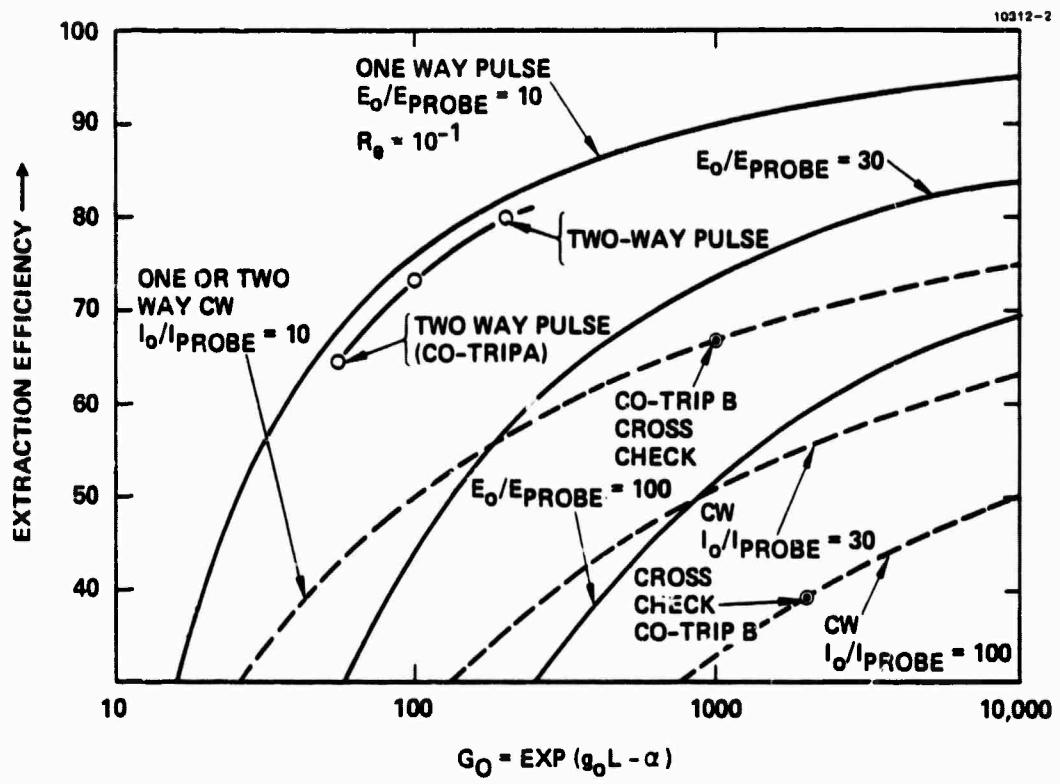
Figure 6-9b. Extraction efficiency versus gain for uniform cross section lasers.

at this end are too weak to completely depopulate the inverted population, and a substantial portion of the stored energy is thereby lost to spontaneous emission.

These curves can also be applied with other values of conjugator reflectivity R_c (differing from unity), and can accommodate various loss factors which may appear in the system. These considerations would suggest that we generalize our definition of F as follows:

$$F = R_o \eta_f R_c \quad \text{(one-way oscillators)} \tag{6-3-6a}$$

$$F = \frac{P_{osc}}{P_{out}} \eta_f R_c \quad \text{(one-way amplifiers)} \tag{6-3-6b}$$

$$F = R_o R_c \eta_f^{1/2} \quad \text{(two-way oscillators)} \tag{6-3-6c}$$

$$F = \left(\frac{P_{osc}}{P_{out}} \eta_f R_c\right)^{1/2} \quad \text{(two-way amplifiers)} \tag{6-3-6d}$$

where R_o is mirror reflectivity for oscillators, R_c is the conjugator reflectivity, and η_f is a loss factor which includes mirror losses, losses from a spatial-filter (if included), and diffraction losses from distant mirrors. The power P_{osc} (P_{out}) are the oscillator (amplifier) power in MOPA systems. With these generalizations, the curves of Figure 6-8 can be applied to a wide range of systems.

Other loss factors should also be mentioned. For example, we have assumed a uniform extraction beam in the transverse direction in generating Figure 6-8. Any departure from this assumption would be expected to produce a transverse "filling-factor" weighting factor which has not been included.

As previously mentioned, the extraction efficiency of these laser systems is appreciably lower at the right (or conjugator) end, because of the smaller fields at this end. Thus, it is helpful to reduce the cross section of the amplifier at this end in order to minimize the required pumping power, which improves the overall efficiency. We have investigated a large number of such cases employing two-and three-stage amplifiers, whose diameters increase from conjugator to output. Typically, we find the expansion ratios of about 1.5:1 (in diameter) are optimum, and that there is a small but worthwile improvement in extraction efficiency by using such an expansion. With expanding stages it is most appropriate to use power or energy density parameters rather than total power or energy. F is then defined as

$$F = \frac{I_{if}}{I_{of}} \text{ (CW systems)} \tag{6-3-7a}$$

or

$$F = \frac{E_{if}}{E_{of}} \text{ (pulse systems)} \tag{6-3-7b}$$

where I's are power densities (in watts/cm^2), P's are powers, E's are energy densities (in joules/cm^2), and W's are energies. Such a definition serves equally well for the uniform cross-section amplifier cases.

The details of the staged amplifier performance vary somewhat from case to case. By way of example, we have chosen two-way CW operation, with rather high gain, with generalized expansion parameters and gains as illustrated in Figure 6-10. As with the uniform cross-section amplifiers, MOPA operation can be described by essentially the same system intensity or energy density parameters with an injected oscillator substituting for the mirror reflection probe signal. The beam (diameter) expansions between stages are M_1 and M_2, as indicated, and the (two-way, small-signal) power gains per stage are G_{oA}, G_{oB}, and G_{oC}. Although we will designate I_{ob} as the "conjugator loading" power
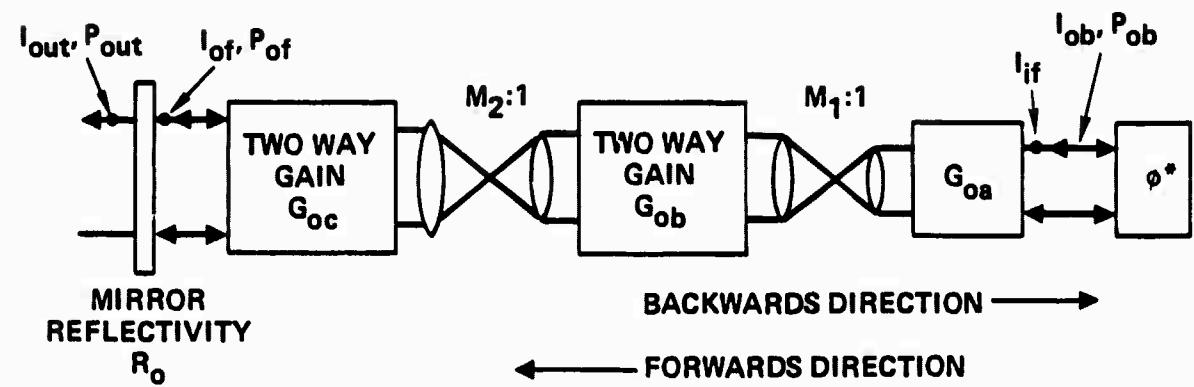
Figure 6-10. A staged oscillator or amplifier system with two-way CW operation.

density, it will be recognized that actual conjugators may well employ additional beam expanders (or compressors) to optimize conjugator performance.

A minicode (CO-TRIP D) was employed to compute the overall extraction efficiency, conjugator power density loadings, and output beam power densities with some typical results being summarized in Table 6-1. The cases which have been compared are low-feedback high-gain cases, as might be appropriate with a reference injection remote from the system. Note that the power densities are all normalized in terms of the saturation intensity I_{SAT}, assumed to be the same for all amplifiers. We have chosen cases wherein all three amplifiers have the same gain.*

The A entry is effectively a uniform cross-section system for purposes of comparison. Case B illustrates that with a beam expansion of 1.5, together with a six-fold reduction in feedback or reference injection levels, the extraction efficiency remains about the same; but the power loading on the conjugator is reduced by about a factor of three. Both the reduced injection level and the reduced conjugator loading are very useful in system design, such that a staged amplifier is well worth having.

Example C illustrates a case where staging is used to achieve some of the above objectives, and simultaneously to improve the extraction efficiency (from 61 to 64%). The reductions in conjugator loadings and required injection signal are not as dramatic here, but are still demonstrably useful.

Case D illustrates that still larger beam expansion ratios are counter-productive. Comparison with case B, for example, illustrates that efficiency is down to 55%, and that the conjugator loading and feedback factors are up.

6.4 BEAM DIRECTOR & OPTICAL TRAIN COMPENSATION

6.4.1 General Concepts and Problem Areas

A potentially important class of systems employs nonlinear phase conjugation for compensation of an entire optical train, including the beam director.

---

*A limited number of explorations have so far disclosed no advantage in varying the gains.

Table 6-1. Typical Results with Saturated Gain and Staged Gain for the System of Figure 6-10

Case	Small-Signal Stage Power Gains $G_{oA}=G_{oB}=G_{oC}$	Expansion Ratios M_1	M_2	Conj Reflectivity R_c	Conj I_{ob}/I_{sat}	System Output I_{out}/I_{sat}	Extraction Efficiency η_{ext}	Conj. Loading Factor $F=\dfrac{P_{iF}}{P_{out}}$	Feedback Factor R_o
A	35	1	1	1	0.1	6.5	61%	0.015	20×10^{-5}
B	35	1.5	1.5	1	0.1	3.5	60%	0.0056	13×10^{-5}
C	35	1.5	1.5	1	0.2	3.72	64%	0.0106	10×10^{-5}
D	35	2	2	1	0.2	2.56	55%	0.0154	4×10^{-5}

The reference can be injected via a diffraction grating on the primary mirror of the beam director as illustrated in Figure 6-11, an approach under investigation as a technique of reference injection for conventional adaptive optics.

In the nonlinear phase compensation system illustrated, the diffraction grating both diffracts and reflects at the same wavelength as the outgoing beam. Since polarization sensitive gratings do not appear feasible (because of the circular symmetry), the high-efficiency polarization path separation techniques illustrated in the MOPA systems of part 6.1.2 do not appear feasible. This limitation presents a potentially serious design problem. For example, if a diffraction grating of 10% coupling efficiency is employed, 90% of the signal injected onto the grating is lost to the backwards path. Also 10% of the returning (amplitude) high-power signal is diffracted back into the oscillator, which could lead to serious stability problems. Our basic approach to this problem is to substitute a buried-grating (or dichroic splitter) element for the low efficiency conventional grating with a frequency offset between the probe and signal wavefronts. Three variants on this basic theme are discussed in the subsections which follow.

There are clearly a large number of technology risk areas in the basic approach. It is not within the current state-of-the-art to fabricate perfectly "figured" conventional holographic gratings on large mirrors (two meters and up), let alone buried gratings. One approach is to attempt to fabricate essentially imperfect gratings of reasonable quality, and to compensate them with a fixed holographic grating, either operating in the main probe/signal train, or in the pump paths of a four-wave mixer. We have not investigated the feasibility of this approach, but note that to be successful it must operate in the face of possible secondary mirror-to-primary-mirror positioning errors in the beam director. Thus, we may confront a whole class of compensation requirements whose details depend on this positioning error.

Still other questions concern the offset frequency operation in the amplifier. Unless care is taken, the offset and dispersion can destroy the phase compensation process. The performance loss resulting from offset is shown to be small for reasonable OPD errors in the following section. We discuss how dispersion can be compensated in Subsection 6.4.3.

10589 -35

PHASE
CONJUGATOR

AMPLIFIER

HOLOGRAPHIC
GRATING
PRIMARY

INPUT
(UNDISTORTED
REFERENCE)

OUTPUT
(WAVEFRONT
COMPENSATED)
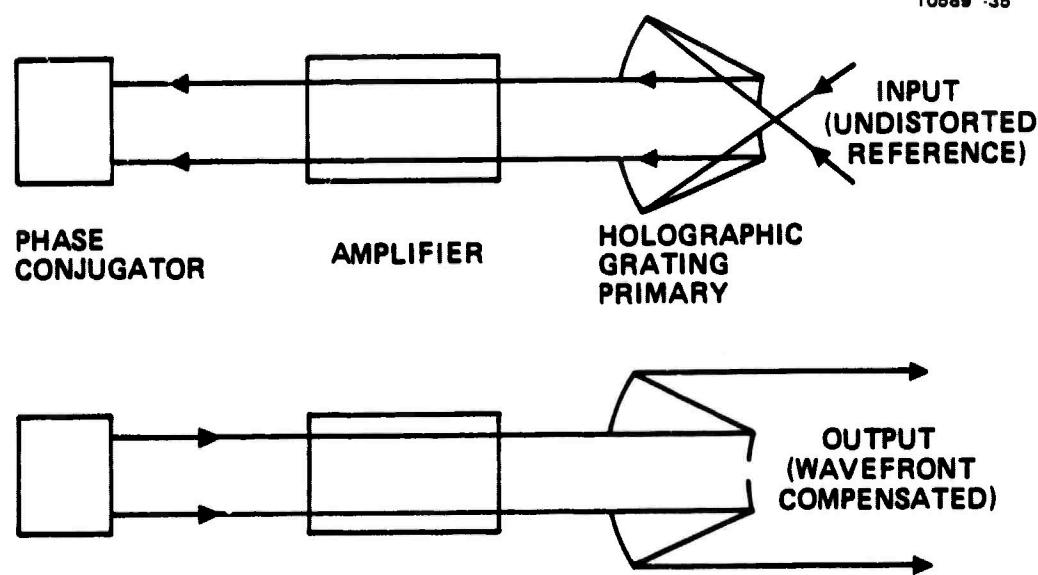
Figure 6-11.   Compensation of the beam director and optical train
via a holographic-grating reference injection.

Although gain may drop to near unity in the reference path as a consequence of the offset, this does not appear to be a serious limitation, since the conjugator power density loadings set the main restriction on the signal extraction efficiency in the amplifier as discussed in Subsection (6.3).

6.4.2 A Frequency-Offset Buried-Grating Approach*

The approach to be discussed employs a buried grating on the primary mirror as illustrated in Figure 6-12. In this case, the frequency offset between the probe at λ_1, and signal at λ_2 is rather small, nominally of the order of $\Delta\lambda/\lambda = 200^{-1}$ (200 wavenumbers at UV), and might be achieved in a first stokes SRS (down shifted) conjugator. It is presumed that this frequency offset is large enough to shift operation with the buried grating from a near null at λ_1 to a reflection peak at λ_2 in the dielectric interference filter (overlaying the buried grating). And further, we assume that the frequency offset $\Delta\lambda$ translates the probe signal well off the gain profile of the laser amplifier.

Since the signal is offset in frequency from the probe, an uncompensated error proportional to $\Delta\lambda/\lambda$ will arise. However, as we will see, for reasonable optical path difference (OPD) errors, the compensation can be excellent. Thus, if the OPD variation is given by $\overline{OPD}(\vec{x})$ and is presumed nondispersive for the moment, then the residual (uncompensated) phase error on the output beam is

$$\phi_e(\vec{x}) = \frac{\Delta\omega}{c} \, OPD(\vec{x}) = 2\pi \left(\frac{\Delta\lambda}{\lambda}\right) \left[\frac{\overline{OPD}(\vec{x})}{\lambda}\right] \quad . \tag{6-4-1}$$

This compares to a (single-pass) error, without conjugation, which is

$$\phi_e(\vec{x}) = 2\pi \left[\frac{OPD(\vec{x})}{\lambda}\right] \quad . \tag{6-4-2}$$

If the spatial distribution in $\overline{OPD}(\vec{x})$ includes a large number of orthogonal components (Zernike components, for example), then the associated far field Strehl ratio, S, is well approximated as

$$S = \exp - <\phi_e^{\,2}(\vec{x})> \quad . \tag{6-4-3}$$

---

*This section reports work performed under HRL IR&D.
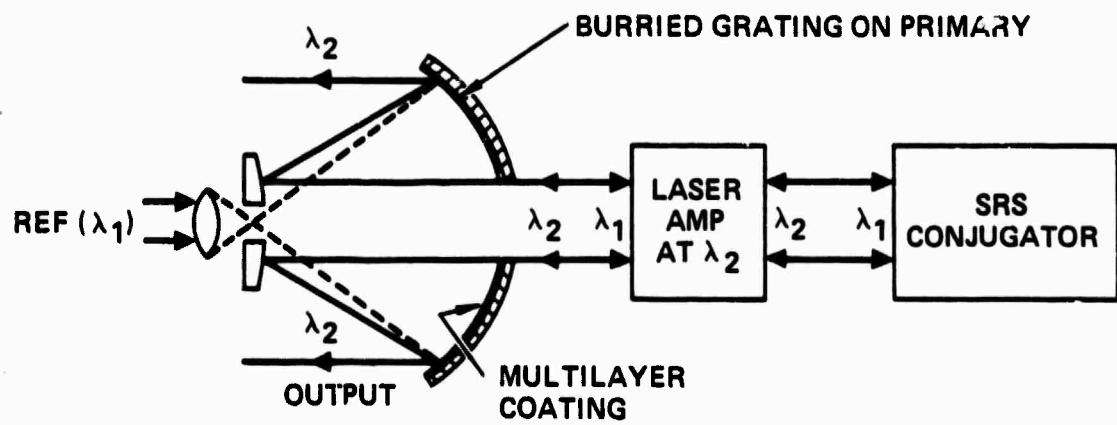
Figure 6-12.   A frequency-offset buried-grating approach.

The Strehl ratios for (6-4-2) and (6-4-1), with $\lambda\Delta/\lambda = 200^{-1}$, are compared in Figure 6-13. The conjugated system is still essentially perfect (S = 0.99) for OPD^S up to 3.5 waves rms, whereas the uncompensated system is quite ineffective (S <0.1) for OPD^S larger than 0.5 waves rms.

Since the dispersion characteristics within a laser amplifier are intensity dependent, there is some concern that the phase compensation may fail to be perfect if the laser intensity profile is not uniform across the beam. We examine this question in the following analysis. The index variation produced by the inverted laser population is, for operation near a single resonance at ω_ℓ, given as

$$\Delta n(\omega,\vec{r}) = [1+R(\omega)N_o(\vec{r})]^{1/2} - 1$$

(6-4-4a)

$$\doteq \frac{1}{2} R(\omega)N(\vec{r}) ,$$

where $R(\omega)$ and $N(\vec{r})$ are separable factors containing the frequency and spatial dependence; specifically,

$$R(\omega) = \frac{\omega-\omega_\ell}{\gamma^2+(\omega-\omega_\ell)^2}$$

(6-4-4b)

$$N(\vec{r}) = \frac{N_o(\vec{r})|\mu_{12}|^2}{2\hbar} ,$$

(6-4-4c)

where $N_o(\vec{r})$ is the inverted population density, which may be spatially dependent as a consequence of pumping variations, μ_{12} is the dipole moment, γ is the natural or laser linewidth, and ω_ℓ is the line center (angular) frequency. If we integrate the index variation within the amplifier over a path parallel to the axis, we obtain a shift $\phi(\vec{x})$, given by

$$\Delta \phi(x,y,\omega) \sim \int_0^L \Delta n(\omega,x,y,z) \ dz = \frac{L}{2} R(\omega) \ \frac{|\mu_{12}|^2}{2\hbar} \ \tilde{N}_o(x,y) , \quad (6-4-5a)$$

10589 - 93
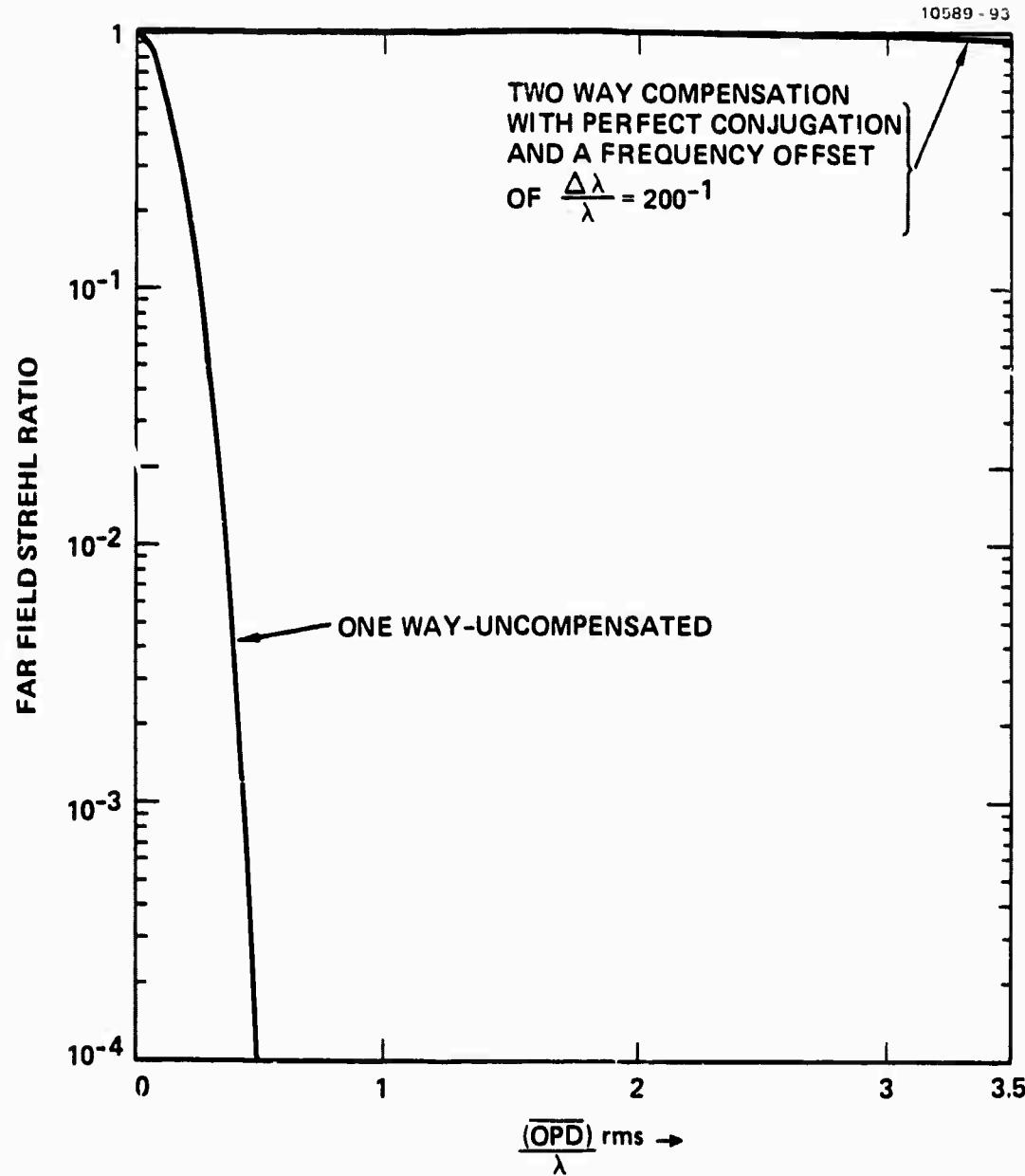
Figure 6-13. Two way compensation with perfect conjugation and a
frequency offset $\Delta\lambda/\lambda$ 200^{-1}

where

$$\tilde{N}_o(x,y) = \int_o^L N_o(x,y,z)\, dz \quad . \tag{6-4-5b}$$

The key point (which results from the separability) is that if $R(\omega)$ can be compensated or equalized at probe and signal wavelengths λ_1 and λ_2, and if the population densities which are seen by the λ probe and signal waves are the same,* then the same phase shift variation is experienced by the signal and probe waves. That is,

$$\Delta\,\phi(x,y,\omega_1) = \Delta\,\phi(x,y,\omega_2) \quad . \tag{6-4-6}$$

Thus perfect compensation can be achieved.

The function $R(\omega)$ is illustrated in Figure 6-14, and it may be observed for any frequency separation $\omega_2-\omega_1$ there exists an ω_2 such that

$$R(\omega_2) = R(\omega_1) \quad . \tag{6-4-7}$$

And, for modest to large frequency separations, ω_2 is near the laser line center.

A similar but more lengthy argument suggests that index variations associated with laser beam intensity variations are also separable and can be similarly compensated.

6.4.3 A Frequency-Doubler Buried-Grating Approach**

Although we have just shown that small frequency offsets ($\Delta\lambda/\lambda \sim 1/200$) do not generally produce a large error in the compensation process, the use of very large offsets might appear dubious. In this section we demonstrate one system which has a very large offset, and yet minimizes $\Delta\lambda/\lambda$ problems.

---

*This would hold in cw operation but not in pulse operation for example.

**This section reports work performed under HRL IR&D.
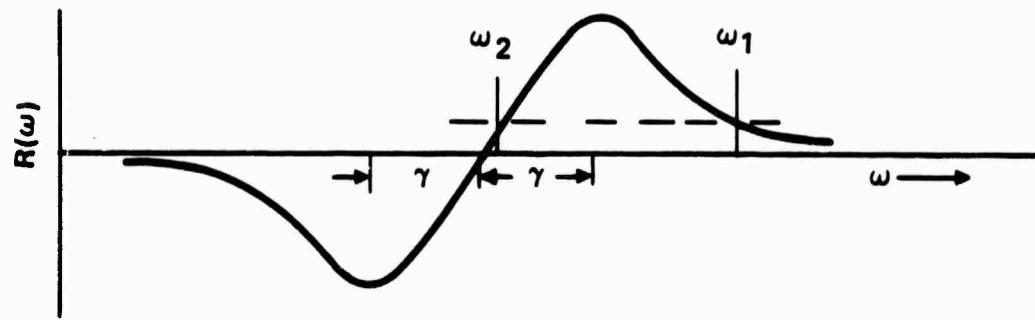
Figure 6-14. Frequency selection of ω_2 and ω_1 for dispersion equalization.

We begin by demonstrating how dispersion-free systems can be precisely compensated, by the approach illustrated in Figure 6-15. A laser oscillator signal of frequency ω_1 is again injected as a reference via a diffraction grating on the primary, with the diffraction grating being a "buried grating," underlying a multilayer dielectric coating. The diffracted beam traverses the amplifier, most probably without amplification, and responds to (spatially modulated) optical path differences which tnereby become encoded as a spatially v jir phase shift on the probe beam, as it impinges on the conjugator. The conjug. then reverses this phase distribution. Further, the polarization of this sig. beam is either rotated in the conjugator or via an auxiliary quarter wave plate, which permits it to be split off from the incoming path with high efficiency. The conjugated wavefront then enters a frequency doubler wherein the inverted spatial phase variations are doubled in magnitude. The amplifier is repassed, and if it is nondispersive and linear (with respect to distortion), the amplifier distortions are compensated, exactly as in a conventional ($\Delta\lambda=0$) system. The frequency doubled conjugated wavefront then reflects off a multilayer dielectric coating on the primary mirror (with nearly 100% efficiency) whereupon it exits the beam director. Under ideal conditions, the optical path differences in the beam director path are also cancelled on the return path.

Note that since the frequency doubler is not a shared path element, it is not compensated by the generic pass-conjugate-repass operation.

The basic dispersion compensation technique discussed in the previous subsection is equally applicable to this system in principle. However, the large frequency separation requires a more complex media model since many resonances may be encountered over the frequency span.

6.4.4 Multiline Laser Accommodation *

We now consider laser amplifiers which operate at high efficiency only if the laser is operated at several wavelengths simultane ·sly, or in a rapid cascade operation. For such lasers the basic grating injection technique illustrated in Figure 6-11 experiences major angular dispersion problems,

---

*This section reports work performed under HRL IR&D. It is included for completeness of the discussion.
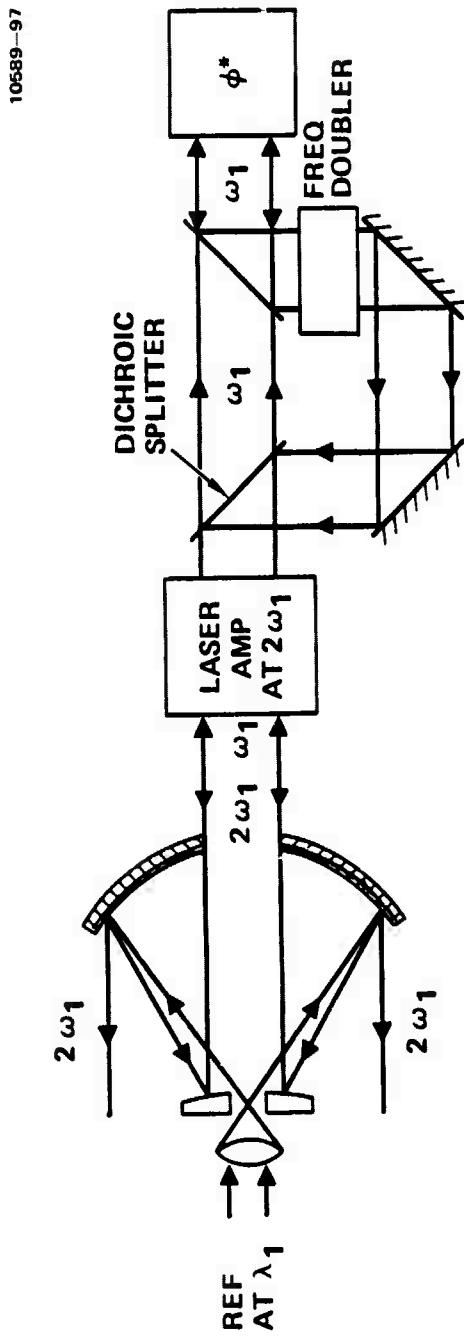
Figure 6-15.   A frequency-double buired-grating system.

since such a grating system can achieve a precision focus (or more generally, a given optical figure) at only one of the multiple wavelengths.

One solution to this problem is illustrated in Figure 6-16a. Here a single reference wavelength, λ_o, near the center of the laser spectral line group is injected at the diffraction grating, and serves as a surrogate for the multiple laser lines. There are good arguments for employing a reference laser line, which is separate and distinct from any of the main amplifier laser lines. This surrogate laser line interferes with a matching pump line at λ_o in a two-level (one photon) four-wave mixer, and forms a (single) volume diffraction grating whose indentations represent the distortions in the wavefront. The second pump is then a multiwavelength source whose discrete lines represent the desired input lines for the multiline power amplifier. This pump is reflected off the deformed hologram, with the inverse phase distribution, or phase conjugate, of the surrogate wave. Each line is reasonably well compensated upon retransmission through the distorting optical train - if dispersion problems can be ignored and if the optical path differences are not too large. Note that the backward pumps, if injected at the exact counter-propagating angle would not satisfy the Bragg condition (would not be phase matched). Thus, if appreciable reflectivity is to result, some provisions must be made to re-establish the Bragg conditions. Our present approach is to employ a grating rhomb system in which the mixer is located between the two gratings, as illustrated in Figure 6-16b. In this way every backward pump wavelength impinges on and exits from the mixer at a slightly offset angle, relative to the reference λ (assuming it were present). With a proper choice in grating designs, the angular dispersion can then be chosen to satisfy the Bragg condition in the mixer hologram for all laser wavelengths simultaneously.

This approach appears to avoid the cross-frequency gratings problems of the type discussed in Section 4.4.3.
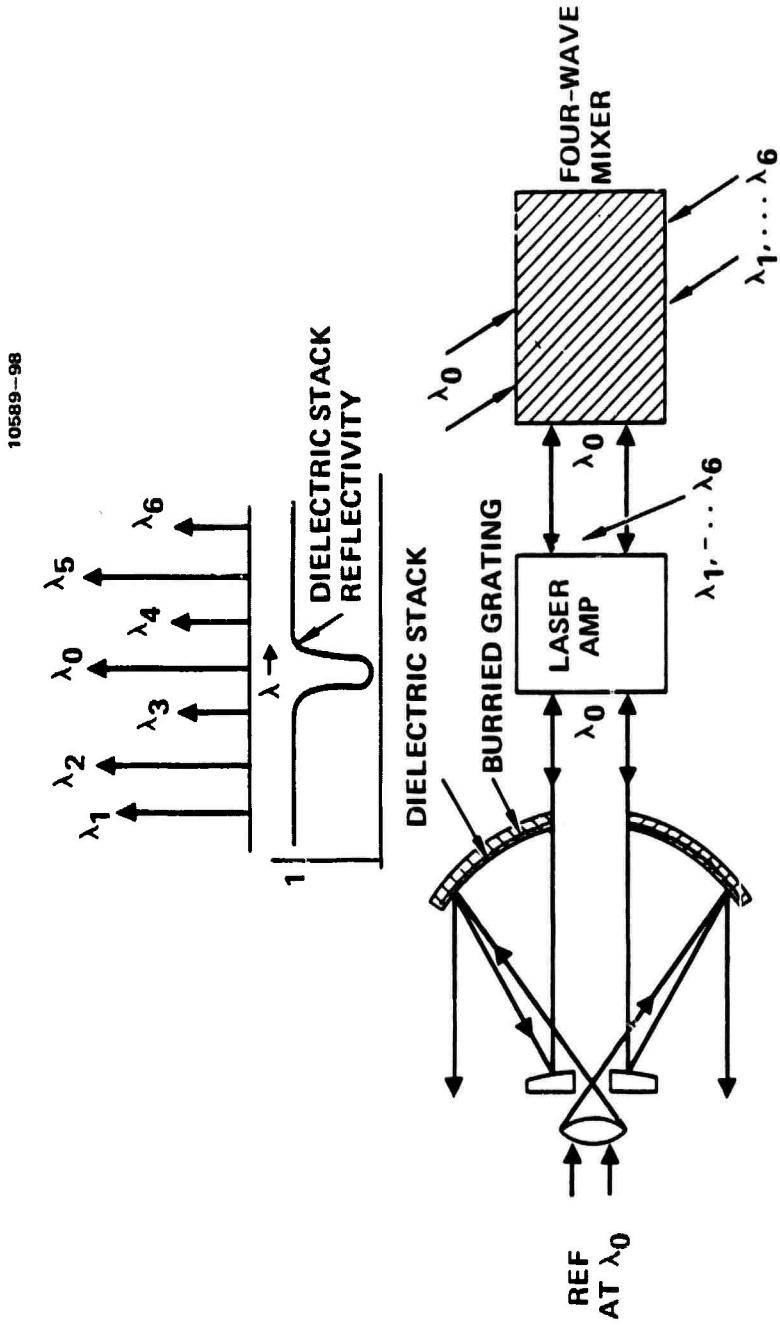
Figure 6-16a. A surrogate reference system for multi-line lasers (simplified, without Bragg matching).
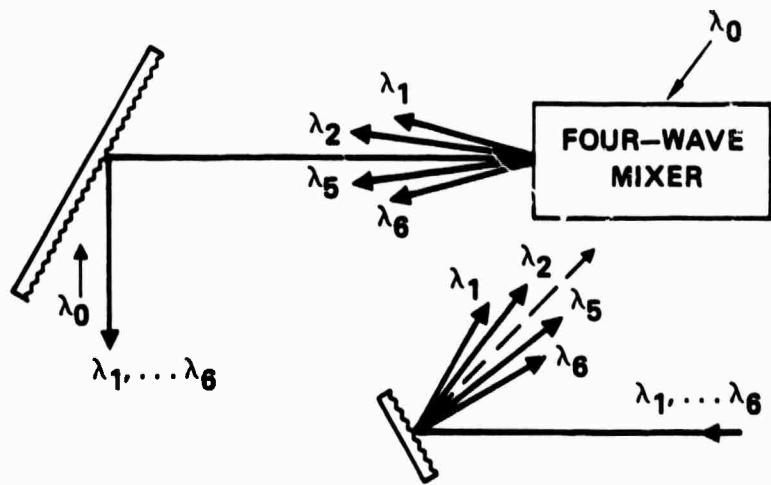
Figure 6-16b. Angular dispersion and recollection
system to satisfy the Bragg condition.

6.5 ORBITING COLLECTORS AND RELAY SYSTEMS

We next consider the problem of transmission of power to a satellite or to
a satellite relay point via a ground station, as illustrated in Figure 6-17.
We presume operation at visible or near UV wavelengths with a large aperture
beam director (4 m and up), such that atmospheric turbulence causes severe
beam spreading. These systems are all operated in MOPA configurations in
which a well controlled reference laser wavefront either originates on (or near)
the satellite, or is reflected from a retro system on (or near) it. Both
pulsed and CW operation are considered.

6.5.1 Distortion Compensation and Moving References

The objective of these systems is to correct both linear and nonlinear
distortions in the laser, the optical train, the beam director and the
atmosphere. The atmospheric path is the key new element to be compensated.
There have been erroneous statements in the literature regarding the ability
of compensation systems using nonlinear phase conjugation to remove thermal
blooming distortions. Although there are some limitations cn the degree
of compensation for both linear and nonlinear atmospheric path distortions,
these limitations relate to the distance of the distortion surce and the
relative size of the received diffracted reference beam relative to the
effective size of the conjugator. The effective conjugator size is the beam
director diameter, assuming there is no other apodization intervening between
the beam director and the conjugator. Although we are continuing to explore
these propagation questions under other contracts, there is good reason to
believe that excellent compensation for both linear and nonlinear effects will
result if the conjugation process is accurate and if the focal point is for
outside the atmosphere.

There are, in addition, problem areas in the laser amplifier compensation
as we have previously discussed.

Due to the long range and high velocities of satellite reference sources,
the system design is much more difficult than for the local referencing systems
previously discussed. In particular, the long ranges (up to 40,000 km),
together with the limited size of a practical reference optics, yields a

ORBITING COLLECTOR
OR RELAY SYSTEM

ORBITING REF SOURCE
OR RETRO SYSTEM

POWER BEAM

- - -REF BEAM

ATMOSPHERE

BEAM
DIRECTOR

LASER
AMPLIFIER ϕ^*

EARTH
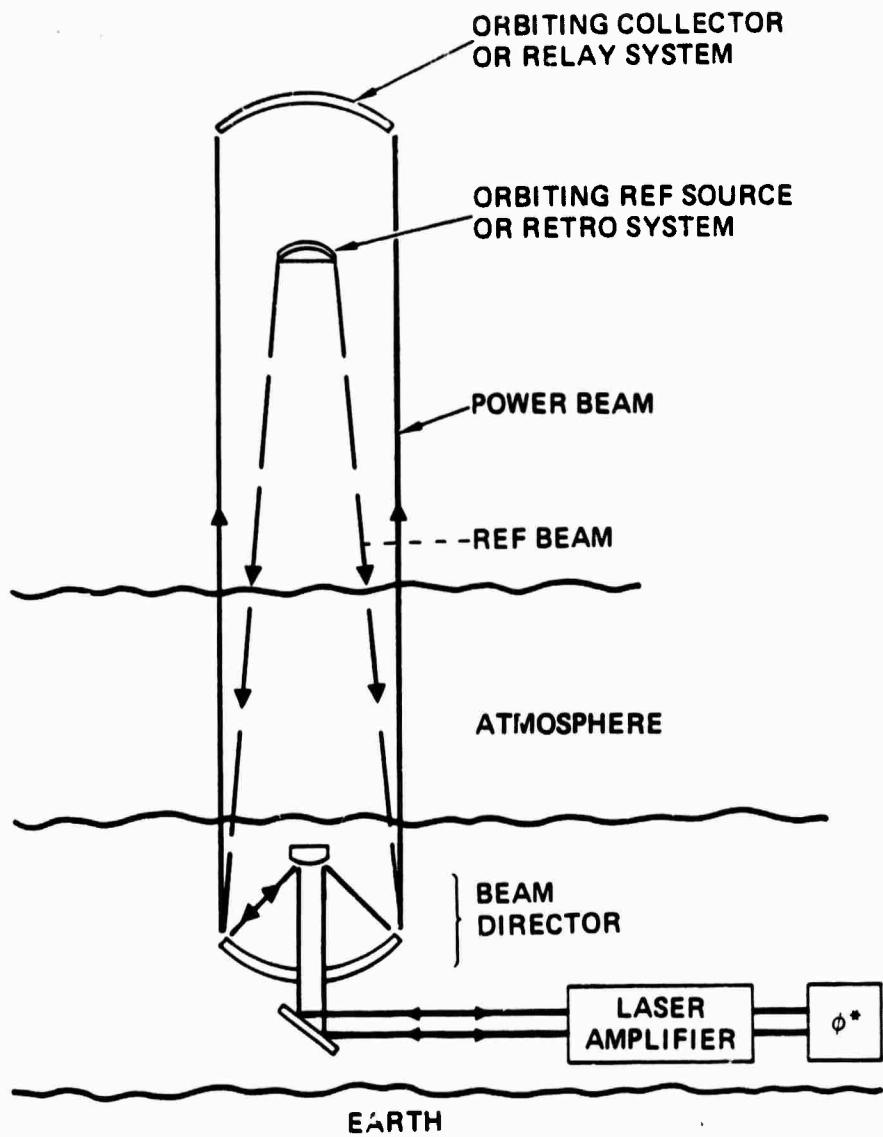
Figure 6-17.   Generalized ground-to-space power transmission
system.

diffraction spreading of the reference beam which gives significant coupling loss on the space-to-ground reference path. This provides another constraint in the gain efficiency trade-off discussed in part 6.3. Much larger laser gains are required to achieve a reasonable extraction efficiency. Thus it is preferable to minimize the gain requirement by operating with strong reference sources, and with reference systems of at least moderate apertures so that the space-to-ground coupling losses are minimized. In some of these systems, it is possible to split out a small portion (<10%) of the main beam at the satellite and relay this beam back to the ground station as a reference. This avoids the burden of having to supply a separate high-power reference source.

A quite different class of problems results from the radial component of reference velocity. If the satellites are in low orbits, large doppler shifts (up to 28 GHz at 0.5 μm) on the reference beam can easily cause either the outgoing wave (or the returning reference wave) to shift far away from the center of the laser gain line. Since the laser amplifier then amplifies only the outgoing path, the gain becomes nearly unidirectional, again strongly impacting the overall gain requirement. More gain length must be included for a given reference power and a desired extraction efficiency.

Doppler shifts also present problems to the conjugator. For conventional counter-propagating, degenerate four-wave mixers, whose depth is on the order of a cm or more, phase mismatch losses become serious with a 28 GHz Doppler shift. Additionally, the highest efficiency four-wave mixers employ a resonant medium, with operation near the resonance. With a doppler shift in the probe, operation may easily shift off of the optimum wavelength with a significant loss in mixer gain. Excepting the latter problem, all of the other can be compensated for by changing the mode of operation of the mixer as discussed in Section 4.5. Nevertheless, the above problems strongly indicate the value in selecting synchronous orbits, wherever possible.

Even in synchronous orbits, however, satellite orbital motion still causes problems to a nonlinear phase conjugation system. If the reference originates on the satellite, then a truly conjugated wavefront retraces a return path coincident with the down-link reference path. Unfortunately, when it arrives

back at the origin point, the satellite has moved on (during the optical round-trip time of flight), and the miss-distance is substantial (20 μrads or 800 meters at synchronous orbits). Yet as we will demonstrate, it is possible to trick or override the conjugator by several different methods, such that the phase variation in the input wavefront is substantially wavefront reversed in the output, except for the tilt component. Thus the "conjugated" output or signal propagation direction is slightly offset* from the input or probe wave. This is more fully discussed in section 4.5.

6.5.2 Reference Locations

In spite of the convenience of locating the reference on the satellite, this location is undesirable because the reference path and outgoing path are anisoplanatic, a problem which is common to conventional adaptive optics and to nonlinear phase conjugation systems. The two paths are anisoplanatic because the turbulent patterns in the atmospheric refractive index are assumed to remain frozen, relative to the earth within a round-trip transit time of the atmosphere. Thus these patterns rotate with the earth, and the outgoing beam transits a somewhat different distribution of turbulence than did the downward reference beam (especially at high altitudes). The magnitude of the resulting loss of path compensation has been studied by Fried[REF] using an MTF theory. We have used this theory in Figure 6-18 to quantify the Strehl ratio as a function of offset angle with a 4.0 m beam director at 0.5 μm. Although the Strehl ratio strongly depends upon the turbulence distribution with altitude, the Strehl ratio, at 20 μrad, is unacceptably low for two commonly used models of atmospheric turbulence as illustrated in Figure 6-18.

---

*The required offset at the conjugator is much more than 20 μrads because of optical demagnification in passing from the primary to conjugator diameters. With a 4 m primary mirror diameter and a 4 cm conjugator about 2 milliradians offset is required.
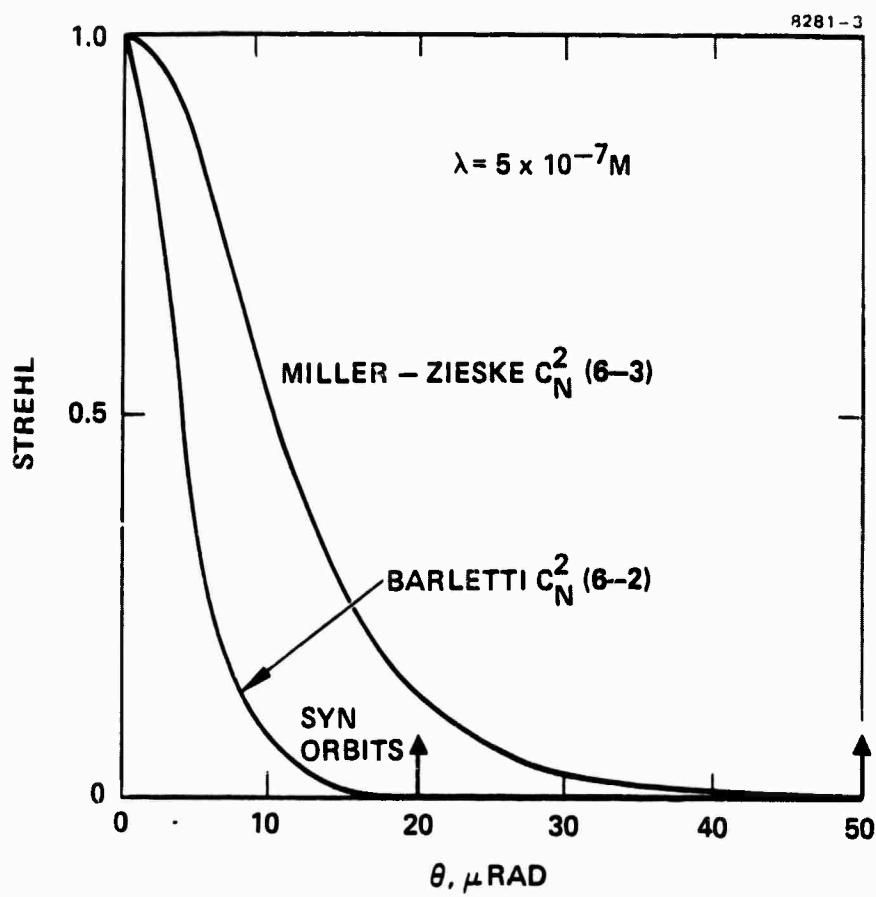
Figure 6-18. The conventional isoplanatic degradation for
$\lambda = 0.5$ μm for a 4.0 meter aperture after
Fried, with ideal adaptive optics. A zenith
path with a coherence length (r_o) of ~60 cm
is assumed.

Anisoplanatism can be avoided by orbiting a reference that is spaced ahead of the main satellite by the point-ahead angle, as illustrated in Figure 6-19. As a secondary benefit, the requirement to offset the conjugator is eliminated, in principle.* Unfortunately, if a simple reflecting "fly-ahead" reference, such as a corner reflector, is employed, the anisoplanatic problem appreciably degrades the injection efficiency of an auxiliary (ground-based) reference laser. This degradation occurs since the illuminator beam for the reference is not well compensated, even if it is formed by a reflection off the conjugator. We will quantify these effects in subsequent discussions.

One concept that avoids this degradation is the extended retroreflector whose general principle is illustrated in Figure 6-20. In this example the corner reflector is separated into two planar mirrors (A and B) which are closely held at 90° angles to each other. Mirror A intercepts a portion of the atmospherically compensated main beam and relays it to mirror B, which lies ahead of A by the point ahead angle (about 20 μrad). Mirror B relays the reference beam from mirror A back parallel to the incident beam on A, - i.e., back to the ground-based beam director. The key point is that if A and B remain orthogonal, their absolute orientation is not critical (with respect to angular errors within the plane of the figure), and such errors are automatically compensated. Since these mirrors are spaced at a relatively small distance, it is far easier to orient them with respect to each other than to orient them to a ground station 40×10^{6} meters away.

6.5.3 Reference Injection and Timing Considerations

Whether or not the reference is flown ahead of the satellite, there are a variety of reference injection and iteration or timing techniques which

---

*From a broader viewpoint it seems unlikely that one would willingly forego the offset capability, since the reference position could easily drift, relative to the main satellite station. It is far more crucial to hit the satellite with the return beam than to eliminate a small anisoplanatic effect.

| (a) t = 0 | (b) t = R/C | (c) t = 2R/C | (d) t = 3R/C |
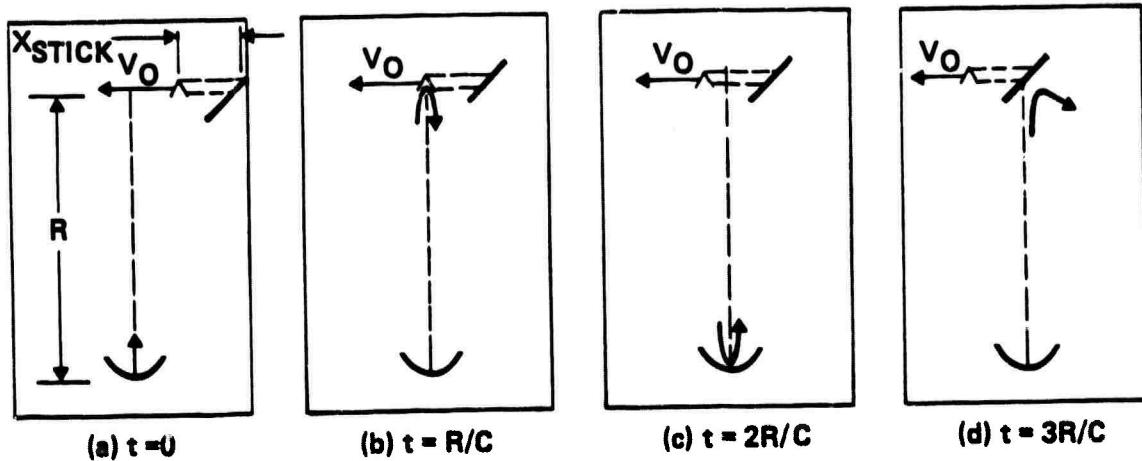
Figure 6-19.   Time progression of a pulsed wavefront in a fly-ahead retro
system.   In the ideal system the initial pulse is launched
to point ahead of the corner reference (a), intercepts it
and is retro reflected.   (b), is reflected and conjugated
at the ground station (c), and intercepts the relay mirror
on axis (d).   Since the conjugated wavefront retraces
approximately the same path the isoplanatic problem is
minimized.
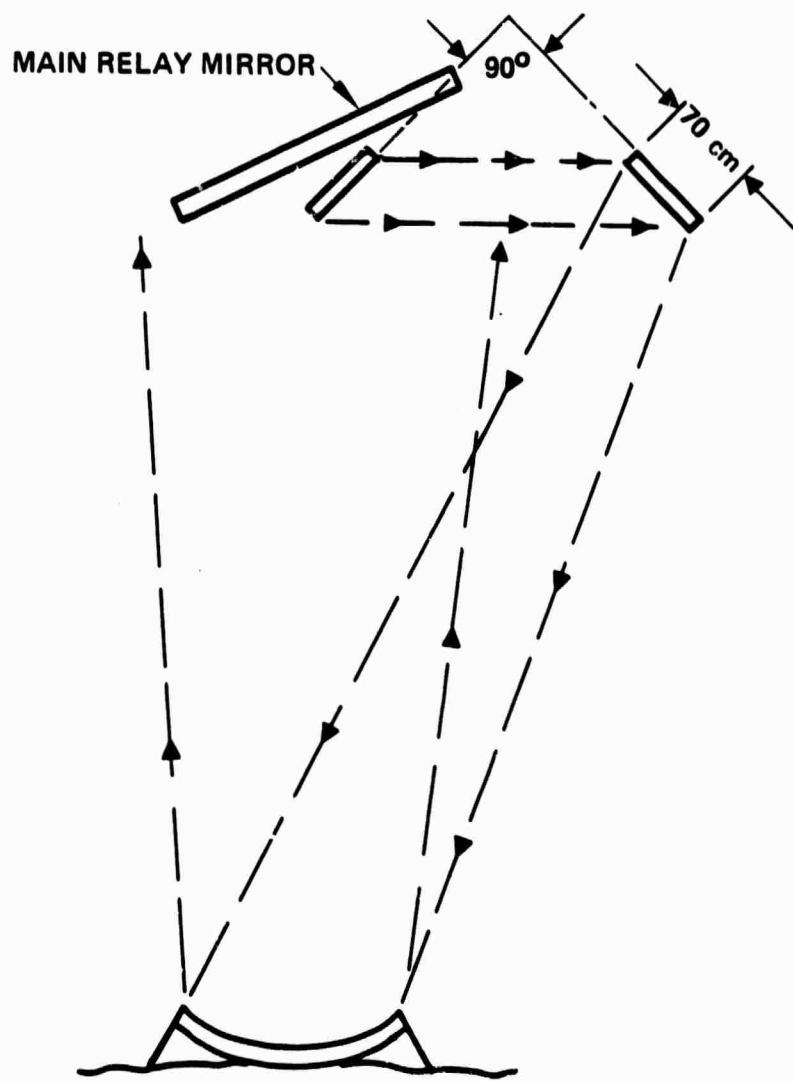
Figure 6-20.   The extended corner reflector system.

need consideration. Some of these are illustrated in Figure 6-21. In Figure 6-21(a) the reference oscillator is in orbit and operation may either be CW or pulsed. In both cases the compensated high-power signal is not reused or iterated. The operation sequence is quite simple. The oscillator output wavefront, which is assumed to be undistorted, transmits downwards "through" the relay mirror, picks up (probes) the atmospheric, optical train and amplifier distortions, "reflects" from the phase conjugator, is again amplified, retransmits through the beam director and the atmosphere, and exits the atmosphere as an undistorted beam. Thus, as the beam propagates to the satellite it is substantially spread only by free-space diffraction. The advantage of such an approach is that the oscillator is coupled with good efficiency to the ground-based beam director; and if Doppler shifts are significant, these are only half the value produced by the retroreflector systems. The drawbacks are substantial, however. One must incorporate a high quality tracker system on the reference satellite, such that the oscillator beam director remains precisely pointed at the ground-based beam director. Independent of tracking problems, the orbital deployment and maintenance of even a modest power laser is troublesome.

The system shown in Figure 6-21(b) avoids the need for a space-based laser. Specifically, a ground-based reference oscillator injects a train of short pulses (typically about 1 μsec) at a desired pulse repetition frequency. Each injected oscillator pulse generates a triplet of pulses (as illustrated in Figure 6-21(b)), roughly spanning the round-trip propagation time. The first pulse of the triplet reflects off of a corner reflector or other retro system, returns after the round trip delay as a second pulse with superimposed atmospheric/amplifier distortions, is conjugated and reamplified, and returns to the satellite as the higher-power and wavefront-compensated third pulse of the triplet. The conjugator or amplifier is then temporarily deactivated such that no further iteration occurs before the next oscillator pulse is injected into the system. A typical timing sequence for this system is illustrated in Figure 6-22(a).

TIME

(a) OSC ON RELAY (CW) (b) OSC ON GROUND (3 PULSE SYSTEM) (c) OSC ON GROUND (ITERATED PULSE)
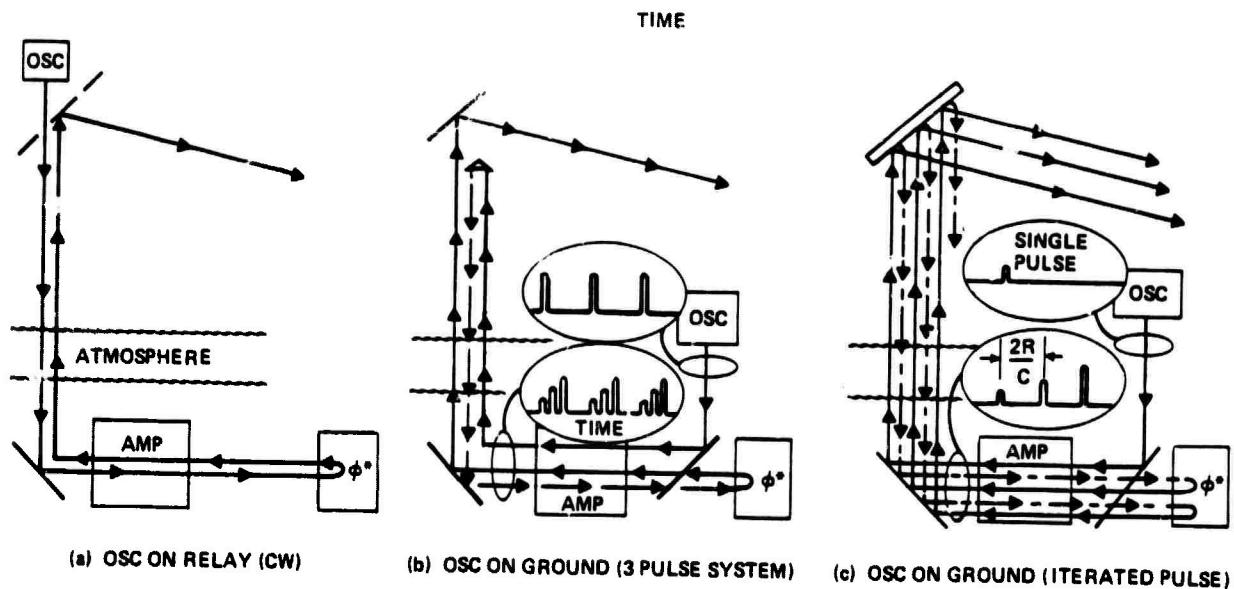
Figure 6-21. Reference injection and iteration techniques. The actual reference (oscillator or retro) position is ahead of the main mirror as illustrated in Figures 6-19 or Figure 6-20.

REF OSC INJECTED
PULSES

SPURIOUS REF PULSES
VIA MAIN ILLUMINATOR REFLECTIONS

TIME →

REF RETURNS FROM REF RETRO

TIME →

MAIN ILLUMINATOR PULSES
(EXITING BEAM DIRECTOR)

$\frac{2R}{C}$ $\frac{2R}{C}$

TIME →
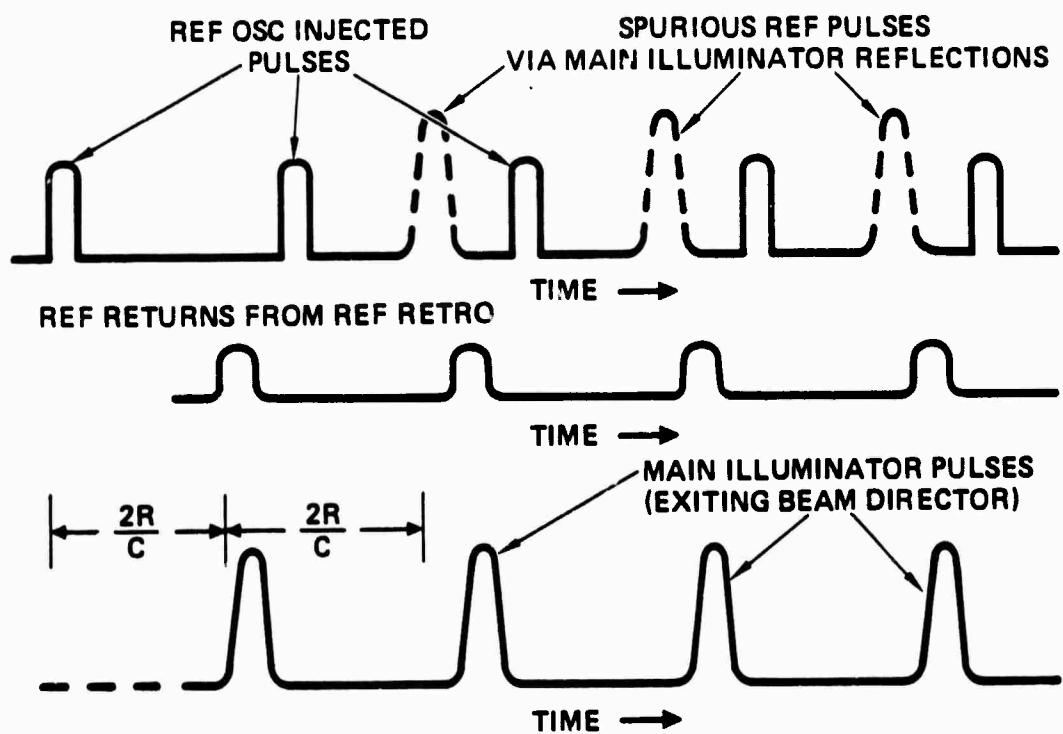
Figure 6-22a.   Triple pulse operation with a satellite reference
reflector.

INITIAL REF
OSC INJECTION

ITERATED
REFERENCE RETURNS

TIME →
REFERENCE RETURNS

TIME →

$\frac{2R}{C}$ $\frac{2R}{C}$

MAIN ILLUMINATOR
PULSES

TIME →
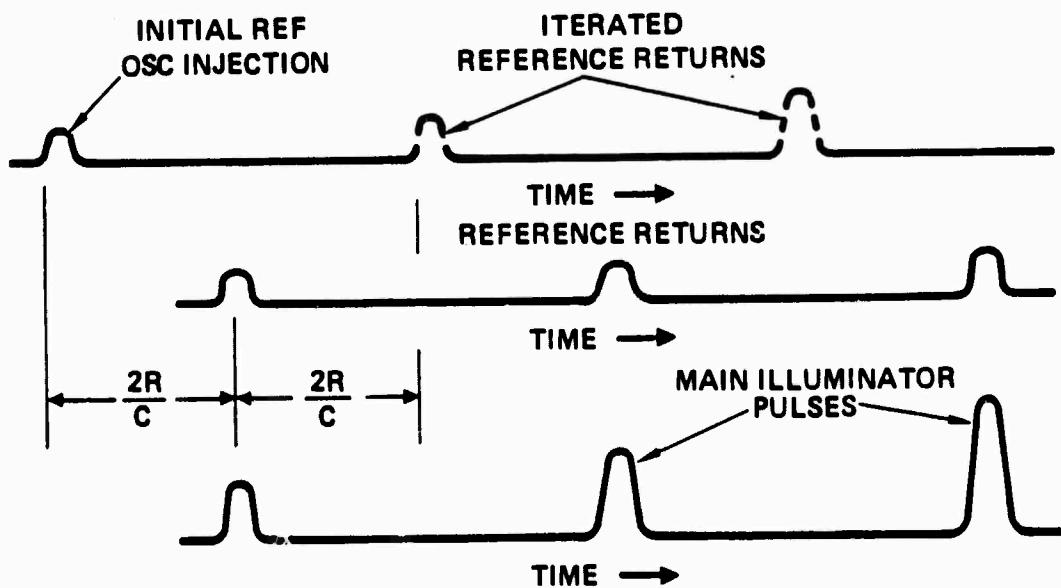
Figure 6-22b.   Iterated pulse operation with a satellite reference
reflector.

Such an arrangement can be aperiodic, and can therefore be employed for a pulse-position-modulation communication system (wherein the satellite is a relay station), since the timing of the final output pulse may be set by perturbing the timing of the initial oscillator input pulse. Although the system can be operated with an output pulse repetition interval corresponding to about two times the one-way propagation time, it can also be operated via pulse interleaving at most shorter pulse repetition intervals. The major drawback of the system shown in Figure 6-21(b) is probably the inefficient coupling of the initial illuminator from the beam director to the reference retroflector. This is a consequence of having an initial illuminator pulse in the triplet which experiences minimal propagation path compensation.

Figure 6-21(c) illustrates a different mode of operation, which we call an iterated-pulse mode. In this mode a single, relatively weak, oscillator pulse is injected to start the operation, and the first three pulses function rather like the B system. In this system, however, a portion of the compensated third pulse is split out* to form the next reference illuminator, and each successive reference is obtained by splitting out a portion of an earlier compensated** pulse, as illustrated in more detail in Figure 6-22(b). We find by computer simulations that typically four to six cycles are required to build up to an essentially steady-state condition. The final output level is largely determined by amplifier saturation. The major advantage, compared to the B system (triple pulse mode), is that the system coupling efficiency is much improved.

---

*The split off is easily achieved with a weak diffraction grating on any conventional flat mirror in the optical relay train or beam director.

**If one illuminates an offset retroreflector via a shared aperture illuminator, then the compensation on the retro illuminator beam is degraded by the atmospheric anisoplanatic problem discussed earlier. But the coupling efficiency improvement is still very substantial.

This system can also be operated quasi-cw by employing an initial oscillator pulse of duration equal to the round-trip time. In such a mode the system iterates indefinitely on the initial pulse, giving a system operation that is effectively cw (i.e., a system that transmits continuously for several seconds or more).

As usual, one pays a price for the improved coupling efficiency permitted by this mode of operation. If a Doppler shift exists, the iteration process progressively accumulates the shift on each iteration, such that the sequence must either be periodically interrupted to "dump" the acquired shift, or the shift must be measured and compensated within the four-wave mixer itself. Further, we can find no really effective method to accommodate a pulse-position modulation format, since the timing of the scheme is intrinsically tied to the round-trip propagation time. As with the B system, when operating in a short-pulse mode, the pulse repetition interval can be effectively reduced by interleaving additional pulses in the middle of the transit interval.

6.5.4 Path Coupling Factors

One of the key differences that we have found between the classes of reference injection systems discussed in the previous section is the relative size of the coupling factors between the reference and the input to the laser on the return path. To be more explicit, Figures 6-23(a) and 6-23(b) define path coupling factors F_p which involve one-way losses for the orbiting oscillator (1a), and two-way losses for the orbiting retro (1b). Amplifier gain factors, $\widetilde{G}_o$ and conjugator reflectivities R_c, are also defined in this figure. In either case, the output power P_{out} on the final pass out of the amplifier is relatable to the oscillator power P_{osc} by the expressions

$$\frac{P_{out}}{P_{osc}} = \widetilde{G}_o{}^2 F_p R_c \quad \text{(orbiting osc)} \tag{6-5-1}$$

and

$$\frac{P_{out}}{P_{osc}} = \widetilde{G}_o{}^3 F_p R_c \quad \text{(retro system)} \tag{6-5-2}$$

6-51
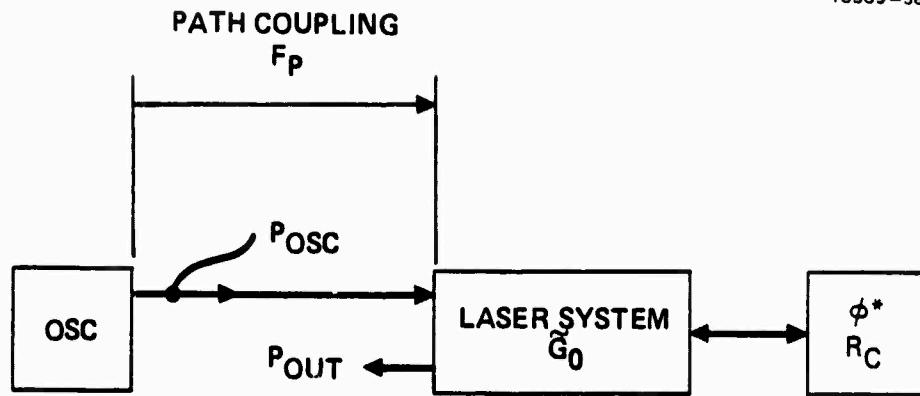
PATH COUPLING
F_P

Figure 6-23a. Path coupling factor and power levels with an orbiting oscillator reference. The parameter $\tilde{G}_0$ is the one way saturated power gain and R_c is the conjugator reflectivity.
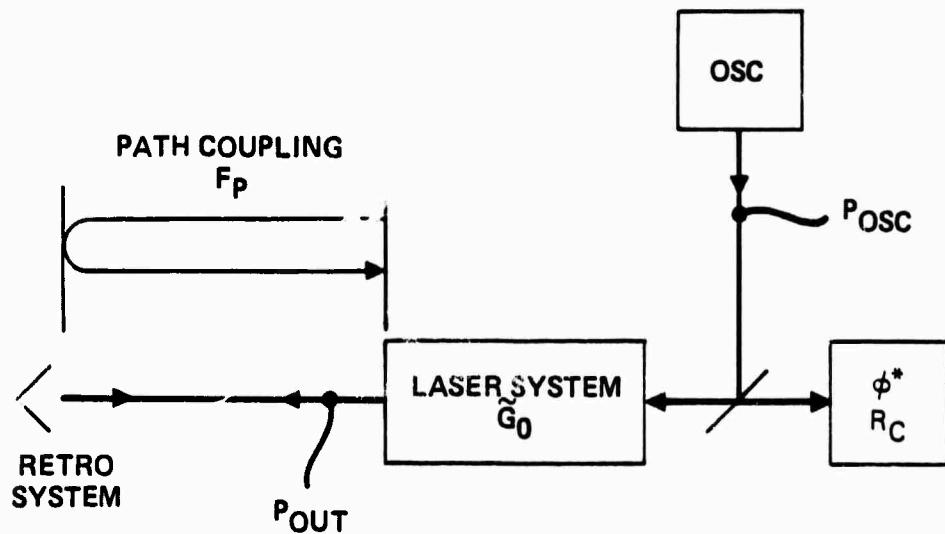
PATH COUPLING
F_P

Figure 6-23b. Path coupling factor and power levels with an orbiting retro system.

where $\tilde{G}_o$ is the one-way gain under actual operating conditions, generally with the amplifier well saturated. Equation 6-5-2 assumes that the beam splitter contributes no path loss and that the main laser is employed for the initial illuminator. Otherwise, self-evident modifications are required.

For example, if we choose to operate an orbiting oscillator system with a reference path coupling factor of 10^{-3}, an amplifier gain of 100, and a conjugator having a reflectivity of unity, then the required oscillator power would be one tenth of the output power - a level which could be prohibitively high. Thus it is important to produce path coupling factors which are as large as possible in these systems.

In order to compare these factors for the various systems previously discussed, we have chosen a stressing case - operation of the relay and reference in synchronous orbits. The ground-based collecting aperture diameter was chosen as 4 meters, and the orbiting oscillator beam director or retro system diameter was chosen as 70 cm, with the resultant total coupling factors illustrated in Table 6-1. The separate factors for the up and down links are also listed. Absorption losses must be factored in for total effective coupling factors. The up-link coupling factors for cases B and C are strongly dependent upon the atmospheric turbulence factors. We have chosen a case corresponding to a coherence length (r_o) of 6 cm. In system B, a partially compensated illuminator aperture of 30 cm diameter (an optimum diameter) is employed with tilt compensation - more specifically, anisoplanatic tilt compensation is assumed. A 3 dB extinction loss was assumed in each direction. As a consequence of the anisoplanatism, the coupling factor depends on the turbulence versus altitude distribution. Two cases are illustrated: (a) the Miller-Zieske Model, and (b) the Barletti Model.

Table 6-1. Example Path Coupling Factors for the
Reference, with Systems A, B, and C

System	Upwards Coupling Factor	Downwards Coupling Factor	Net Coupling Factor
A (Orbiting Ref)		3×10^{-2}	3×10^{-2}
B (Gnd Ref- Triple Pulse)	2.4×10^{-5}	3×10^{-2}	7×10^{-7}
C (Gnd Ref- Iterated Pulse, Simple Retro)	(a) 4×10^{-3} (b) 1×10^{-4}	3×10^{-2}	(a) 1.2×10^{-5} (b) 3×10^{-6}
C' (Gnd Ref- Iterated Pulse, Extended Retro)	3×10^{-2}	3×10^{-2}	9×10^{-4}
(a) Miller-Zieske Model (6-3) (b) Barletti Model (6-2)			

As a consequence of the low degree of compensation of the illuminator
pulse in system B, the up coupling is particularly inefficient. In system C
since the illuminator atmospheric path is (eventually) compensated by the
conjugator, the coupling is much improved. With the extended retro system
(C') the atmosphere produces only a minor correction to the path coupling
factor.

6.5.5 Blue Green Systems

One version of the submarine-laser-communication (SLC) system utilizes a
ground-based communication signal source at 0.5 μm, propagates this source to
a satellite and re-transmits it back to earth. Since large ground-based
optics (∿4m) are required to obtain small diffraction spots at the synchronous
orbits of interest, atmospheric turbulence represents a major potential
performance loss to the system. Also, since conventional adaptive optics are

severely challenged by the SLC system, this seems to be a natural system in which to attempt to include nonlinear correction of atmospheric turbulence. The most promising method for obtaining powers sufficient for SLC in the blue green band is with Raman amplification of an excimer laser. Thus, we will consider possible coupled Raman amplifier, nonlinear phase conjugator systems in this chapter. Chapter 7 gives a more detailed discussion of the properties of a Raman amplifier which are needed for these systems. For reasons given in Chapter 7, it appears sensible to consider a Raman amplifier system in which both the reference wave and the conjugate wave are amplified by forward Raman scattering in the same Raman cell. As shown in Figures 6-24 and 6-25 this requires a bidirectional pumping system with an optical delay line to avoid overlapping pump pulses and possibly competing Raman processes. Figure 6-24 shows an orbiting reference oscillator, while Figure 6-25 shows an orbiting retroreflector. We discuss each of these in the subsections which follow.

6.5.5.1 Orbiting Retroflector Systems

For a communications application, Figure 6-22 details a triple pulse system (after system B of Section 6.5.3), with the timing of the initial pulse ultimately setting the temporal position of the final communication pulse. Thus, in addition to the basic Raman pumping pulses for the reference and conjugate wavefronts, a third pumping pulse may be employed (with the B approach), which pumps the amplifier for the initial retro illumination pulse in the triple pulse sequence. The pump pulses for the initial pair of signal pulses (reference illuminator and returning probe) need not be at the full signal strength required for the main output signal. Since the path coupling factors, as discussed in the previous section, are extremely low for this class of system, the design is stressed by the gain requirements on the SRS amplifier. We will discuss this later in more detail.

An alternative to configuring a triple pulse communication system is to use a separate amplifier and (possibly) a separate beam director. For the initial pulse approach, this would require a second precision pointing and
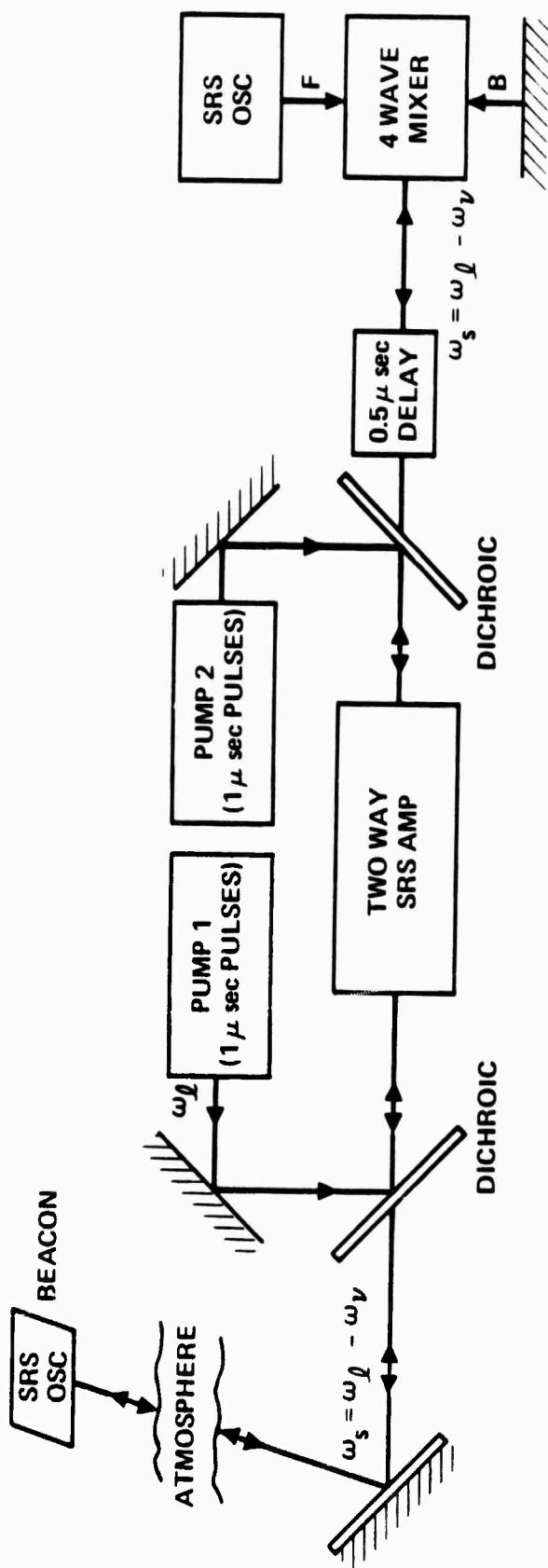
Figure 6-24. SRS amplifier system with remote orbiting reference.
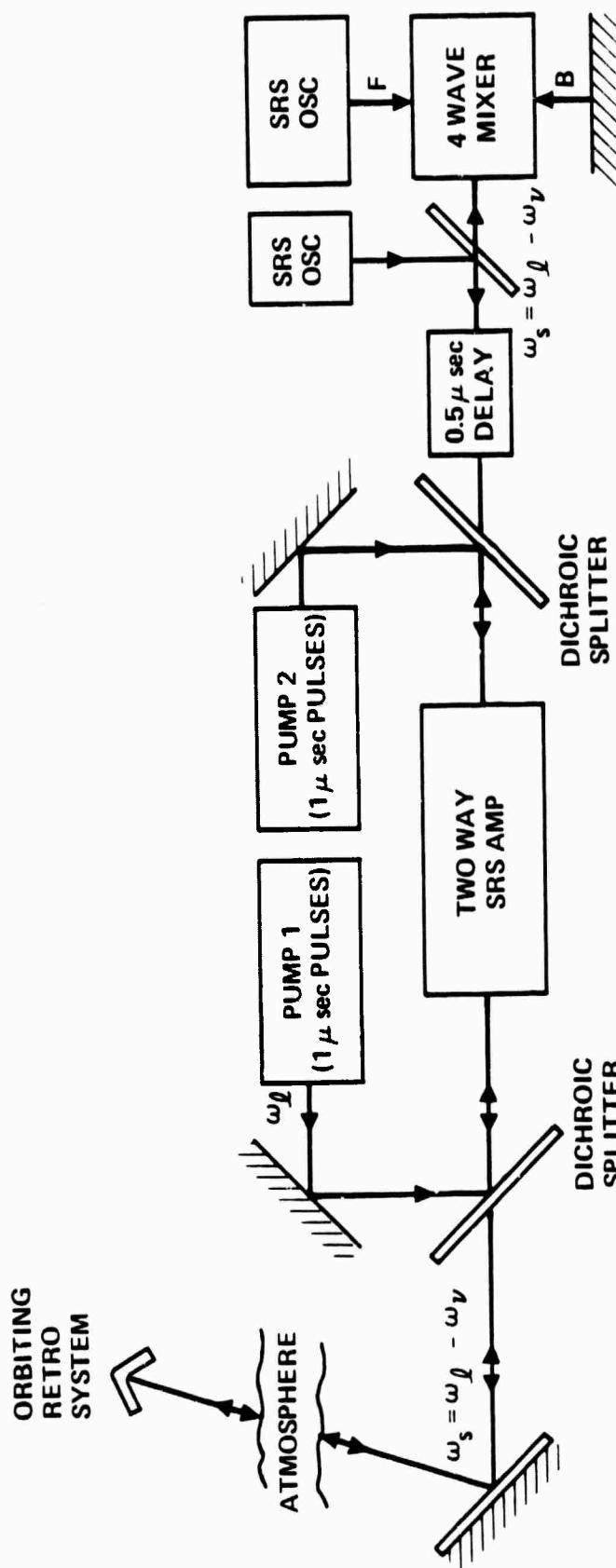
Figure 6-25. SRS amplifier system with a retro reflector reference.

tracking system for the initial pulse illuminator, which could be coaxially mounted (in the obscuration zone) on the main beam director. In any event, the initial illuminator would employ a reduced aperture for optimum performance, with fast tracking (tilt) compensation*. Under these assumptions the optimum illuminator diameter is about 30 cm with an atmospheric r_o = 6 cm.

For a retro illuminator system with neither high-order adaptive optics nor nonlinear phase compensation, the illuminator beam in the retro plane will be broken up by atmospheric turbulence producing a radiation speckle pattern with a minimum spatial scale of about 60 m at synchronous altitude and an illuminator 30 cm in diameter. Since this far exceeds a practical retro size, the field incident on the retro will strongly scintillate, as will the received reference field. This will cause a pulse-to-pulse amplitude modulation, including possible pulse "drop outs", which are particularly undesirable in a communications system. The problem is not fundamental, however, and one obvious approach is to reduce the size of the illuminator aperture and accept a loss in coupling efficiency.

A better approach is to conical scan the illuminator beam very rapidly so the the beam averages over many speckle patterns during an illuminator pulse. The same scan can fullfill a tracking function. Note that the system then operates with two independent tracker sensors: (1) A (outgoing-wave) conical scan tracker sensor which accurately measures any slowly varying registration error between the beam and the reference, but is too slow** to accurately assess the atmospherically induced tilt errors; (2) A (return-wave) quadrant detector or similar tracker which accurately measures the high-bandwidth tilt variations introduced by the atmosphere, but provides a biased measure of average positional error, since the measurement provides information about where the reference was rather than where it is. This bias can be estimated and eliminated, but a combining algorithm which

---

* The tilt compensation is subject to anisoplanatic degradation unless a second retro is employed ahead of the main retro, with a corrective system.

** The bandwidth is limited by the round trip transit time which creates a dead time in the servo.

utilizes both estimates is probably the optimum approach. Such systems have yet to be investigated. In any event, the redundancy available from two classes of tracking systems improves reliability at minimal systems cost.

In order to investigate the laser gain requirements, we have chosen a 30 cm reference illuminator aperture and a 70 cm retro with atmospheric factors, as described in Section 6.5.4. The net (illuminator to retro- to beam director) path coupling factor for this system is about 7×10^{-7}, as illustrated in Table 6-1 and Figure 6-26. The illustrated system is intended to produce an output of 4 KJ, 1 µsec pulses at a PRF of 30 pps, which is well coupled to the relay mirror if the conjugator performs correctly. The internal (peak) power levels at key points are also indicated in Figure 6-25. These numbers are intended to reflect saturated conditions in the amplifier. Unfortunately, we have no code to represent the saturation behavior in Raman amplifiers, so we have used a surrogate code employing conventional laser saturation behavior, as described in Subsection 6.3, to obtain a rough estimate of the saturated numbers. This model also predicts the extraction efficiency which, for this case, was 55%. Note that the required small signal gain, $G_o = Exp\, G_{o1}$, is 4×10^4, which would probably be obtained from a cascade of two amplifiers with $G_o = 200$. In the illustrated system, an auxiliary illuminator is employed whose output power is one tenth of the main amplifier output power, 4×10^9 W peak. Note that the average power loading on the conjugator is about 2 kW, which is by no means negligible.

If we take an output beam power density of 10^8 watts/cm^2 as typical of current Raman amplifier state-of-the-art, then about 40 cm^2 in amplifier cross section is required to achieve the desired 4 KJ, 1 µsec pulse.

The key limitation on Raman amplification appears to stem from a parasitic signal generated from thermally excited phonons which couple to the medium by rotational excitation. As an equivalent input signal, this signal has been estimated as about 2 watts/cm^2 (in a H_2 cell at 300° C).[7] With the area cited above, this is effectively an 80 W signal, which is dominated by the 300 W return signal shown in Figure 6-26.
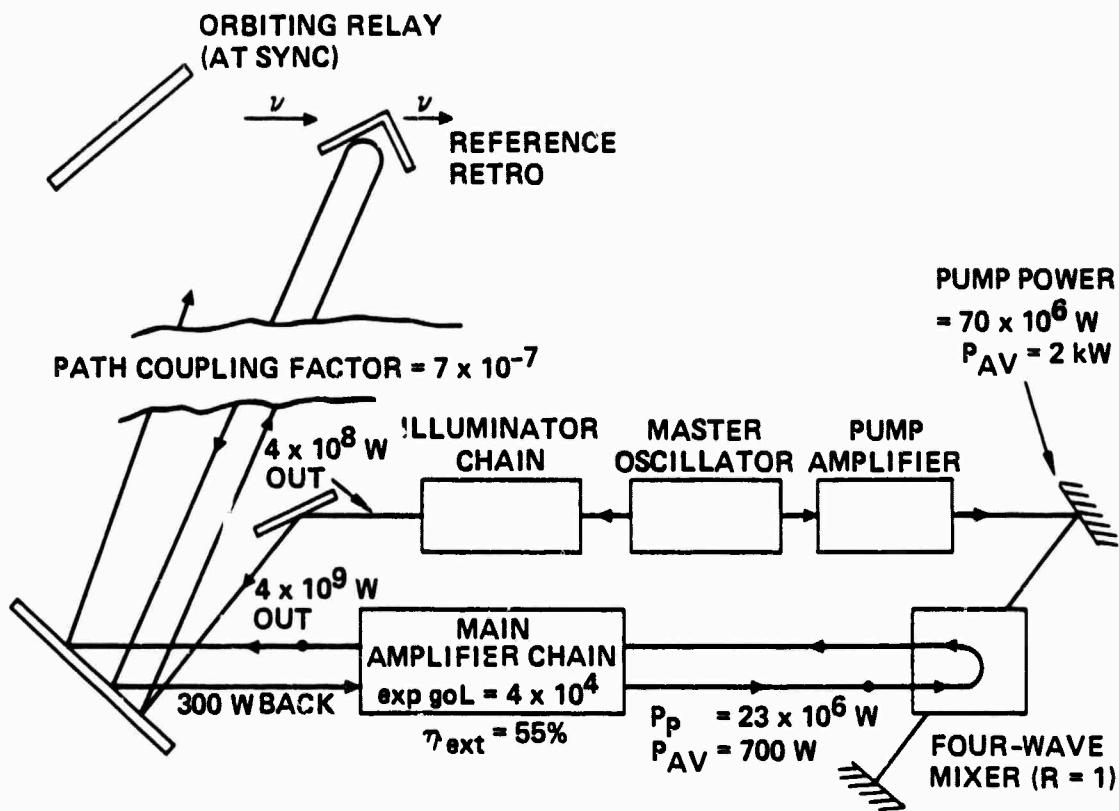
Figure 6-26. A candidate uplink system concept operating with a retro reference.

6.5.5.2 Orbiting Oscillator Systems

This subsection considers the alternative approach wherein an orbiting oscillator injects a reference signal from a dedicated fly-ahead platform as illustrated in Figure 6-27. For a pulse-position communication system, the timing of the oscillator reference pulse controls the ultimate timing of the signal delivered to the relay mirror. Basically, the advantage of this approach is the much higher coupling factors it permits, which reduce the required gain, permitting easier avoidance of parasitic signals.

A secondary laser source (not illustrated in the figures) is required to provide a beacon signal for the pointing and tracking system, which holds the orbiting osc (reference) beam director pointed at the main (4m) ground-based beam director. An alternative tracking system is a high speed conical scan of the space-based beam, operating with a microwave return signal to the space-based beam director. This provides an improved S/N error signal, assuming that the available power from the space laser oscillator would be higher than for the ground beam.

The power levels chosen for the example are illustrated in Figure 6-27. The desired output levels and the laser modeling assumptions are the same as for the orbiting retro system.

6.5.6 UV Pulsed Laser Systems

The system shown in Figure 6-28 uses a pulsed excimer laser with a nonlinear phase conjugator to transmit 25 to 100KJ, one μsec pulses to space. As with the other systems we have discussed, addition of the nonlinear phase conjugator to the excimer system changes the overall configuration. Major considerations in designing such a system are overall efficiency, size of reference beam, size of conjugator, and amplification of noise. Before discussing how these factors are interrelated in the design of a high-energy NPC/excimer system, we should review a few relevant parameters of excimer lasers.

ORBITING LASER BEACON   15 kW 1 μ sec PULSES (P_{AV} = 450 mW)

PATH COUPLING FACTOR = 0.03

PUMP POWER = $\begin{cases} 70 \times 10^6 \text{ W PEAK} \\ 2 \text{ kW AV} \end{cases}$

PUMP LASER

4-WAVE MIXER R = 1

4×10^9 W out

$P_p = 23 \times 10^6$

300 W in

AMPLIFIER CHAIN

exp goL = 4×10^4
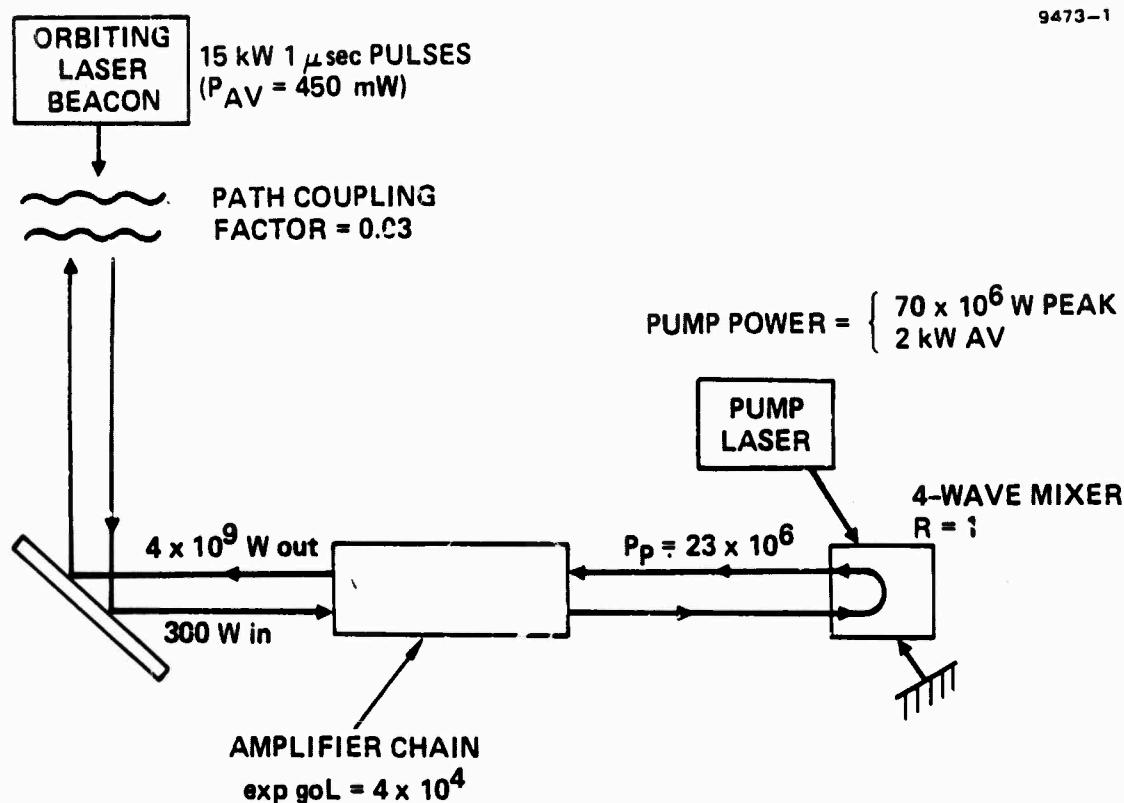
Figure 6-27. Orbiting oscillator candidate uplink system concept.

BEAM DIRECTOR/RCVR

AMP 1 I_2 IN   AMP 2 $\phi *$
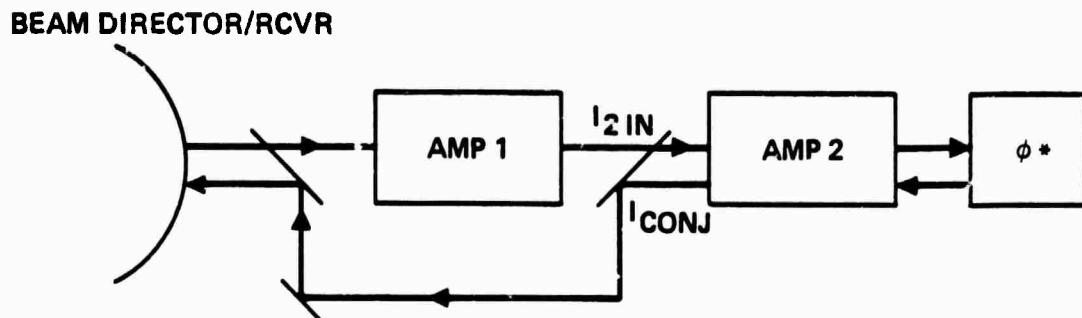
I_{CONJ}

Figure 6-28. A high-gain candidate system for use with excimer lasers. In this mode of operation a preamplifier laser (amp 1) is employed which avoids saturation from I_{conj}.

Table 1 lists typical saturation intensities and small signal gains g_o for excimer lasers. Since pulse lengths of excimer lasers (∿1 usec) are long compared to the gain rise time, and the length of the laser cavities divided by the speed of light, a cw analysis is applicable.[6-4] The intensity I is then given (for one way transmission) by

$$\frac{dI}{dz} = \frac{g_o I}{1+I/I_{sat}} - \alpha I \qquad (6-5-3)$$

The absorption coefficient α is typically an order of magnitude less than the small signal gain g_o in 6-5-1. Equation (6-5-3) can, of course, be solved small signal gain g_o in 6-5-1. Equation (6-5-3) can, of course, be solved in general terms. But for our purposes it is important to use three limiting expressions:

Unsaturated
$$I_{out} = I_{in} e^{(g_o - \alpha)L} \qquad (6-5-4a)$$

Weak saturation
$$I_{out} = I_{sat} g_o L + I_{in} \qquad (6-5-4b)$$

The optimum operating conditions for best extraction of laser energy have been studied,[6-4, 6-8] and similar calculations would clearly be relevant for the whole excimer laser-NPC system.

The overall feasibility of the excimer laser amplifier/phase conjugator chain can be evaluated as follows. The reference irradiance reflected from the target back into the system is assumed to be 1% of the energy reaching the relay. The effective path coupling loss, estimated in Table 6-1, is $4 \cdot 10^{-4}$, allowing for a path absorption loss of 3 dB. Thus, the reference power P_{ref} for a 25 kJ pulse system is

$$P_{ref} = \frac{25 \cdot 10^3 j}{10^{-6} sec} \cdot 4 \cdot 10^{-4} \cdot 10^{-2} = 100 \text{ kW.}$$

Table 6-1. Gain and Saturation Parameters for Rare Gas Halide Lasers
The supercripts are references

Rare Gas Halide	I_{sat}	$g_o (\%/cm)$
KrF	$0.47 \ MW/cm^2$	$3.7^{(6-4,6-5)}$
XeF	$0.088^{(6-4)}$	$\sim 1^{(6-6)}$
XeCl	$0.13^{(6-7)}$	$3.5^{(6-4,6-7)}$
XeBr	$0.27^{(6-4)}$	

Assume amplifier 1 is 10 cm in radius with $g_o L = 5$. Spreading P_{ref} over a circle 10 cm in radius yields $I_{ref} = I_{1in} = 318 \ w/cm^2$. Since amplifier 1 is unsaturated, 6-5-4a gives

$$I_{1out} = I_{1in}e^5 = 47.2 \ kW/cm^2 \quad .$$

Assume amplifier 2 is 1.0 m in radius with $g_o L = 5$ then

$$I_{2in} = .472 \ kW/cm^2$$

Assuming that the conjugate and reference waves are not simultaneously in amplifier 2, we obtain

$$I_{2out} = .472 \ e^5 = 69.9 \ kW/cm^2 \quad .$$

The output irradiance, after amplification, of the conjugate wave is via[6-5-4b],

$$I_{2out}^{conj} = I_{sat}g_oL = 1 \text{ MW/cm}^2 \quad ,$$

which represents a gain of 14.

If the reference wave and the conjugate wave propagate through amplifier 2 simultaneously, the equations for the intensities are coupled:

$$\frac{dI_{ref}}{dz} = \frac{g_o I_{ref}}{1 + \frac{I_{ref} + I_{conj}}{I_{sat}}}$$

$$\frac{dI_{conj}}{dz} = \frac{g_o I_{conj}}{1 + \frac{I_{ref} + I_{conj}}{I_{sat}}}$$

These equations can be solved in general.[6-8]

This reference demonstrates that the total gains of the conjugate wave and the reference wave in amplifier 2 are equal. This may mean that the reference signal requires a second stage of independent amplification, or that both reference and conjugate signals require two stages of amplification.

The requirement of efficient extraction from the last stage of a high-power amplifier means that amplitude variations of the output conjugate field are largely independent of those on the input conjugate field. If·these distortions are required in the correction process (e.g. turbulence scintillations), then saturated operation degrades the performance of the full NPC-laser system.

Major issues that require work before a NPC-excimer system can be designed are related to conjugator materials and performance. Phase conjugation in the UV has been demonstrated recently,[6-9] but major advances are required before one can confidently design a phase conjugator for 25 to 100 kJ, μsec pulses, operating at high average powers.

REFERENCES

6-1. D.M. Pepper and A. Yariv, "Compensation for Phase Distortions in Nonlinear Media by Phase Conjugation," Opt. Lett. 5, 59, February 1980.

6-2. R. Barletti, Et al. "Mean Vertical Profile of Atmospheric Turbulence Relevant for Astronomical Seeing," J. Opt. Soc. Am., 66, 1380 (1976)

6-3. M.G. Miller and P.L. Zieske "Turbulence Environment Characterization," AVCO Everett Interim Technical Report for Contract F30603-76-C-0054 (1976).

6-4. M. Rokni, J.A. Mangano, J.H. Jacob, and J.C. Hsia, "Rare Gas Fluoride Lasers," IEEE J. Quantum Electron., QE-14, 464 (1978).

6-5. R.S. Bradford, Jr., W.B. Lacina, E.R. Ault, and M.L. Bhaumik, "KrF Small Signal Gain Measurements and Kinetic Modeling," in Electronic Transition Lasers eds L.E. Wilson, S.N. Suchard, and J.I. Steinfeld, MIT Press, Cambridge, 1977 p.3.

6-6. C.H. Fisher and R.E. Center, "Threshold Power Density Measurements for Electron Beam Sustained Discharge Excitation of XeF and KrF," in Electronic Transition Lasers eds L.E. Wilson, S.N. Suchard, and J.I. Steinfeld, MIT Press, Cambridge, 1977 p.3.

6-7. R.T. Brown and W.L. Nighan, "UTRC Blue/Green Laser Research," in Strategic Laser Communications Program, Vol. 1 Naval Ocean Systems Command Technical Document 352, 1980 p. 249.

6-8. W.W. Rigrod, "Saturation Effects in High-Gain Lasers," J. Appl. Phys., 36, 2487 (1965).

6-9. B.J. Feldman, R.A. Fisher, and S.L. Shapiro, "Ultraviolet Phase Conjugation," Opt. Lett., 6, 84, 1980.

6-10. Wang, Chen-Show, "Theory of Stimulated Raman Scattering," Physical Review, 182, Number 2, June 10, 1969.

CHAPTER 7

USE OF A RAMAN AMPLIFIER AND A NONLINEAR CONJUGATOR IN AN HEL SYSTEM

7.1 INTRODUCTION

There are two major reasons why a Raman amplifier may replace a conventional laser power amplifier in the classes of nonlinear conjugation systems discussed in Chapter 6. First, some high energy systems require use of a Raman amplifier to shift the system wavelength into an atmospheric or oceanic transmission window. Second, the Raman amplifier may provide significant system advantages over the power amplifier in areas such as gain, efficiency, reference injection, and wavefront fidelity. In the next section we discuss the basic properties of a Raman amplifier in a nonlinear conjugation system. Section 7.3 derives general relations for the gain and efficiency of the Raman amplifier. Saturation effects are discussed in Section 7.4. Section 7.5 gives a preliminary discussion of wavefront fidelity in Raman amplifiers. And in Section 7.6, illustrative numbers are given for H_2 used as a Raman medium to shift to the blue green wavelength, 500 nm.

7.2 BASIC PROPERTIES OF NONLINEAR CONJUGATOR/RAMAN AMPLIFIER SYSTEM

Two typical Raman amplifier, nonlinear conjugator systems are shown in Figures 7-1a and 1b. Although the systems are similar to the laser amplifier systems discussed in Chapter 6, there are a number of essential differences. The Raman amplifier operates by converting pump laser photons to signal photons plus vibrational phonons. Thus saturation occurs when all of the pump photons are converted to signal photons or when the vibrational state saturates. In addition, higher order processes such as second-order Raman scattering, anti-Stokes cattering, and backward Raman scattering, may remove energy from the amplified signal. In contrast to conventional amplifiers, pump, as well as medium aberrations may be transferred to the signal. Also, in Raman amplifiers the gain and amplification in the forward and backward

directions are unequal. When signal and pump are copropagating, the gain is normally higher,[7-1] and in many cases, the signal pulse shape replicates that of the pump. In the backward or counterpropagating direction, the gain is usually lower, but the amplified signal is greatly compressed.

The usual requirement that the reference field and its conjugate reflection propagate through the same distorting media means that the Raman amplifier shown in Figures 7-1a and 7-1b must be used in both directions. The alternatives are two separate Raman amplifiers, one on each path, or one amplifier on the outgoing path alone, and none for the reference. The obvious disadvantage of these alternatives is that the Raman medium and optics distortions are not compensated. Thus we assume, as Figure 7-1a indicates, that both signals propagate through the same SRS amplifier. There are at least four modes of operation with both signals using the same amplifier:

(1) Put both reference and conjugate waves in the amplifier simultaneously and adjust length of reference pulse so that compressed pulses are of desired length.

(2) Pump amplifier from both directions simultaneously.

(3) Use a delay line in Case (1), so that reference and conjugate waves are not in the amplifier simultaneously.

(4) Use a delay line and pump alternately from each side so that both the reference and the conjugate signal are amplified by forward SRS.

(5) Use polarization diversity in Case (1).

All of these cases, with the exception of Case (4), correspond to unexplored modes of operation of an SRS amplifier. Case (4) is shown in Figure 7-1b, and dealt with using results for conventional SRS amplifiers; its major problems are the delay line and the two pumps. Results which give necessary conditions for operation of an SRS amplifier in Case (4) are expected to be relevant to the other cases, but these cases may have additional requirements. For instance, in Case (1), although SRS has been observed simultaneously in both directions in the same gas cell, to the best of our knowledge, simultaneous amplification of input signals in both the forward and backward direction has
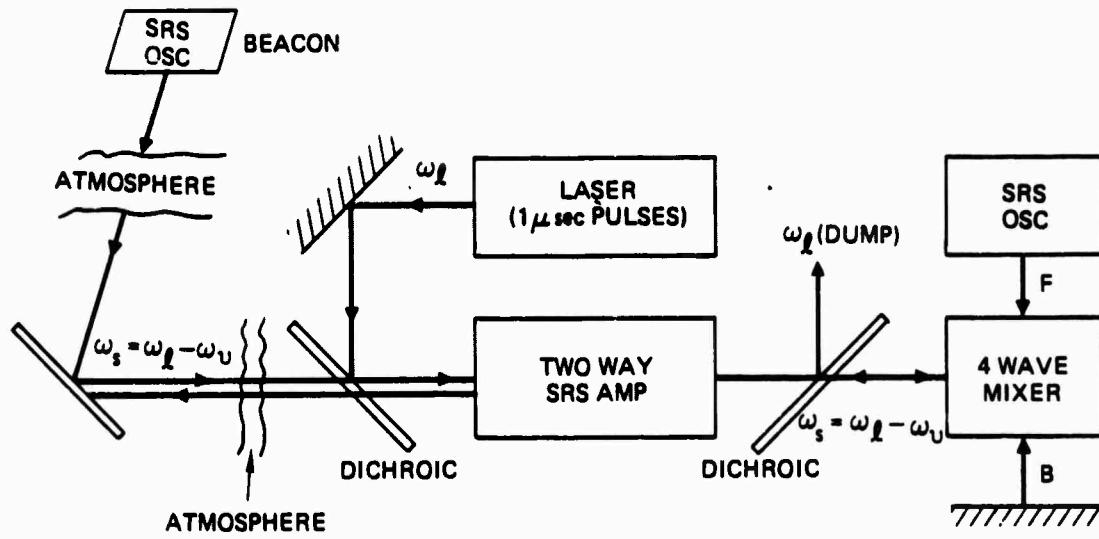
Figure 7-1a. A general block diagram of SRS amplifier/conjugator system with remote (orbiting) reference.

10689—27
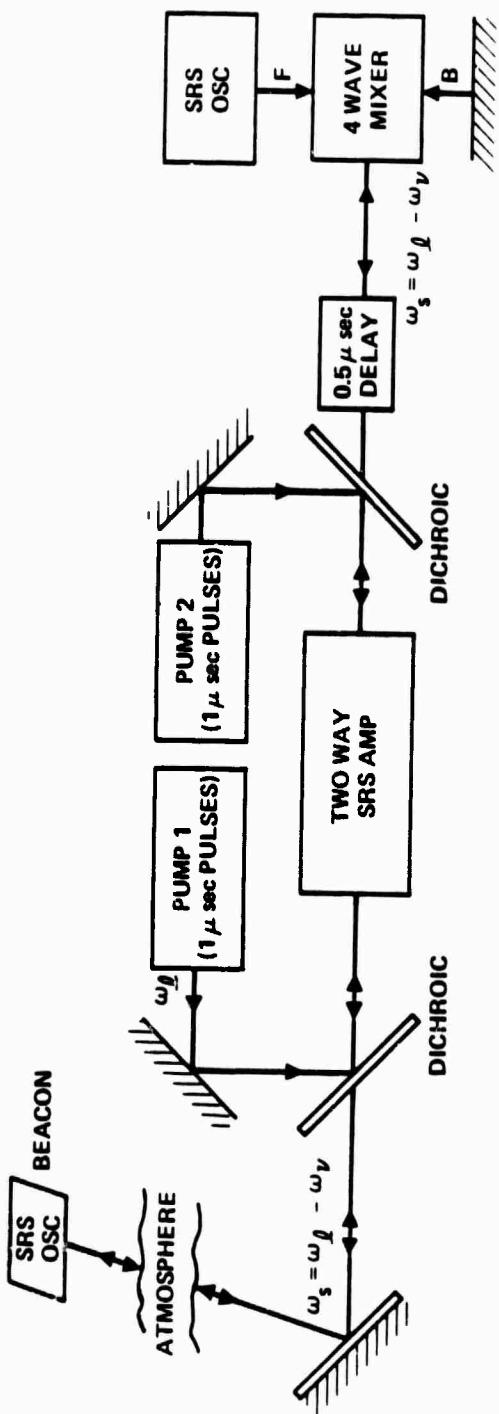
Figure 7-16. SRS amplifier using forward SRS for amplication of both reference and conjugate wave.

not been reported. While there appears to be no fundamental reason why two-way amplification cannot be achieved, it seems likely that the large ratio of outgoing-to-reference intensities will cause problems in amplifying the reference signal. These include competition between other orders of Stokes and anti-Stokes waves and the desired signal, as well as growth from noise competing with amplification of the input signal.

In the next three sections, we discuss SRS amplification of one signal in the forward direction. These results are then applicable only to the fourth case, or mode of operation, discussed above. However, it is expected that if the gains, efficiencies, and wavefront fidelity for a simple forward SRS amplifier are unacceptable, then these properties for Cases (1), (2) and (3) will also be unacceptable.

7.3 SRS GAIN AND EFFICIENCY

In this section we derive expressions for the gain and efficiency of a forward SRS amplifier, in the absence of saturation, second and higher order Stokes scattering and anti-Stokes scattering. The basic equations for forward SRS are [7-1 to 7-3].

$$\frac{\partial E_s}{\partial z} + \frac{1}{v_s} \frac{\partial E_s}{\partial t} = -iK_2 Q^* E_L \tag{7-1}$$

$$\frac{\partial E_L}{\partial z} + \frac{1}{v_L} \frac{\partial E_L}{\partial t} = -iK_2 \frac{\omega_L v_L}{\omega_s v_s} Q E_s \tag{7-2}$$

$$\frac{\partial Q^*}{\partial t} + \Gamma Q^* = +iK_1 E_L^* E_s \tag{7-3}$$

7-5

$$\text{where} \qquad K_2 = \frac{\pi N \omega_s v_s \mu_{12} \mu_{23}}{c^2 h \Delta_L} \qquad\qquad (7\text{-}4)$$

$$K_1 = \frac{\mu_{12} \mu_{23}}{2h^2 \Delta_L} \qquad\qquad (7\text{-}5)$$

E_s is the signal or Stokes field strength

E_L is the laser or pump field strength

$\omega_s(\omega_L)$ is the signal (laser) frequency

$v_s(v_L)$ is the signal (laser) group velocity

Q is the vibrational coherence (off-diagonal matrix element between levels 1 and 3)

μ_{12} and μ_{23} are the dipole matrix elements between the levels shown in Figure 7-2

N is the atomic number density

$\Delta_L = \omega_{21} - \omega_L$ (assuming $\Delta_L \gg \Delta_s \equiv \omega_{31} - (\omega_L - \omega_s)$)

ω_{12} and ω_{31} are the transition frequencies

Γ = dephasing rate for the vibrational coherence.

If the laser and signal time variations are slow compared to Γ^{-1}, Equation (7-3) may be solved

$$Q* = iK_1 \Gamma^{-1} E_L * E_s \quad . \qquad\qquad (7\text{-}6)$$

Substituting Equation (7-6) into (7-1) and (7-2) and writing $I_{L,s} = |E_{L,s}|^2$ yields

$$\frac{\partial I_s}{\partial z} + \frac{1}{v_s} \frac{\partial I_s}{\partial t} = K_1 K_2 \Gamma^{-1} I_s I_L \qquad\qquad (7\text{-}7)$$

$$\frac{\partial I_L}{\partial z} + \frac{1}{v_L} \frac{\partial I_L}{\partial t} = -K_1 K_2 \Gamma^{-1} \left(\frac{\omega_L v_L}{\omega_s v_x} \right) I_s I_L \quad . \qquad\qquad (7\text{-}8)$$
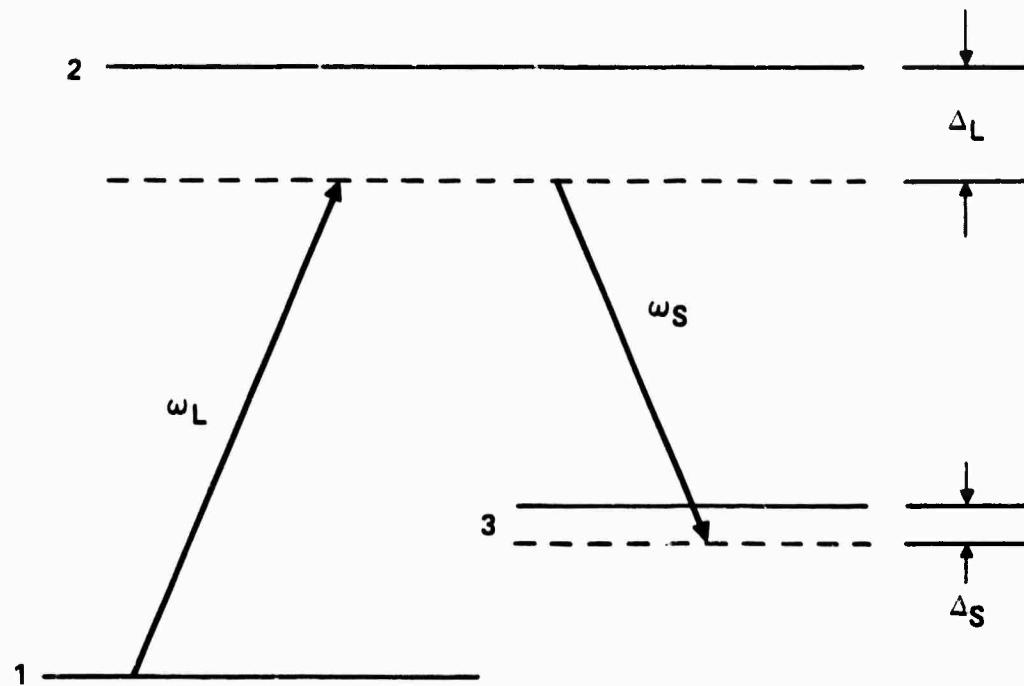
Figure 7-2. Three level system interacting with a pump laser at frequency ω_L and a Stokes signal at ω_S. [7-2]

Equations (7-7) and (7-8) are more conveniently written in terms of the number of photons per cm^3 in the Stokes and laser signals, n_s and n_L. In addition, we set $v_s = v_L$, since our interest is in weakly dispersive gases such as H_2. The equations are then

$$\frac{\partial n_s}{\partial z} + \frac{1}{v} \frac{\partial n_s}{\partial t} = \gamma n_s n_L \qquad (7-9)$$

$$\frac{\partial n_L}{\partial z} + \frac{1}{v} \frac{\partial n_L}{\partial t} = -\gamma n_s n_L \quad , \qquad (7-10)$$

where $n_{s,L} = I_{s,L}/\hbar\omega_{s,L} I$, $\gamma = K_1 K_2 \Gamma^{-1} \omega_L$, and $v_L = v_s = v$. Note that in forward SRS the total photon number density $n_T = n_s + n_L$ is conserved at each point in space.

The solution to Equations (7-9) and (7-10) for an infinite medium (no spatial dependence in γ) and for initial conditions:

$$n_s (t = 0, z) = n_{so}(z) \qquad (7-11)$$

$$n_L (t = 0, z) = n_{Lo}(z) \qquad (7-12)$$

$$n_T (t = 0, z) = n_{so}(z) + n_{Lo}(z) \qquad (7-13)$$

$$n_s(t,z) = \frac{n_{so}(z-vt)}{\left[1 - \frac{n_{so}(z-vt)}{n_T(z-vt)}\right] \exp\left[-n_T(z-vt)vt\right] + \frac{n_{so}(z-vt)}{n_T(z-vt)}} \qquad (7-14)$$

$$n_L(t,z) = n_T(z-vt) - n_s(t,z)$$

Several features of forward SRS amplifications are given by Equations (7-14) and (7-15). Under conditions in which the input Stokes pulse is as

7-8

long or longer than the laser pulse, the Stokes intensity is much less than the laser intensity, and the Raman medium is sufficiently long, one finds that the output Stokes pulse will replicate the laser pulse. If the input Stokes signal is zero or less than the noise level at points where the laser pulse is non-zero, then the noise will be amplified at these points. The small signal gain at the center of the pulse is $\gamma n_T(0)$, but is much lower at the edge of the pulse. These ideas are illustrated in Figure 7-3 which shows the propagation of a gaussian Stokes pulse in a gaussian laser pulse for Stokes pulse length less than, equal to and greater than the laser pulse. Note that when the ratio of the laser to Stokes pulse lengths squared equals ten, the output pulse has not replicated the laser pulse even at $\xi = \gamma n_T(0)vt = 100$. In such a case, the output pulse will very likely be corrupted by amplification of noise. In ordinary SRS generation of wavelength-shifted light, amplification of noise is not a problem. In our case, the amplified noise will contain spurious phase information and may defeat the purpose of the nonlinear conjugator.

The efficiency η of the Raman amplifier may be defined as[7-1]

$$\eta = \frac{n_s(t) - n_s(0)}{n_L(0)} \tag{7-16}$$

For equal laser and Stokes pulse shapes, the efficiency is given by

$$\eta = r_{in} \left[\frac{1 - e^{-\xi}}{r_{in} + e^{-\xi}} \right] \tag{7-17}$$

where $r_{in} = n_s(0)/n_L(0)$ and $\xi = \gamma n_T(t)vt$. Figure 7-4 shows the efficiency as a function of ξ for $r_{in} = 0.001$, 0.01 and 0.1. For practical purposes, the impact of Figures 7-3 and 7-4 is that $\xi \simeq 10$ is required for efficient
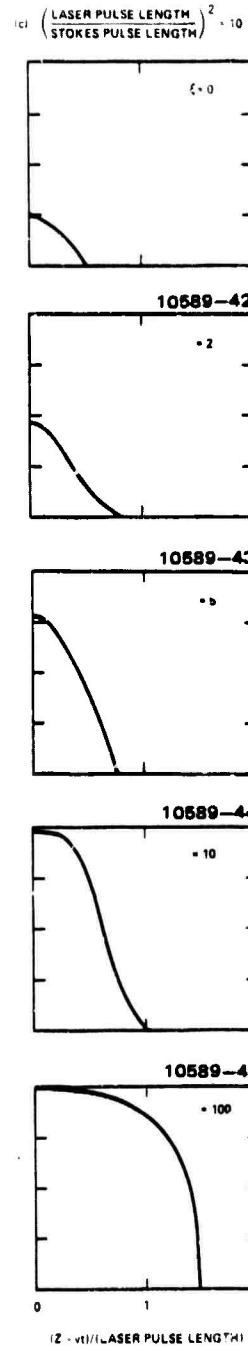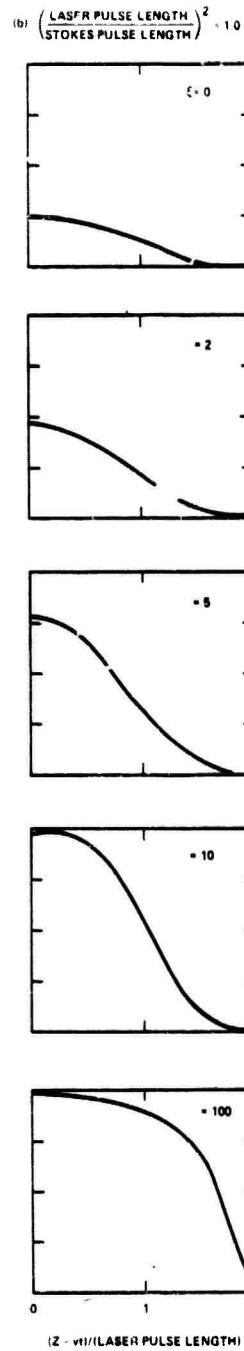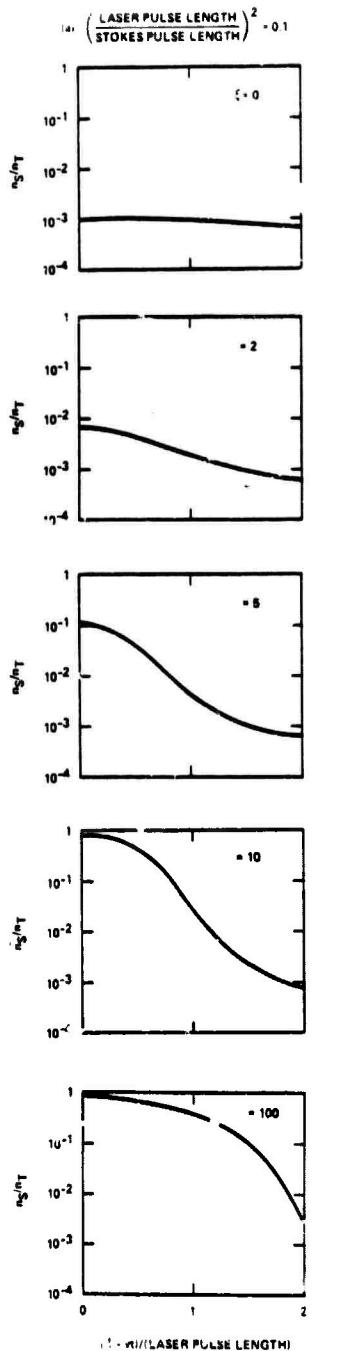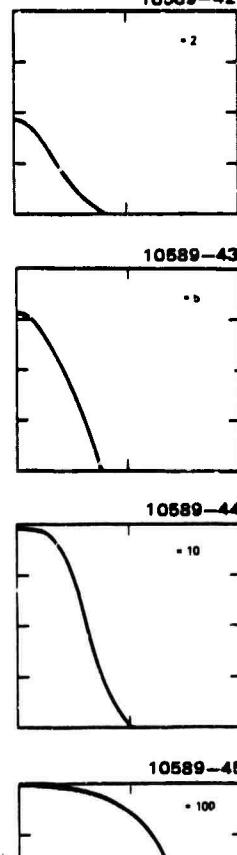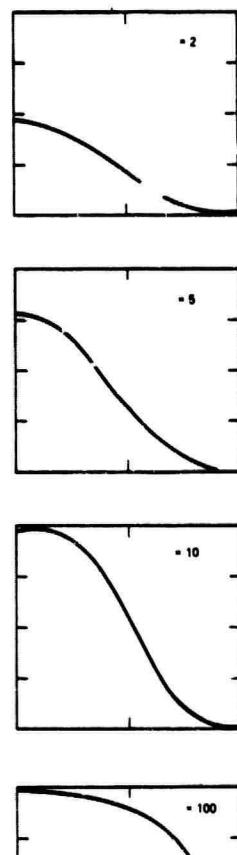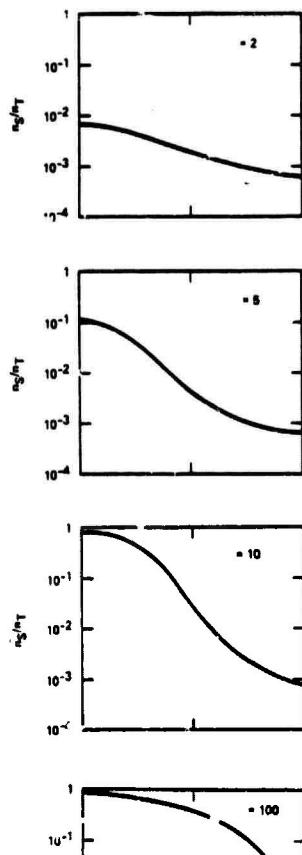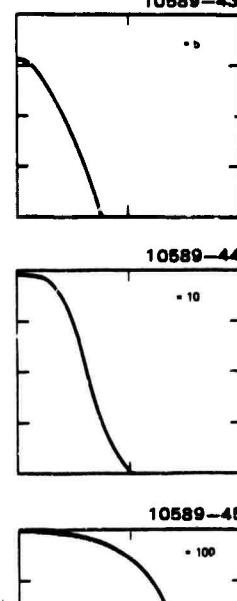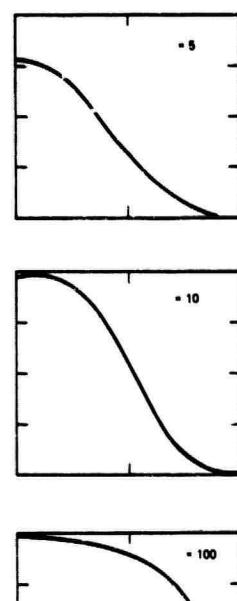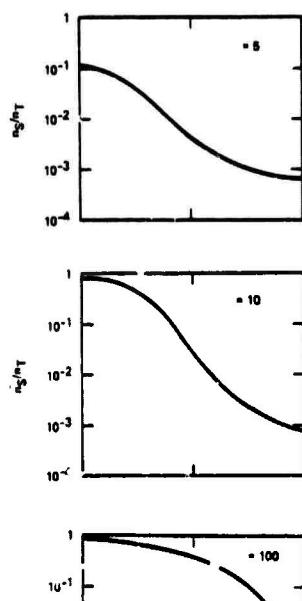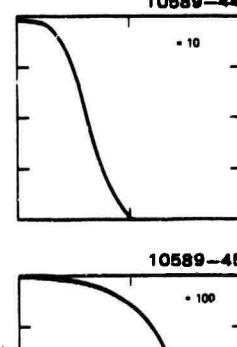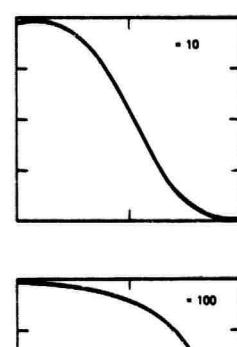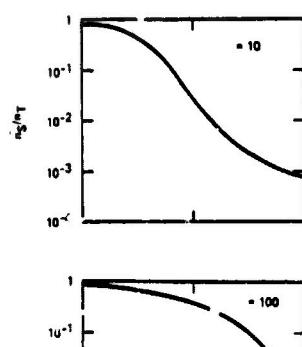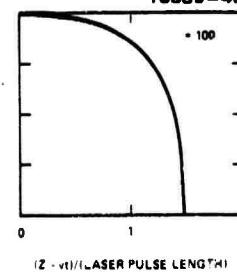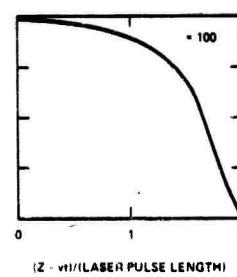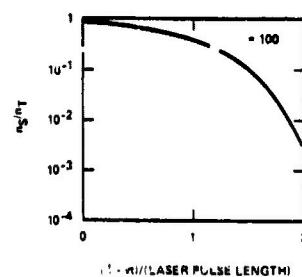
Figure 7-3. Stokes pulse shape distribution as a function of $\xi = \gamma n_T(0) \, t$.
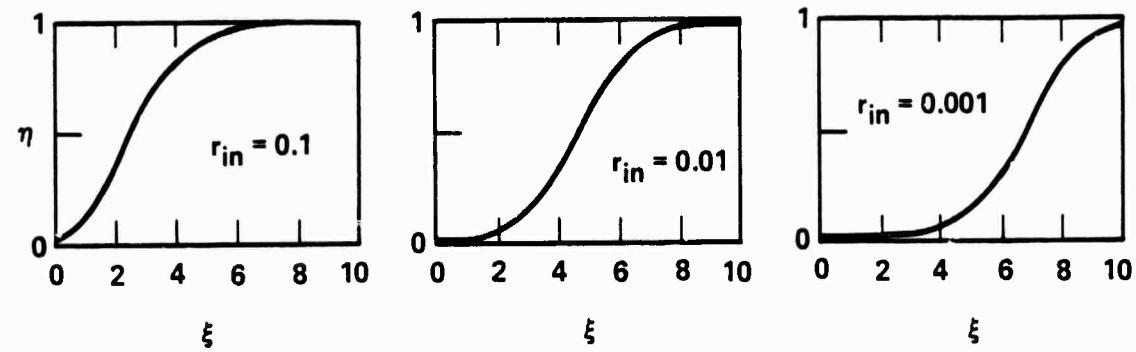
Figure 7-4.   Efficiency η as a function of $\xi = \gamma n_T vt$.

SRS amplifier operation. For a given material γ is a constant, and the condition $\xi \simeq 10$ implies what pump intensities and amplifier lengths are required. A numerical illustration of these requirements is given in Section 7.6.

7.4 HIGHER-ORDER SATURATION EFFECTS

Although the Stokes wave solution presented in the previous section may be said to saturate when the pump photons are entirely converted to Stokes photons, there are several other processes that also may limit the intensity of the first-order Stokes scattering. Before all the pump photons are converted to first Stokes photons, the first Stokes radiation may be converted to second Stokes radiation. In addition, as the vibrational state is populated, the first Stokes signal and the pump signal may both be converted to anti-Stokes radiation. The anti-Stokes scattering from the first Stokes signal is, of course, radiation at the pump frequency. Finally, backward Raman scattering may grow from noise, and take energy out of either the pump or first Stokes wave.

Second-order Stokes scattering has been investigated by several authors[7-5, 7-6, 7-7]. Von der Linde et al.[7-5] solved the following set of equations numerically:

$$\frac{dI_L}{dz} = - g_o I_{S1} I_L - \alpha_o I_L \tag{7-18}$$

$$\frac{dI_{S1}}{dz} = g_{S1}(I_{S1} I_L - I_{S1} I_{S2}) - \alpha_o I_{S1} \tag{7-19}$$

$$\frac{dI_{S2}}{dz} = g_{S2}(I_{S2} I_{S1} - I_{S2} I_{S3}) - \alpha_o I_{S2} \quad \text{etc. ,} \tag{7-20}$$

where I_L, I_{S1}, I_{S2} are the pump, first Stokes and second Stokes intensities, g_o, g_{S1}, g_{S2} are the gain coefficients, and α_o is a wavelength independent absorption coefficient. Figure 7-5, reproduced from [7-5] shows the pump and Stokes intensities as a function of distance and initial pump intensity. Note that by proper choice of the product $Z = zg_o I_L(0)$, it is possible to exit the cell with most of the output intensity in the desired Stokes order. Similar results are found in [7-6]. More complicated results are presented by Butylkin et al.[7-17] They observed generation of second Stokes radiation, both by Raman scattering and by a parametric four-wave interaction. They also observed parametric conversion of radiation at the pump frequency from a combination of second Stokes and first Stokes radiation.

Saturation of SRS due to a population inversion in the vibrational state gives rise to saturation terms analogous to the two-level laser term $(1+I/I_{sat})^{-1}$. This saturation occurs at irradiances on the order of 100's MW/cm. A more important effect of saturation is that it provides a means of potential conversion of pump amplitude variations to Stokes phase variations, which may degrade the compensation system performance as discussed in the next section.
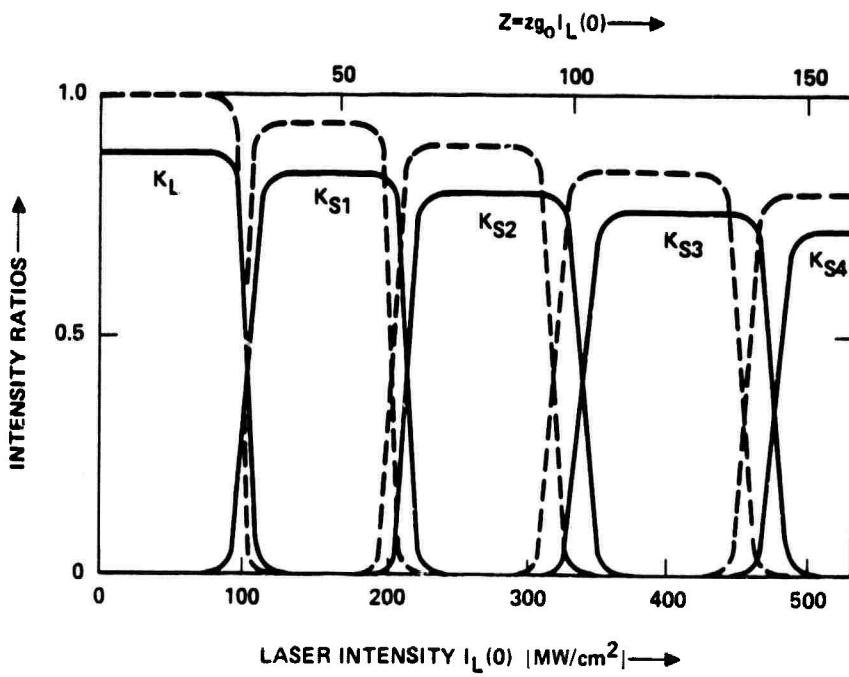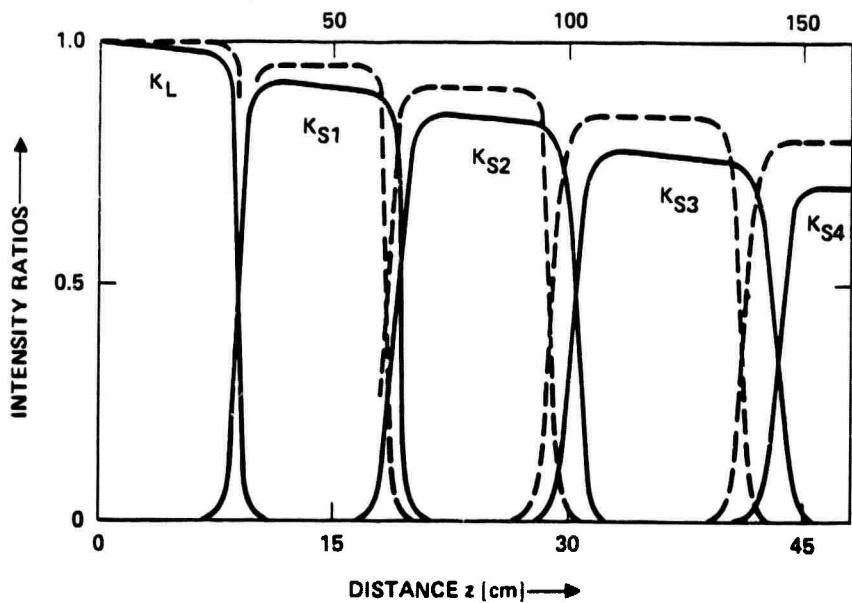
Figure 7-5. Intensity ratios, $I_{L,si}/I_L(0)$ as a function of distance and initial pump laser intensity for absorption coefficients $\alpha_0 = 3 \cdot 10^{-3}$ cm^{-1} (solid curve) and 10^{-4} cm^{-1} (broken curve) from Reference [7-5].

7.5 WAVEFRONT FIDELITY IN SRS AMPLIFICATION

The combination of amplifiers used in a nonlinear phase compensation system must, in general, introduce only reciprocal phase and amplitude aberrations during amplification. For example, in the forward SRS amplifier system shown in Figure 7-1b, linear refractive index fluctuations that vary slowly compared to a pulse length are reciprocal, and hence compensated. On the other hand, aberrations that depend on non-repeatable details of the pump laser, or on the level of amplification, are not the same on each pass through the amplifier. Hence, they are not reciprocal, and not compensated. This section discusses two mechanisms that may cause such uncompensated aberrations, fast pump variations, and vibrational saturation.

Discussion of phase and amplitude transfer from pump to Stokes wave in an SRS amplifier is complicated by what appear to be conflicting results in the literature. Some authors [7-1, 7-8, 7-9] give results that indicate that good Stokes beam quality may be obtained with aberrated pumps, while other results results [7-2, 7-10, 7-11, 7-12] indicate that the Stokes wave will pick up both pump aberrations and the pump spectral distribution. If the pump has good beam quality, the Stokes radiation has been observed to be nearly diffraction limited [7-13]. Buth such a requirement on the pump may greatly decrease the ability of an SRS amplifier to reach high powers. Thus, while a plane wave, uniform-amplitude pump should be sufficient for use in an SRS amplifier for the NPC system, we want to determine the necessary requirements.

There are two basic reasons why these apparently conflicting results have been obtained. First, there are two separate regimes in SRS, depending on whether pump temporal fluctuations are slow or fast, compared to the vibrational coherence dephasing time. Fast pump fluctuations are coupled to the Stokes wave through the vibrational coherence; slow fluctuations are washed out. Second, many of the results on SRS in the literature are oscillator results in which the Stokes signal grows from noise. For a signal which grows from noise, the highest gain is obtained when the Stokes and pump amplitude and phase match [7-3, 7-10].

In order to quantify these ideas we can solve Equations (7-1) through (7-3) for arbitrary pump fluctuations

$$Q* = e^{-\Gamma t} \int_{-\infty}^{t} dt' e^{\Gamma t'} \left[iK_1 E_L^*(t') E_s(t') \right]$$ (7-21)

and

$$\frac{\partial E_s}{\partial z} + \frac{1}{v_s} \frac{\partial E_s}{\partial t} = K_1 K_2 E_L(t) e^{-\Gamma t} \int_{-\infty}^{t} dt' e^{\Gamma t'} E_L^*(t') E_s(t') \quad .$$ (7-22)

If $E_L(t)$ and $E_s(t)$ vary slowly compared to Γ^{-1}, then the integral can be performed so that

$$\frac{\partial E_s}{\partial z} + \frac{1}{v_s} \frac{\partial E_s}{\partial t} = \frac{K_1 K_2}{\Gamma} |E_L(t)|^2 E_s(t) \quad .$$ (7-23)

This equation was obtained directly by setting $\partial Q*/\partial t = 0$ in Equation (7-6), i.e., by assuming the vibrational coherence is time-independent. Substituting $E_s = \varepsilon_s e^{i\phi_s}$ into Equation (7-23) and equating real and imaginary parts yields (since K_1, K_2, Γ and $|E_L|^2$ are real):

$$\frac{\partial \phi_s}{\partial z} + \frac{1}{v_s} \frac{\partial \phi_s}{\partial t} = 0 \quad .$$ (7-24)

If $E_L(t)$ and $E_s(t)$ do not vary slowly compared to Γ^{-1}, then the right hand side of Equation (7-22) is a complex variable and

$$\frac{\partial \phi_s}{\partial z} + \frac{1}{v_s} \frac{\partial \phi_s}{\partial t} \neq 0 \quad .$$ (7-25)

7-16

Typical values of Γ^{-1} are 3 to 300 psec (0.1 to 10 cm^{-1})[7-1], so that pump fluctuations faster than 3 to 300 psec can cause phase transfer. These fluctuations can be due to a pulse shorter than Γ^{-1}, a rise-time shorter than Γ^{-1} or temporal spikes faster than Γ^{-1}.

If the pump laser is a multi-longitudinal mode device, as is true of many excimer lasers, fast temporal spikes may be due to the random interference of the longitudinal modes. Thus it is useful to examine the multi-mode case in detail. Following [7-3], we may write the Stokes and pump amplitude equations in the limit $\Delta\omega_j/\Gamma >> 1$ as

$$\frac{\partial E_{sj}}{\partial z} = \frac{g_o}{4} E_{pj}\left(\sum_i E_{si} E_{pi}^*\right) - \frac{i\Delta\omega_j}{v_s} E_{sj} \qquad (7-26)$$

$$\frac{\partial E_{pj}}{\partial z} = -\frac{\omega_p}{\omega_s}\frac{g_o}{4}\left(\sum_i E_{pi} E_{si}^*\right) - \frac{i\Delta\omega_j}{v_p} E_{pj} \quad , \qquad (7-27)$$

where E_{pj} and E_{sj} are the complex amplitudes of the j-th pump and Stokes mode, $\Delta\omega_j$ is the j-th longitudinal mode offset, and $g_o = 4K_1 K_2/\Gamma$. For a single longitudinal mode

$$\frac{\partial E_{S1}}{\partial z} = \frac{g_o}{4} E_{p1} (E_{S1} E_{p1}^*) - \frac{i\Delta\omega_1}{v_s} E_{S1} \quad , \qquad (7-28)$$

which is the same as (7-23); that is the coefficients are real. For two modes

$$\frac{\partial E_{S1}}{\partial z} = \frac{g_o}{4} E_{p1} (E_{S1} E_{p1}^* + E_{S2} E_{p2}^*) - \frac{i\Delta\omega_1}{v_s} E_{S1} \quad . \qquad (7-29)$$

The second term on the right hand side of Equation (7-29) is complex. This term is a four-wave mixing term in which the phase of E_{S1} is determined by the product $E_{p1}E_{S2}E_{p2}^*$. Unless E_{p1} and E_{p2} and E_{S1} and E_{S2} have the same phase, this term will mix phase. For n-modes, n-1 terms on the right of the analog of Equation (7-29) will mix phase. If the pump laser longitudinal mode spacing $\Delta\omega_j$ exceeds the dephasing rate Γ_1, we conclude that sufficient conditions for use of an SRS amplifier without phase corruption are (1) single longitudinal mode operation, or (2) identical phase aberrations on all pump modes. Necessary conditions are not yet worked out.

There is an additional mechanism that can couple pump amplitude variations to Stokes phase at high intensities. Saturated dispersion, analogous to that found in two-level systems [7-14], can cause this transfer. The basic equations for the phase under saturated conditions can be obtained for Equation (8b) of Reference [7-2]. The amplitude-to-phase transfer is negligible unless the vibrational population becomes of the order of the ground-state population. Detailed calculations[7-15] show that the phase is approximately given by

$$\phi_s \sim \frac{\pi\mu_{23}^2 I_p(0)}{\hbar^2 c\Gamma\Delta_L} \ln\left[I_s(z)/I_s(0)\right] \quad,$$

where $I_p(0)$ and $I_s(0)$ are initial pump and Stokes intensity. Typically, $I_p(0) = 100$ MW/cm^2 and $I_s(z)/I_s(0) = 10^3$, and ϕ_s is 0.01 to 0.5 radians, depending on the material. Thus, the phase due to saturated dispersion may limit operation to less than a few hundred watts/cm^2.

7.6 ILLUSTRATIVE CALCULATIONS FOR H$_2$ IN AN SLC-TYPE SYSTEM

Use of Raman scattering in H$_2$ for blue-green communication with a 308 nm pump laser (XeCl) requires three orders of Raman scattering, since $\nu_{vib} = 4155$ cm^{-1} [7-6]

$$\nu_\ell = 32,467 \text{ cm}^{-1}$$

$$\nu_{S1} = 28,312$$

$$\nu_{S2} = 24,157$$

$$\nu_{S3} = 20,003 \quad (\lambda = 0.5 \ \mu m).$$

We assume that the second Stokes radiation at 24,157 cm^{-1} is generated by an oscillator amplifier system and used as the pump shown in Figure 7-1 for the SRS amplifier in the reference-conjugate wave optical train.

The Raman gain coefficient g_o in H_2 is given by [7-14]

$$g_o = \frac{Nc^2 (d\sigma/d\Omega)_{90^o}}{3\hbar\nu_s^3 (c/v_s)^2 \Gamma} \quad ,$$

where $(d\sigma/d\Omega)_{90^o}$ is the differential cross section for Raman scattering, ν_s is the Stokes frequency, v_s is the Stokes group velocity, Γ is the vibrational linewidth, and N the atomic number density. For H_2, illustrative numbers are [7-1, 7-14]

$$N = 30 \ \text{amagat} = 30 \cdot 2.7 \cdot 10^{19} \ cm^{-3}$$

$$\Gamma = 0.75 \cdot 10^{-3} \cdot 30 \ cm^{-1}$$

$$v_s/c = 1$$

$$d\sigma/d\Omega = 1.6 \cdot 3.31 \cdot 10^{-30} \ cm^2/sr \cdot mol \quad ,$$

and we obtain $g_o = 3.33 \cdot 10^{-3}$ cm/MW. To obtain good efficiency, we require $\xi = g_o I_p(0) L \simeq 10$, where L is the length of the Raman cell. Assuming that an SLC system might operate with the following parameters,

Average power	100 kW
Repetition rate	30 Hz
Pulse length	1 μsec
Energy per pulse	4 kjoule,

we obtain average power during the pulse of 10^9. The beam size should be on the order of 3-5 cm in radius in order to obtain $g_o I_p(0) L \simeq 10$ in a reasonable cell length. These requirements must be matched to the saturation requirements of little higher-order Stokes radiation, little antistokes radiation, and little saturated dispersion. Since these effects all become important at a few hundred MW/cm^2, there is an operating range for H_2/SRS amplification in an SLC-type of system.

REFERENCES

7-1 J.R. Murray, J. Goldhar, D. Eimerl, and A. Szöke, "Raman pulse compression of excimer lasers for application to laser fusion", *IEEE J. Quantum Electron.*, QE-15, 342 (1979).

7-2 M.G. Raymer, J. Mostowski, and J.L. Carlsten, "Theory of stimulated Raman scattering with broad-band lasers", *Phys. Rev. A*, 19, 2304 (1979).

7-3 J. Eggleston and R.L. Byer, "Steady-state stimulated Raman scattering by a multimode laser". *IEEE J. Quantum Electron.*, QE-16, 850 (1980).

7-4 M. Maier, W. Kaiser, and J.A. Giordmaine, "Backward stimulated Raman scattering", *Phys. Rev.*, 177 580 (1969).

7-5 D. von der Linde, M. Maier and W. Kaiser, "Quantitative investigations of the stimulated Raman effect using subnanosecond light pulses", *Phys. Rev.*, 178, 11 (1969).

7-6 H. Komine, E.A. Stappaerts, W.H. Long, Jr., "Efficient Raman conversion of XeCl laser into the blue-green region", NOSC Technical Document 352, Vol. 1, p. 183 (1980).

7-7 V.S. Butylkin, G.V. Venkin, L.L. Kulyuk, D.I. Maleev, Yu. G. Khronopulo, and M.F. Shalyaev, "Role of the parametric and Raman processes in the generation of the second axial Stokes component of the stimulated Raman scattering", *Sov. J. Quantum Electron.*, 7, 867 (1977).

7-8 D.P. Bortfeld and W.R. Sooy, "Gain in a diffusely pumped Raman amplifier", *Appl. Phys. Lett.*, 7, 283 (1965).

7-9 A.A. Betin and G.A. Pasmanik, "Conservation of spatial coherence of Stokes beams amplified in a multimode pumping field", *JETP Lett.*, 23, 528 1976.

7-10 W. Trutna, Jr., Y.K. Park and R.L. Byer, "The dependence of Raman gain on pump laser bandwidth", *IEEE J. Quantum Electron.*, QE-15, 648 (1979).

7-11 B. Ya. Zel'dovich and V.V. Shkunov, "Wavefront reproduction in stimulated Raman scattering", *Sov. J. Quantum Electron.*, 7, 610 (1977).

7-12 B. Ya. Zel'dovich, N.A. Mel'nikov, N.F. Pilipetskii and V.V. Ragul'skii, "Observation of wave-front inversion in stimulated Raman scattering of light", *JETP Lett.*, 25, 36 (1977).

7-13 A.Z. Grasyuk, I.G. Zubarev, V.I. Mishin, and V.G. Smirnov, "Dynamics of the emission and amplification of light in stimulated Raman scattering", *Sov. J. Quantum Electron.*, 3, 380 (1974).

7-14 A. Yariv, _Quantum Electronics_, Wiley, New York, (1975) p. 155.

7-15 G.C. Valley, "Phase Preservation in Raman Amplifiers," submitted
       to _IEEE J. Quantum Electronics_, (1981).